Evaluation of Nitric Oxide Regarding the Functionality of the Gas Exchanger of an Extracorporeal Lung Support Device

Dissertation

zur Erlangung des Doktorgrades der Naturwissenschaften
(Dr. rer. nat.) der Fakultät für Chemie und Pharmazie der
Universität Regensburg

vorgelegt von

Moritz Köglmaier

aus Biburg

2024

Diese Doktorarbeit entstand im Zeitraum vom März 2021 bis September 2024 am Institut für physikalische und Theoretische Chemie der Universität Regensburg unter der Betreuung von Prof. Dr. Werner Kunz.

Abgabe der Promotion: **03.09.2024**

Datum des Promotionskolloquiums: **23.10.2024**

Promotionskomitee:

1. Gutachter: Prof. Dr. Werner Kunz

2. Gutachter: Prof. Dr. Rainer Müller

3. Prüfer: Prof. Dr. Frank-Michael Matysik

Vorsitzender: Prof. Dr. Oliver Tepner

Acknowledgments

This work was made possible by the support and contributions of many people I want to thank in this chapter.

Firstly, I want to thank Professor Dr. Werner Kunz for the opportunity to complete my dissertation as a member of his institute and for his support during this time. Likewise, I want to thank Professor Dr. Rainer Müller and Professor Dr. Michael Matysik for being the second and third referees for this dissertation and Professor Dr. Oliver Tepner for chairing the defense.

I want to thank the team at Hemovent GmbH, Dr. Oliver Marseille, Thilo Joost, Stefan Nötzel, and Dr. Georg Wagner, for their close cooperation and support in terms of knowledge and material throughout and beyond the NOAMED cooperation project. I also want to thank Dr. Rainer Köbrich from EKU Elektronik GmbH for providing the necessary equipment and valuable feedback during the project.

I want to thank the Zentrum für Innovation und Mittelstand (ZIM) for financing the NOAMED research project.

I thank Prof. Dr. Arno Pfitzner and his research group for granting permission to use the FTIR-ATR and SEM devices. I also want to thank Ulrike Schiessl for producing the SEM recordings shown in this thesis.

I thank Dr. Günter Auernhammer, Anja Caspari, Stefan Michel, and Niklas Gerlach at the Leibniz Institute for Polymer Research Dresden for conducting zeta potential and dynamic contact angle measurements.

I want to thank Dr. Matthias Kronseder for conducting and analyzing the XPS measurements shown in this thesis.

I want to thank Christine Driesslein and Taisia Horsun for their contributions to this thesis as part of their research lab course and bachelor's thesis, respectively.

I also want to thank Chantal Walser, Selina Reigl, Vanessa Rudolph, Maximilian Rauch, Lisa Tetek, Julia Neugebauer, and Jennifer Schuster for the pleasant and productive office atmosphere.

Finally, I want to thank my parents, Bernhard and Christine Köglmaier, for their unconditional support throughout this time.

Abstract

Extracorporeal membrane oxygenation (ECMO) is a method of mechanical ventilation that bypasses the patient's lung and oxygenates the blood in an external circuit utilizing an "oxygenator". The oxygenator investigated in this thesis was part of the so-called "Mobybox" ECMO circuit developed and manufactured by Hemovent GmbH. A significant weakness of these devices is the formation of thrombi in the oxygenator, which limits usage time. The thesis aimed to evaluate the use of nitric oxide (NO) as an additive to the oxygenator sweep gas capable of suppressing the thrombus formation. The central aspect investigated was the interaction of NO with the polymer materials of which the oxygenator was constructed. These materials included the hollow fiber membrane made of polymethylpentene (PMP), the inlet/outlet cap, and the gas cap, both made of methylmethacrylate acrylonitrile butadiene styrene (MABS), methylene diisocyanate (MDI) and trimethylolpropane (TMP) based polyurethane (PU) which constitutes the main structural components, a silicone gasket sealing the gas cap to the oxygenator body, a UV-activated adhesive containing 2-hydroxyethyl methacrylate, isobornyl acrylate, and 1-vinylhexahydro-2H-azepine-2-one, and the blood and gas hoses both manufactured from polyvinyl chloride (PVC) and plasticized with tris(2-ethylhexyl) trimellitate (TEHTM) and bis(2-ethylhexyl) terephthalate (DOTP), respectively. The interaction between NO and these materials was investigated using Fourier-transform infrared attenuated total reflectance spectroscopy (FTIR-ATR), dynamic and static contact angle measurements, zeta potential measurements, scanning electron microscopy (SEM), and x-ray photoelectron spectroscopy (XPS). Additionally, the influence of NO on the hemolytic properties of the oxygenator was investigated using UV/Vis spectroscopy, vapor pressure osmometry, and pH measurements. The investigations with FTIR-ATR showed that the interaction between the polymer materials and NO led to the formation of nitro and nitrate ester functional groups and the adsorption of HNO_3 molecules on the polymer surfaces with MABS and PU. With PVC, only nitrate ester groups and HNO_3 molecules were formed. PMP, the silicone gasket, and the UV-activated adhesive remained largely unaffected by the NO treatment below concentrations of 10,000 ppm. These effects on the surface chemistry of the polymers proved to be stable and long-lasting. The XPS measurements confirmed these results and revealed that the reactions occurred exclusively on the polymer surfaces. The contact angle measurements showed that the formation of these functional groups and the adsorption of HNO_3 molecules led to an increase in surface hydrophilicity for MABS and PU. PMP was again unaffected. The zeta potential measurements showed that PU likely had the highest surface concentration of HNO_3 molecules as it was the only material that showed a shift in the potential curve towards a more acidic surface. The SEM images recorded of the different polymer materials showed no change in surface morphology or porosity of the samples. The investigation on the hemolytic properties of the oxygenator showed no significant influence of NO either. Overall, the results obtained throughout this thesis showed that NO had no adverse effects on the oxygenator's functionality, structural integrity, blood compatibility, or hemolytic properties despite the changes to the surface chemistry it caused with most of the polymer materials.

Zusammenfassung

Extrakorporale Membranoxygenierung (ECMO) ist eine Methode der mechanischen Beatmung, die die Lunge des Patienten umgeht und dessen Blut in einem externen Kreislauf mit Hilfe eines sogenannten „Oxygenators“ oxygeniert. Der Oxygenator, der in dieser Arbeit untersucht wurde, war Teil des sogenannten „Mobybox“-ECMO-Kreislauf, der von der Hemovent GmbH entwickelt und hergestellt wird. Eine große Schwachstelle dieser Geräte ist die Formation von Thromben im Oxygenator, was die Laufzeit dieser Kreisläufe einschränkt. Das Ziel dieser Arbeit war die Evaluierung der Nutzung von Stickstoffmonoxid (NO) als Additiv zum Beatmungsgas des Oxygenators, welches die Thrombusformation unterbinden kann. Hauptsächlich untersucht wurde die Interaktion von NO mit den Polymermaterialien, aus denen der Oxygenator aufgebaut ist. Diese Materialen waren die Hohlfasermembranen, hergestellt aus Polymethylpenten (PMP), der Einlass-/Auslassdeckel und die Gaskappe hergestellt aus Methylmethacrylat-Acrylnitril-Butadien-Styrol (MABS), Polyurethan (PU) bestehend aus Methylendiisocyanat (MDI) und Trimethylolpropan (TMP) Monomeren, welches als primäre strukturelle Komponente agierte, eine Silikondichtung welche die Gaskappen abdichtete, einen UV-aktivierten Klebstoff bestehend aus 2-Hydroxyethylmethacrylat, Isobornylacrylat, and 1-Vinylhexahydro-2H-azepine-2-on und die Blut- und Gasschläusche, welche beide aus Polyvinylchlorid (PVC) hergestellt waren und jeweils den Weichmacher Tris(2-ethylhexyl)trimellitat (TEHTM) und Bis(2-ethylhexyl)terephthalat (DOTP) beinhalteten. The Interaktion von NO mit diesen Materialien wurde untersucht mit Fourier-Transform-Infrarotspektroskopie mit abgeschwächter Totalreflektion (FTIR-ATR), dynamischen und statischen Kontaktwinkelmessungen, Zetapotentialmessungen, Rasterelektronenmikroskopie (REM) und Röntgenphotoelektronenspektroskopie (XPS). Zusätzlich wurde der Einfluss von NO auf die hämolytischen Eigenschaften des Oxygenator mit Hilfe von UV/Vis-Spektroskopie, Dampfdruckosmometrie und pH-Messungen untersucht. Die Untersuchungen mit FTIR-ATR zeigten, dass die Interaktion zwischen den Polymermaterialien und NO zur Formation von Nitro- und Nitratgruppen, sowie zur Adsorption von HNO_3-Molekülen auf den Oberflächen der MABS- und PU-Polymere führten. Im Falle von PVC formierten sich lediglich Nitrat-Gruppen und HNO_3-Moleküle an der Oberfläche. PMP, die Silikondichtung und der UV-aktivierte Klebstoff zeigten keine sichtbare Reaktion durch die NO-Behandlung bei Konzentrationen unterhalb von 10.000 ppm. Diese Einflüsse auf die Oberflächenchemie der Polymere erwiesen sich als

langzeitstabil. Die XPS-Messungen bestätigten diese Resultate und zeigten, dass die Reaktionen ausschließlich an den Oberflächen der Polymere stattfanden. Die Kontaktwinkelmessungen zeigten, dass die Formation dieser funktionalen Gruppen und die Adsorption der HNO_3-Moleküle im Falle von MABS und PU zu einem Anstieg der Oberflächenhydrophilie führten. PMP blieb wiederum unbeeinflusst. Die Zeta-Potentialmessungen zeigten das PU sehr wahrscheinlich die höchste Oberflächenkonzentration an HNO_3-Molekülen besaß, da es das einzige Polymer war, dass eine Veränderung der Potentialkurve typisch für eine azidere Oberfläche zeigte. Die REM-Bilder der unterschiedlichen Polymere zeigten keine Veränderungen im Hinblick auf Oberflächenmorphologie und Porosität der Proben. Die Untersuchungen bezüglich der hämolytischen Eigenschaften des Oxygenators zeigten ebenfalls keinen signifikanten Einfluss von NO. Insgesamt zeigten die Ergebnisse, die im Rahmen dieser Arbeit erzeugt wurden, dass NO keine negativen Effekte auf die Funktionalität, die strukturelle Integrität, die Blutkompatibilität oder die hämolytischen Eigenschaften des Oxygenators hatte, trotz der Veränderungen der Oberflächenchemie bei den meisten Polymermaterialien.

Abbreviations

ABS	Acrylonitrile butadiene styrene
ADP	Adenosine diphosphate
ARDS	Acute respiratory distress syndrome
cGMP	Cyclic guanosine monophosphate
CMF-DPBS	Calcium and magnesium-free Dulbecco’s phosphate-buffered saline
COVID-19	Coronavirus disease 2019
DEHP	Di-2-ethylhexyl phthalate
DEPA	Bis(2-ethylhexyl) adipate
DMO	Direct membrane osmometry
DOTP	Bis(2-ethylhexyl) terephthalate
ECMO	Extracorporeal membrane oxygenation
EDRF	Endothelium-derived relaxing factor
FAD	Flavin adenine dinucleotide
FMN	Flavin mononucleotide
FPO	Freezing point osmometry
FTIR-ATR	Fourier transform infrared attenuated total reflection
G6PD	Glucose-6-phosphate dehydrogenase deficiency
GP	Glycoprotein
GPVI	Glycoprotein VI
HCl	Hydrochloric acid
HIT	Heparin-induced thrombocytopenia
H_2SO_4	Sulfuric acid
HDPE	High-density polyethylene

HNO	Nitroxyl
HNO_2	Nitrous acid
HNO_3	Nitric acid
IEP	Isoelectric point
IP_3	Inositol 1,4,5-triphosphate
IRE	Internal reflection element
MABS	Methyl methacrylate-acrylonitrile-butadiene-styrene
Met-Hb	Methemoglobin
MDI	Methylene diphenyl diisocyanate
N_2O_3	Dinitrogen trioxide
NADPH	Nicotinamide adenine dinucleotide phosphate
NMDAR	N-methyl-D-aspartate receptors
NO	Nitric oxide
NOS	Nitric oxide synthase
eNOS	Endothelial constitutive NO synthase
iNOS	Inducible NO synthase
nNOS	Neuronal constitutive NO synthase
NO_2	Nitrogen dioxide
$ONOO^-$	Peroxynitrite
Oxy-Hb	Oxyhemoglobin
PEG	Polyethylene glycol
PI3-K	Phosphoinositide 3-kinase
PKG	Protein kinase
PMMA	Polymethylmethacrylate
PMP	Polymethylpentene

PU	Polyurethane
PVC	Polyvinyl chloride
PVC-C	Chlorinated PVC
PVC-P	Plasticized PVC
PVC-U	Unplasticized PVC
RNOS	Reactive nitrogen oxide species
RVAD	Right ventricular assisted device
SARS-CoV-2	Severe acute respiratory syndrome coronavirus 2
SCR	Selective catalytic reduction
SEM	Scanning electron microscopy
SET	Single electron transfer
sGC	Soluble guanylate cyclase
SNCR	Selective non-catalytic reduction
SO_2	Sulfur dioxide
SO_3	Sulfur trioxide
TEM	Transmission electron microscopy
TMP	Trimethylolpropane
TOHTM	Tris(2-ethylhexyl) trimellitate
TXA_2	Thromboxane A_2
UV	Ultraviolet light
VC	Vinyl chloride
Vis	Visible light
VPO	Vapor pressure osmometry
XPS	X-ray photoelectron spectroscopy

Units

cN	Tensile strength in centinewton
CPS	Counts per second
eV	Binding energy in electron volt
g/cm^3	Density in grams per cubic centimeter
g/L	Mass concentration
GPa	Tensile strength/modulus in gigapascal
kJ/m^2	Unnotched impact strength in kilojoule per square meter
L/min	Flow rate in liters per minute
mOsmol/kg	Osmolality in milliosmoles per kilogram
MPa	Tensile strength/modulus in megapascal
mV	Streaming potential in millivolt
nm	Wavelength in nanometer
phr	Plasticizer concentration in parts per hundred rubber
ppm	Gas concentration in parts per million
wt%	Weight percent

Contents

1. Introduction

1.1 ECMO, Covid 19, and NO

Central to this thesis is a medical technique known as extracorporeal membrane oxygenation (ECMO). ECMO is a method of mechanical ventilation that has been a part of the medical landscape since the first successful trial in the 1970s [1]. The technique works as follows: Blood is pumped from the patient's bloodstream, oxygen is added to, and CO_2 is removed from the blood in a so-called oxygenator, and the blood is pumped back into the patient. The main application of this technique is with patients suffering from conditions such as acute respiratory distress syndrome (ARDS) [2, 3]. It has seen a steady increase in use compared to other mechanical ventilation techniques up to the present day, with strong increases in usage over the last two decades with generally superior health outcomes compared to other ventilation techniques [4].

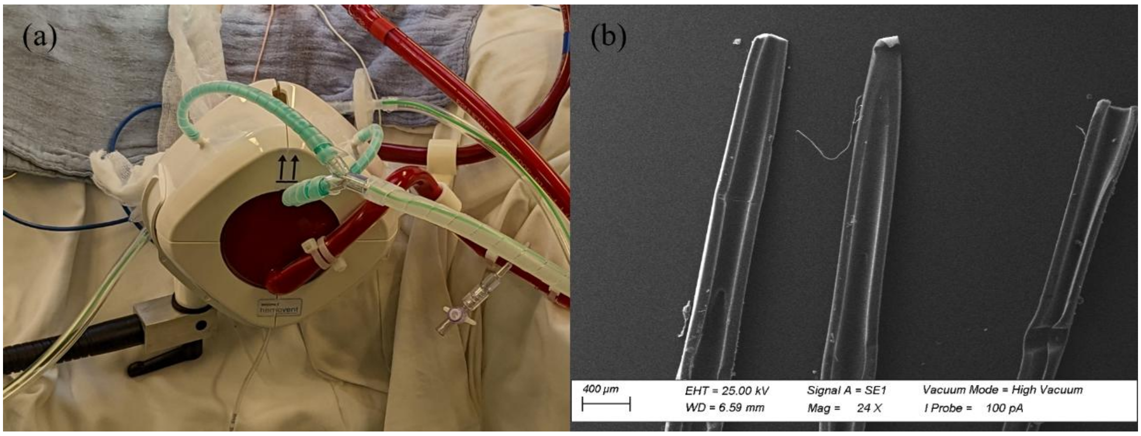

Figure 1.1: (a) Picture of the oxygenator of the “Mobybox” produced by Hemovent during use. (b) SEM image of the hollow fiber membranes of the oxygenator cut apart lengthwise.

ECMO gained significant importance with the arrival of the coronavirus disease 2019 (COVID-19) in late 2019 and early 2020 [5]. The disease is caused by an infection with the severe acute respiratory syndrome coronavirus 2 (SARS-CoV-2) and developed into a worldwide pandemic throughout early 2020. In most cases, the disease expresses itself as a mild to moderate infection of the upper airways. In severe cases, the disease can progress to pneumonia and, finally, ARDS, necessitating the usage of artificial ventilation. The infection can progress further to complete respiratory and multi-organ failure [6]. ECMO played an essential role in supporting these patients, with its usage increasing significantly in 2020 compared to 2019 [5]. Despite ECMO’s rise in importance, certain weaknesses remain. One of these weaknesses and the focus of this thesis is the formation of thrombi in the ECMO circuit. These thrombus formations pose a risk to both patients in the form of thromboembolisms and to the ECMO circuit itself by limiting the lifespan and efficiency of the ECMO circuit. Therefore, further development of ECMO circuits is still necessary to improve patient outcomes [7–9].

One potential route of improving the long-term performance of ECMO circuits that has been investigated is using nitric oxide (NO) to suppress the thrombus formation in the ECMO circuit. NO is a reactive gas with a wide variety of physiological functions (more details in Chapter 2.2.2) [10, 11]. Most importantly, for its application in ECMO circuits, it is part of the natural blood coagulation process. Here, it acts as a regulating agent for the aggregation of blood platelets [12, 13]. Different techniques of adding NO to ECMO circuits have been tried in the past, such as using NO-releasing polymers [14]. However, the direct addition of NO to the sweep gas mixture remains under-discussed, which is thus the focus of the thesis presented in the following chapters.

1.2 Goals of this Dissertation

This dissertation is based on research conducted as part of the project "NOAMED – Stickstoffmonoxid zur Oberflächenmodifikation beim Einsatz von Gasaustauschern bei der extrakorporalen Lungenunterstützung". The project was a cooperation between the company Hemovent GmbH (Aachen, Germany) and the chair of physical chemistry and solution chemistry of Professor Dr Werner Kunz at the University of Regensburg (Regensburg, Germany). The project was funded by the "Zentrales Innovationsprogramm Mittelstand" (ZIM) or "Central Innovation Program for Small and Medium-sized Enterprises" financed by the Federal Ministry for Economic Affairs and Climate Action. The goals of the project were to evaluate the viability of adding NO to the sweep gas of an ECMO circuit, specifically the so-called "Mobybox" produced by Hemovent. Investigations were focused on the oxygenator of the ECMO circuit. On the side of the University, investigations focused on the effects of NO on the polymer materials that make up the oxygenator. The goal was to find suitable analytical techniques to analyze these effects and to find interpretations explaining the observed effects. A further goal included investigations into the solubility and distribution of NO in blood-analogous fluids. Hemovent's part of the project focused on adapting the oxygenator design based on these findings and developing a way to add NO to the sweep gas for the commercial product. This thesis will focus on the methods and results of the University of Regensburg.

2. Fundamentals

2.1 Extracorporeal Membrane Oxygenation (ECMO)

2.1.1 History

Extracorporeal membrane oxygenation (ECMO) is a medical technique for supporting patients suffering from conditions degrading their respiratory function to a point where internal respiration is no longer sufficient to sustain the patient. The most common patient condition to which this technique is applied is ARDS. Other, more short-term scenarios include patient support during cardiac surgery or lung transplants [2]. The history of ECMO devices goes back to the early middle of the 19th century, beginning with relatively simple isolated experiments concerning artificial blood oxygenation [15]. Throughout the early 20th century, the first mechanical oxygenators were developed (see Figure 2.1) [16–19].

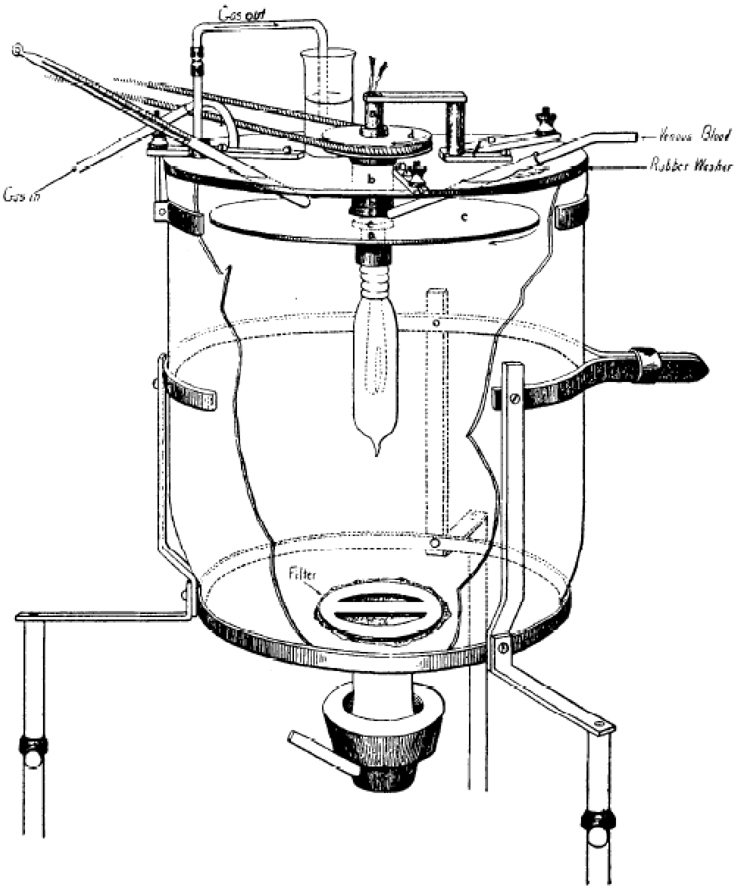

Figure 2.1: Schematic depiction of an early mechanical oxygenator (called an “apparatus for aerating blood”) utilizing a rotating rubber disc (letter c in the depiction). Blood enters the oxygenator from the top, lands on the rubber disc, is thrown outwards, runs down a thin film exposed to the air, and finally pools at the bottom of the oxygenator [17].

An essential early milestone in the development of ECMO devices during the same time frame was the discovery of heparin in 1916 [15, 20]. This discovery made it possible to reliably prevent blood coagulation, significantly increasing the oxygenator's use time. Important mechanical designs include the film oxygenator by Gibbon et al. [16, 21–23], the rotating disc oxygenator by Bjork et al. [24], and the all-glass bubble oxygenator by Clarke et al. [25], introduced in 1937, 1948, and 1952 respectively. All of these designs were so-called direct contact oxygenators, meaning the sweep gas mixture was brought into direct contact with the patient's blood. This method of oxygenation resulted in overall low efficiency compared to modern oxygenators. It also led to high degrees of mechanical stress on the blood, resulting in hemolysis, coagulation disorders, and protein denaturation in the blood [15]. These deficiencies led to a maximum period of use of about four hours [26]. The oxygenator designs remained in widespread clinical use until the 1970s despite their shortcomings [15].

As early as the 1940s, alternatives to direct oxygenation were developed. The designs included a protective membrane between the sweep gas mixture and the blood [27]. The central advantage of such a barrier between blood and gas was decreased blood trauma compared to direct oxygenation. Central to the development of these oxygenators was the selection of the membrane material. The material needed to ensure sufficient gas transfer of both oxygen and CO_2, have suitable mechanical properties, and cause no issues when interfacing with blood [15]. Ethyl cellulose and polyethylene were the starting points for the membrane development [28]. Throughout this development, these materials were replaced by polymers such as polytetrafluoroethylene [29], which were then replaced by silicone membranes starting in the late 1950s [30]. Silicone membrane oxygenators remain in clinical use up to the modern day [31]. The development focus then shifted from the membrane material to oxygenator geometry. The thickness of the bloodstream was the primary factor limiting the efficiency of thin film membrane oxygenators. This limited the contact area between blood and membrane and, therefore, also the gas transfer efficiency [32]. To increase the efficiency, silicone capillary oxygenators were developed. These capillaries are generally referred to as hollow fibers [33]. Early configurations of such hollow fiber oxygenators channeled the blood flow through the inside of the hollow fiber, with the sweep gas being channeled around the outside of the fibers [34]. In addition to the geometry development, microporous membranes were developed as alternatives to solid silicone membranes [35]. Microporous polypropylene emerged as the material of choice, having a sufficiently small pore size and being cheap and reliable to manufacture [15]. Such microporous membranes were subsequently used as hollow fiber membranes, improving efficiency compared to silicone membranes [36]. Using microporous hollow fiber membranes also decreased manufacturing complexity and cost [15].

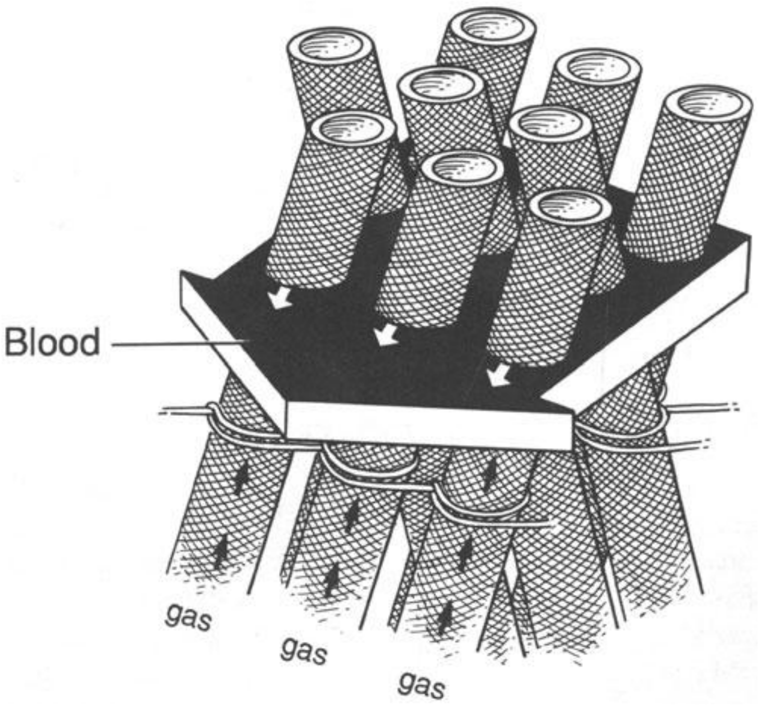

Figure 2.2: Schematic depiction of the oxygenator sweep gas flowing inside the hollow fiber membrane while the blood flows past on the outside of the fibers [37].

The next significant development step in oxygenator geometry was the switch from a hollow fiber oxygenator with the blood flow on the inside of the hollow fiber to blood flow on the outside of the hollow fiber. This switch led to decreased pressure on the inside of the hollow fiber membrane and an increase in efficiency due to the larger outer surface area of the hollow fiber acting as the contact surface between blood and the gas mixture [36, 37]. The final step of development, leading to the technological state of the oxygenator discussed in this thesis, was the introduction of polymethylpentene as a membrane material. PMP led to extended oxygenator life spans while maintaining the same oxygenation efficiency as microporous polypropylene [38, 39].

2.1.2 Working Principle

ECMO devices can be operated in two modes: veno-venous and veno-arterial [2]. With VV ECMO, two common cannulation approaches are taken, using a femoral vein as the drainage point in both cases. Either the other femoral vein or a jugular vein is used for infusion. A further variant of VV ECMO is the so-called dual lumen single bicaval cannulation, where drainage and infusion are handled via a single cannulation into a jugular vein [2, 40]. VA ECMO generally uses six different cannulation approaches. Four of these are peripheral cannulation approaches. Three of the peripheral cannulation approaches use a femoral vein for drainage and either an axillary, carotid, or femoral artery for infusion [2]. The fourth peripheral cannulation approach, the so-called sport configuration, uses a jugular vein for drainage and an axillary artery for infusion [41]. The central cannulation approach and the right ventricular assisted device (RVAD) access the right atrium for drainage and the ascending aorta or the pulmonary artery for infusion [2]. The central cannulation approach is generally used in short-term scenarios, such as patient support during surgery. Peripheral cannulation is used in longer-term scenarios [41]. Overall, this paragraph provides an overview of the basic cannulation techniques used with ECMO devices. More advanced techniques such as Veno-arterio-venous (VAV) ECMO exist but are not discussed further here, as they just represent further variations of existing cannulation geometries utilizing the same blood vessels [40].

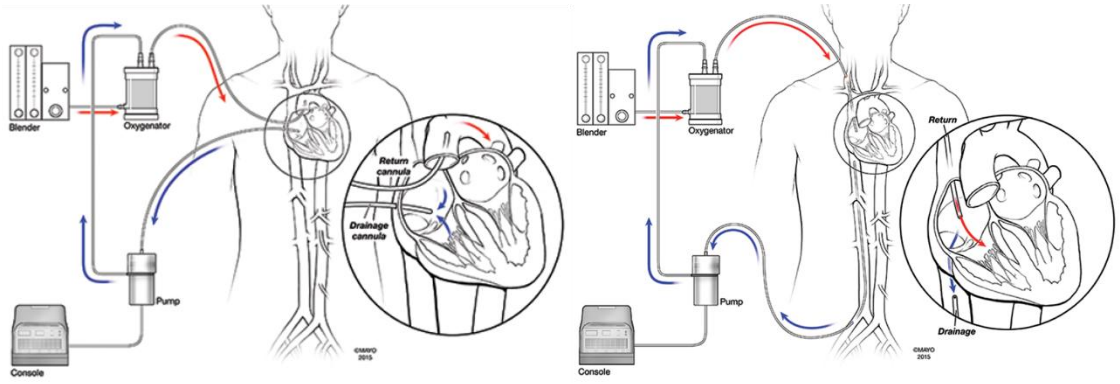

Figure 2.3: On the left: Schematic depiction of a central veno-arterial cannulation. On the right: Schematic depiction of a central veno-venous canulation [42].

VV and VA ECMO have advantages and disadvantages, leading to different application scenarios. VV ECMO requires a patient with stable hemodynamics to be implemented as this cannulation technique does not bypass the heart or lung, maintaining pulmonary blood flow [2]. It is mainly used in cases of severe respiratory failure [43, 44]. VA ECMO bypasses both heart and lung entirely, with only the RVAD cannulation technique channeling blood through one half of the heart, providing respiratory and hemodynamic support [2]. It is commonly employed during heart transplantations or as an alternative to a cardiopulmonary bypass [43]. VA ECMO generally provides better oxygenation efficiencies than VV ECMO, as the externally oxygenated blood is mixed with arterial blood and can directly perfuse distal organs [2]. VA ECMO also results in less frequent oxygenator failure than VV ECMO [45]. Regarding patient survival rates, research is somewhat inconclusive, with some seeing an advantage for VV ECMO, while others do not see an advantage for either technique [43, 45, 46].

After the blood is taken from the patient, it travels through hoses toward the oxygenator. In most cases, this blood flow is driven by a pump that sits in between the drainage cannulation site and the oxygenator. The two most common pump types employed in ECMO devices are centrifugal and peristaltic pumps [47]. These types of pumps cause significant amounts of mechanical stress to the blood, which leads to hemolysis and thrombus formation [48, 49]. Centrifugal pumps have been found to have a generally better performance in this regard compared to peristaltic pumps, although the issue is still present with this pump type as well [49, 50]. A membrane pump was used in the ECMO device investigated in this thesis to improve the hemolytic and thrombogenic properties. This two-chamber membrane pump used a polyurethane membrane integrated into a pump body made from MABS plastic. The membrane was pneumatically driven by the sweep gas flow to avoid the usage of an external power supply [51].

As discussed previously, throughout the development history of ECMO, a wide variety of oxygenators were developed and produced (see Chapter 2.1.1). Even just the oxygenators still in use today represent a wide variety of shapes and sizes [52]. The following discussion of the oxygenator’s construction is limited to the oxygenator contained in the so-called “Mobybox” produced by Hemovent, as it is the only oxygenator relevant to this thesis.

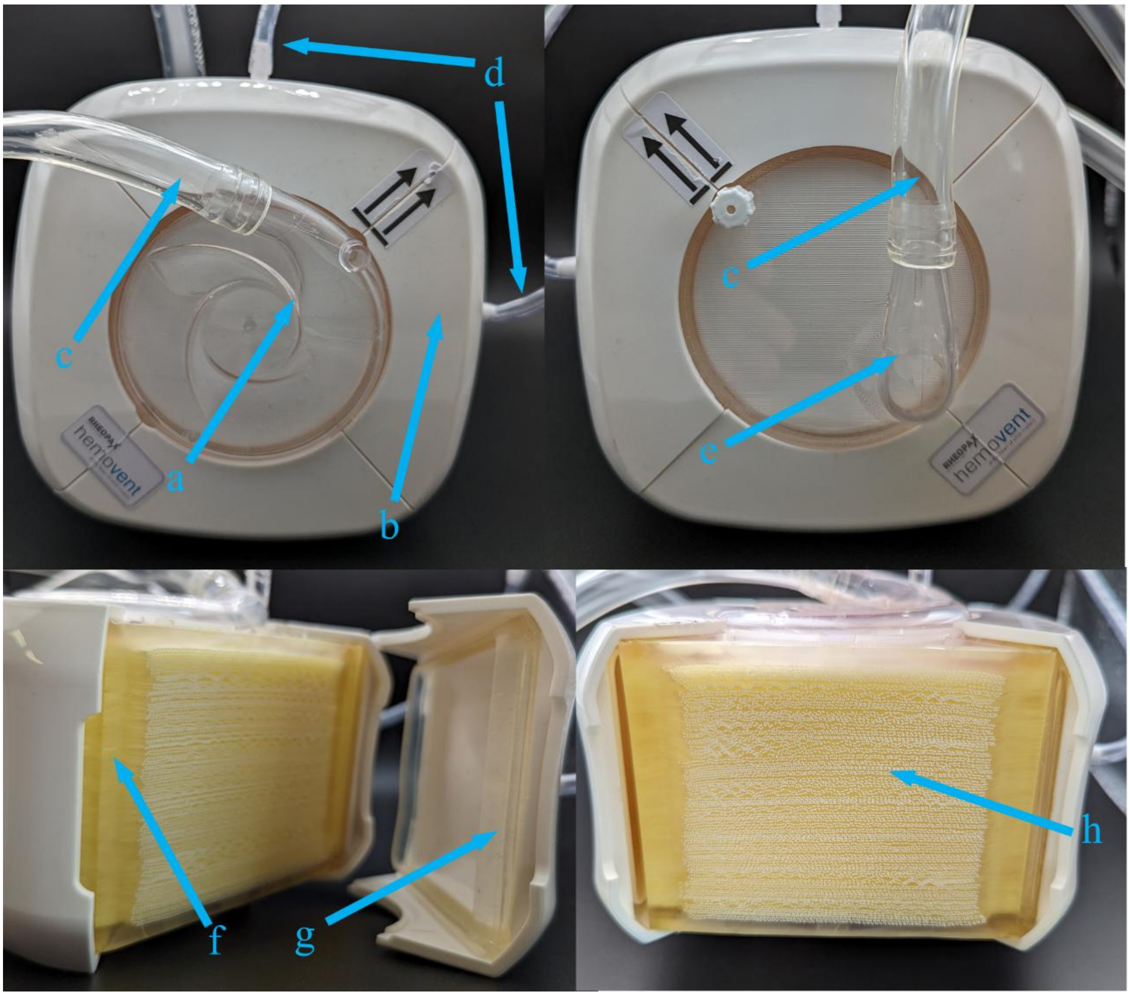

Figure 2.4: Overview of the constituent parts of the oxygenator: (a)The inlet cap (MABS), including the hose connection for the blood hose. The hollow fiber membrane (PMP) is visible through the inlet cap. (b) The gas cap (MABS) clipped to the side of the oxygenator body. Two of the gas caps have integrated hose connectors and are sealed to the oxygenator body using a (g) silicone gasket. (c) The blood hoses (PVC) are connected to the inlet and outlet cap hose connectors. (d) The gas hoses (PVC) are connected to two of the four gas caps via the integrated hose connectors. (e) The outlet cap (MABS), including the hose connection for the blood hose. The hose connection is attached to the outlet cap using a UV-activated adhesive. The hollow fiber membrane is visible through the outlet cap. (f) PU-Material constituting the primary structural element of the oxygenator body. (h) The ends of the hollow fiber membrane (PMP) encased in the PU-Material.

The oxygenator used in this device utilizes PMP hollow fiber membranes arranged in mats. These mats are layered on top of each other in an alternating fashion, with the fiber direction of every other mat layer oriented perpendicular to the layer above and below. Each fiber has an outer diameter of 380 µm and an inner diameter of 200 µm, with a wall thickness of 80 µm. The total surface area of the hollow fiber used in the oxygenator is 1.6 m^2 [8]. The ends of these hollow fibers are encased in PU, which forms the main structural component of the oxygenator. The PU material was cut down to size, exposing the hollow fiber openings at each fiber end. The cavity in the middle of the PU material containing the exposed hollow fiber is closed off with an inlet and an outlet cap, both made from MABS plastic, containing the connectors for the blood hoses. Clipped to the outside of the oxygenator are the so-called gas caps. Two of these gas caps are sealed to the PU body with a silicone gasket. Due to the gaskets, the sweep gas flow connected to these two gas caps is forced to flow through the hollow fibers. During operation, CO_2-rich venous blood flows through the hollow fiber membrane mats perpendicular to the fiber orientation. As the blood flows through the oxygenator, its pressure drops by around 19 mmHg at a flow rate of 4 L/min. This represents a relatively low pressure drop compared to other oxygenators [8]. The oxygen in the sweep gas mixture diffuses into the blood through the hollow fiber membrane. At the same time, the CO2 present in the blood diffuses into the hollow fiber membrane. In animal testing, maximum oxygen transfer rates of around 220 mL/min and CO_2 transfer rates of 283 mL/min were achieved [8]. The now oxygenated blood exits the oxygenator and flows back into the patient. The sweep gas mixture travels along inside the hollow fibers, being vented into the surrounding air at the end of the fibers.

2.1.3 Complications

ECMO treatment can lead to a wide range of possible complications. A common complication is bleeding at the cannulation site, as well as internal hemorrhaging in various locations. Bleeding and hemorrhaging primarily arise due to the heparinization of the ECMO circuit, leading to a decreased blood clotting ability [2, 53]. The most common cause of death for ECMO patients is intracranial hemorrhaging, with 43% of deaths being associated with this condition [54]. The choice of anticoagulant can also cause issues. Heparin is the most common anticoagulant for ECMO circuits. However, patients can develop antibodies to platelet factor four, leading to Heparin-induced thrombocytopenia (HIT). This complication can be mitigated by switching to other anticoagulants [55, 56]. Neurological complications are also a known risk, with seizures, infarction, and intracranial hemorrhage being common symptoms [57, 58]. ECMO patients commonly suffer from medical complications like hypertension, arrhythmia, oliguria, and gastrointestinal hemorrhage [2]. Due to the ECMO circuit being a large foreign body in the bloodstream, septic complications are also well-known [59].

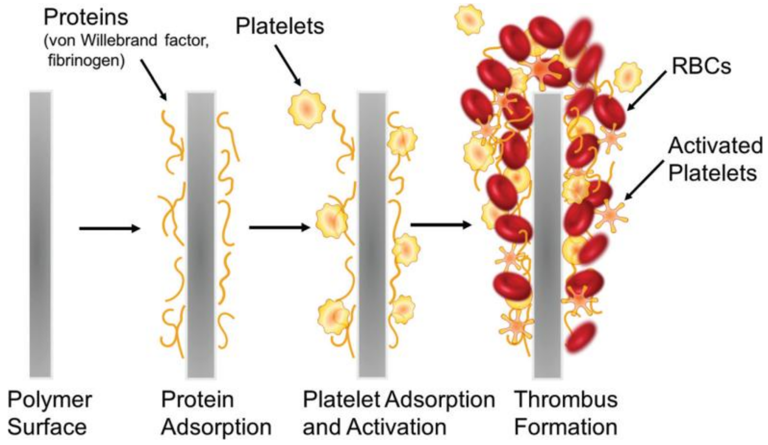

Figure 2.5: Simplified schematic depiction of the mechanism of thrombus formation in blood-containing biomedical devices [60].

Thrombus formation is another common complication in ECMO devices and the focus of this thesis. The oxygenator and pump are significant contributors to thrombus formation, as are the connection points of the blood hoses. The moving parts of the pump and the complex surface of the oxygenator cause turbulent blood flow, where thrombi preferentially form [7]. On the one hand, thrombus formation represents a medical risk for the patient. It can potentially cause systemic, cardiac, and pulmonary thromboembolisms as well as consumption coagulopathy [2, 61]. However, the risk for thromboembolisms can be largely mitigated by monitoring the ECMO circuit [61]. The main issue with thrombus formation is mechanical. The ECMO circuit becomes increasingly occluded as more and larger thrombi form in the ECMO circuit, especially around the oxygenator and the pump [50]. This leads to a decrease in pump efficiency and blood flow rate, decreasing the oxygenation efficiency [8, 9]. The ultimate result of this development is oxygenator failure. This means that the oxygenator has to be replaced, especially if more prominent thrombi form [7]. Replacement of parts of the ECMO leads to an interruption in patient support for the duration of the procedure and further dilution of the blood. Inflammation is also a risk factor due to renewed surface contact activation [62].

2.2 Nitric oxide (NO)

2.2.1 General Information

Nitric oxide (NO) is a highly reactive diatomic free radical. The gas is industrially produced using the Ostwald method. In this process, a mixture of ammonia and air is passed over a heated platinum catalyst, resulting in the formation of nitric oxide and water [63]:

$$4\ NH_3 + 5\ O_2 \longrightarrow 4\ NO + 6\ H_2O \qquad (1)$$

NO is naturally produced via the oxidation of one of the guanidino groups of L-arginine, catalyzed by the enzyme nitric oxide synthase (NOS) [64].

2.2.2 Environmental Role

Nitrogen oxides present in the atmosphere originate from a wide variety of sources. Among them are natural causes such as the stratosphere-troposphere exchange, lightning, and microbial processes in the soil [65]. Besides the natural, anthropogenic sources play an ever-increasing role in the atmospheric concentration of these compounds. The main sources of anthropogenically created NO are burning fossil fuels and biomass and agricultural emissions. The burning of fossil fuels is the source of various pollutants, including carbon monoxide, unburned hydrocarbons, and nitrogen oxides [66, 67]. In agriculture, the primary source of NO emissions is the use of ammonium-based fertilizers. Only about half of the fertilizer applied to a given crop field is absorbed by the plants. The remaining fertilizer is left to react further through reactions catalyzed by bacteria or fungi. Ammonia is produced in the first step, followed by NO_3^- through nitrification. NO_3^- can then be reduced and forms nitrogen oxides such as N_2O and NO through the so-called denitrification [68]. Unlike greenhouse gases such as CO_2, N_2O, or methane, NO does not directly absorb radiation. Instead, it leads to an increased production of O_3 in the troposphere. The highly reactive nature of NO also leads to further reactions, with the potential of altering the atmospheric chemistry [67, 69].

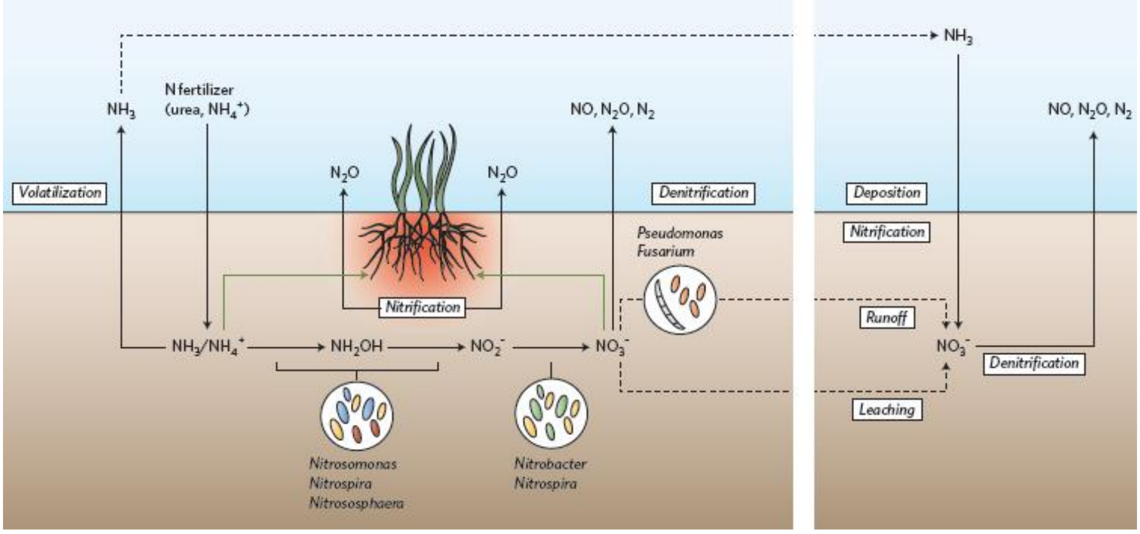

Figure 2.6: Schematic depiction of the processes nitrogen-based fertilizers undergo after their addition to agricultural systems [68].

A variety of strategies to avoid the release of NO into the atmosphere have been developed over time. One of the most prominent is the three-way catalytic converter employed in automobiles. The widespread introduction of these catalytic converters in cars throughout the 1970s and 80s has curbed the emission of nitrogen oxides in general and NO specifically in recent decades, with conversion rates upwards of 80 percent [70]. For industrial sources of nitrogen oxides, a variety of methods has been employed, ranging from modifications to combustion processes to exhaust treatment methods such as selective catalytic reduction (SCR) and selective non-catalytic reduction (SNCR) [71, 72]. The mitigation of emissions from agriculture, mainly through fertilization, proved more challenging. Potential pathways are more precision in the application of fertilizer to reduce excess concentrations of nitrogen species or the application of nitrification inhibitors, which include compounds such as dicyandiamide or nitrapyrin. As these compounds have significant drawbacks in terms of both cost and pollution risks, research into biological nitrification inhibitors such as brachialactone or 1,9-decanediol has also been conducted [68].

2.2.3 Biological Role

2.2.3.1 Overview

Until the 1980s, NO was almost exclusively discussed as an environmental pollutant. In the late 1970s and 80s, research led to the first discoveries concerning the biological role of NO [73]. F. Murad et al. discovered that NO increases the activity of guanylate cyclase and the accumulation of cyclic guanosine monophosphate (cGMP) in animal tissue samples [74]. During the 1980s, R.F. Furchgott et al. conducted extensive investigations into vasodilators such as acetylcholine, bradykinin, and ATP. These investigations led to the discovery of a connection between these compounds' vasodilatory effect and endothelial cells' presence. Vasodilation only occurred when endothelial cells were present, and the so-called endothelium-derived relaxing factor (EDRF) was identified as the compound responsible for this behavior. It was discovered that compounds like acetylcholine do not cause vasodilation directly but merely stimulate the release of EDRF from endothelial cells. EDRF itself then acts as the vasodilator. However, the exact mechanism of how EDRF causes vasodilation, as well as the structure of EDRF, remained unclear [75–78]. In 1987, L.J. Ignarro et al. were able to determine the structure of EDRF. Investigation had shown that EDRF had similar effects on tissue to NO, crucially the accumulation of cGMP leading to the relaxation of smooth muscle cells, resulting in vasodilation. Further research based on these similarities ultimately led to the identification of NO as the key component of EDRF [79].

After identifying the vasodilatory function of NO, the mechanisms of biological NO production were elucidated. NO is produced enzymatically from L-arginine with the help of a group of enzymes called NO synthase (NOS), which exists in various cell-specific isoforms. The first isoform is the neuronal constitutive NO synthase (nNOS) found in neuronal cells. It is responsible for NO production in the central and peripheral nervous systems. The second isoform is the endothelial constitutive NO synthase (eNOS) found in vascular smooth cells and responsible for NO production in the cardiovascular system. The final isoform is the inducible NO synthase (iNOS). iNOS is not specific to a particular cell type but can be induced in various cells. The significant difference between iNOS and the other isoforms is that its activity is independent of the Ca^{2+}-concentration [64, 80–83].

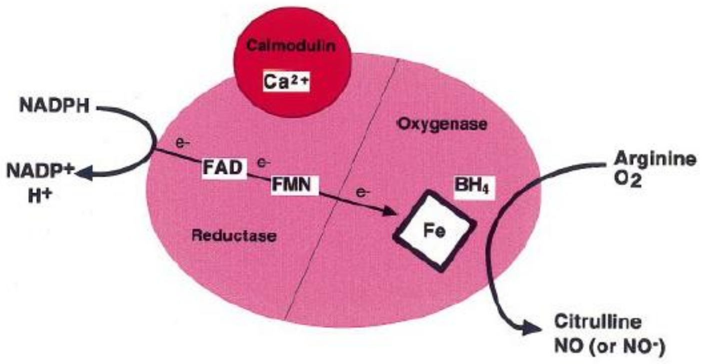

Figure 2.7: Schematic depiction of the NOS-catalyzed process of NO production [84].

NOS is generally composed of an oxygenase domain containing binding sites for L-arginine, the cofactor tetrahydrobiopterin, and ferric heme, and a reductase domain binding nicotinamide adenine dinucleotide phosphate (NADPH) as well as the cofactors flavin adenine dinucleotide (FAD), and flavin mononucleotide (FMN). Activation of NOS results in the transfer of electrons from NADPH through a Ca^{2+}-calmodulin complex to the heme group bound to the oxygenase domain, leading to oxygen being bound to the heme groups. A five-electron oxidation occurs at the guanidine nitrogen of L-arginine bound to the oxygenase domain, resulting in the formation of nitric oxide and L-citrulline. Following the reaction, L-citrulline is converted back into L-arginine through a reaction catalyzed by arginosuccinate lyase, keeping the L-arginine levels in the respective cell constant [10, 84–88]. The NO formed through this reaction generally has a biological half-life of between 3 and 30 seconds. This short half-life is mainly due to NO readily binding to oxyhemoglobin (Oxy-Hb) [11].

A wide variety of biological functions have been identified since the discovery of the vasodilatory function of NO. This includes both functions based on its vasodilatory functions and its capabilities as a signaling molecule. NO occupies regulatory functions in the central nervous, pulmonary, gastrointestinal, and cardiovascular systems, among others [10, 11].

In the central nervous system, NO plays a vital role as a potent vasodilator involving a variety of agonists, such as acetylcholine, serotonin, and oxytocin. NO in the central nervous system is not solely derived from endothelial cells but is also produced by neurons and glia [11]. The vasodilatory function of NO is used in scenarios like the regulation of the basal cerebral vascular tone or mediation of cerebral blood flow to manage seizure and cortical depression [89, 90]. NO also plays a role in hypoxia and ischemia recovery [89, 91]. Apart from the functions based on its vasodilatory function, NO acts as a neurotransmitter. This can be an anterograde neurotransmitter at the presynaptic end of peripheral nitrergic nerves, regulating pain transmission between primary and secondary neurons in the spinal cord, among other functions [10, 92, 93]. NO also acts as a retrograde neurotransmitter, taking part in the activation of N-methyl-D-aspartate receptors (NMDAR) [10, 94, 95].

In the pulmonary system, NO mediates regulatory mechanisms such as cholinergic bronchoconstrictor and adrenergic bronchodilator neural mechanisms. The vascular dilatory function of NO plays a role in controlling the vascular tone of the pulmonary system. Additionally, S-nitrosothiols formed from the reaction between NO and protein thiols can control bronchodilation [96, 97]. NO’s influence on the pulmonary system is also utilized in a pharmaceutical context as an inhalation gas acting as a selective pulmonary vasodilator. It dilates the alveoli's blood vessels, improving ventilation-perfusion matching and increasing lung efficiency. The gas concentrations are typically chosen at 80 ppm and below [11, 98, 99].

NO occupies a central role in the cardiovascular system due to its vasodilatory function, being the central compound determining both intravascular volume and vascular tone and playing a central role in the maintenance of vascular homeostasis [11]. NO also has an atheroprotective role through the inhibition of lipoprotein oxidation and a role in counteracting membrane injury caused by free radicals [11, 100, 101]. Furthermore, NO plays a role in the hypoxia response by counteracting the vasoconstrictive effects of hypoxia, thus increasing perfusion levels [11, 102]. Another important NO function in this context is its antithrombotic properties, which will be discussed in more detail in chapter 2.2.3.2.

In the gastrointestinal system, NO acts as a vasodilator as part of the system’s regulatory functions. Among the vasodilation-based regulatory functions are systems like the mucosal blood flow, maintaining mucosal integrity, and preventing the formation of ulcers. NO also regulates hemodynamic responses to liver disease, hepatocyte synthetic function, and relaxation of the muscolaris [11, 103, 104].

Besides its role as a vasodilator, NO also acts as a signaling molecule. High reactivity and short physiological half-life mean only short-range signaling directly happens through NO. In contrast, longer-range signaling processes occur through intermediary molecules such as nitrites or S-/N-nitroso proteins. These more stable compounds can travel longer distances, releasing NO at the target destination [10, 105]. Long-range signaling is generally called the classical mechanism, whereas short-range signaling is summarized under the non-classical mechanism [10]. The classical mechanism works through the activation of guanylate cyclase, with NO binding to the heme group of the enzyme, thereby catalyzing the formation of cGMP from guanosine 5'-triphosphate. cGMP then activates cGMP-dependent serine/threonine protein kinase (PKG), through which various cellular processes are modulated. This includes cardioprotection, neurotransmission, and platelet aggregation [106–110]. The non-classical mechanism involves NO's covalent modification of biomolecules, such as the S-nitrosylation of protein thiols or the metal nitrosylation of transition metals. S-nitrosylation can regulate conformational changes of the protein and internal processes of cells, like DNA transcription, repair, or growth. Metal nitrosylation of transition metals occurs mainly with heme groups. NO can block the function of cytochrome C or hemoglobin (Hb) by binding to their respective heme groups. It can also activate proteins like soluble guanylate cyclase (sGC) through the same reaction [111–114].

The regulatory functions presented in this chapter represent only a very brief and compact overview of some of NO's biological functions. It did not touch on subjects such as NO's antibacterial or antiviral properties. The primary purpose was to showcase the versatility of this simple molecule, which plays a role in a wide variety of physiological systems.

2.2.3.2 Inhibition of Blood Clotting

Chapter 2.2.3.1 showcased NO's versatility in the physiological context. This chapter discusses the NO functionality central to this thesis's research objectives: its role in regulating blood coagulation.

The blood coagulation process generally occurs according to the following mechanism: a blood vessel is damaged, disrupting its endothelium. This disruption exposes the parts of the vessel walls underneath the endothelium where platelets can adhere. Soluble factors such as epinephrine, ADP, serotonin, or thrombin amplify the platelet membrane signal generated through platelet adhesion throughout the blood plasma. This leads to further platelets being activated and accumulating at the wound site. This increase in activated platelets ultimately leads to platelet aggregation. Platelet aggregation happens by activating lipid-metabolizing enzymes like the phospholipases A and C. These enzymes catalyze the reorganization of the platelets' cytoskeleton, leading to the release of platelet constituent compounds to extracellular compartments. The aggregation is amplified by ADP, thromboxane A_2 (TXA_2), and gelatinase A [12, 115]. In its final stage, platelet aggregation leads to the formation of a network of bridges between the platelets consisting of fibrinogen and Willebrand Factor. These bridges are formed due to conformational changes in the integrin receptors IIb and IIIa. In addition to the fibrinogen network, the platelets also form aggregates with leukocytes through P-selectin, which has been translocated to the platelet surface [12].

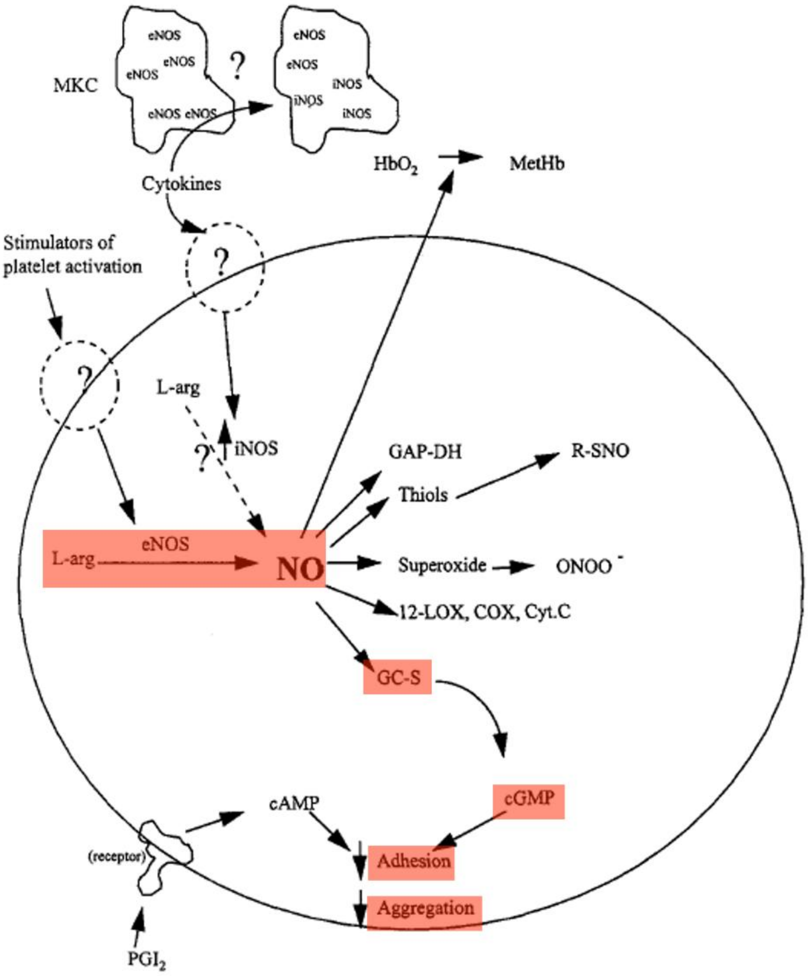

Figure 2.8: Overview of the mechanisms of both NO synthesis and subsequent reactions of NO. Marked in red is the mechanism of platelet aggregation suppression [12].

NO can influence blood coagulation at all stages of development by inhibiting platelet activation, adhesion, and aggregation. Research generally differentiates between two types of NO inhibiting the blood coagulation cascade: autocrine NO, produced in the platelets themselves, and paracrine NO, generated outside the platelets [12, 13, 116]. Coagulation regulation through paracrine NO generally happens through continuous generation from endothelial cells and leukocytes, keeping the platelets inactive under regular conditions [117]. In the case of injury, a combination of autocrine and paracrine NO is produced. NOS in the platelet is activated by collagen through the glycoprotein VI (GPVI) receptor in a process sensitive to the Ca^{2+} concentration in the platelet [118–120]. The NOS subsequently produces NO from L-arginine (see Chapter 2.2.3.1). NO then activates sGC by binding to the heme group of the enzyme, leading to the formation of cGMP. cGMP then activates cGMP-dependent PKG [121]. Platelet activation itself is then inhibited through several pathways. These pathways include decreasing cytosolic Ca^{2+} levels by inhibiting the release of Ca^{2+} from the sarcoplasmic reticulum, which is stimulated through inositol 1,4,5-triphosphate (IP_3) [122]. cGMP also increases the intracellular cyclic adenosine monophosphate (cAMP) level by inhibiting phosphodiesterase 3 (PDE 3) and, therefore, the breakdown of cAMP. Both enzymes then act synergistically to inhibit platelet aggregation [118, 123]. cGMP is also able to inhibit phosphoinositide 3-kinase (PI3-K), which mediates the activation of glycoprotein (GP) IIb-IIIa fibrinogen receptors [124, 125]. The third and final mechanism by which cGMP can inhibit platelet function is by activating PKG. PKG then phosphorylates the TXA_2 receptors, thereby inhibiting them [126].

2.2.3.3 Side Effects

As mentioned in chapter 2.2.3.1, NO is already used as an inhalant, acting as a selective pulmonary vasodilator and counteracting conditions such as pulmonary hypertension [98]. However, in this context, it is also necessary to consider the side effects of NO being used in this fashion. They encompass a variety of different mechanisms, including both nitrosative and oxidative stress and the formation of methemoglobin (Met-Hb) [127]. The most prominent among these mechanisms is the latter. NO possesses an affinity to Oxy-Hb 1500 times higher than even CO [128]. After inhalation, NO is absorbed rapidly by Oxy-Hb. NO then oxidizes the ferrous ion of Hb to a ferric ion, forming Met-Hb. Met-Hb possesses a reduced oxygen-carrying ability compared to regular Hb. The remaining heme sites also display an increased oxygen affinity, impairing the unloading of oxygen to the tissue [129]. This effect usually does not pose a severe threat to patients as Met-Hb is rapidly reduced to Hb through Met-Hb reductase. However, accumulation of Met-Hb is possible in cases of Met-Hb reductase deficiency or excess concentrations of NO through its use as an inhalant [130–132].

Nitrosative stress occurs through the formation of nitrosamines and S-nitrosothiols associated with conditions of cardiovascular function or cancer [127, 133]. These compounds are formed through metal-mediated nitrosation. Here, S-nitrosothiols and nitrosamines are formed from the reactive nitrogen oxide species (RNOS) and metal complexes such as sodium nitroprusside or heme complexes [134]. A variety of proteins, such as cobalamin, catalyzes these reactions [135]. In the context of nitrosative stress, RNOS can originate from three different sources: The autoxidation of naturally occurring NO and the NO/O_2-reaction under excess NO concentration, leading to the formation of NO_2 and nitrous acid (HNO_2). The primary intermediate of these reactions is dinitrogen trioxide (N_2O_3). The reaction equations are as follows [127, 136]:

$$2\,NO + O_2 \longrightarrow 2\,NO_2 \tag{2}$$

$$NO_2 + NO \rightleftharpoons N_2O_3 \tag{3}$$

$$N_2O_3 + H_2O \longrightarrow 2\,HNO_2 \tag{4}$$

Higher concentrations of the RNOS are only present due to excess NO concentration during inhalation and do not occur in significant concentrations under natural conditions [127].

Looking at oxidative stress, high concentrations of RNOS due to excess NO concentrations are again the origin. In this case, the RNOS consist of NO_2, nitroxyl (HNO), and peroxynitrite ($ONOO^-$) [127]. Oxidative stress includes phenomena such as the oxidation of DNA leading to strand breaks, the oxidation of lipids leading to lipid peroxidation, and the oxidation of proteins. These effects can limit cellular functionality [137].

2.3 Nitrogen Dioxide (NO_2)

2.3.1 General Information

NO_2 is the second important gas for the research conducted for this thesis. Like NO, NO_2 is also a highly reactive free radical. Both gases are closely related, as one primary source of NO_2 is the oxidation of NO with ambient oxygen. NO_2 is a volatile, reddish-brown gas under standard ambient conditions despite its boiling point of 21.15 °C due to its low partial pressure in the atmosphere. The gas is heavier than air, strongly oxidizing, and corrosive [138, 139].

2.3.2 Environmental Role

The primary source of anthropogenically produced NO_2 in the atmosphere is combustion processes producing a mixture of different nitrogen oxides. Over 90 % of the emitted nitrogen oxides are NO, with the remaining percentage being NO_2. NO is then rapidly oxidized in contact with the air to NO_2 (see Equation 2). NO_2 can also be produced directly through oxidation at elevated temperatures according to the following reaction:

$$N_2 + 2\ O_2 \longrightarrow 2\ NO_2 \qquad (5)$$

Due to the rapid oxidation of NO under ambient temperatures, NO_2 is generally considered the primary atmospheric pollutant [138, 140]. NO_2 can also stem from natural sources. NO_2 occurs naturally in the atmosphere through intrusion from the stratosphere, bacterial and volcanic activity, and forest fires or lightning. These natural sources result in a background concentration of NO_2 of around 0.0001 ppm. Emissions from the combustion of fossil fuels are the primary source of anthropogenic emissions, with the transportation sector and indoor heating being the most significant contributors to NO_2 exposure [141]. The major environmental impact of NO_2 is its role in the formation of acid rain. Acid rain is a phenomenon caused by emissions of both sulfur dioxide (SO_2) and nitrogen oxides like NO_2. SO_2 produces sulfuric acid (H_2SO_4) through the intermediate sulfur trioxide (SO_3), while NO_2 forms nitric acid (HNO_3) in contact with water. Acid rain has various effects on the environment: it increases the nitrate levels in the soil, leading to nitrate saturation and a decrease in calcium and magnesium levels. It also leads to the formation of aluminium nitrate and sulfate, which are toxic to tree life and many aquatic organisms. The precipitation of acid on vegetation negatively affects the photosynthetic capacity and growth of the affected plants as leaves and needles are damaged. This leads to an increase in draught and disease susceptibility. Soil fertility is decreased as potassium and phosphorus levels are reduced and bodies of water are acidified, leading to the loss of fish life [142, 143].

As discussed for NO (see Chapter 2.2.1), nitrogen oxide emissions have been mainly mitigated in the present day by the use of catalytic converters for cars beginning in the 1970s/80s, as well as the introduction of methods such as SCR and SNCR in factories and power plants. Due to these countermeasures and considerable regulatory efforts, acid rain has been largely mitigated in the present-day [70–72, 142, 144].

2.3.3 Toxicity

Besides the more significant environmental impact, the toxicity and health impacts of NO_2 are essential factors to consider. Individual exposure through sources such as indoor stoves or occupational exposures is particularly relevant in this context. At the same time, the general background concentration of NO_2 also plays a role in the form of busy roadways or industrial compounds in proximity to residential areas. However, the research into the effects of NO_2 has produced results not yet entirely conclusive. Despite this, a variety of effects on human health have been identified [145]. The acute effects of NO_2 exposure include a reduction in pulmonary function and an increase in bronchial reactivity. Long-term exposure can lead to effects on various organs. The lung is the primary target, but organs such as the spleen, liver, and blood are also affected [146]. NO_2 can cause a change in cell types in tracheobronchial and pulmonary regions, as well as emphysema-like effects. The susceptibility of the lung to both bacterial and viral infections is also increased, although the precise mechanism behind this effect remains unidentified [145, 147]. Upper and lower viral respiratory tract infections are possible results of increased NO_2 exposure [148, 149]. People who have asthma, in particular, are at risk from NO_2 pollution as it can both cause and exacerbate the disease [145]. There are also studies suggesting a connection between NO_2 and increases in stroke-related mortality rates [150]. Connections between NO_2 exposure and cardiac disease, cardiac failure, ischemic heart disease, myocardial infarction, and total cardiovascular failure have also been reported [151]. At exceptionally high concentrations of $NO_{2,}$ severe lung injury and death are possibilities [145].

2.3.4 Reactions with Polymers

Extensive research has been done to examine the interactions between NO_2 and polymers. The initial research on the interaction between polymers and NO_2 was conducted by T. Ogihara et al. in the mid-1960s, focussing on the reaction between polyethylene and the addition reaction to C-C double bonds [152, 153]. The research was expanded throughout the 1960s and 70s by H. Jellinek et al. It encompassed reactions of both NO_2 and SO_2 with polymers like butyl rubber, polyethylene, polypropylene, polystyrene, and polyurethane. A variety of possible reactions was identified, ranging from the simple addition reaction of NO_2 to double bonds in the polymer chains forming nitro groups to reactions such as chain scissions and crosslinking reactions [154–160].

The first reaction to look at is the electrophilic addition of NO_2 to C-C double bonds. The first step is the addition of one NO_2 molecule to the double bond, leading to the formation of a nitro group and a radical:

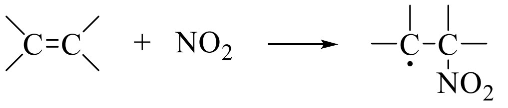

$$>C=C< \; + \; NO_2 \longrightarrow -\underset{\bullet}{\overset{|}{C}}-\underset{NO_2}{\overset{|}{C}}- \qquad (6)$$

In the second step, a second NO_2-molecule is added, leading to the formation of either dinitro nitro-nitrite compounds:

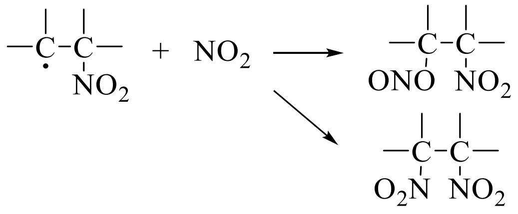

$$-\underset{\bullet}{\overset{|}{C}}-\underset{NO_2}{\overset{|}{C}}- \; + \; NO_2 \longrightarrow -\underset{ONO}{\overset{|}{C}}-\underset{NO_2}{\overset{|}{C}}- \;\; \text{or} \;\; -\underset{O_2N}{\overset{|}{C}}-\underset{NO_2}{\overset{|}{C}}- \qquad (7)$$

Early experiments found an equal proportion of both compounds in the final product, with an overall ratio of nitro to nitrite ester groups of 3:1 [153]. The nitrite groups formed because of this reaction are unstable and can react further to form nitrate ester groups, among other possible secondary reactions [152, 161]:

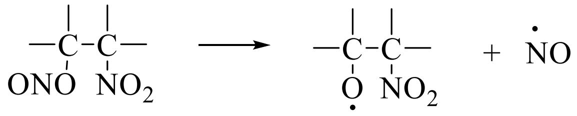

$$-\underset{ONO}{\overset{|}{C}}-\underset{NO_2}{\overset{|}{C}}- \longrightarrow -\underset{\underset{\bullet}{O}}{\overset{|}{C}}-\underset{NO_2}{\overset{|}{C}}- \; + \; \dot{N}O \qquad (8)$$

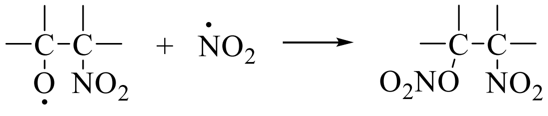

$$-\underset{\underset{\bullet}{O}}{\overset{|}{C}}-\underset{NO_2}{\overset{|}{C}}- \; + \; \dot{N}O_2 \longrightarrow -\underset{O_2NO}{\overset{|}{C}}-\underset{NO_2}{\overset{|}{C}}- \qquad (9)$$

Other secondary reactions include the formation of hydroxy groups or carbonyl groups [152].

The second category of possible reactions is chain scissions. Chain scission reactions generally occur along similar mechanisms depending on the affected polymer. The following mechanism of chain scission in polystyrene acts as an example of these reactions: In the first step, a hydrogen atom from the polymer chain is abstracted by NO_2, leading to the formation of a radical site in addition to an HNO_2 molecule:

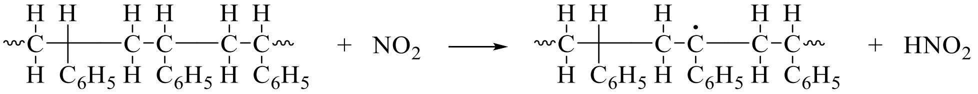
(10)

The radical site reacts with NO_2 again, forming either nitro or nitrite ester groups identically to the above mechanism (see Equations 6 and 7). Both functional groups can then lead to chain scission through the following mechanism [154]:

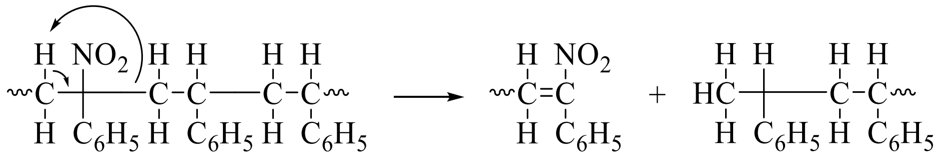
(11)

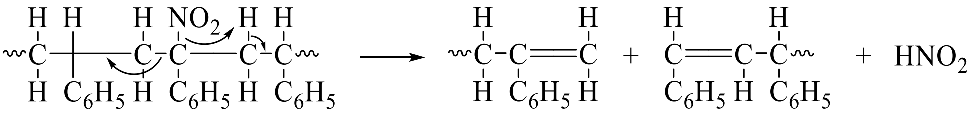
(12)

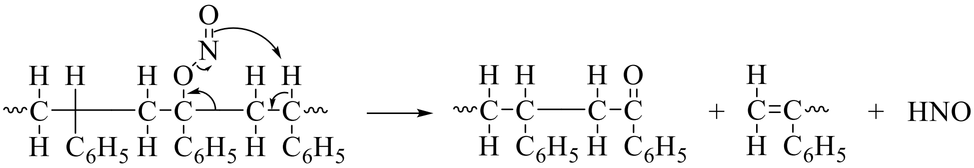
(13)

$$2\ HNO \longrightarrow H_2N_2O_2 \qquad (14)$$

The final category of reactions is the cross-linking reactions. These reactions are possible following the first steps of addition reactions (see Equation 6) and chain scission reactions (see Equation 10). The radical formed in these initial reaction steps can react with another radical, leading to crosslinking in the polymer. An example of such a process is the crosslinking reaction of polyurethane [159]:

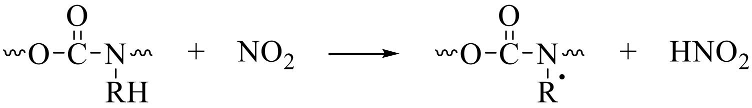
(15)

$$\sim O{-}\overset{O}{\overset{\|}{C}}{-}\underset{RH}{N}\sim + NO_2 \longrightarrow \sim O{-}\overset{O}{\overset{\|}{C}}{-}\underset{R^{\bullet}}{N}\sim + HNO_2 \qquad (15)$$

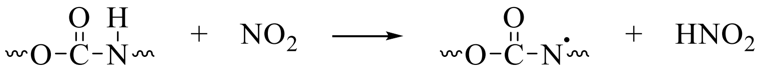

$$\sim O-\overset{O}{\overset{\|}{C}}-\overset{H}{\overset{|}{N}}\sim \; + \; NO_2 \longrightarrow \sim O-\overset{O}{\overset{\|}{C}}-\dot{N}\sim \; + \; HNO_2 \qquad (16)$$

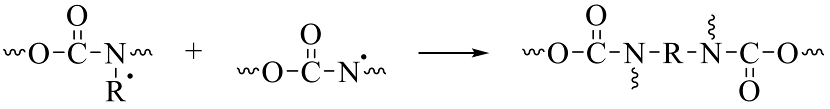

$$\sim O-\overset{O}{\overset{\|}{C}}-\underset{\dot{R}}{\underset{|}{N}}\sim \; + \; \sim O-\overset{O}{\overset{\|}{C}}-\dot{N}\sim \longrightarrow \sim O-\overset{O}{\overset{\|}{C}}-\underset{\wr}{N}-R-\overset{\wr}{N}-\underset{O}{\underset{\|}{C}}-O\sim \qquad (17)$$

The ratio between addition reaction, chain scission, and crosslinking depends on the treated polymer. The addition reaction generally accounts for most reaction products, with chain scission and crosslinking being side reactions. Polymers such as butyl rubber show an increased tendency towards chain scission, while polybutadiene and polyisoprene tend to exhibit a higher tendency towards crosslinking [157, 160].

Since the publications of Jellinek et al., more research has been conducted, expanding the range of tested polymers and treatment conditions. Work by E. Davydov et al., for example, expanded the research through the testing of polymers, such as polyamides and imides, at elevated temperatures and NO_2 concentrations. Under these conditions, hydrogen abstraction was observed even from stable N-H bonds present in amides and imides [162]. Further investigations, both experimental and simulated, were performed, with a few selected examples of this research contained in the rest of the paragraph: Investigations of the reaction of NO_2 with alkenes in solution led to a better understanding of the reaction rates of the addition reaction through the work of D. Giamalva et al. [163]. I. Oluwoye et al. performed DFT simulations, contributing to a better understanding of the transition states of the addition reaction [164]. J. Powell et al. proposed an alternative pathway for the initial step of the addition reaction based on data from ^{15}N nuclear polarization. This alternative pathway utilizes N_2O_4 instead of the successive addition of two NO_2 molecules (see Equations 6 and 7). The proposed mechanism is displayed below [165]:

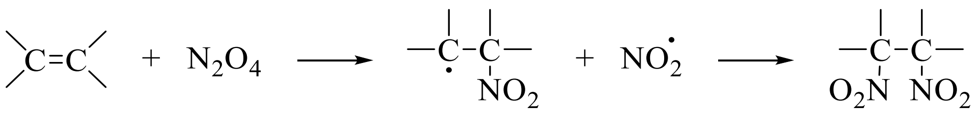

$$>C=C< \; + \; N_2O_4 \longrightarrow -\underset{\bullet}{\overset{|}{C}}-\underset{NO_2}{\underset{|}{\overset{|}{C}}}- \; + \; \dot{NO_2} \longrightarrow -\underset{O_2N}{\underset{|}{\overset{|}{C}}}-\underset{NO_2}{\underset{|}{\overset{|}{C}}}- \qquad (18)$$

2.4 Polymers

2.4.1 Polymethylpentene (PMP)

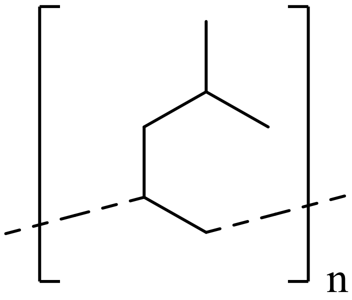

Figure 2.9: Chemical structure of polymethylpentene (PMP) [166].

PMP is a semi-crystalline, linear α-polyolefin composed of 4-methyl-1-pentene monomers. It is a thermoplastic polymer with a high thermal stability and chemical resistance [166]. The polymer is produced according to the following mechanism: In the first step, propene is dimerized using an alkali metal catalyst to produce the 4-methyl-1-pentene monomer. The polymer itself is then produced through a Ziegler-Natta process involving chromium, zirconium, titanium, or vanadium-based transition metal catalysts acting as heterogeneous Ziegler-Natta coordination catalysts [166–168]. The reaction mechanism largely follows that of polyethylene or polypropylene [169]. Alternative mechanisms, such as cationic polymerization, are also possible [170].

PMP possesses a density of 0.828 and 0.838 g/cm^3 in crystalline and amorphous domains, respectively [171, 172]. It is also a polymorph that can crystallize in various crystal structures depending on the crystallization conditions, with five different crystal modifications. The glass transition temperature sits at 40 °C and the melting point at 245 °C [173]. Thermal degradation occurs at temperatures ranging from 291 to 355 °C [174]. The mechanical properties of PMP are similar to high-density polyethylene (HDPE), with, on average, slightly lower values. The tensile modulus of PMP sits between 0.8 and 1.2 GPa, with a tensile strength of 23-28 MPa at yield and 17-20 MPa at break. The elongation at break reaches values between 10 and 25 % [166]. PMP also possesses a high radiation stability, being two to six times more resistant than comparable polymers such as polyethylene and polypropylene [175].

PMP is used in several applications due to its high melting point, low density, and good chemical resistance. It can be injection or blow molded, extruded, spun into fibers, or cast into sheets or films [166]. PMP permeability to oxygen led to applications as a membrane material, specifically for hollow fiber membranes [39]. PMP's gas permeability generally depends on its crystallinity, with permeability increasing as crystallinity decreases [176].

The PMP material investigated in this thesis was the 3M Membrana OXYPLUS, Capillary Membrane, Type PMP 90/200 (3M Deutschland GmbH, Wuppertal, Germany). These hollow fiber membranes have an outer diameter of 380 µm and an inner diameter of 200 µm, a wall thickness of 90 µm, and a material porosity of around 50 %. The tensile strength of these fibers is around 60 cN, with an elongation at break of around 60 %.

2.4.2 Methylmethacrylate Acrylonitrile Butadiene Styrene (MABS)

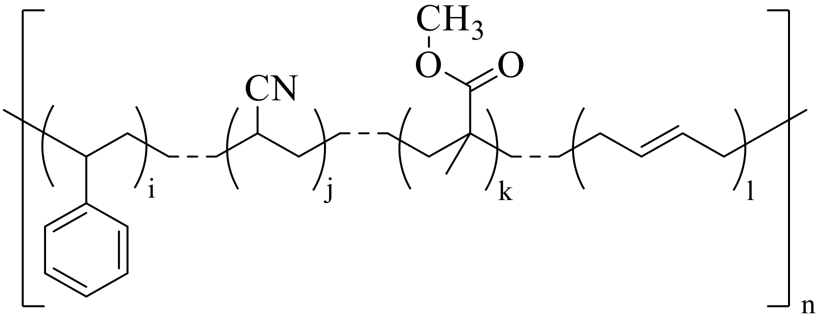

Figure 2.10: Chemical structure of methylmethacrylate acrylonitrile butadiene styrene (MABS) [177].

Methylmethacrylate acrylonitrile butadiene styrene (MABS) is a copolymer consisting of four different monomers. Published research on MABS is scarce and rarely deals directly with its properties. Therefore, this chapter is mainly based on industry sources.

MABS is a transparent, amorphous, thermoplastic polymer. It combines the properties of acrylonitrile butadiene styrene (ABS) plastic, namely high rigidity and toughness, with the transparency of polymethylmethacrylate (PMMA). MABS also possesses high impact strength and high chemical stability and is sterilizable, making it suitable for medical devices. MABS is mainly used in injection molding processes [178–180].

The MABS material used in the context of this thesis was Terlux HD 2802 (INEOS Stryrolation Group GmbH, Frankfurt am Main, Germany). This polymer has a density of 1.08 g/cm^3, a tensile modulus of 2.0 GPa, and a tensile strength at yield of 48 MPa. The unnotched impact strength reaches a value of 120 kJ/m^2, while the melting temperature range sits at 230-260 °C [181].

2.4.3 Polyurethane (PU)

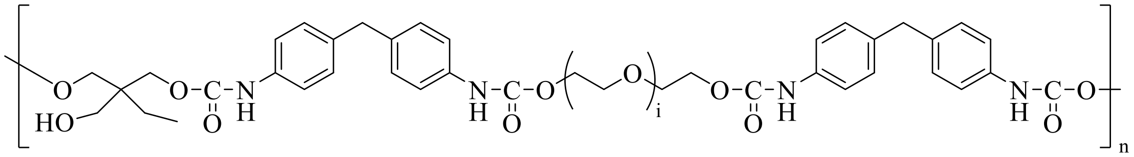

Figure 2.11: Chemical structure of polyurethane (PU) consisting of methylene diphenyl diisocyanate (MDI), polyethylene glycol (PEG), and trimethylolpropane (TMP) monomers [182, 183].

Polyurethanes (PU) are a class of polymers made up of polyol and di- or polyisocyanate monomers. The polymer is produced through a polyaddition reaction between the different monomers, forming the carbamate group characteristic of this class of polymer. Various polymeric components can be realized depending on the choice of the monomers encompassing duroplastic, thermoplastic, and elastomeric compounds. PU is most used in the form of flexible and rigid PU foams, known as insulation materials, furniture cushions, and packaging materials, among other applications. However, the PU class of interest within the scope of this thesis is the PU elastomers [184, 185].

PU elastomers are block copolymers. They are structurally characterized by the presence of both rigid and flexible chain segments. The soft segments contain the polyols. The rigid segments contain the isocyanate molecules and, depending on the polymer, also short-chain polyols, so-called chain extenders. The elastic properties are caused by crosslinking enabled by the chain extenders. PU elastomers are generally synthesized via two different pathways: the prepolymer and the “one shot“ method. Diisocyanate and long-chain polyol are mixed in a ratio depending on the desired concentrations of flexible and rigid segments for the prepolymer method. The reaction is carried out until all available hydroxyl groups have reacted. The resulting oligomers of alternating diisocyanate and long-chain polyol are then mixed with the chain extender to create the final polymer chains [184, 186]. The “one-shot” method involves the combination of the diisocyanate, the long-chain diol, and the chain extender in a single step [187].

The properties of the PU elastomers are highly dependent on the length and concentration of the rigid and flexible segments. These structural factors govern parameters such as morphology and mechanical properties [184, 188]. The tensile strength and general stress-strain properties of PU elastomers range from soft rubber to hard resins. The rigid segments are primarily responsible for the higher strength of a given elastomer through energy dissipation, deflection of cracks, cavitation, and plastic deformation. The flexible parts of the polymer chain also contribute to the strengthening of the material through processes like viscoelastic energy dissipation and strain-induced crystallization [189]. The effects of the rigid segment generally increase with its concentration, while the effect of the flexible segment reaches a maximum between 40 and 60 % [190]. The polymer's tensile strength, modulus, and hardness depend on the diisocyanate's structure, with symmetric molecules resulting in higher strength materials with MDI resulting in the overall highest values. Tensile strength is also affected by the type of chain extender used and the composition of the flexible segments. Polyester-based PU generally possesses higher tensile strength than polyether-based PU [184].

The PU material used to construct the oxygenator investigated in this thesis was a two-component PU system. This system consisted of the resin Biresin DR404 containing TMP and the hardener Biresin DH41 containing a prepolymer consisting of MDI and glycols, both produced by Sika Deutschland GmbH (Stuttgart, Germany). The TMP acts as the chain extender and enables crosslinking through its third hydroxyl group. The resulting PU resin is sterilizable [191–193].

2.4.4 Polyvinyl chloride (PVC)

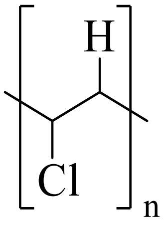

Figure 2.12: Chemical structure of polyvinyl chloride (PVC).

Polyvinyl chloride (PVC) is, similar to PU, a very widely used thermoplastic polymer, with the fourth highest annual production volume of all thermoplastics behind polypropylene and both high-density and low-density polyethylene [194]. The monomer vinyl chloride was initially discovered in 1835 by Liebig and Regnault [195]. The production process of PVC was then developed by F. Klatte in 1913. Commercial production of the polymer started in the late 1920s and early 1930s, driven primarily by companies such as Union Carbide and DuPont in the USA and IG Farben in Germany. The polymer reached mass market relevance in the 1960s with steadily increasing production volumes until today [196]. PVC has a wide variety of applications, the most prominent being in the construction sector, where it is used in window frames, flooring, and sewage pipes, among many others. Applications also extend into fields such as electrical devices, the automotive industry, and, most notably for this thesis, medical applications. Medical applications of PVC include blood and plasma bags, tubing for dialysis, feeding systems, and extracorporeal life support [197].

PVC is produced through a process of free radical polymerization. The monomer vinyl chloride (VC) itself is produced through the chlorination of ethene. This process involves two different chlorination mechanisms: direct chlorination and oxychlorination. Direct chlorination involves the direct catalyzed reaction between ethene and chlorine (Cl_2). Oxychloronation involves the reaction of ethene with hydrochloric acid (HCl), recovered from the following cracking process, and oxygen. In both processes, 1,2-dichloroethane is formed as the product. In a second step, called EDCL cracking, VC and HCl are produced from 1,2-dichloroethane. PVC is then produced from VC through radical polymerization using compounds such as organic peroxides as initiators. The initiator compounds are chosen based on the desired properties of the final product. The polymerization reaction itself is strongly exothermic. This polymerization process can be conducted as a suspension, micro-suspension, emulsion, and bulk polymerization [197, 198].

An important aspect of PVC application is the use of plasticizers. Plasticizers are used to increase the flexibility of PVC and make it suitable for various applications. The plasticizers lower the polymer's glass transition temperature, in some cases, as far as the ambient temperature. PVC has a high plasticizer compatibility compared to other polymers. A wide range of plasticizers is used in combination with PVC. These compounds include phthalate, trimellitate, aliphatic, and phosphate esters. The impact of plasticizers on the properties of PVC is described in the next paragraph [197, 199].

Regarding material properties, five different variants of PVC are generally differentiated. These are unplasticized PVC (PVC-U), impact-modified PVC-U, plasticized PVC (PVC-P), chlorinated PVC (PVC-C), and PVC-U foam. The density of PVC is among the highest for a thermoplastic polymer, ranging from 1350 to 1700 kg/m^3, with PVC-U and PVC-C generally occupying the lower and central part of that range, while PVC-P occupies the entire spectrum. PVC-U foam density sits at around 700 kg/m^3. PVC-U has the highest tensile strength of 50-75 MPa, followed by PVC-C at 50-55 MPa, impact-modified PVC-U at 40-50 MPa, PVC-P at 10-25 MPa, and PVC-U foam at 15 MPa. PVC-U possesses a surface Shore-D hardness of 83-84, impact-modified PVC-U 80, and PVC-U foam of 40-70. PVC-P possesses a Shore-A hardness of 60-90 [197].

The PVC compounds of interest in the scope of this thesis are Rauclair-E, produced by Rehau SE (Bern Switzerland), used for the gas hoses of the oxygenator, and Raumedic ECC noDOP 7536, produced by Raumedic AG (Helmbrechts, Germany), used for the blood hoses. These compounds used the plasticizers bis(2-ethylhexyl) terephthalate (DOTP) (32.7 wt%) (information provided directly by the manufacturer) and tris(2-ethylhexyl) trimellitate (TEHTM) respectively [200]. The following chapters, 2.4.4.1 and 2.4.4.2, give a short overview of both plasticizers.

2.4.4.1 Bis(2-ethylhexyl) Terephthalate (DOTP)

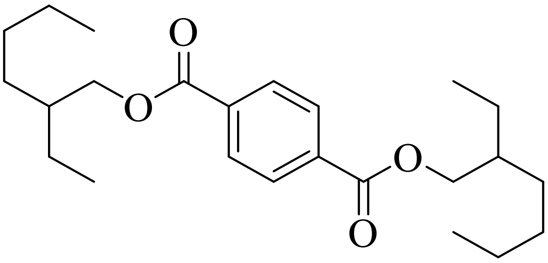

Figure 2.13: Chemical structure of the bis(2-ethylhexyl) terephthalate (DOTP) plasticizer compound [201].

Bis(2-ethylhexyl) terephthalate (DOTP) is an alternative, phthalate-free, general-use plasticizer. Terephthalate-based plasticizers were introduced as a direct replacement for ortho-phthalate esters due to their better toxicological properties [202]. Of these phthalate-free plasticizers, DOTP is the most widely used [203]. It is a structural isomer of di-2-ethylhexyl phthalate (DEHP), the previously most widely used plasticizer [204]. The use of DEHP has been restricted in the USA and Europe due to its toxicity [205, 206].

DOTP is produced through processes of either esterification or transesterification. These processes combine 2-ethyl hexanol with terephthalic anhydride or acid in the case of esterification or terephthalate esters in the case of transesterification. These reactions are conducted in a hydrocarbon solvent utilizing homogenous catalysis. Organometallic compounds containing titanium or zirconium are used as catalysts [203, 207].

When used as a plasticizer of PVC, DOTP shows a much better migratory behavior than comparable phthalate-based plasticizers, with less of the compound leaching out of the polymer in the same time frame. The tensile strength of PVC is lowered from 50-75 MPa for PVC-U down to around 22 MPa at a concentration of 40 phr of DOTP and around 11 MPa at 80 phr. Elongation at break increases from around 650 % at 40 phr to around 900 % at 80 phr. The surface hardness decreases from a Shore-D value of 83-84 for PVC-U to around 65 at 80 phr [197, 208].

2.4.4.2 Tris(2-ethylhexyl) Trimellitate (TEHTM)

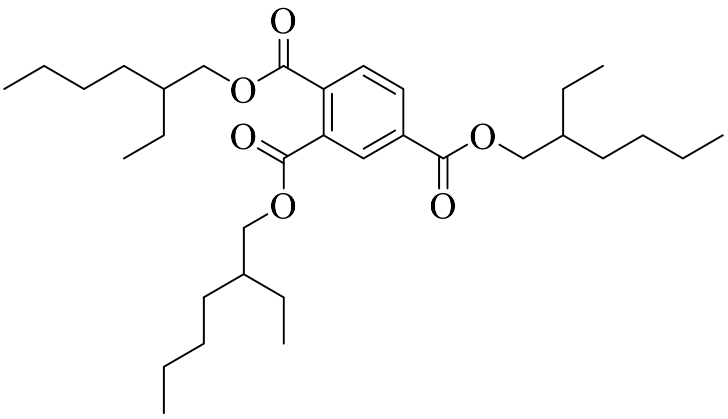

Figure 2.14: Chemical structure of the tris(2-ethylhexyl) trimellitate (TEHTM) plasticizer compound [201].

Like DOTP, tris(2-ethylhexyl) trimellitate (TEHTM) is a phthalate-free plasticizer with a close structural relationship to DEHP. TEHTM is used primarily as a plasticizer for PVC. PVC plasticized with TEHTM is widely used in medical applications behind DEHP, bis(2-ethylhexyl) adipate (DEPA), and DOTP in terms of commonality. Compared to DEHP, TEHTM possesses improved toxicological properties [209, 210].

TEHTM is produced through the esterification of trimellitic acid/anhydride and 2-ethylhexanol. The reaction can be catalyzed with a variety of compounds ranging from acids such as sulfuric acid to organometallic compounds such as titanium isopropoxide [211].

At 50 phr, TEHTM decreases the tensile strength of PVC to 20.4 MPa from 50-75 MPa for PVC-U, with the elongation at break sitting at 339 %. The surface hardness is decreased to a Shore-A value of 88 [212].

2.5 Fourier-Transform Infrared Attenuated Total Reflectance Spectroscopy (FTIR-ATR)

2.5.1 Basic Principle

Infrared spectroscopy is based on the interaction of electromagnetic radiation with molecular vibrations. IR spectra result from transitions between molecular vibrational energy levels through the absorption of IR radiation. The central parameters characterizing IR radiation are its frequency ν, wavelength λ, and wavenumber $\tilde{\nu}$. The relationship between these parameters is expressed by the following equation:

$$\tilde{\nu} = \frac{\nu}{c} = \frac{1}{\lambda} \tag{19}$$

c is the speed of light. The energy of an IR photon is given by the following equation:

$$E = h\nu \tag{20}$$

h is the Planck's constant. In IR spectroscopy, the wavenumber is the parameter commonly chosen to describe the IR radiation [213]. A molecular vibration caused by the absorption of IR radiation can be understood by approximating the bond between two atoms as a harmonic oscillator, with the bond between the atoms acting as a spring. For simple diatomic molecules, the classical harmonic oscillator can act as a good model for molecular vibrations. The relationship between the different parameters is described in the following equation:

$$\tilde{\nu} = \frac{1}{2\pi c}\sqrt{K\left(\frac{1}{m_1} + \frac{1}{m_2}\right)} \tag{21}$$

K is the spring constant, c is the speed of light, and m_1 and m_2 are the atomic masses. K is dependent on the strength of the bond. The vibrational frequency can, therefore, be determined based on the bond energy and the masses of the atoms involved [213, 214]. The classical harmonic oscillator is no longer a sufficient model for larger, more complex molecules. The quantum mechanical harmonic oscillator provides a closer approximation. Here, the energy E_i of the different vibrational levels is given by the following equation:

$$E_i = \left(\upsilon_i + \frac{1}{2}\right) h\nu \tag{22}$$

ν is the vibrational frequency of the oscillator, while υ is the quantum number of the energy state, which can only assume integer values. This leads to discreet, quantized energy states. Transitions can only happen from one state to the next higher or lower state. These transitions are called fundamentals. The quantized energy states of these quantum mechanical models also directly correlate to the well-defined resonance frequencies observable in the IR spectra. To take a step further towards a realistic model system, the harmonic oscillator can be exchanged for the anharmonic oscillator. For the anharmonic oscillator, the energy states are defined by the following equation:

$$E_{\upsilon} = h\nu_e\left(\upsilon + \frac{1}{2}\right) - h\chi_e\nu_e\left(\upsilon + \frac{1}{2}\right)^2 \qquad (23)$$

The term $\chi_e\nu_e$ defines the degree of anharmonicity. In the case of an anharmonic oscillator, transitions between energy states are no longer strictly limited to fundamental transitions. Transitions between states with $\Delta\upsilon = 2$, so-called overtones, are also possible, though much rarer than fundamental transitions. The distance between the energy states is no longer equidistant, as in the case of the harmonic oscillator. Instead, the distance between energy states decreases with increasing energy [213, 215, 216].

IR spectroscopy is conducted over all existing IR frequencies. This spectrum is generally divided into three sections: Near-IR from 14.000 to 4000 cm^{-1}, mid-IR from 4000 to 400 cm^{-1}, and far-IR from 400 to 10 cm^{-1}. IR spectra are obtained by plotting the signal intensity against the wavenumber. Depending on the measurement geometry, the intensity represents either absorbance or transmittance. The frequencies at which signals in the spectra appear correspond to fundamental transitions between vibrational energy states. A change in the molecule's dipole moment must occur for these transitions to be IR-active. This means that homonuclear diatomic molecules are not IR active, while heteronuclear molecules are. Another determining factor for IR activity is the symmetry of the molecule. If a vibration changes molecular symmetry, it is IR active; if the symmetry is maintained, it is inactive. This condition only applies to molecules with centers of symmetry [213, 217].

If a molecule possesses bonds or functional groups with vibrational frequencies significantly different from surrounding bonds and functional groups, so-called group frequencies become visible in the spectrum. These group frequencies are caused by vibrations localized almost entirely at the bonds of a specific functional group due to the significant differences with their immediate environment. These group frequencies can be approximated through a system of coupled oscillators. Vibrational frequencies are again dependent on the mass of the involved atoms and the strength of the bonds, but also on the angle between coupled oscillators. For a model system with three atoms of the masses m_1, m_2, and m_3, the out-of-phase stretching vibration between the masses m_1 and m_2 is described by the following equation:

$$\tilde{\nu}_{op} = \frac{1}{2\pi c}\sqrt{K\left(\frac{1}{m_1} + \frac{1 - \cos\alpha}{m_2}\right)} \tag{24}$$

The in-phase vibration is described by the following equation:

$$\tilde{\nu}_{ip} = \frac{1}{2\pi c}\sqrt{K\left(\frac{1}{m_1} + \frac{1 + \cos\alpha}{m_2}\right)} \tag{25}$$

K is the spring constant, c is the speed of light, m_1 and m_2 are the masses of the atoms, and α is the angle between m_1, m_2, and m_3. In-phase stretching vibrations refer to vibrations where the bonds between m_1 and m_2 and m_2 and m_3 contract and expand simultaneously. Out-of-phase stretching vibrations, on the other hand, refer to vibrations where one bond contracts while the other expands and vice versa [213, 218, 219].

As part of this thesis, measurements were conducted in the spectral range from 4000 to 500 cm^{-1}. Within this range, several different regions can be differentiated according to the characteristic signals of various functional groups: The area between 3700 and 2500 cm^{-1}, where the most common signals are produced by O-H and N-H, and aromatic and aliphatic C-H stretching vibrations. 2500 to 2000 cm^{-1}, containing stretching vibrations of triple bonds and asymmetric stretching vibrations of extended double bond systems. The region from 1800 to 1650 cm^{-1} contains the signals of carbonyl groups with varying environments. The region from 1650 to 1500 cm^{-1}, where signals corresponding to the stretching vibrations of aromatic and olefinic C-C double bonds and the stretching vibration of C=N and N-O bonds are located. Between 1500 and 1300 cm^{-1} are the signals of deformation vibrations of aliphatic compounds, and above that, between 1300 and 1000 cm^{-1} are the C-O single bond stretching vibrations of ethers, esters, and alcohols. The region above 1000 cm^{-1} finally contains the stretching vibrations of carbon-halogen bonds [213, 220].

2.5.2 Fourier-Transform Infrared Spectroscopy (FTIR)

FTIR is an instrumentation variant of IR spectroscopy. Spectroscopes built for FTIR integrate a Michelson interferometer geometry.

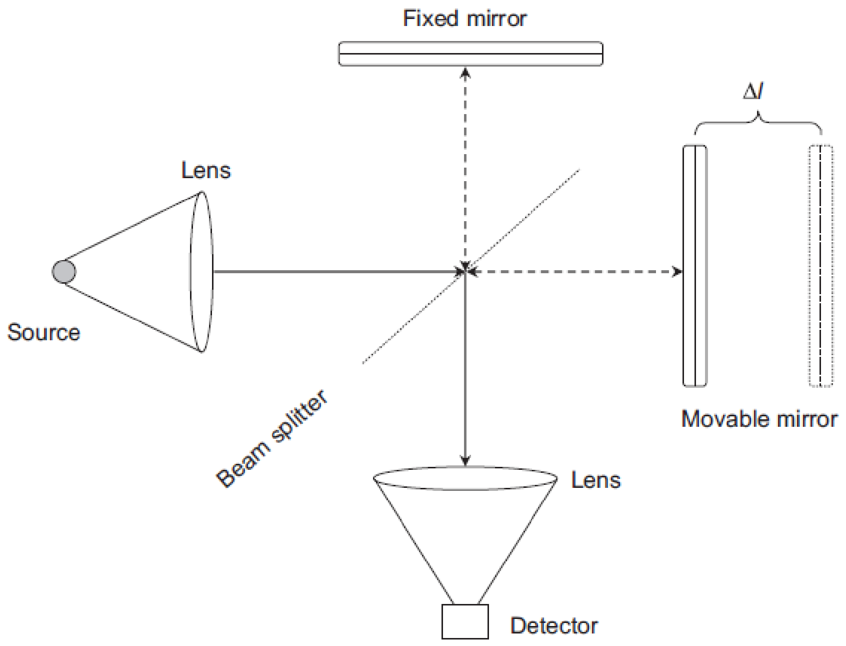

Figure 2.15: Schematic depiction of a Michelson interferometer with Δl indicating the positional difference of the movable mirror [213].

This geometry includes a radiation source directed at a beam splitter. The IR beam is split into two beams. One of the beams is directed at a fixed mirror, while the other is directed at a movable mirror. Both beams are directed back at the beam splitter, where they are then redirected to the sample and detector. Throughout the measurement, the movable mirror moves at a constant speed. The result is a sine wave, as the beams alternate between constructive and destructive interference. The resulting sinusoidal interferogram is then Fourier transformed, resulting in the finished IR spectrum [213, 221].

2.5.3 Attenuated Total Reflectance (ATR)

IR spectroscopy uses various sampling techniques. These include transmission techniques such as capillary and cast films and KBr discs. The other group of sampling techniques is reflective techniques. These include diffuse reflectance (DRIFTS) and, crucially for this thesis, attenuated total reflectance (ATR).

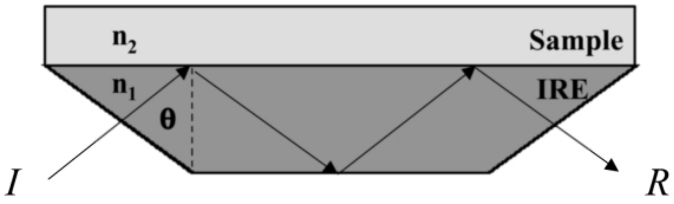

Figure 2.16: Schematic depiction of an ATR sampler. Θ is the angle of incidence, n_1 is the refractive index of the IRE, and n_2 is the refractive index of the sample [222].

ATR samplers are constructed around an internal reflection element (IRE). The IRE is a crystal with good IR transmitting properties and a high refractive index, which has direct contact with the sample during an IR measurement. Materials chosen for the IRE are diamond, germanium, zinc selenide (ZnSe), or silicon. The sampling technique overall is based on the phenomenon of internal reflection. Internal reflection occurs when the IR radiation's incidence angle exceeds the critical angle θc. θc is defined by the following equation:

$$\theta_C = \sin^{-1}\left(\frac{\eta_2}{\eta_1}\right) \tag{26}$$

η_1 and η_2 are the refractive indices of the IRE and the sample material, respectively. The high refractive index of the IRE leads to a moderate critical angle when investigating organic compounds. The following equation defines the refractive index of the sample material:

$$\eta = n + ik \tag{27}$$

The real part of the equation n is the refractive index when no absorption occurs. The imaginary part of the equation ik is the material's refractive index within an absorption band, with the parameter k directly linked to the extinction coefficient of the Lambert-Beer law. The intensity of absorption is described by the following equation:

$$A(\theta) = \int_0^\infty \alpha(z) e^{-\frac{z}{d_p}} dz \tag{28}$$

$A(\theta)$ is the absorption intensity dependent on the incident angle. $\alpha(z)$ is the absorption coefficient of the sample as a function of the depth z. The parameter d_p is the effective penetration depth of the IR radiation into the sample, defined by the following equation:

$$d_p = \frac{\lambda}{2\pi n_p\left(\sin^2\theta - n_{sp}^2\right)^{\frac{1}{2}}} \tag{29}$$

λ is the wavelength of the IR radiation, n_p is the refractive index of the IRE, θ the angle of incidence, and n_{sp} is the ratio between the refractive indices of the sample and the IRE. The penetration depth is defined as the distance to the contact surface between the sample and IRE, where the intensity of the evanescent wave reaches roughly 37 % of its original value. In most cases, this results in a sampling depth between 2 and 15 µm, depending on the sample material and the wavelength of the radiation. The sampling depth increases with decreasing wavenumber.

ATR is particularly suited for liquids or soft solids that are unsuitable for transmission IR. It is a comparatively quick and non-destructive sampling method that usually requires little to no sample preparation. The only requirement for the samples is complete contact with the IRE [213, 223].

2.6 Scanning Electron Microscopy (SEM)

2.6.1 Basic Principle

Electron microscopy is a subcategory of microscopy utilizing high-energy electron beams instead of electromagnetic radiation used in optical microscopy. The central advantage of electron microscopy is the much higher resolution when compared with optical microscopy due to the much shorter wavelength of electrons [224, 225]. This wavelength is determined by the following equation:

$$\lambda = \frac{hc}{\sqrt{eV(2mc^2 + eV)}} \tag{30}$$

λ is the wavelength of the electron, h the Planck constant, c the speed of light, e the elementary charge, V the potential, and m the mass of the electron [226]. This results in a resolution limit far below the 200 nm of optical microscopy [227, 228].

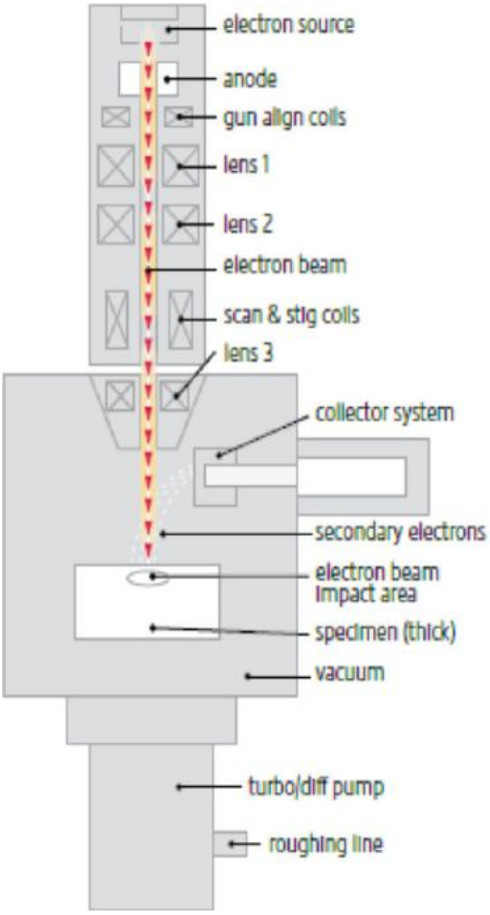

Figure 2.17: Schematic depiction of a scanning electron microscope (SEM) [229].

The electron beam is shaped and focused through electron optics utilizing electromagnetic fields [225, 230]. The combination of the electron source and the electron optics is known as the electron column, which connects to the sample space. The sample space contains the sample itself as well as the detectors. Electron microscopy encompasses a variety of different methods, with the two most common being transmission electron microscopy (TEM) and scanning electron microscopy (SEM). TEM is the original electron microscopy method, where the electron beam travels through a thin material sample before reaching the detector. The entire sample is illuminated simultaneously, creating the image [231]. SEM represents a further development of the electron microscope with even higher resolution. Here, the electron beam is focused on a single point of the sample [232]. The electron beam is then deflected using a magnetic field to scan across the sample, producing the sample image. The electron beam does not travel through the sample, in contrast to TEM, but the imaging is based on a variety of different interactions with the sample material captured by detectors located to the side and ahead of the sample. All electron microscopy methods are conducted under vacuum to avoid the electron beam being scattered by the air molecules, reducing the intensity of the electron beam. The samples are mounted conductively to prevent charge accumulation on the sample caused by the electron beam, which can interfere with the signal detection. Conductive samples such as metals can be analyzed with little additional sample preparation. Non-conductive samples, such as the polymers in the case of this thesis, are commonly sputter-coated with gold to facilitate electron discharge through the sample mounting [225, 229, 231].

2.6.2 Backscattered Electron Detector

SEM images are produced utilizing a variety of different detectors. These include secondary electron, Auger electron, back-scattered electron, characteristic X-ray, and cathodoluminescence detectors capturing various emission signals caused by the electron beam. Here, the back-scattered electron detector is discussed in more detail. Backscattering is based on the elastic interaction of the primary electrons of the electron beam with the sample material. The primary electrons are reflected from the sample through two different scattering events. The first event is a single large deflection caused by the strong Coulomb field around an atomic nucleus. The second event is comprised of a series of low-angle deflections. Among these primary electrons are also some secondary electrons caused by slight inelastic effects. Backscattered electrons originate from a deeper penetration depth than the more commonly used secondary electrons, allowing for the analysis of sample composition and crystal structure [225, 233].

Detectors commonly used for back-scattered electron detection are semiconductor-based solid-state detectors. Here, the back-scattered electrons strike the surface of the detector, causing inelastic scattering and leading to the formation of electron-hole pairs. These electron-hole pairs can be separated before recombination, leading to the generation of an external charge collection current [233, 234]. These detectors allow for several different contrasts, such as topographical, atomic number, and crystal orientation [235].

2.7 X-Ray Photoelectron Spectroscopy (XPS)

X-ray photoelectron spectroscopy (XPS) is an experimental technique developed in the 1960s utilizing the photoelectric effect to analyze sample surfaces selectively [236]. The samples are analyzed by irradiating their surfaces with soft X-rays. A complete transfer of the x-ray energy to an electron located in the 1s-orbital of a sample atom leads to the emission of the electron. The kinetic energy (E_{kin}) of the emitted electron is equal to the difference between the energy of the x-ray (hν) and the binding energy (E_{bind}) of the electron as expressed by the following equation:

$$\mathrm{E_{bind}} = \mathrm{h\nu} - \mathrm{E_{kin}} - \Phi_{\mathrm{spec}} \tag{31}$$

Φ_{spec} is the spectrometer work function, a constant dependent on the instrument used. XPS can detect all elements except hydrogen. When using insulating compounds as samples, an additional term has to be added to the equation to account for the surface charging occurring during the measurement in the shape of the charge constant C [237–239]:

$$\mathrm{E_{bind}} = \mathrm{h\nu} - \mathrm{E_{kin}} - \Phi_{\mathrm{spec}} - \mathrm{C} \tag{32}$$

As mentioned, XPS is a surface-selective analytical method because although the X-ray can penetrate deep into the sample, the photoelectrons can only escape the sample material near the sample surface. The sampling depth (d) is defined by the following equation:

$$\mathrm{d} = 3\lambda \sin\theta \tag{33}$$

Here, λ is the attenuation length of the photoelectron, and θ the angle between the sample surface and the analyzer. The sampling depth typically ranges from around two to five nanometers [237, 240].

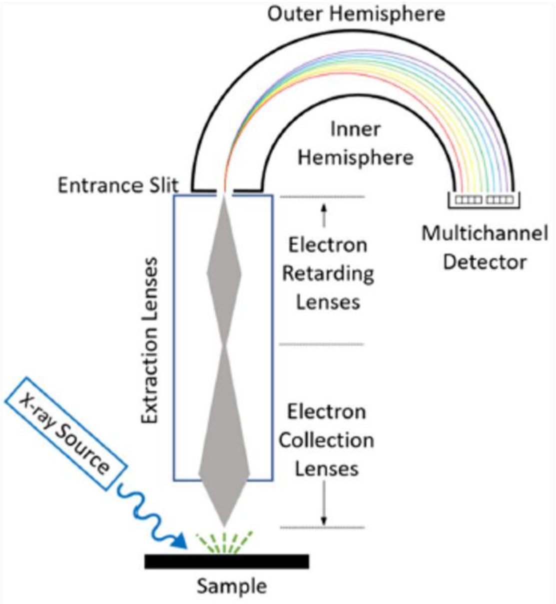

Figure 2.18: Schematic depiction of an XPS spectroscope [238].

XPS measurements are conducted in an ultra-high vacuum to avoid scattering the photoelectrons on their way to the analyzer. Contained within the vacuum is the X-ray source, the sample stage, the extraction lenses, the analyzer, and the detector. In modern XPS devices, monochromatic X-ray sources are used. The X-ray beam is directed at the sample, where the photoelectrons are produced. The photoelectrons then enter a set of lenses called the extraction lenses. These consist of both the electron collection and the electron retarding lenses. The location and size of these lenses relative to the sample determine the acceptance angle. After the photoelectrons have passed the collection lens, they are slowed down by the electron retarding lenses to improve the energy resolution of the XPS. After the electrons pass the electron retarding lenses, they arrive at the analyzer, which in modern XPS devices is a concentric hemispherical analyzer. This analyzer consists of two hemispheres. Voltages are applied to both, with the outer hemisphere being more negatively charged. Variation in these voltages allow for the selection of electron energies necessary to pass through the analyzer without colliding with either hemisphere [238].

2.8 Contact Angle Measurements

2.8.1 Basic Principle

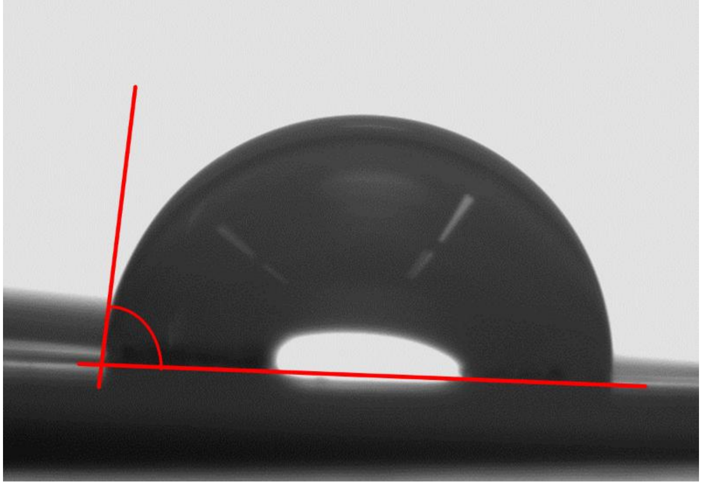

Figure 2.19: Image of a sessile drop with the contact angle indicated by the red lines.

Contact angle measurements are a method to determine the wetting properties of a given surface in a partial wetting regime. The contact angle is defined as the angle between the surface of a solid and the surface of a liquid in contact with the solid. For smooth solid surfaces, the contact angle is governed by the Young equation:

$$\cos\theta = \frac{\gamma_{\mathrm{sv}} - \gamma_{\mathrm{sl}}}{\gamma_{\mathrm{lv}}} \tag{34}$$

θ is the contact angle, γ_{sv} is the solid-vapor surface tension, γ_{sl} the solid-liquid surface tension, and γ_{lv} the liquid-vapor surface tension [241]. From a thermodynamic point of view, surface wetting phenomena are divided into two regimes. The first regime is total wetting, where the liquid spreads completely in contact with the solid surface due to $\gamma_{sv} = \gamma_{sl} + \gamma_{lv}$ leading to a contact angle of $\theta = 0°$. The second regime is partial wetting, where $\gamma_{sv} < \gamma_{sl} + \gamma_{lv}$ leading to a contact angle of $\theta > 0°$. Hydrophobic surfaces generally result in contact angles > 90°, while hydrophilic surfaces result in contact angles < 90°, assuming water as the liquid [242, 243]. The Young equation is modified by the so-called line tension. Line tension is the influence of the solid on γ_{lv} at the contact line. γ_{lv} is, therefore, dependent on the distance from the solid. Accounting for this change in surface tension leads to the following equation:

$$\cos\theta_{\mathrm{i}} = \cos\theta - \frac{\tau}{r_{\mathrm{b}}\gamma_{\mathrm{lv}}} \tag{35}$$

θ_i is the ideal contact angle, τ the line tension, and r_b the radius of the base of the droplet [244, 245]. The order of magnitude of the line tension falls somewhere between 10^{-11} and 10^{-6} N [246]. The shape of the liquid droplet used for contact angle determinations, either as a sessile or pendant drop, is determined by the Young-Laplace equation:

$$\Delta P = \gamma_{lv}\left(\frac{1}{R_1} + \frac{1}{R_2}\right) \qquad (36)$$

ΔP is the pressure difference across the liquid-vapor interface, and R_1 and R_2 are the radii of curvature [243, 247].

The Young equation presumes an ideal solid surface that is completely smooth, chemically homogenous, insoluble, and unreactive. However, surface smoothness and homogeneity can differ substantially from the ideal case and can have a significant impact. Both factors lead to local variations in contact angle along the contact line of a droplet. These localized contact angles are referred to as the actual contact angle. For ideal cases of sample heterogeneity, the Cassie equation can be applied to determine the overall contact angle:

$$\cos\theta_C = f_1 \cos\theta_1 + f_2 \cos\theta_2 \qquad (37)$$

The angle θ_C is the Cassie angle, f_1 is the fractional surface area with the contact angle θ_1, and f_2 is the fractional surface area with the contact angle θ_2. The Cassie equation is more precise in describing real surface systems than comparable models such as Wenzel's model. However, it still fails to describe systems with randomly heterogeneous surfaces accurately [242, 248]. Localized variations of the contact angle are not observable directly, as the contact angle is only observed macroscopically as the so-called apparent contact angle. Surface roughness and chemical heterogeneity, however, do influence dynamic contact angle measurements by causing contact angle hysteresis, a difference between the advancing (θ_A) and receding contact angle (θ_R) [249, 250]:

$$H = \theta_A - \theta_R \qquad (38)$$

2.8.2 Static Contact Angle

Static contact angle measurements are performed by recording the contact angle between the liquid and the solid at a single point in time. This technique is comparatively simple and quick to execute but carries certain limitations. As discussed previously (see Chapter 2.8.1), inhomogeneities of the sample, both in terms of surface roughness and chemical composition, can lead to local variations of the contact angle, which are not observable using this method. It also cannot analyze the slip/stick behavior of the liquid droplet on the surface [251, 252].

2.8.3 Dynamic Contact Angle

In contrast to static contact angle measurements, dynamic contact angle measurements involve constantly monitoring the contact angle throughout the measurement process. The process itself consists of slowly increasing and decreasing the volume of the liquid droplet [253] or, in the case of the Wilhelmy method, inserting a solid surface into the liquid and retracting it again [254]. These measurements result in the recording of two values, the advancing θ_A and the receding angles θ_R. The difference between these two angles is known as the contact angle hysteresis. The size of the contact angle hysteresis depends on the degree of inhomogeneity and roughness of the sample surface and can, therefore, be used as a measure for both. This method also provides information about the stick/slip behavior of the liquid because the contact angles are measured continuously [251–253].

2.8.4 Sessile Drop Method

The sessile drop method is a common technique to determine the contact angle based on the Young equation. A droplet of liquid with a predetermined volume is deposited on the solid surface using a syringe. The droplet is then photographed after a set amount of time, and the contact angle is determined based on the angles formed by the horizontal solid surface and the tangents of the droplet surface at the contact line. In the case of the static contact angle measurement, a single photograph is taken. The dynamic contact angle measurement, on the other hand, involves continuous monitoring of the contact angles while adding and removing liquid from the droplet [242, 255].

2.8.5 Wilhelmy Method

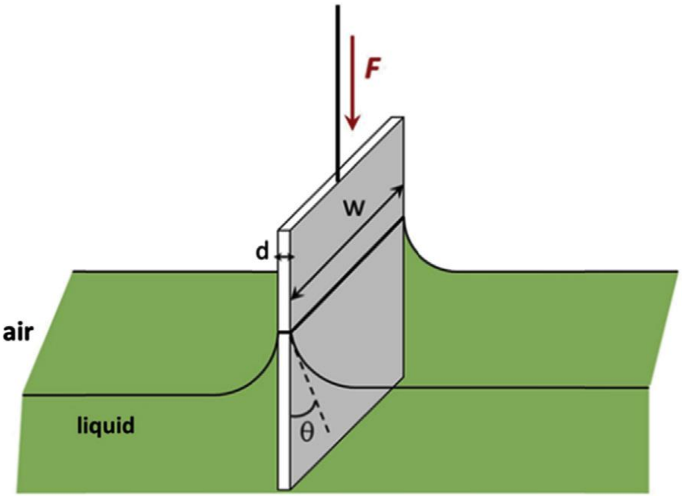

Figure 2.20: Graphical depiction of the Wilhelmy method with θ as the contact angle, d as the thickness of the plate, W as the width of the plate, and F as the downward force acting on the plate [242].

The Wilhelmy method is an alternative method for dynamic contact angle measurements for materials, such as fibers, that do not form flat surfaces suitable for the sessile drop technique [254]. Here, the advancing and receding angles are calculated using the Wilhelmy equation:

$$F_w = \pi d \gamma_{lv} \cos\theta \tag{39}$$

F_w is the measured force, d is the diameter of the fiber, and γ_{lv} the liquid-vapor surface tension [243, 256]. The measurement is conducted by inserting the fiber into a pool of liquid with a known surface tension and retracting it again, measuring the force throughout the process [254].

2.9 Zeta-Potential Measurements

2.9.1 Theoretical Background

Zeta potential is a phenomenon that occurs on charged solid surfaces in contact with aqueous solutions. The surface charge is formed due to processes such as acid-base reactions between the aqueous solution and the functional groups located on the solid surface. Functional groups such as carboxylic acids, sulfonic acid, and hydroxyl groups can dissociate to become negatively charged, while functional groups such as amine groups become positively charged after dissociation. The central driving force behind this mechanism of surface charge formation is the pH value of the aqueous solution [257]. The second mechanism is the adsorption of water ions to the surface. These ions accumulate on unfunctionalized hydrophobic surfaces, replacing water molecules. This mechanism is again pH-dependent. High pH values result in an increased surface concentration of OH^--ions on the surface, leading to a negative surface charge. In contrast, low pH values lead to increased H_3O^+-ion concentration and a positive surface charge. OH^--ions are generally more hydrophobic than the H_3O^+-ions, which leads to hydrophobic surfaces typically exhibiting a negative surface charge [258].

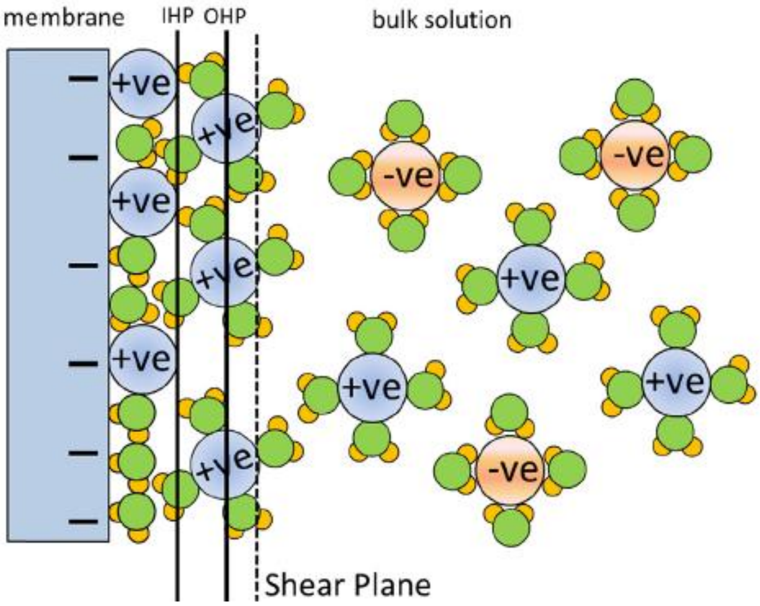

Figure 2.21: Graphical depiction of the electrical double layer on a membrane surface [259].

The surface charge causes an accumulation of counterions close to the solid surface. A stationary layer of counterions is formed in the immediate vicinity of the surface. This layer remains stationary due to the strong interactions between the counterions and the surface charges. This stationary layer can be further subdivided into the Stern layer, consisting of ions in direct contact with the solid surface, and the outer Helmholtz layer, which consists of ions firmly bound to the surface but not in direct contact. Outside that stationary layer, a gradient of counterion concentration is observable, where the counterion concentration decreases exponentially towards the bulk concentration. This area is called the diffuse layer. The interface between the stationary and diffuse layers is called the outer Helmholtz plane. Outside the outer Helmholtz plane, a thin hydrodynamically stagnant layer exists, which is differentiated from the remaining hydrodynamically active diffuse layer. The interface between these two parts of the diffuse layer is called the slip plane. The zeta potential is the difference in electrical potential between the slip plane and the bulk solution [257, 260–262].

The zeta potential is a parameter characterizing the surface charging behavior of a solid in contact with a liquid. It is determined through the measurement of an electrokinetic effect. The electrokinetic effect represents a coupling of a mechanical and an electrical force, which can be determined if the liquid phase moves tangentially to the solid surface. There is a variety of different electrokinetic effects grouped into two categories. The first category is effects, where movement is caused by electricity, which includes effects such as electrophoresis or electrokinetic sonic amplitude. The second category is effects, where movement causes electricity. This includes effects like sedimentation or the streaming potential [257, 260].

2.9.2 Streaming Potential Method

The streaming potential method is an experimental technique that involves streaming an aqueous solution through a capillary system. This capillary system can take a variety of shapes depending on the sample material. There are irregular capillary systems consisting of particles, fibers, or generally samples of irregular shape where the measurement is conducted in the so-called permeation mode, where the sample material is arranged in a plug that the aqueous solution flows through [263].

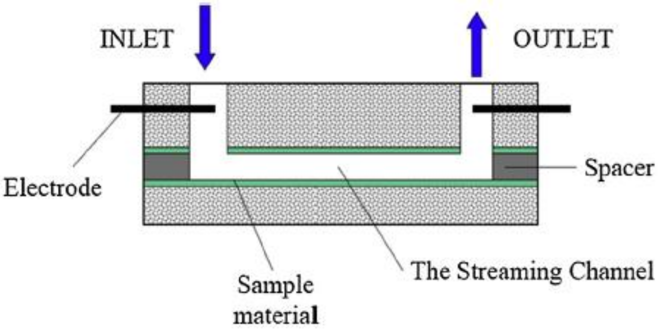

Figure 2.22: Schematic depiction of a gap cell used for conducting streaming potential measurements [259].

For macroscopic materials with flat surfaces, two samples are arranged opposite each other in the measuring cell with a thin slit between both, where the aqueous solution passes in between the samples. This is the so-called tangential mode [264]. As the aqueous solution flows through the capillary system, shear forces act upon the counterions, forming the stationary layer on the sample surface and compensating the surface charge. Because of that, the ions move in the direction of the liquid flow. The high-impedance circuit used for streaming potential measurements then leads to a charge separation between the inlet and the outlet of the capillary system [260]. As a result of this charge separation, an electric force occurs in the capillary system, counteracting the liquid flow. The concentration of counterions on one end of the capillary system leads to an opposing current of ions inhibiting further ion travel in the flow direction. The charge separation resulting from the liquid flow leads to an electrical potential difference between both ends of the capillary system called the streaming potential. This potential is measured using electrodes situated at both ends of the capillary system [259].

The streaming potential depends on several factors, including the flow rate through the capillary system and the ionic strength of the solution. The higher the flow rate, the higher the streaming potential as the shear rate of the counterions increases with increasing liquid flow. An increase in ionic strength of the aqueous solution leads to a lower streaming potential, as the counterions that are displaced by the liquid flow are readily replaced by the ions from the solution, leading to a decrease in charge separation [259].

The central equation for the calculation of the zeta potential from the streaming potential measurements is the Helmholtz-Smoluchowski equation, which for streaming potential measurements of planar samples looks as follows:

$$\zeta = \frac{dU_{str}}{d\Delta p} \cdot \frac{\eta}{\varepsilon \cdot \varepsilon_o} \cdot \frac{L}{A} \cdot \frac{1}{R} \tag{40}$$

ζ is the zeta potential, U_{str} is the streaming potential, Δp is the flow rate of the aqueous solution expressed as the differential pressure in the measuring cell, η is the viscosity of the aqueous solution, ε its relative permittivity, and ε_0 the relative permittivity of the vacuum. L is the channel length between the two material samples, and A is its cross-section. Both parameters together form the cell constant. R is the electrical resistance of the electrical circuit. The cell constant and the electrical resistance can be summarized as the electrical conductance κ leading to the following equation:

$$\zeta = \frac{dU_{str}}{d\Delta p} \cdot \frac{\eta}{\varepsilon \cdot \varepsilon_o} \cdot \kappa \tag{41}$$

For irregular samples where the cell constant is unknown, an approximation can be made by replacing κ with the conductance of the bulk solution κ_B [257].

The electrolyte solution's pH value is the central parameter influencing the zeta potential. Therefore, zeta potential measurements are typically conducted over a wide range of pH values to determine the respective sample material's pH dependence and the isoelectric point (IEP). The zeta potential generally increases with decreasing pH value due to increasing adsorption of H_3O^+-ions and increasing protonation of functional groups on the material surface. The zeta potential stays negative for samples with many acidic functional groups on the surface until low pH values are reached, with an IEP below seven. Amphoteric materials have an IEP of seven, while materials with many basic functional groups reach the IEP at high pH values. The surface charge at the IEP does not disappear but is an equilibrium of positive and negative charges. Overall, the IEP can act as a good indicator of the properties of the functional groups on the material surface [259].

In application, zeta-potential measurements are a good tool for comparative measurements between samples, particularly in cases of surface modification processes. Both the value of the zeta potential and the position of the IEP can serve as indicators for processes like the formation of functional groups on the material surface or for surface adsorption processes [265, 266].

2.10 Hemocompatibility Tests

2.10.1 Hemolysis

Hemolysis describes the destruction or disruption of the red blood cell membranes, causing the release of Hb into the surrounding blood plasma.

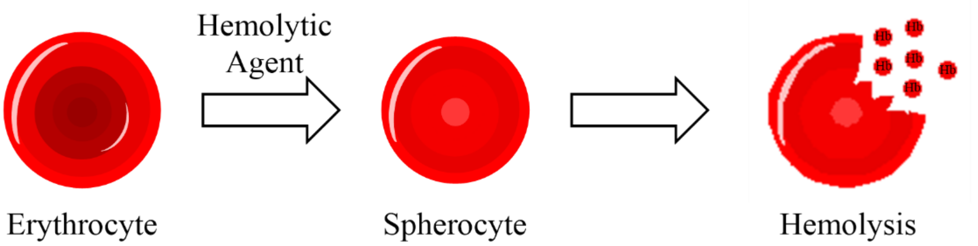

Figure 2.23: Graphical depiction of the basic mechanism of hemolysis. Inspired by a figure in publication [267].

Various conditions can cause hemolysis, generally differentiated as intravascular and extravascular hemolysis. Intravascular hemolysis can be caused by enzymopathies such as glucose-6-phosphate dehydrogenase deficiency (G6PD), and pyruvate kinase deficiencies, and infections such as HIV, Malaria, and Bartonella. Other factors include alloimmune diseases such as transfusion reactions, thrombotic microangiopathies such as the HELLP syndrome and thrombotic thrombocytopenic purpura [268]. Also included in this category is trauma caused by mechanical stress induced by devices such as ECMO circuits. Here, hemolysis is induced through shear stress, pressure variations, and turbulences. The pumps of these circuits, in particular, cause hemolysis due to their moving part, such as impellers and rollers, which cause shear stress and turbulences, as well as high-pressure areas close to the moving parts. At the same time, blood traveling through the circuit tubing experiences low-pressure areas [269]. Another factor contributing to the hemolytic properties of these external circuits is the large blood-contacting polymer surfaces [270].

Extravascular hemolysis includes membranopathies such as hereditary spherocytosis and elliptocytosis. Hemoglobinopathies such as sickle cell disease and thalassemia also play a role. Other sources for extravascular hemolysis are factors relating to the phlebotomy method, such as needle size and shape, tube size and material, blood draw method, drawing site, and tourniquet time. Hemolysis also occurs after the blood has been drawn, with both processing and storage parameters influencing its progression. For processing, the time delay until centrifugation, as well as the centrifugation parameters such as time, temperature, and force, play a role, while for storage, both storage time and temperature are decisive [271–273].

Red blood cells have a lifetime of about 120 days after being released from the bone marrow. If the red blood cell hemolysis progresses faster than they can be replaced, a condition known as hemolytic anemia arises. Hemolytic anemia is a condition that causes nonspecific symptoms such as fatigue, dyspnea, and hypertension. Specific symptoms of chronic anemia include lymphadenopathy, hepatosplenomegaly, cholestasis, and choledocholithiasis [268].

2.10.2 Drabkin’s Method

Drabkin’s method is a technique to determine the plasma Hb content of blood samples. Here, Hb is oxidized using potassium ferricyanide to form Met-Hb. Met-Hb then reacts further with potassium cyanide to form the cyanmethemoglobin complex. For application purposes, potassium ferricyanide and potassium cyanide are combined in an aqueous solution called the Drabkin’s reagent. The reaction proceeds according to the mechanism shown below:

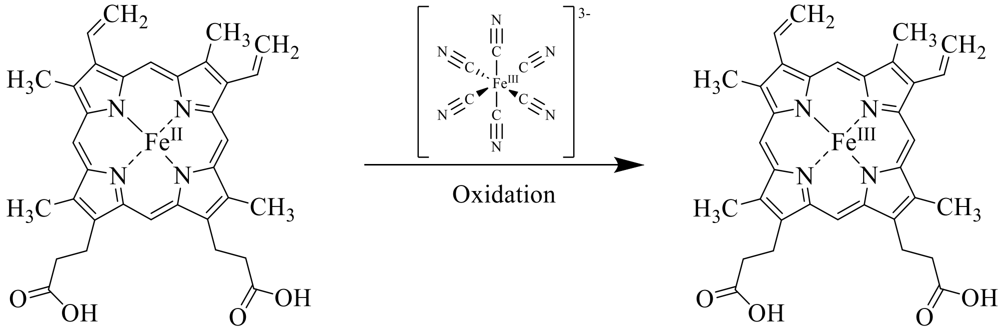

(42)

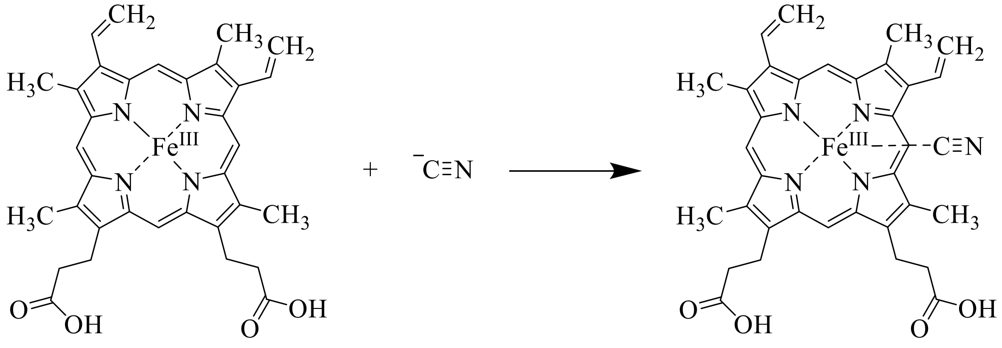

(43)

The cyanmethemoglobin complex resulting from this reaction is a stable pigment possessing a bright red color. The complex shows a strong absorption band at 540 nm, allowing for the quantification of Hb using UV/Vis spectroscopy [274–276].

2.10.3 UV/Vis Spectroscopy

UV/Vis spectroscopy is one of the standard methods of chemical analysis. It utilizes electromagnetic radiation in the ultraviolet and visible range ranging from 100 to 800 nm. This radiation excites the outer electrons of so-called chromophore molecules through the absorption of the radiation, leading to transitions into higher electronic energy states. Due to the quantization of these energy states, absorption is only possible at specific wavelengths, leading to narrow absorption bands. The combined positions of these absorption bands in the resulting spectra can then be used to identify the analyzed compounds [277, 278].

The decrease in radiation intensity at specific wavelengths due to the absorption processes can be utilized to perform quantitative analysis in addition to the qualitative identification of compounds. The relation between incidence radiation intensity (I_0) and transmitted radiation intensity (I) is called transmittance (T). UV/Vis spectra commonly use the absorbance (A) parameter in relation to the wavelength. This parameter is derived from transmittance and the radiation intensities according to the following equations:

$$A = -\log T = -\log \frac{I}{I_0} \qquad (44)$$

The dependence of the absorbance of a signal on the concentration of the respective compound is given by the Lambert-Beer law:

$$A = \varepsilon \cdot c \cdot l \qquad (45)$$

Here, ε stands for the extinction coefficient, c for the concentration, and l for the path length. The extinction coefficient is a constant characteristic of the analyzed compound under a defined set of conditions. The path length is determined by the thickness of the sample container at the point where the radiation travels through the sample [277, 279, 280].

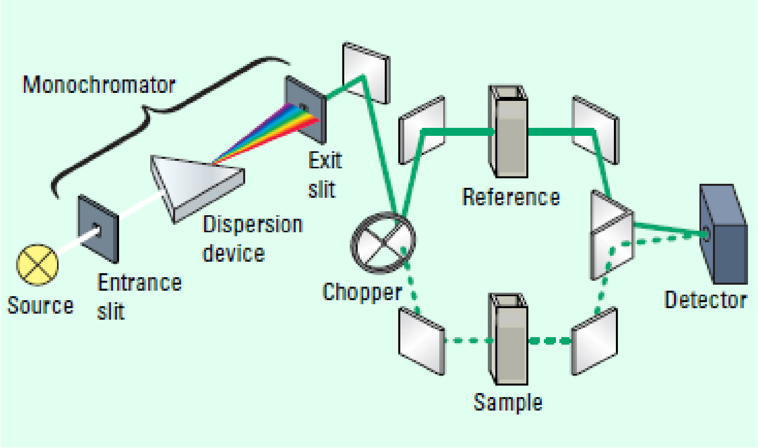

Figure 2.24: Schematic depiction of a dual beam spectrophotometer [277].

UV/Vis spectra are recorded using UV/Vis spectrophotometers. These devices use a broad-band radiation source such as deuterium arc, tungsten halogen, or xenon lamps. A dispersive element, such as a prism or holographic grating, is then used in combination with an exit slit to select individual wavelengths from the continuum of the source. The radiation beam then travels through the sample until it reaches the detector. The detector is typically a photomultiplier tube or photodiode detector. Various measurement configurations exist, including single-beam, dual-beam, and split-beam designs. The configuration used for the measurements of this thesis was a dual beam configuration. This configuration uses a so-called chopper, which is a moving part that facilitates the alternate illumination of the sample and the reference, allowing for simultaneous measurement of both with a single detector [277, 278].

2.10.4 Vapor Pressure Osmometry (VPO)

The term osmometry encompasses several different methods measuring the osmotic pressure (π) and other related colligative properties of dilute solutions, such as vapor pressure lowering or freezing point depression. These methods can determine the osmolality of dilute solutions, as well as the average molecular weight of polymers in solution [281, 282]. Techniques included under the term osmometry are direct membrane osmometry (DMO), freezing point osmometry (FPO), and vapor pressure osmometry (VPO) [283–286]. VPO is the relevant technique for this thesis. It is a technique based on the change in vapor pressure of a solvent caused by the dissolution of non-volatile compounds. For infinitely dilute systems, the change is described by Raoult's Law:

$$p_s = x_s p_s^* = (1 - x_a) p_s^* \qquad (46)$$

p_s is the vapor pressure of the solvent containing non-volatile solutes, x_s is the mole fraction of the solvent, x_a is the mole fraction of the solute, and p_s^* the vapor pressure of the pure solvent [283, 287]. At higher solute concentrations, the behavior of the solvent diverges from the linear behavior outlined by Raoult. The behavior is instead described by the by the Raoult-Lewis equation:

$$\pi = \frac{-RT \cdot \ln(x_s)}{v_s} \cong \frac{RT}{v_s} \cdot x_a \tag{47}$$

R is the gas constant, T is the temperature, x_s is the mole fraction, and V_s is the molar volume of the solvent [283, 288]. The relation between the ideal osmotic pressure (π_{ideal}), described by the Raoult-Lewis equation, and the real osmotic pressure (π_{real}) is expressed as the osmotic coefficient g, which is defined by the following equations:

$$g = \frac{\pi_{real}}{\pi_{ideal}} \tag{48}$$

$$\pi_{real} = g \cdot \pi_{ideal} \tag{49}$$

Therefore, the Raoult-Lewis equation is modified for the description of π_{real} as follows [289]:

$$\pi_{real} = \frac{-RT \cdot g \cdot \ln(x_s)}{v_s} \cong \frac{RT}{v_s} \cdot g \cdot x_a \tag{50}$$

VPO devices consist of a thermally insulated chamber with a reservoir of pure solvent at the bottom, which leads to an internal atmosphere saturated with the solvent. The internal temperature of this chamber is electronically controlled. Built into this chamber are two thermistors, which are part of the circuit. This circuit includes a Wheatstone bridge to quantify the potential difference between both thermistors. A drop of pure solvent is placed on the tip of each thermistor to establish a zero point. One of the droplets is then replaced with the analyte solution. The compounds dissolved in that solution lead to a decrease in vapor pressure (Δp) compared to the pure solvent (see Equation 46) [290, 291]. This pressure difference is proportional to the molar fraction of the solute, leading to the following equation:

$$\frac{\Delta p}{p_s^*} = g \cdot x_a \tag{51}$$

Which, in combination with equation 50, leads to [289]:

$$\frac{\Delta \mathrm{p}}{\mathrm{p}_{\mathrm{s}}^{*}} = \pi_{\mathrm{real}} \cdot \frac{\mathrm{v}}{\mathrm{RT}} \tag{52}$$

The difference in vapor pressure causes condensation of the surrounding solvent vapor onto the solution droplet until the vapor pressure between both droplets is equalized. The increase in vapor pressure of the solution droplet leads to a rise in temperature [290, 291]. The connection between the temperature difference (ΔT) and the vapor pressure difference (Δp) is described using the Clausius-Clapeyron equation:

$$\Delta \mathrm{T}_{eq} = \frac{\Delta \mathrm{p}}{\mathrm{p}_{\mathrm{s}}^{*}} \cdot \frac{\mathrm{RT}^{2}}{\Delta \mathrm{H}_{\mathrm{v}}} = \frac{\mathrm{RT}^{2}}{\Delta \mathrm{H}_{\mathrm{v}}} \cdot \mathrm{g} \cdot \mathrm{x}_{\mathrm{a}} = \mathrm{K}_{eq} \cdot \mathrm{g} \cdot \mathrm{x}_{\mathrm{a}} \tag{53}$$

ΔH_v is the vaporization enthalpy, ΔT_{eq} the temperature difference under equilibrium conditions, and K_{eq} is a proportionality constant under equilibrium conditions. This equation would apply given the existence of a thermodynamic equilibrium. Under the steady state conditions the method operates under, the following equation applies:

$$\Delta \mathrm{T}_{\mathrm{ss}} = \mathrm{K}_{\mathrm{ss}} \cdot \mathrm{g} \cdot \mathrm{x}_{\mathrm{a}} \tag{54}$$

The VPO instrument is calibrated before the measurement itself using a substance of known molecular weight, leading to the following equation:

$$\Delta \mathrm{T}_{\mathrm{ss}} = \mathrm{K}_{\mathrm{ss}} \cdot \pi_{\mathrm{real}} \cdot \frac{\mathrm{v}_{\mathrm{s}}}{\mathrm{RT}} = \left(\frac{\mathrm{K}_{\mathrm{ss}} \mathrm{v}_{\mathrm{s}}}{\mathrm{RT}}\right) \cdot \frac{\mathrm{c}}{\mathrm{M}_{\mathrm{cal}}} = \mathrm{K}_{\mathrm{ss}}' \cdot \frac{\mathrm{c}}{\mathrm{M}_{\mathrm{cal}}} \tag{55}$$

c is the concentration of the calibration substance, and M_{cal} is its molecular weight. In practice, the instrument measures the potential difference between both thermistors using the Wheatstone bridge. This potential difference E is related to the concentration (c_a) and molar mass (M_a) of the solute through the following equation:

$$\frac{\mathrm{E}}{\mathrm{K}_{\mathrm{ap}}} = \frac{\mathrm{c}_{a}}{\mathrm{M}_{a}} \tag{56}$$

K_{ap} is the apparatus constant, which depends on the solvent and temperature used for the measurement. It can be determined through calibration measurements [289, 292].

3. Experimental

3.1 Materials

NO (10,000 ppm in N_2), NO (1000 ppm in N_2), and NO_2 (1000 ppm in N_2) were purchased from basi Schöberl GmbH & Co. KG (Rastatt, Germany). Samples of the individual gas exchanger components, including hollow fiber membranes (PMP), inlet/outlet caps (MABS), gas caps (MABS), polyurethane sheets (PU), silicone gaskets, UV-activated adhesive, gas hoses (PVC), and blood hoses (PVC) in addition to fully assembled oxygenators were provided by Hemovent GmbH (Aachen, Germany). The hollow fiber membrane was a 3M Membrana OXYPLUS, type 90/200 (3M Deutschland GmbH, Wuppertal, Germany). The MABS used for both the inlet/outlet caps and the gas caps was Terlux 2802, produced by INEOS Stryrolation Group GmbH (Frankfurt am Main, Germany). The PU was made up of a prepolymer consisting of methylene diphenyl diisocyanate (MDI) and glycols (Biresin DH41 Komp. B, Sika Deutschland GmbH, Stuttgart, Germany) and trimethylolpropane (TMP) (Biresin DH404 Komp. A, Sika Deutschland GmbH, Stuttgart, Germany) (information provided directly by Sika Deutschland GmbH). The gas hoses were produced by Rehau SE (Bern, Switzerland) as Rauclair-E, containing the plasticizer bis(2-ethylhexyl) terephthalate (DOTP) (32.7 wt%) (information provided directly by Rehau SE). The blood hoses were produced by Raumedic AG (Helmbrechts, Germany) under the name Raumedic ECC noDOP 7536, containing the plasticizer tris(2-ethylhexyl) trimellitate (TEHTM) [200]. The UV-activated adhesive was produced by Dymax Europe GmbH (Wiesbaden, Germany) as 1197-M containing 2-hydroxyethyl methacrylate, isobornyl acrylate, and 1-vinylhexahydro-2H-azepine-2-one [293]. The silicone gasket was produced by Hokosil Elastomertechnik GmbH (Bredenbek, Germany) as HokoFLEX – Silikonprofile Extrusion – 35° Shore A – STQ/STQplus +250. Sodium chloride (>99.5 %) and potassium dihydrogen phosphate were purchased from Merck KGaA (Darmstadt, Germany). Heparin lithium salt from porcine intestinal mucosa (≥150 USP units/mg), potassium ferricyanide (III) (99 %), potassium cyanide (≥98.0 %), Brij L23 solution (30 %(w/v) in H_2O), hemoglobin porcine lyophilized powder and calcium and magnesium free Dulbecco’s phosphate buffered saline (CMF-DPBS), and sodium hydrogen carbonate were purchased from Sigma-Aldrich Chemie GmbH (Steinheim, Germany). High-density polyethylene sheets were purchased from McMaster-Carr

Supply Company (Elmhurst, IL, USA). Samples of pigs' blood were provided by the butcher's shop and restaurant Bachhuber (Abensberg, Germany).

Millipore water (≥ 18 MΩ·cm) was used in all experiments unless mentioned otherwise.

3.2 Analysis of NO Gas Treatment on the Oxygenator Materials

3.2.1 Gas Treatment with NO and NO_2 at various Concentrations

The material samples were prepared by cutting pieces from the oxygenator components, which were between around 0.5 and one centimeter in both length and width. The samples were placed in a chamber for the gas treatment, and the gas mixture was added at a continuous flow rate of 2 L/min for up to four hours. For samples treated for 17 hours or longer, the gas mixture was added to the treatment chamber for 15 minutes to ensure complete displacement of the ambient air. The chamber was then closed to keep the gas concentration constant for the duration of the treatment. The treatment of PMP was slightly different for NO concentrations of 80 ppm. Instead of placing samples in the treatment chamber, the gas mixture was pumped through fully assembled oxygenators, with PMP samples being cut from the oxygenator at regular intervals. PMP was treated identically to the other materials for all other gas concentrations and treatment procedures. Gas treatments were conducted at 10,000, 1000, and 80 ppm for NO and 1000, 500, and 50 ppm for NO_2. The usual treatment durations were 30 minutes, one, two, four, and 17 hours. Treatment durations of up to 10 and 15 days were also tested for the NO concentrations of 80 and 1000 ppm, respectively. Gas treatments at 1000 and 10,000 ppm were conducted by connecting the gas bottles directly to the treatment chamber, using a GT1355 Sho-Rate G rotameter (Brooks Instruments, Hatfield, PA, USA) to control and monitor the gas flow. At concentrations lower than 1000 ppm, a NO-A nitric oxide delivery system (EKU Elektronik GmbH, Leiningen, Germany) was used to add the desired NO/NO_2 concentration to the airflow created by an Aquaforte Hi-flow V60 pump (Sibo Fluidra Netherlands b.V., Doornhoek, Netherlands). The gas flow rate was monitored using a SpiroScout EKU flowmeter (Ganshorn Medizin GmbH, Niederlauer, Germany).

3.2.2 Determination of Temporal Stability

The temporal stability of the gas treatment effects was tested with material samples treated with either NO or NO_2 at 1000 ppm for 17 hours. These tests were conducted under dry and wet conditions, with the tests under wet conditions limited to samples treated with NO (1000 ppm). The tests under dry conditions were conducted by leaving the samples just in contact with ambient air for a predetermined amount of time after the end of the gas treatment. FTIR-ATR measurements were performed after two, four, six, and 24 hours, as well as five, ten, and 15 days after the end of the gas treatment for the tests under dry conditions. The tests under wet conditions involved submerging the samples in either Millipore water or physiological sodium chloride solution. The tests under wet conditions were limited to measurements five and ten days after the end of the gas treatment. The samples tested under wet conditions were dried in a desiccator over silica gel for 24 hours before the FTIR-ATR measurements were conducted. The samples submersed in sodium chloride solution were rinsed with Millipore water before drying to avoid salt deposits on the sample surface.

3.2.3 FTIR-ATR Measurements

The FTIR-ATR measurements were conducted using an Agilent Varian 670 IR spectroscope (Agilent Technologies Inc., Santa Clara, CA, USA) with a Pike Technologies GladiATR probe head (Pike Technologies, Fitchburg, WI, USA). The spectra recorded cover a range of wavenumbers from 4000 to 500 cm^{-1}, with a resolution of 2 cm^{-1}. The samples were pressed down onto the diamond of the ATR probe head with the built-in clamp to achieve consistent and complete coverage, ensuring reproducible signal intensities. The spectra were recorded against a background measurement of the unoccupied sample space. Difference spectra were recorded using untreated material samples as the background. All experiments were reproduced three times.

3.2.4 Scanning Electron Microscopy

SEM images of the polymer materials were recorded to determine whether the gas treatment had any macroscopic impact on the surface morphology of the polymers. Samples roughly one by one centimeter in size were cut from the polymer materials. Single fibers were used for the hollow fiber membrane, either whole or cut in half lengthwise. Both untreated samples and samples treated with NO (1000 ppm) for 17 hours were examined. The samples were sputtered with gold using a Quorum SC 7620 sputter coater (Quorum Technologies, Lewes, United Kingdom) for 30 seconds. A Zeiss EVO

MA15 scanning electron microscope (Carl Zeiss Ag., Oberkochen, Germany) with a backscattered electron detector was used to record the SEM images. The images were recorded by Ulrike Schiessl from the chair of inorganic chemistry of Professor Dr. Arno Pfitzner at the University of Regensburg. Images of both the inside and the outside of the fibers were recorded for the hollow fiber membrane. The images of the remaining polymer materials were recorded on the side of each material that has direct contact with the treatment gas in the fully assembled oxygenator.

3.2.5 X-Ray Photoelectron Spectroscopy

The XPS measurements were conducted using a Physical Electronics PHI 5700 (Physical Electronics GmbH, Feldkirchen, Germany). All measurements were performed by Dr. Matthias Kronseder from the Institute of Experimental and Applied Physics at the University of Regensburg. The polymer samples were analyzed untreated and after treatment with NO (1000 ppm) for 17 hours. The samples were each measured both in their original state and after sputtering. The sputtering process consisted of Ar-ion-bombardment for ten minutes with a 1.9 kV acceleration voltage. The samples were sputtered in a square area, 49 mm^2 in size. This process removed several nanometers of material from the sample's surface. A neutralizer was used during both the measurement and the sputtering process to suppress the charging effects of the insulating samples. The measurements were limited to PMP, MABS (inlet/outlet cap), and PU due to time constraints and the physical shape of the PVC samples not being suitable for XPS measurements.

Additionally, long-term stability tests were performed with measurements conducted with MABS and PU directly after the gas treatment and six and 13 days after the end of the gas treatment. The samples were treated with NO (1000 ppm) for 17 hours, and XPS measurements were performed directly after the gas treatment and six and 13 days after the end of the gas treatment. The samples were left in contact with air at room temperature between measurements. The stability of the treatment effects was quantified based on the area of the peak at 407.6 eV.

3.2.6 Contact Angle Measurements

Contact angle measurements were conducted to determine the influence of the gas treatment on the surface hydrophilicity of the polymers. Both static and dynamic contact angle measurements were used to achieve that goal.

3.2.6.1 Static Contact Angle Measurements

Static contact angle measurements were conducted using a Dataphysics OCA 15plus (Dataphysics Instruments GmbH, Filderstadt, Germany). Samples roughly two centimeters in length and one centimeter in width were cut from the polymer materials. The material selection was narrowed down from the FTIR-ATR measurements because this experimental technique required a flat, uniform surface to be conducted properly. The materials analyzed were, therefore, limited to the outlet cap (MABS), the gas cap (MABS), and the PU sheets. The material samples were treated with NO and NO_2 identically to the FTIR-ATR samples regarding gas concentrations, with treatment times being limited to a maximum of 17 hours. These samples were analyzed directly after the end of the treatment. Additional measurements were conducted to determine the stability of the contact angle effect of the gas treatment by reexamining samples treated with 10,000 ppm of NO after one month. Further measurements were conducted with these samples after submerging them in water for 24 hours and drying them in a desiccator over silica gel afterward.

The sessile drop technique was used for these experiments. A drop with a volume of approximately 5 µL was deposited on the polymer surface, and a photograph of the drop was recorded approximately 15 seconds after the droplet was deposited. The contact angles on both sides of the droplet were determined using the software SCA20 (Dataphysics Instruments GmbH, Filderstadt, Germany). Both angles were averaged for each droplet deposition. Three drops in total were deposited on each sample, and the experiments for each gas concentration were reproduced three times.

3.2.6.2 Dynamic Contact Angle Measurements

The static contact angle measurements conducted for this thesis contained several factors of uncertainty, in particular, the manual droplet deposition and the variations in time between deposition and image recording. It was also impossible to meaningfully analyze the hollow fiber membranes (PMP), which constituted the biggest blood-contacting surfaces. So, to mitigate these uncertainties and expand the method to include the hollow fiber membranes (PMP), dynamic contact angle measurements were conducted by Stefan Michel and Niklas Gerlach as part of a cooperation with Dr. Auernhammer's group at the Leibniz Institute for Polymer Research Dresden.

The dynamic contact angle measurements were conducted using a Dataphysics OCA 35L (Dataphysics Instrument GmbH, Filderstadt, Germany). The results of these measurements were analyzed using the software SCA202. The selection of materials was further limited to just the polymer in direct contact with patient blood, meaning the hollow fiber membrane (PMP), the inlet/outlet cap (MABS), and the PU sheets. MABS and PU samples were analyzed using the sessile drop technique, while the hollow fiber membranes (PMP) were analyzed using the Wilhelmy method.

3.2.6.3 Sessile Drop Technique

For the sessile drop technique, samples with a size of two by one centimeter were cut from the larger material samples. Because variations in surface roughness could have substantially affected the results, care was taken to ensure consistent surface morphologies for both MABS and PU by cutting the samples from the same larger material samples and analyzing the same side of all these samples [242, 249]. Treatment of the samples was limited to NO (1000 ppm) for 17 hours to ensure a clearly defined treatment impact. The measurements were conducted by depositing a droplet of water on the sample surface with an initial volume of 5 µL of water. During the measurement of the advancing angle, water was added to the droplet at a rate of 0.1 µL/s up to a total volume of 20 µL. The receding angle was then measured by completely removing the droplet from the surface at a rate of 0.1 µL/s. Three repeat measurements were conducted for all samples.

3.2.6.4 Wilhelmy Method

For the Wilhelmy method, single fibers of the hollow fiber membrane (PMP) with a length of approximately 40 mm were used. The lower ends of the fibers were pressed shut to prevent water from ingressing into the internal space of the fiber and impacting the measurements. Gas treatment of these fibers was again limited to NO (1000 ppm) for 17 hours. For the measurements, a cuvette was filled with Millipore water, and the fiber was inserted into the liquid to a total depth of 12 mm with a rate of 6 mm/min and then pulled back at the same rate, measuring both advancing and receding contact angles during this process. Three repeat measurements were conducted for all samples.

3.2.7 Zeta Potential Measurements

The zeta potential measurements were conducted using a SurPASS 3 (Anton Paar, Graz, Austria). The measurements were performed by Anja Caspari in cooperation with Dr. Auernhammer's group at the Leibniz Institute for Polymer Research Dresden. The polymer materials were analyzed in the untreated state and treated with NO (1000 ppm) for 17 hours. MABS and PU samples two by one centimeters in size were used. Similar to the contact angle measurements, care was taken to keep the side of the sample material that was analyzed the same to avoid introducing inconsistencies into the measurements, as surface morphology could have impacted the measurements [294]. For this purpose, the backsides of the individual samples were marked before cutting them from the larger piece of sample material. Both materials were analyzed using an adjustable gap cell, with the gap being adjusted to around 100 µm. The pressure applied to the cell ranged from 600 to 200 mbar. PMP was analyzed using a cylindrical cell. The hollow fiber membranes were packed tightly into the cell, with 150 mg of PMP per measurement. The resulting permeability index of the cell was approximately 100. All measurements used a KCl solution (10^{-3} mol/L) as the electrolyte. They were conducted over a pH range of three to ten, with HCl and NaOH solutions (0.05 mol/L) used to adjust the pH. Measurements were started at a neutral pH and adjusted up or down, with two PMP samples and four MABS and PU samples being used per measurement to cover the entire pH range.

3.3 Hemocompatibility Tests

Hemocompatibility experiments were conducted to determine whether the addition of NO to the perfusion gas mixture impacts the hemocompatibility of the oxygenator. These experiments were based on previous investigations undertaken to ensure hemocompatibility and, therefore, closely modeled on the ISO-10993-4 standard [295]. Hemocompatibility is quantified based on the inducement of hemolysis.

3.3.1 Sample Preparation

3.3.1.1 Drabkin's Reagent

Drabkin's reagent was prepared by weighing potassium ferricyanide (III) (200 mg), potassium cyanide (50 mg), and potassium dihydrogen phosphate (140 mg) into a 1L bottle and adding Millipore water (1000 mL). After dissolving the compounds, a Brij L23 solution (0.5 mL) was added. When not used, the Drabkin's reagent was stored in the fridge at 4 °C. Before beginning any experiments, the reagent was left to come to room temperature for at least 30 minutes. A new reagent solution was prepared at the beginning of each week.

3.3.1.2 Calibration Curve

A calibration curve was recorded using the lyophilized porcine Hb. The calibration samples were prepared by dissolving 14.4 mg of Hb in 10 mL of Drabkin's reagent. A dilution series of this base sample was prepared, consisting of samples with Hb concentrations of 0.72, 0.6, 0.3, 0.15, 0.06, and 0.03 g/L in addition to one blank sample. The samples were analyzed using UV/Vis spectroscopy (see Chapter 3.3.3.1).

3.3.1.3 Blood Samples

Pigs' blood was chosen for these experiments due to its availability and broad similarity with human blood [296]. A sterilized PET bottle was prepared with 15 mg of the anti-coagulant heparin. A sample of around 300 mL of fresh pigs' blood was then obtained from the butcher's shop and restaurant Bachhuber (Abensberg, Germany). The Hb concentrations in both the whole blood and the blood plasma were determined. Samples of 0.02 mL of blood and 5 mL of Drabkin's reagent were prepared to determine the total Hb content. The samples were mixed and left for 15 minutes to allow the Drabkin's reagent to react with the Hb. To determine plasma Hb, 8 mL of blood were centrifuged at 800 g and 20 °C for 15 minutes using a Sigma 3-18KHS (Sigma Laborzentrifugen GmbH, Osterode am Harz, Germany). 2 mL of the supernatant and 2 mL of Drabkin's reagent were then mixed and left to react for 15 minutes at room temperature. The samples were analyzed using UV/Vis spectroscopy (see Chapter 3.3.3.1). The Hb contents of the whole blood and the plasma were determined based on the calibration measurements. All samples were prepared in triplicate. The blood sample was accepted for further use if the plasma Hb values remained below 2 g/L. The blood was then diluted with CMF-DPBS to reach a Hb concentration of 10 g/L, based on the whole blood's Hb content. The Hb concentration of the diluted blood solution was then confirmed by an additional UV/Vis measurement with samples of 0.02 mL diluted blood and 5 mL Drabkin's reagent. The composition of the solution was adjusted accordingly if the Hb concentration was below 9 or above 11 g/L. In that case, the Hb concentration was determined again using the same method to obtain the final concentration.

3.3.2 Extraction Method

3.3.2.1 Experimental Procedure

Around 700 mL of CMF-DPBS was filled into an oxygenator with attached blood hoses for the extraction procedure. A section of flexible silicone tubing was connected to both blood hoses via hose connectors, completing the circuit. The filled oxygenator was placed in a drying oven, and the silicone tubing section was placed in a type 10-40-00 peristaltic pump (Stöckert Instrumente GmbH, Munich, Germany). The oxygenator was kept at a temperature of 50 °C for 72 hours while the liquid was circulated at a rate of 2 L/min using the peristaltic pump. The sweep gas mixture perfused through the oxygenator throughout this period consisted of either pure air or air with NO (40 ppm) added to it. After the extraction, three samples of 7 mL each were taken from the oxygenator, and 1 mL of diluted blood was added. The samples were mixed and kept at 37 °C for three hours, being carefully inverted every 30 minutes to ensure homogeneity. The samples were then centrifuged at 800 g and 20 °C for 15 minutes using a Sigma 3-18KHS (Sigma Laborzentrifugen GmbH, Osterode am Harz, Germany). Afterward, 2 mL of supernatant was taken from the sample, mixed with 2 mL of Drabkin's reagent, and left to react for 15 minutes at room temperature. The samples were then analyzed using UV/Vis spectroscopy (see Chapter 3.3.3.1). Additional samples were taken from the oxygenator circuit to perform measurements of both osmolality (see Chapter 3.3.3.2) and pH value (see Chapter 3.3.3.3). Due to sizeable statistical variance, both variants of gas perfusion were repeated a total of five times.

3.3.2.2 Control Samples

Several sets of control samples were prepared for each extraction process. A set of control blank samples containing 8 mL of CMF-DPBS, a set of positive control samples containing 8 mL of Millipore water, and a set of negative control samples containing 8 mL of CMF-DPBS and HDPE sheets at a concentration of 3 cm^2/mL. All sample sets consisted of three samples each. The samples were put in a sand bath at 50 °C for 72 hours, being stirred throughout. Afterward, 7 mL of each sample was mixed with 1 mL of diluted blood and kept at 37 °C for three hours, being carefully inverted every 30 minutes. 2 mL of each sample was then mixed with 2 mL of Drabkin's reagent and left to react for 15 minutes at room temperature. The samples were analyzed together with the corresponding extraction samples using UV/Vis spectroscopy (see Chapter 3.3.3.1).

The blank control samples were further analyzed concerning both their molality (see Chapter 3.3.3.2) and pH value (see Chapter 3.3.3.3).

3.3.3 Analytical Methods

3.3.3.1 UV/Vis Spectroscopy

UV/Vis spectroscopy was the primary analytical method for the hemocompatibility tests. A PerkinElmer Lambda 18 UV/Vis spectroscope (PerkinElmer Inc., Waltham, MA, USA) was used for all measurements, with a spectroscopic range from 300 to 700 nm being recorded. Pure Drabkin’s reagent was used as the background for all measurements. Quartz cuvettes with a thickness of one centimeter were used as sample vessels. The results were quantified using the absorbance of the signal at 540 nm.

3.3.3.2 VPO Measurements

Osmometry measurements were conducted to determine the molality of the extraction and blank control samples (see Chapters 3.3.2.1 and 3.3.2.2). A Knauer vapor pressure osmometer K-7000 (Knauer Wissenschaftliche Geräte GmbH, Berlin, Germany) was used for the measurements. The measurements were conducted using the extraction and control samples before mixing with the diluted blood at 25 °C using Millipore water as the solvent, with a measurement length of 300 seconds. Nine values were recorded for each sample. The molality of the samples was determined based on a calibration measurement of a NaCl standard solution with a molality of 400 mmol/kg.

3.3.3.3 pH Measurements

pH measurements were conducted using a VWR pHenomenal IS 2100 L (VWR International GmbH, Darmstadt, Germany) pH meter with a VWR pHenomenal 211 pH-electrode (VWR International GmbH, Darmstadt, Germany). The measurements were conducted using the extraction and blank control samples before they were mixed with diluted blood (see Chapters 3.3.2.1 and 3.3.2.2). The samples were measured at room temperature under constant stirring until a stable pH value was established.

4. Results and Discussion – NO Treatment of Oxygenator Materials

The first part of this thesis's Results and Discussion chapter focuses on the impact of treating the oxygenator's polymer materials with NO gas of various concentrations. Parts of this chapter were published in the articles "Characterization of the interaction of nitric oxide/nitrogen dioxide with the polymer surfaces in ECMO devices" [297] and "Impact of nitric oxide on the surface properties of selected polymers" [298].

4.1 Optical Changes of the Polymer Materials

As a first step, the change in coloration of the samples after the gas treatment was evaluated. The gas treatment was performed as described in chapter 3.2.1.

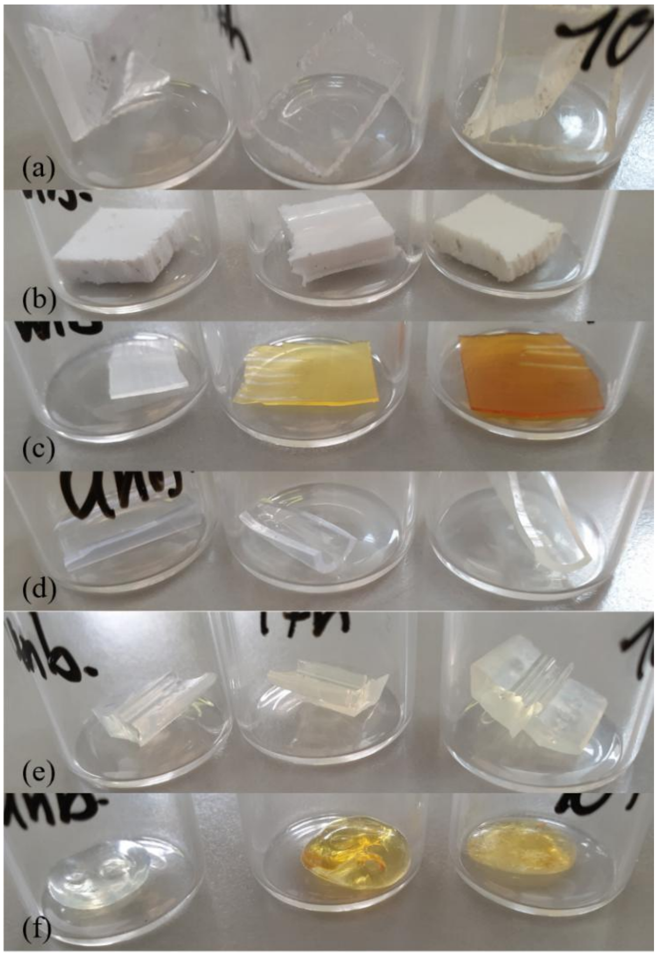

Figure 4.1: Color change of the sample materials after the treatment with NO (10.000 ppm) for 17 hours and ten days. The samples shown are (a) the inlet/outlet cap (MABS), (b) the gas cap (MABS), (c) the PU material, (d) the gas hose (PVC), (e) the silicone gasket, (f) the UV-activated adhesive. The gas treatment was performed as described in chapter 3.2.1.

All materials except PMP changed color due to the gas treatment. The most significant change was displayed by PU, turning yellow after 17 hours and yellowish-brown after ten days (see Figure 4.1 (c)). The coloration effect for MABS (both inlet/outlet cap and gas cap) was more subtle, with only a slight yellowing effect after ten days (see Figure 4.1 (a), (b)). Both PVC and silicone showed little but visible change after ten days, with a yellowing effect slightly weaker than MABS (see Figure 4.1 (d), (e)). Apart from the color change, no apparent change in mechanical properties could be observed. The exception was the UV-activated adhesive, which yellowed after 17 hours to a similar degree as PU. The coloration did not intensify after ten days of gas treatment (see Figure 4.1 (f)). However, the material softened noticeably after those ten days of gas treatment. This softening effect led to a redesign of the outlet cap of the oxygenator. The redesigned cap integrated the hose connector into the cap construction rather than being a separate part glued to the cap.

4.2 FTIR-ATR Spectra of the Oxygenator Materials

FTIR-ATR measurements were the primary analytical method employed to analyze the impact of the NO treatment on the oxygenator materials. The spectra were analyzed regarding the position of the signals caused by the gas treatment, the height of those signals compared to treatment length and treatment gas concentration, and the stability of these signals after the end of the gas treatment. The gas treatments and the FTIR-ATR measurements were performed as described in chapters 3.2.1, 3.2.2, and 3.2.3

4.2.1 Signal Attribution

The first step in analyzing the FTIR-ATR spectra was to identify and attribute the signal caused by the gas treatment.

4.2.1.1 Treatment with NO (10,000 ppm)

Initial experiments examining the interaction between the oxygenator materials and NO gas were conducted using the highest available concentration of NO, 10.000 ppm. The goal was to see whether any interaction between the polymers and the gas could be observed at all.

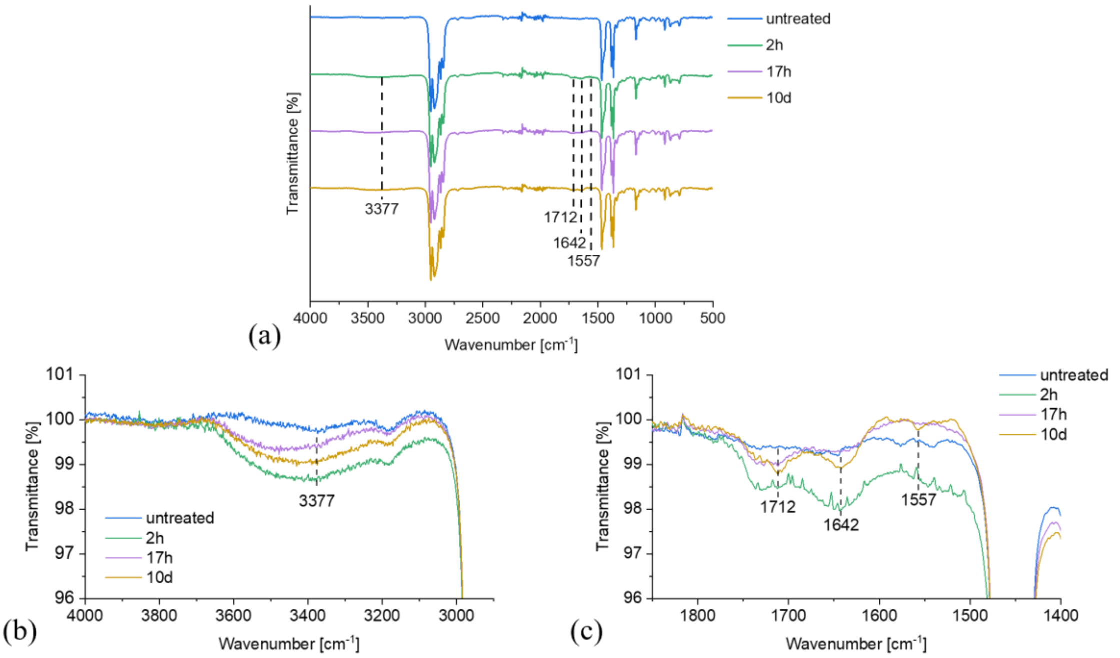

Figure 4.2: FTIR-ATR spectra of PMP untreated and treated with NO (10,000 ppm) for two and 17 hours and ten days. (a) Overview of the spectra. (b) The signal at 3377 cm^{-1} caused by gas treatment. (c) Signals at 1712, 1642, and 1557 cm^{-1} caused by gas treatment. The marked signals were chosen based on the spectrum of the sample treated for ten days. The experiments were performed according to chapters 3.2.1 and 3.2.3.

The spectra of the individual materials showed signals caused by both the materials themselves and the gas treatment. The major signals for PMP were around 3000 cm^{-1}, corresponding to C-H stretching vibrations. At wavenumbers above 1500 cm^{-1}, a variety of absorption bands were observed corresponding to bending vibrations of the polymer chain, with the most significant signals sitting at 1466, 1385, 1365, and 1169 cm^{-1} (see Figure 4.2 (a)) [213, 220]. The gas treatment caused a total of four identifiable signals. The first signal was a broad peak with its highest point at around 3377 cm^{-1} (see Figure 4.2 (b)). The other three signals were small peaks at 1712, 1642, and 1557 cm^{-1} (see Figure 4.2 (c)).

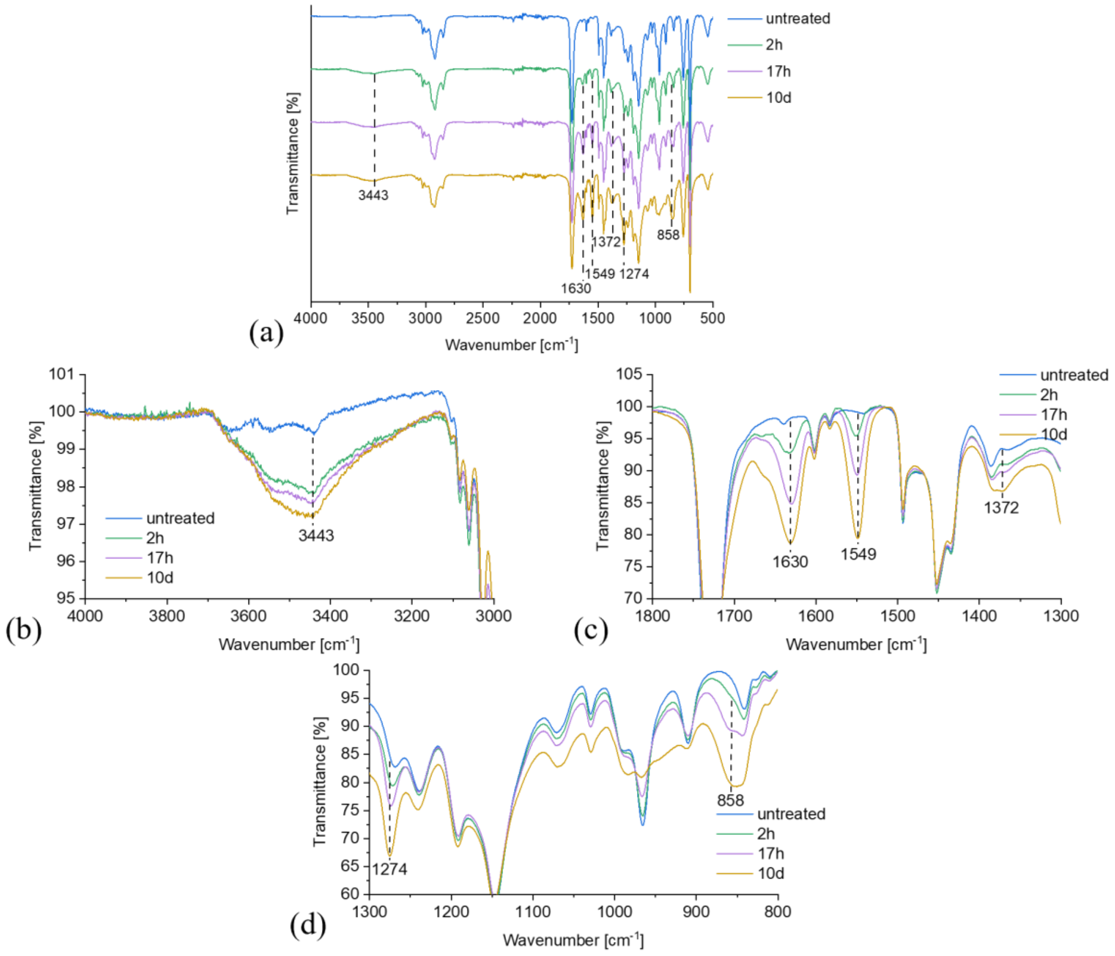

Figure 4.3: FTIR-ATR spectra of MABS (inlet/outlet cap) untreated and treated with NO (10,000 ppm) for two and 17 hours and ten days. (a) Overview of the spectra. (b) The signal at 3443 cm^{-1} caused by gas treatment. (c) Signals at 1630, 1549, and 1372 cm^{-1} caused by gas treatment. (d) Signals at 1274 and 858 cm^{-1} caused by gas treatment. The experiments were performed according to chapters 3.2.1 and 3.2.3.

For MABS, signals around 3000 cm^{-1} corresponding to C-H stretching vibration were observed. At 1727 cm^{-1}, the material showed a signal corresponding to a carbonyl group's

C-O double bond stretching vibration. The small signal at 1600 cm^{-1} was caused by the quadrant stretching mode of the benzene rings contained in the styrene monomers (see Figure 2.3). Above 1500 cm^{-1}, a series of signals caused by the polymer's C-H and C-C bending vibrations was visible. The most significant signals in this region were located at 1494, 1452, 1239, 965, 758, and 698 cm^{-1}. The signal at 1146 cm^{-1}, meanwhile, was likely caused by a C-O stretching vibration of the ester group of the methyl methacrylate monomers (see Figure 4.3 (a)) [213, 220]. The gas treatment resulted in more clearly visible signals than with PMP. A broad signal appeared at 3443 cm^{-1} (see Figure 4.3 (b)). Further signals became visible at 1630, 1549, and 1372 cm^{-1} (see Figure 4.3 (c)), as well as 1274 and 858 cm^{-1} (see Figure 4.3 (d)). The height of these additional signals showed a clear dependence on gas exposure time.

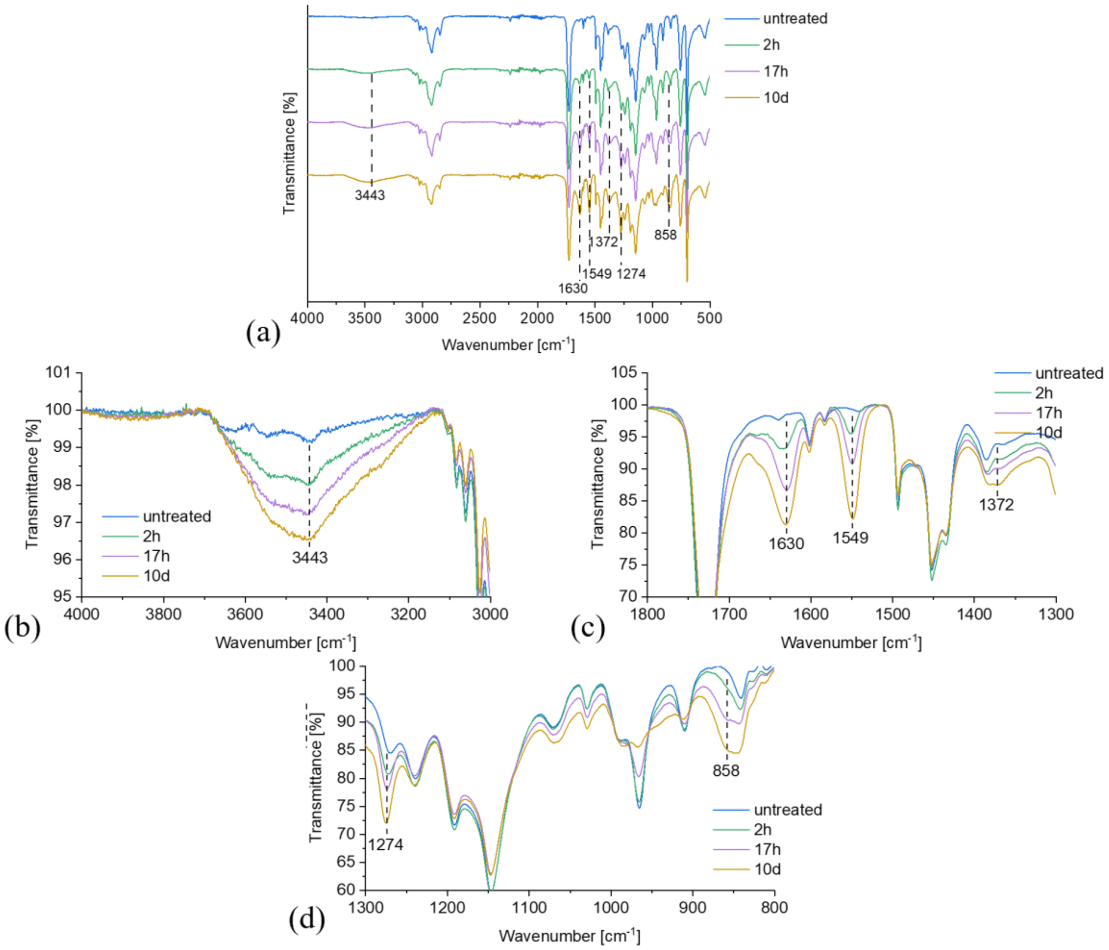

Figure 4.4: FTIR-ATR spectra of MABS (gas cap) untreated and treated with NO (10.000 ppm) for two and 17 hours and ten days. (a) Overview of the spectra. (b) The signal at 3443 cm^{-1} caused by gas treatment. (c) Signals at 1630, 1549, and 1372 cm^{-1} caused by gas treatment. (d) Signals at 1274 and 858 cm^{-1} caused by gas treatment. The experiments were performed according to chapters 3.2.1 and 3.2.3.

Apart from minor shifts in the fingerprint region, likely due to a coloring agent in the polymer, the FTIR-ATR spectra of the MABS plastic of the gas caps were largely identical to the inlet/outlet caps (see Figure 4.4 (a)). The signals caused by the gas treatment were similarly identical in both position and peak height (see Figure 4.4 (b) - (d)).

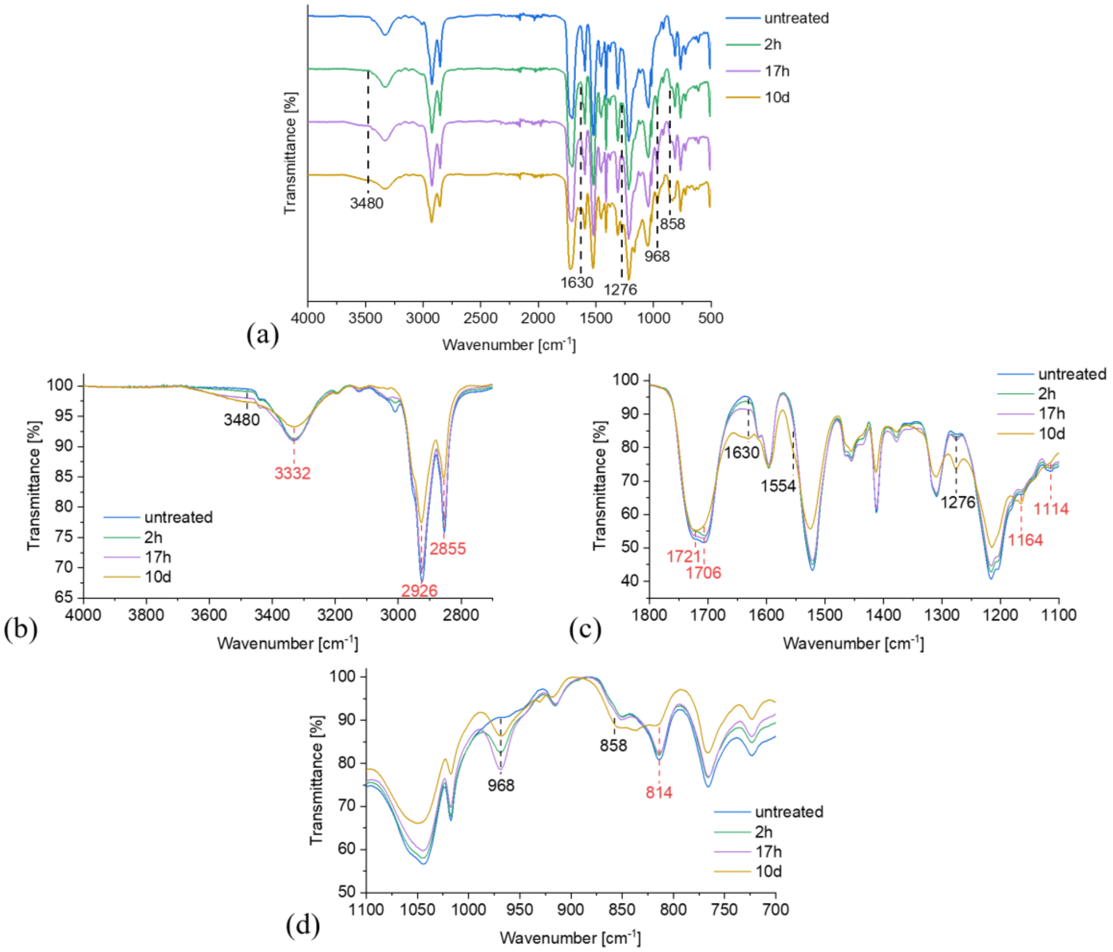

Figure 4.5: FTIR-ATR spectra of PU untreated and treated with NO (10,000 ppm) for two and 17 hours and ten days. (a) Overview of the spectra. (b) The signal at 3480 cm^{-1} caused by gas treatment. (c) Signals at 1630, 1554, and 1276 cm^{-1} caused by gas treatment. (d) Signals at 968 and 858 cm^{-1} caused by gas treatment. Marked in red are the signals impacted by potential cross-linking and chain scission reactions at 3332, 2926, 2855, 1721, 1706, 1164, 1114, and 814 cm^{-1}. The experiments were performed according to chapters 3.2.1 and 3.2.3.

The PU material resulted in a signal at 3332 cm^{-1} corresponding to an N-H stretching vibration caused by the N-H bonds of the polyurethane chain's carbamate groups. A group of signals corresponding to C-H stretching vibrations could be observed at 2926 and 2855 cm^{-1}. At 1706 cm^{-1}, a signal corresponding to the C-O double bond stretching vibration of the carbonyl group contained in the carbamate group was visible. A further signal appeared at 1597 cm^{-1}, caused by the quadrant stretching mode of benzene rings contained in the MDI monomers. At 1523 cm^{-1}, a signal corresponding to the C-N-H bending vibration of the carbamate group was visible. Above 1500 cm^{-1}, a series of signals corresponding to the polymer chain's C-H and C-C bending vibrations appeared, with significant signals at 1309, 1045, 767, and 511 cm^{-1}. The signals at 1413 and 1217 cm^{-1} were likely caused by O-H bending vibrations of the glycol or TMP monomers and C-N stretching vibrations of the carbamate group, respectively (see Figure 4.5 (a)) [213, 220]. The gas treatment resulted in the following changes: A broad signal at around 3480 cm^{-1} appeared as a shoulder of the N-H signal (see Figure 4.5 (b)), in addition to signals at 1630, 1554, 1276, and 1164 cm^{-1} (see Figure 4.5 (c)) as well as signal at 968 and 858 cm^{-1} (see Figure 4.5 (d)). The gas treatment also decreased the heights of several PU signals, with the most relevant located at 3332, 2926, 2855, 1114, and 814 cm^{-1} (see Figure 4.5 (b), (c), and (d)). The carbonyl signal changed shape with the peak maximum shifting from 1706 to 1721 cm^{-1} (see Figure 4.5 (c)).

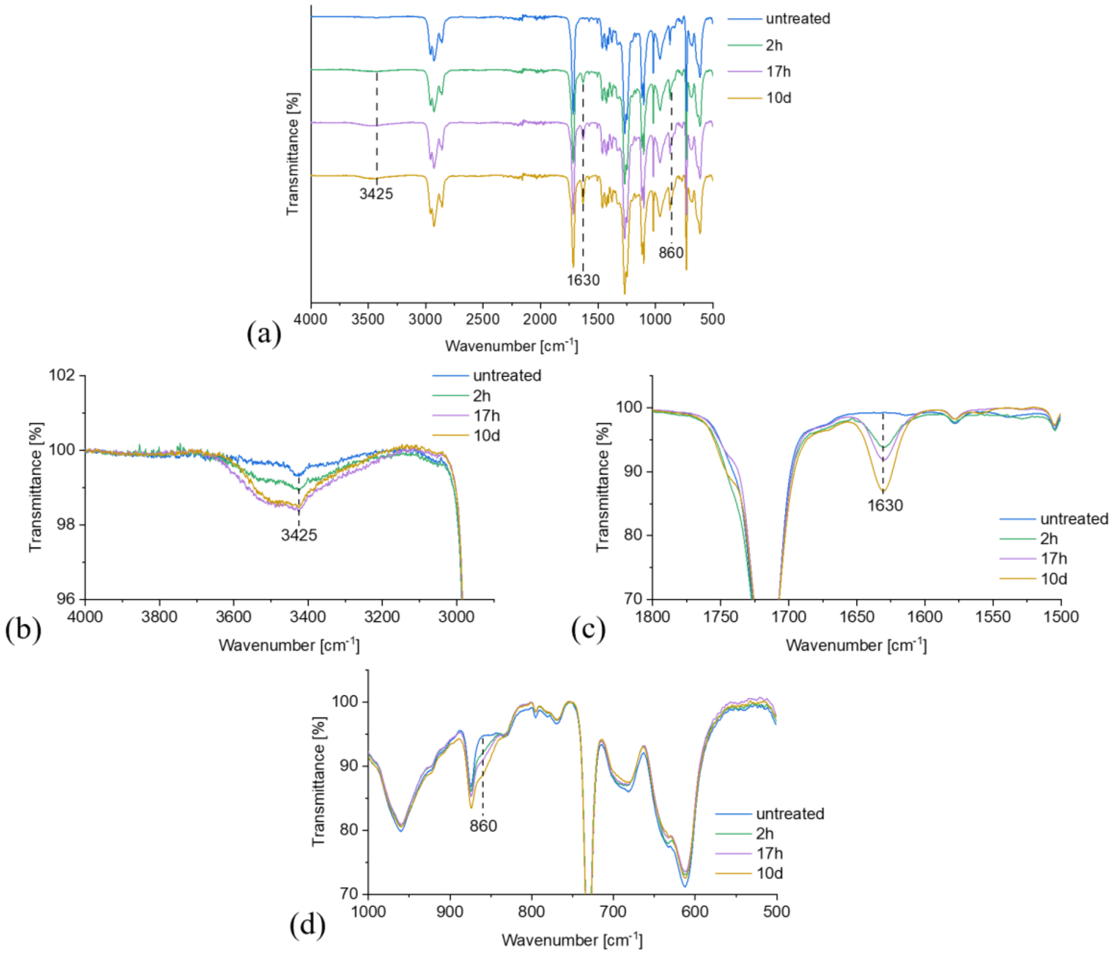

Figure 4.6: FTIR-ATR spectra of PVC (gas hose), untreated and treated with NO (10,000 ppm) for two and 17 hours and ten days. (a) Overview of the spectra. (b) The signal at 3425 cm^{-1} caused by gas treatment. (c) Signal at 1630 cm^{-1} caused by gas treatment. (d) Signal at 860 cm^{-1} caused by gas treatment. The experiments were performed according to chapters 3.2.1 and 3.2.3.

The PVC spectra showed signals corresponding to C-H stretching vibrations at around 3000 cm^{-1} caused by both the polymer itself and the plasticizer DOTP. The signals at 1716 and 1267 cm^{-1} were caused by the plasticizer DOTP, corresponding to the C-O stretching vibrations of its ester groups. Between 1500 and 1350 cm^{-1}, a group of signals corresponding to semicircle stretching vibrations of the aromatic ring of DOTP appeared. The most significant signals above 1350 cm^{-1} not already discussed were located at 1102, 1019, and 611 cm^{-1}, caused by C-C and C-H bending vibrations of both the polymer and the plasticizer. The signal at 730 cm^{-1} was caused by the C-Cl stretching vibrations of the polymer (see Figure 4.6 (a)) [213, 220]. The gas treatment resulted in three visible signals at 3425 cm^{-1} (see Figure 4.6 (b)), 1630 cm^{-1} (see Figure 4.6 (c)), and 860 cm^{-1} (see Figure 4.6 (d)).

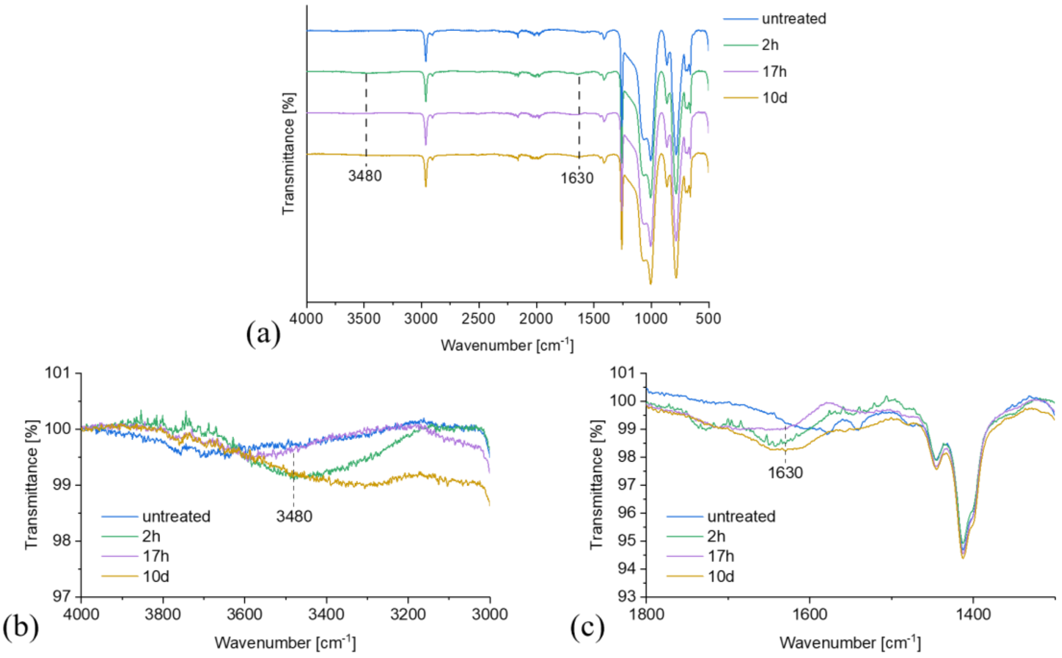

Figure 4.7: FTIR-ATR spectra of the silicone gasket, untreated and treated with NO (10.000 ppm) for two and 17 hours and ten days. (a) Overview of the spectra. (b) The signal at 3480 cm^{-1} caused by the gas treatment. (c) The signal at 1630 cm^{-1} caused by the gas treatment. The experiments were performed according to chapters 3.2.1 and 3.2.3.

The silicone gasket displayed several signals at around 3000 cm^{-1}, corresponding to the C-H stretching vibrations of the carbon side chains of the polymer. The signals between 1500 and 1300 cm^{-1} were caused by C-H bending vibrations. The signal at 1257 cm^{-1} was caused by Si-C stretching vibrations, while the signals at 1065 and 1007 cm^{-1} were due to Si-O-Si stretching vibrations of the siloxane groups in the polymer chain. The final signal of note was the peak at 785 cm^{-1}, which was caused by Si-O-Si bending vibrations (see Figure 4.7 (a)) [213, 220, 299–301]. The silicone material of the gasket showed little influence of the gas treatment, unlike materials such as MABS or PVC. Only two additional signals could be identified. One broad peak at 3480 cm^{-1} (see Figure 4.7 (b)) and one at 1630 cm^{-1} (see Figure 4.7 (c)). The height of both signals was inconsistent, with no clear relationship between gas treatment length and signal height. The signal intensities were also low compared to those seen for some of the other materials (see Figure 4.3), roughly in line with the signal strengths seen for PMP (see Figure 4.2).

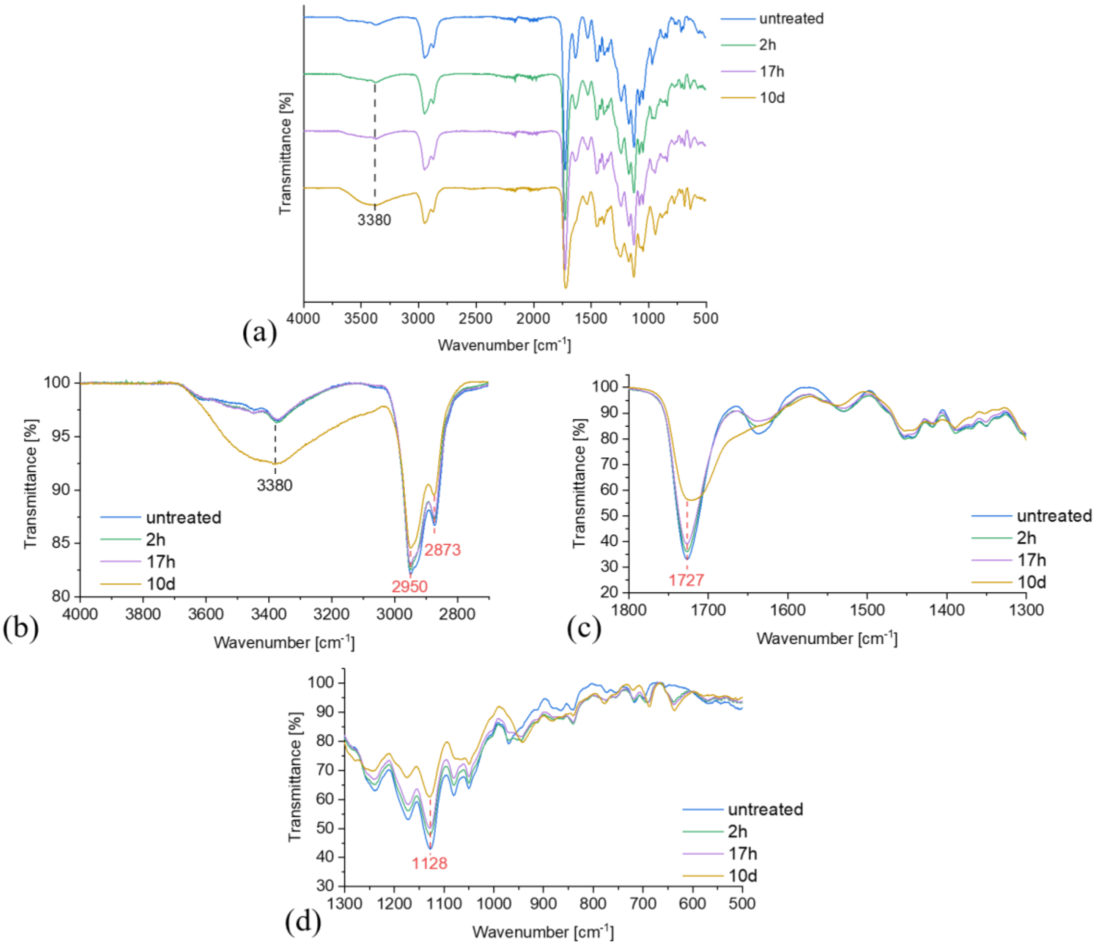

Figure 4.8: FTIR-ATR spectra of the UV-activated adhesive, untreated and treated with NO (10.000 ppm) for two and 17 hours and ten days. (a) Overview of the spectra. (b) The signal at 3380 cm^{-1} caused by the gas treatment. (c) Detailed view of the spectra from 1800 to 1300 cm^{-1}. (d) Detailed view of the spectra from 1300 to 500 cm^{-1}. Marked in red are the signals impacted by potential cross-linking and chain scission reactions at 2950, 2873, 1727, and 1128 cm^{-1}. The experiments were performed according to chapters 3.2.1 and 3.2.3.

The spectra of the UV-activated adhesive showed signals at 3380 and around 3000 cm^{-1} corresponding to O-H and C-H stretching vibrations, respectively. The O-H stretching vibrations were likely caused by the hydroxy group of the 2-hydroxyethyl methacrylate. The signals at 1727 and 1636 cm^{-1} appeared due to C-O stretching vibrations of the carbonyl groups in all the UV-activated adhesive components. The signal at 1727 cm^{-1} was likely caused by both 2-hydroxyethyl methacrylate and isobornyl acrylate, which featured the carbonyl group as part of a β-unsaturated ester group. The signal at 1636 cm^{-1} likely stemmed from 1-vinylhexahydro-2H-azepin-2-one, where the carbonyl group neighbored a tertiary amine group. The following signal at 1530 cm^{-1} likely corresponded to the C-N-H bending vibration from the carbamate groups of the urethane compounds present in the product. C-H and C-C bending vibrations appeared above 1500 cm^{-1}, with the most significant signals being 1239, 1127, and 1049 cm^{-1}. The signal at 1172 cm^{-1} was caused by C-O stretching vibrations of the ester groups of 2-hydroxyethyl methacrylate and isobornyl acrylate. The signal at 1080 cm^{-1}, on the other hand, was caused by the C-O stretching vibrations of the hydroxy group of 2-hydroxyethyl methacrylate (see Figure 4.8 (a)) [213, 220]. The gas treatment with NO resulted in the generation of only one visible signal at 3380 cm^{-1}. Apart from this single signal, which only visibly changed after the maximum exposure time of ten days, a decrease in signal height could be observed at 2950, 2873, 1727, and 1128 cm^{-1} (see Figure 4.8 (b), (c), and (d)).

In addition to these regular spectra, difference spectra were recorded. The difference spectra used measurements of the untreated material samples as the background measurements compared to the empty sample space of the regular spectra. This led to much lower signal intensities of the peaks caused by the polymers themselves, allowing for better identification and separation of signals caused by the NO treatment. This was especially useful for signals appearing in the fingerprint region of the spectra, where they overlapped with the multitude of material peaks, and PU, where almost all gas treatment-related signals heavily overlapped with existing material peaks. These spectra were only used to better separate the signals caused by the gas treatment from the material signals. They were not used to analyze signal heights due to inconsistencies arising from using untreated materials in the background measurements. No new signals caused by the gas treatment were identified in these difference spectra.

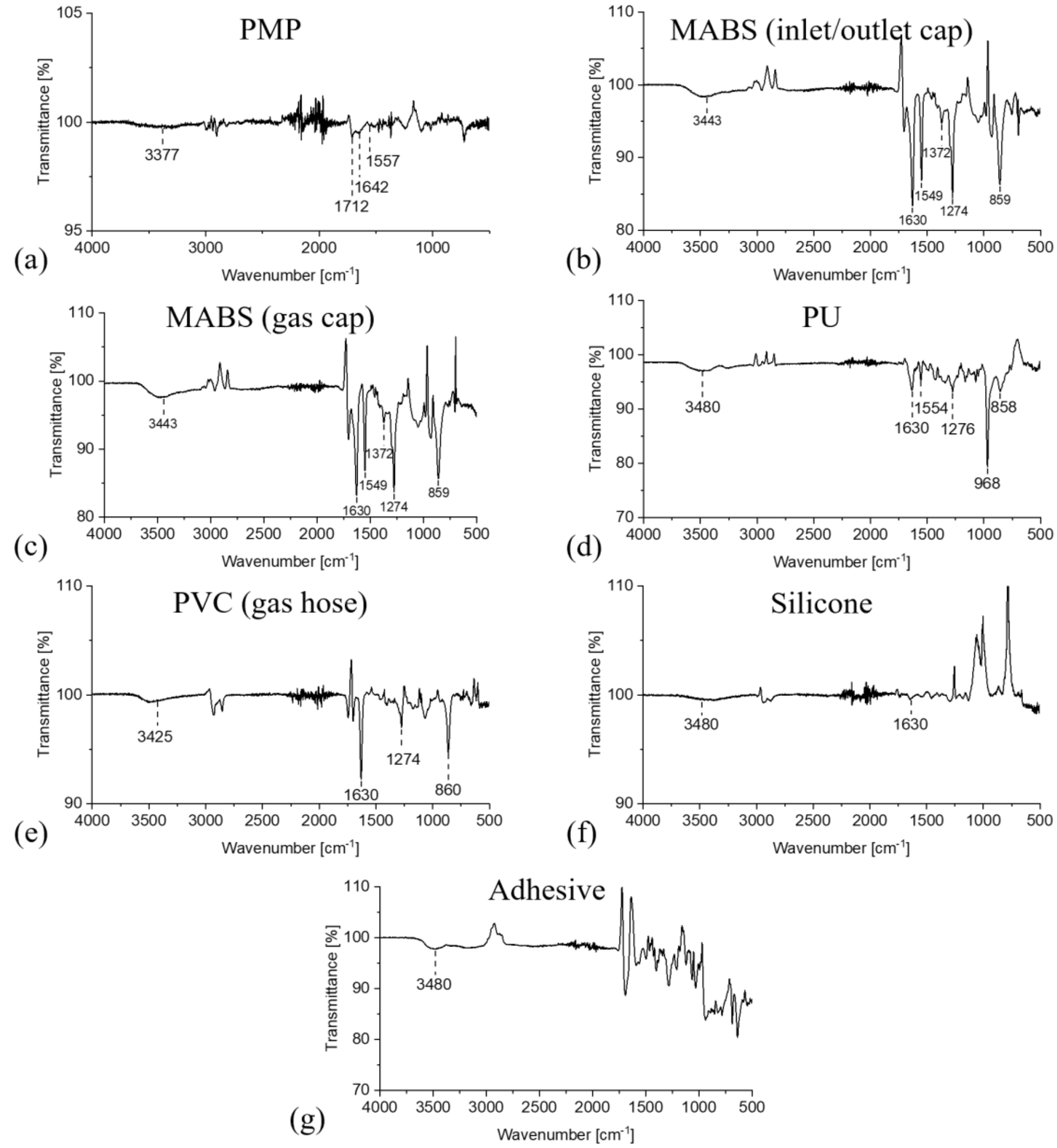

Figure 4.9: FTIR-ATR difference spectra of (a) PMP, (b) MABS of the inlet/outlet cap, (c) MABS of the gas cap, (d) PU, (e) PVC, (f) the silicone gasket, and (g) the UV-activated adhesive, treated with NO (10,000 ppm) for 17 hours, using the respective untreated material as the background. The experiments were performed according to chapters 3.2.1 and 3.2.3.

Analyzing the difference spectra resulted in, for the most part, identical findings to the regular spectra. A broad signal between 3500 and 3300 cm^{-1} was present for all materials. The signal at 1712 cm^{-1} was only visible for PMP, while the signal at 1642/1630 cm^{-1} was visible in all spectra except for the UV-activated adhesive. The signal at 1557-1549 cm^{-1} was the only signal where changes compared to the regular spectra were observed. The signal was present in the PMP spectra and both MABS samples. It also appeared in the spectrum of PU, in contrast to the regular spectra, where it likely overlapped with signals from the material itself. The signal at 1372 cm^{-1} only appeared for MABS samples, while the 1276/1274 cm^{-1} signal was visible for MABS, PU, and PVC. The signal at 968 cm^{-1} only appeared for PU, and the 860-858 cm^{-1} signal appeared for MABS, PU, and PVC.

Looking at the results of the gas treatment in both regular and difference spectra led to the identification of a total of eight different signals caused by the gas treatment. These signals could be attributed to a small selection of different functional groups being formed on the material surfaces. The signals at 1642/1630, 1276/1274, and 860/858 cm^{-1} were attributed to the formation of nitrate ester groups. The signal at 1642/1630 cm^{-1} was caused by the in-phase stretching vibration of the functional group, while the signal at 1276/1274 cm^{-1} was caused by its out-of-phase stretching vibration. The signal at 860/858 cm^{-1} was caused by the N-O stretching vibration of the group. The signals at 1549-1557 cm^{-1} and 1372 cm^{-1} resulted from the formation of nitro groups on the polymer surfaces. The signal at 1549-1557 cm^{-1} was caused by the out-of-phase stretching vibration of the group, while the in-phase stretching vibration caused the signal at 1372 cm^{-1} [213, 220]. The signals at 3500-3300, 1712, and 968 cm^{-1} were caused by the adsorption of HNO_3 on the polymer surface. The signal at 3500-3300 cm^{-1} was caused by the O-H stretching vibration of the molecules, while the signal at 1712 cm^{-1} was caused by the NO_2 out-of-phase stretching vibration, and the NO_2 in-plane bending vibration caused the signal at 968 cm^{-1} [213, 220, 302].

This attribution of the signals meant that HNO_3 was deposited on all polymer materials. PMP, MABS, and PU showed signals indicating that nitro and nitrate ester groups were formed on the surface of these materials. Both PVC and the silicone gasket showed only signals corresponding to nitrate ester groups but not nitro groups, while the UV-activated adhesive showed no signals corresponding to the formation of these functional groups. Of these materials, both PMP and the silicone gasket showed signals that were comparatively small in height compared to materials like MABS or PVC.

Fundamental to the reactions the gas treatment caused on the polymer surfaces was the reaction of NO with oxygen forming NO_2 (see Chapter 2.3.2) and the subsequent formation of HNO_3 through the reaction of NO_2 with water [303, 304]:

$$2\ NO + O_2 \longrightarrow 2\ NO_2 \tag{57}$$

$$4\ NO_2 + 2\ H_2O + O_2 \longrightarrow 4\ HNO_3 \tag{58}$$

In the context of the gas treatments conducted with NO (10,000 ppm), these reactions occurred as the treatment chamber was flooded with treatment gas for the first time. As the air was displaced from the chamber, the NO gas reacted rapidly with the oxygen of the air to form NO_2 [305, 306]. NO_2 then reacted with the moisture in the air to form HNO_3. Both reactions ultimately left NO_2 and HNO_3 as the reactive agents.

The nitro groups on the surfaces of the polymers were formed through various mechanisms, with the addition reaction to C-C double bonds being the most common. These addition reactions led to the formation of nitro and nitrite ester groups in a 3:1 ratio [152]. Possible attack points for this type of reaction would have been the double bonds of the butadiene monomers of MABS or the C-C double bonds in all three major components of the UV-activated adhesive. Another possible pathway for the formation of nitro groups is the electrophilic aromatic nitration reaction caused by HNO_3. In a first step, NO_2^+-ions were formed through the reaction of the HNO_3 molecules with an acid:

$$HNO_3 + H^+ \rightleftharpoons NO_2^+ + H_2O \tag{59}$$

The NO_2^+-ion then reacted with an aromatic ring to form a nitro group. This reaction took place in a continuum between two different mechanisms. The first of these mechanisms was the polar mechanism:

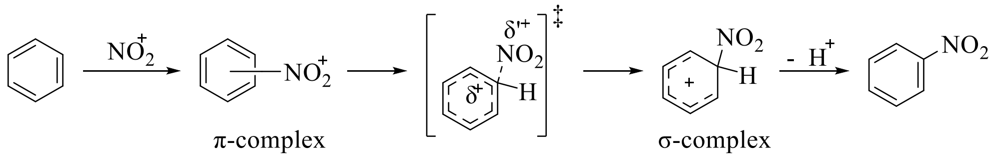

(60)

The second mechanism was the single-electron transfer (SET) mechanism:

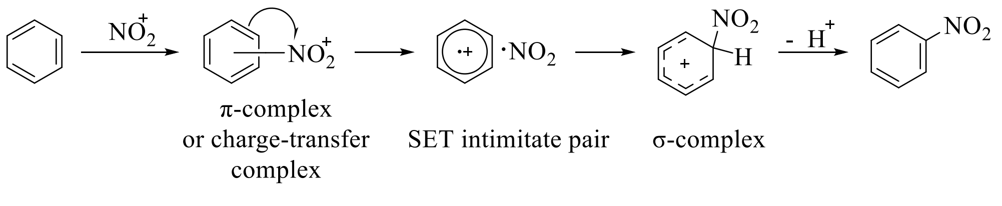

(61)

In the case of both the polar and the SET mechanism, the NO^{2+}-ion formed an π-complex with the aromatic ring. In the case of the polar mechanism, the reaction proceeded through a transition state, while a SET intimate pair was formed in the case of the SET mechanism. Both mechanisms then moved to a σ-complex followed by a proton abstraction to form the final product [307, 308]. The potential attack points for this reaction would have been the aromatic systems of the MDI monomers of PU, the aromatic ring of the plasticizer DOTP contained in PVC or the styrene monomer of MABS.

The formation of nitrate ester groups also had multiple possible pathways. The most straightforward mechanism was a secondary reaction following the addition reaction of NO_2 (see Chapter 2.3.4, Equations 6-9). Here, the unstable nitrite ester groups formed through the addition reaction of NO_2 with C-C double bonds reacted further with NO_2 to form nitrate ester groups. This reaction would also explain the absence of any IR signals related to the formation of nitrite ester groups [153, 161]. A second possible mechanism would have been a reaction of HNO_3 with hydroxy groups [309, 310]:

$$HNO_3 + HNO_3 \rightleftharpoons H_2NO_3^+ + NO_3^- \qquad \text{(fast)} \qquad (62)$$

$$H_2NO_3^+ \rightleftharpoons NO_2^+ + H_2O \qquad \text{(slow)} \qquad (63)$$

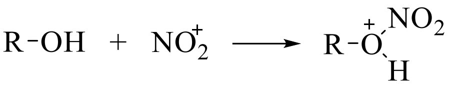

$$R{-}OH + NO_2^+ \longrightarrow R{-}\overset{+}{O}\genfrac{}{}{0pt}{}{NO_2}{H} \qquad \text{(slow)} \qquad (64)$$

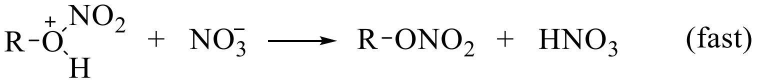

$$R{-}\overset{+}{O}\genfrac{}{}{0pt}{}{NO_2}{H} + NO_3^- \longrightarrow R{-}ONO_2 + HNO_3 \qquad \text{(fast)} \qquad (65)$$

Possible attack points for this reaction would have been unreacted hydroxy groups in the TMP monomers of PU, where the third hydroxy group was not involved in cross-linking or the 2-hydroxyethyl methacrylate of the UV-activated adhesive. Further attack points were possible when considering a potential variant of this mechanism. This variant involved an acid-catalyzed hydrolysis of an ester group as a first step [311]:

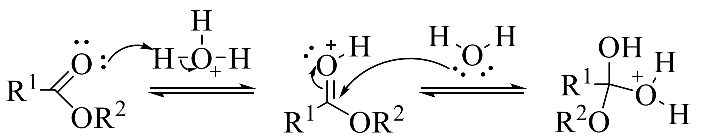

(66)

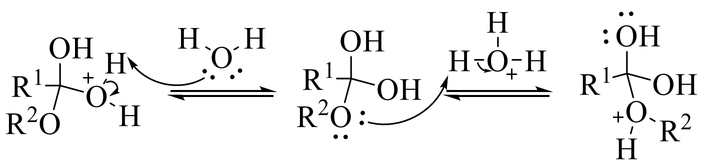

(67)

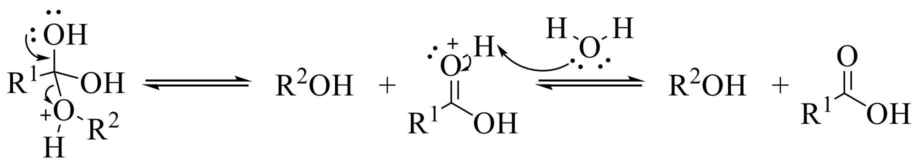

(68)

This reaction was followed by the hydroxy groups' nitration reaction (see Equations 62-67). Possible points of attack for this reaction would have been the ester groups in the methyl methacrylate monomer of MABS, in 2-hydroxyethyl methacrylate and isobornyl acrylate contained in the UV-activated adhesive, and in the plasticizer DOTP contained in PVC.

Connecting these mechanisms with the results obtained from the FTIR-ATR measurements resulted in the following interpretations: PMP and the silicone gasket lacked any structural features necessary for the reaction mechanisms described in the prior paragraphs. PMP only consists of C-C single bonds with no additional functional groups. The silicone used for the gasket likely only consists of a Si-O-Si main chain with aliphatic side chains based on the IR signals of the material itself. The small signals observed, despite the absence of necessary structural features, stemmed most likely from reactions between the treatment gas and residual monomers contained in both materials. MABS, on the other hand, contained a variety of structural features capable of interacting with both NO_2 and HNO_3. These structural features included the double bonds in the butadiene monomers, the styrene monomers' phenyl group, and the methyl methacrylate's ester group. PU also contained structural features that made the interaction with both reactive agents possible. Here, the MDI monomers' aromatic rings and the unreacted hydroxy groups of the TMP monomers were the likeliest attack points. The results for PVC were of note, as the polymer itself did not contain any functional groups or structural features that would have made reactions with either NO_2 or HNO_3 possible. Instead, the reactions forming nitrate ester groups only occurred with the plasticizer DOTP, which made up 32.7 wt% of the sample, likely through the acid-catalyzed hydrolysis of their ester groups, followed by nitration reactions with the resulting hydroxy groups, leading to the formation of nitrate ester groups. The carboxylic acid groups formed because of the ester hydrolysis likely also contributed part of the signal at 3425 cm^{-1} (see Figure 4.6 (b)). Despite the presence of an aromatic ring in the plasticizer, no nitro groups were detected. The likely reason for this behavior was high steric hindrance preventing the aromatic nitration reactions. The UV-activated adhesive produced the most surprising results, which showed no reaction with either NO_2 or HNO_3 despite the individual components all containing necessary structural features in the form of C-C double bonds and ester groups. The absence of nitro group formation was likely explained by the double bonds' absence due to the components' complete polymerization in the hardened samples.

The reason why no reactions with the ester groups of these compounds took place remained unclear.

For PU and the UV-activated adhesive, this attribution of the signals caused by the gas treatment still left some effects of NO on the FTIR-ATR spectra unexplained (see Figures 4.5 and 4.8). For PU, the gas treatment decreased the signal heights of various signals, especially in the region above 1500 cm^{-1}, and led to the formation of a signal at 1164 cm^{-1}. The most relevant signals for this discussion were located at 3332, 2926, 2855, 1706, 1164, 1114, and 814 cm^{-1} (see Figure 4.5 (b), (c), and (d)). The likely explanation for these changes was both cross-linking and chain scission reactions. The cross-linking reaction of PU proceeded as described in equations 15, 16, and 17 (see Chapter 2.3.4). The chain scission reaction followed from equation 16 and proceeded according to the following mechanism [159, 312]:

$$\sim\mathrm{O}-\overset{\mathrm{O}}{\overset{\|}{\mathrm{C}}}-\dot{\mathrm{N}}\sim \longrightarrow \sim\mathrm{O}-\overset{\mathrm{O}}{\overset{\|}{\mathrm{C}}}\cdot + \mathrm{H}\dot{\mathrm{N}}\sim \longrightarrow \sim\cdot + \mathrm{CO_2} \qquad (69)$$

Chain scission reactions were related to the drop in signal heights at 2926, 2855, 1114, and 814 cm^{-1}, in addition to signal height decreases for most of the signals above 2500 cm^{-1} [313–315]. Cross-linking reactions, meanwhile, were connected to the signal height decrease at 3332 cm^{-1}, the reduction in the height of the carbonyl signals at 1706 cm^{-1}, and the appearance of the signal at 1164 cm^{-1} (see Figure 4.5 (b), (c), and (d)) [316–318]. None of the other polymer materials showed signs of either reaction (see Figures 4.2-4.4 and 4.6-4.8). Chain scission reactions, in particular, were a potential concern for the mechanical stability of the PU materials if the reactions occurred in the bulk of the polymer. These concerns were somewhat mitigated by existing research, where chain scission and cross-linking reactions were only minor side reactions compared to the addition reaction of NO_2 with C-C double bonds [157, 160]. The potential impact of chain scission reactions was further explored based on the XPS and SEM measurements presented in chapters 4.3 and 4.4. These reactions also had the potential to cause the formation of nitro groups through a side reaction between the product of equation 16 and NO_2 [312]. However, the side reaction character of the chain scission and cross-linking reactions made it unlikely that this nitration reaction substantially contributed to the nitro group formation.

Cross-linking and chain scission reactions likely also played a role in the UV-activated adhesive, with the signals at 2950, 2873, 1727, and 1128 cm^{-1} decreasing in height due to the gas treatment [309–314]. The impact of these reactions seemed to have been more substantial here than with PU, as the material became observably softer after the gas treatment, which led to its removal from the oxygenator design (see Chapter 4.1).

4.2.1.2 Treatment with NO (1000 ppm and 80 ppm)

The initial experiments with 10,000 ppm of NO proved that NO interacted with the oxygenator's polymer materials (see Chapter 4.2.1.1). Further gas treatment experiments were conducted, lowering the NO concentration to 1000 and 80 ppm, closer to the planned final application concentration of below 100 ppm, to see whether these interactions would remain visible. The UV-activated adhesive was not further analyzed from this point forward, as it had been removed from the oxygenator design (see Chapter 4.1). The blood hoses (PVC) of the oxygenator were added to the selection of polymer materials as it emerged that the gas and blood hoses used different plasticizers (see Chapter 2.4.4). This difference in material composition could have led to differences in the interaction with NO. Therefore, PVC (blood hose) was analyzed separately from the PVC (gas hose) from this point forward. Samples treated with NO (1000 ppm) were used for a wider variety of experiments than the other concentrations (see Chapters 4.3-4.5) due to the good compromise between achievable signal heights and gas consumption.

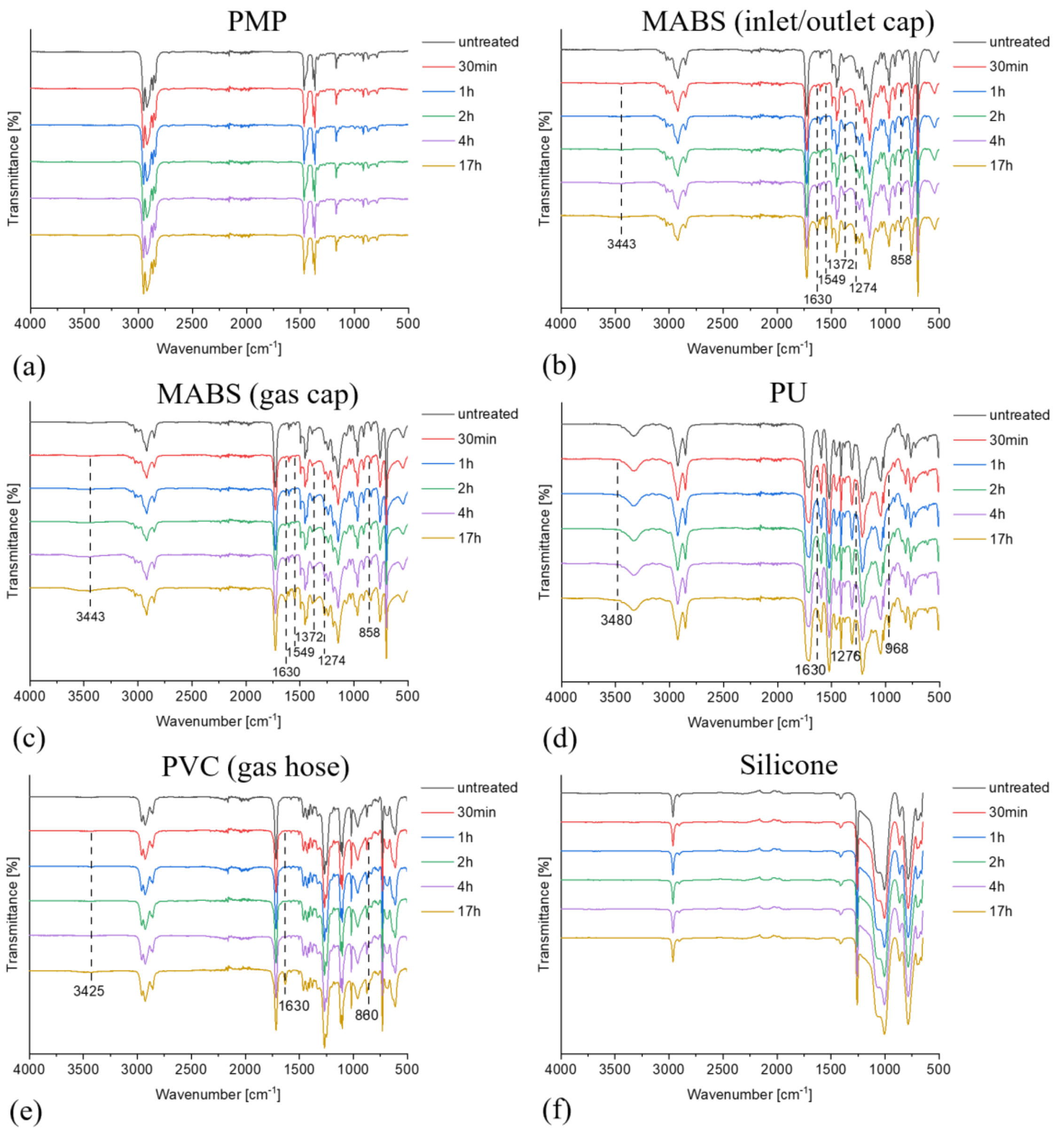

Figure 4.10: Overview of the spectra of (a) PMP, (b) MABS (inlet/outlet cap), (c) MABS (gas cap), (d) PU, (e) PVC (gas hose), and (f) silicone treated with NO (1000 ppm) for 30 minutes, one, two, four, and 17 hours. The experiments were performed according to chapters 3.2.1 and 3.2.3.

Treatment of the polymer materials with NO (1000 ppm) resulted in very similar behavior to the treatment with 10,000 ppm. The MABS, PU, and PVC samples showed the same signals with visually lower signal intensities compared to the treatment with NO (10,000 ppm) (see Figure 4.10 (b-e)). The signal at 1554 cm^{-1} was no longer visible due to the decreased signal strength and overlap with the PU signal at 1523 cm^{-1}. PU showed no indications for chain scission or cross-linking reactions within the first 17 hours of treatment time, with the signals discussed in this context in chapter 4.2.1.1 showing no changes (see Figure 8.1). Prolonging the treatment duration up to 15 days revealed slight changes in the signals at 1706, 1721, and 814 cm^{-1}, consistent with crosslinking and chain scission reactions (see Figure 8.2). However, the effect was much weaker than with 10,000 ppm of NO (see Figure 4.5). PMP and silicone showed no or only negligible signals after the gas treatment (see Figure 4.10 (a), (f)). Both materials already showed only small signals after the treatment with NO (10,000 ppm) (see Figures 4.2 and 4.7), with both materials lacking any of the structural features necessary to react with either NO_2 or HNO_3 (see Chapter 4.2.1.1). This led to an absence of any additional signals at lower NO concentrations. Analysis of PMP was carried out throughout the remaining experiments, as the material was central to the functionality of the oxygenator. On the other hand, the silicone gasket was only an easily replaceable accessory to the oxygenator and, therefore, not considered in the remaining experiments.

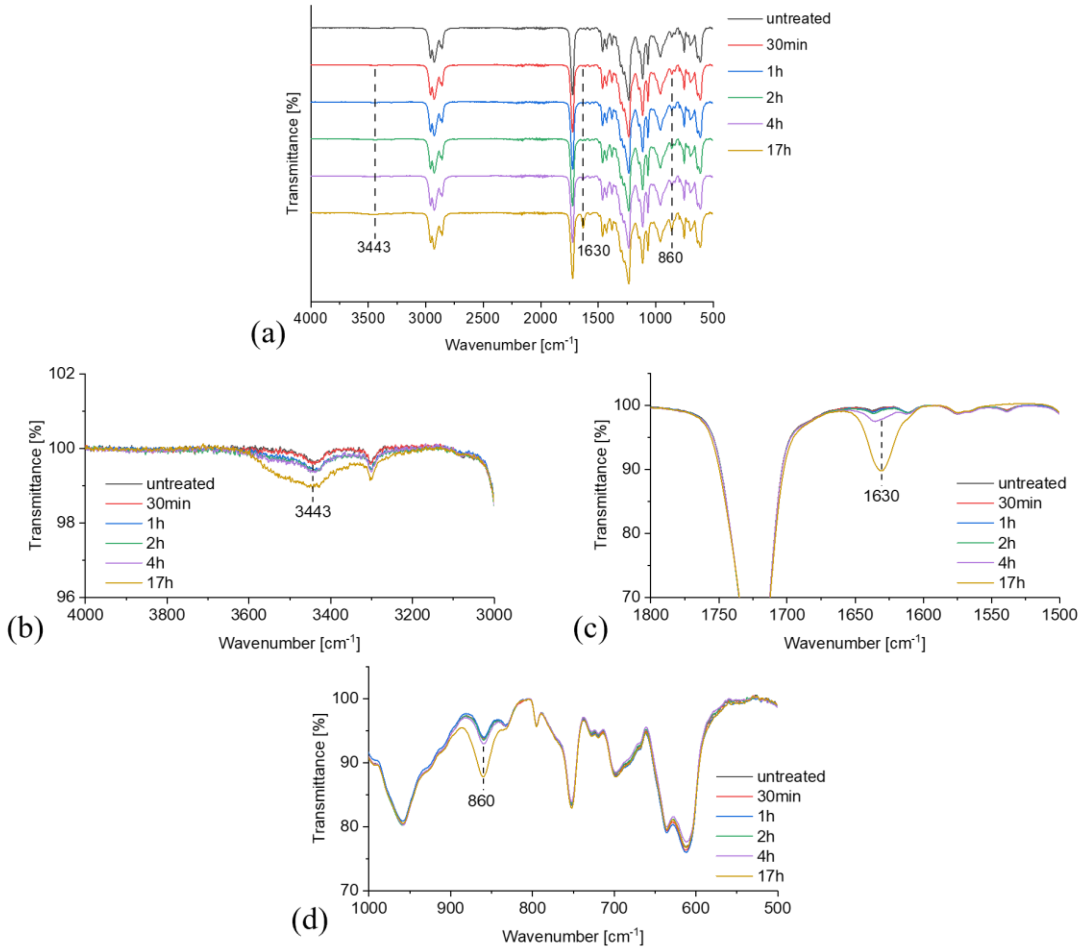

Figure 4.11: FTIR-ATR spectra of PVC (blood hose), untreated and treated with NO (1000 ppm) for 30 minutes, one, two, four, and 17 hours. (a) Overview of the spectra. (b) The signal at 3425 cm^{-1} caused by gas treatment. (c) Signal at 1630 cm^{-1} caused by gas treatment. (d) Signal at 860 cm^{-1} caused by gas treatment. The experiments were performed according to chapters 3.2.1 and 3.2.3.

The PVC (blood hose) spectra were largely similar to those of PVC (gas hose). At around 3000 cm^{-1}, a group of signals was visible, corresponding to C-H stretching vibrations caused by both the polymer itself and the plasticizer TEHTM. At 1722 and 1234 cm^{-1}, two signals from the ester groups of TEHTM appeared. Between 1500 and 1350 cm^{-1}, a group of signals corresponding to semicircle stretching vibrations of the aromatic ring of TEHTM was visible. The most significant signals in terms of height above 1350 cm^{-1} were located at 1114, 1067, 959, 752, and 612 cm^{-1}. The signal at 752 cm^{-1} corresponded to the C-Cl stretching vibration of PVC, while the remaining signals were caused by C-C and C-H bending vibrations of both the polymer and the plasticizer (see Figure 4.11 (a)). The gas treatment caused the formation of a total of three signals at 3443, 1630, and 860 cm^{-1} (see Figure 4.11 (b), (c), and (d)). They corresponded to the adsorption of HNO_3 in the case of the signal at 3443 cm^{-1} and the formation of nitrate ester groups in the case of the signals at 1630 and 860 cm^{-1} [213, 220]. Identically to the PVC (gas hose) samples, the nitrate ester groups were formed through the reaction of the plasticizers (in this case TEHTM) ester groups with HNO_3 in an ester-catalyzed ester hydrolysis followed by a reaction between the resulting hydroxy groups and HNO_3. In the case of PVC (blood hose), TEHTM’s exact concentration was unknown. However, given the similarities in mechanical properties and measurement results, it was likely similar to the 32.7 wt% of DOTP contained in the PVC (gas hose) samples. Like with DOTP, aromatic nitration reactions leading to the formation of nitro groups were likely suppressed due to steric hindrance.

The NO concentration was further reduced following the experiments at 1000 ppm to 80 ppm, approximating the final application concentration planned below 100 ppm.

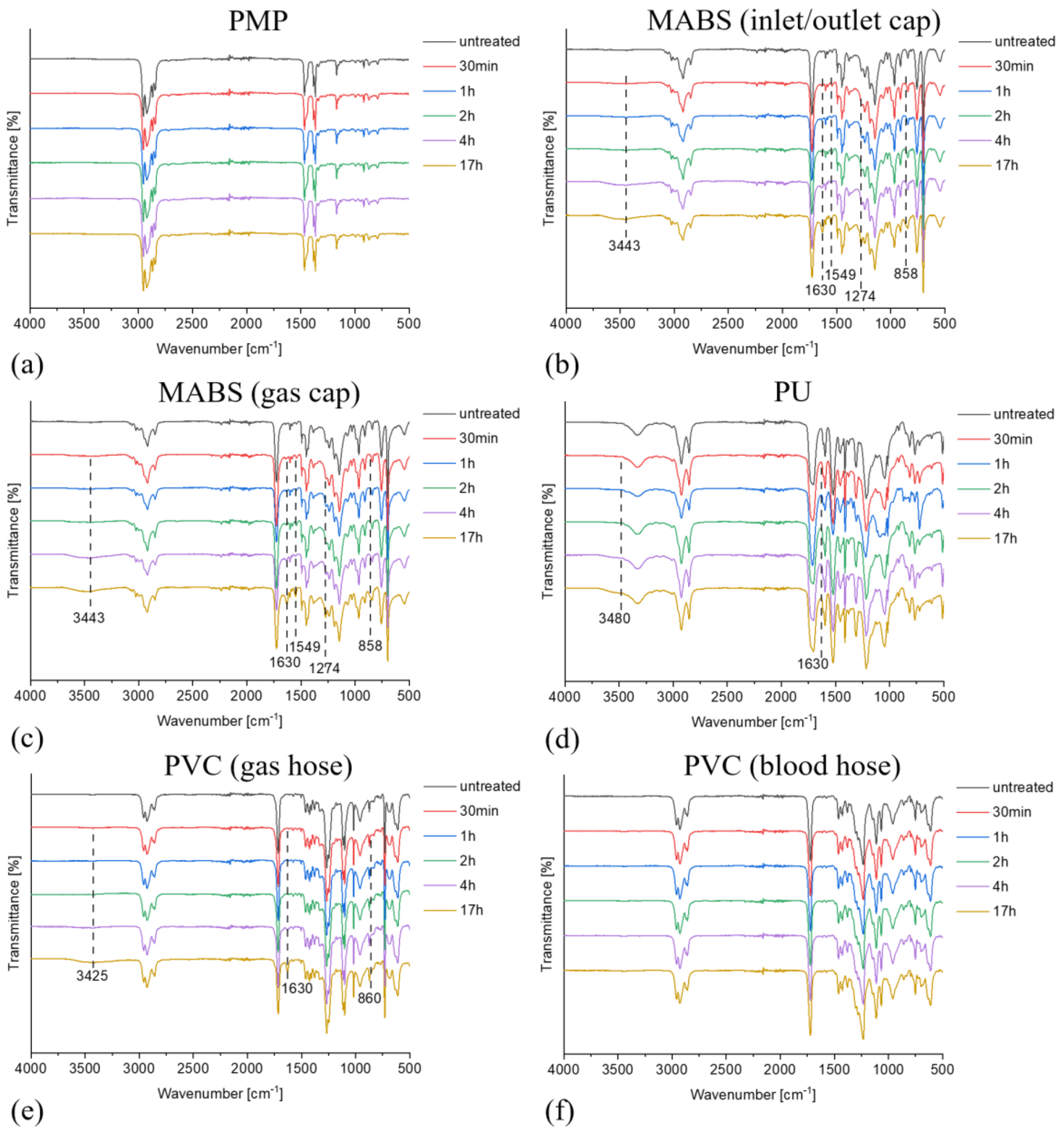

Figure 4.12: Overview of the spectra of (a) PMP, (b) MABS (inlet/outlet cap), (c) MABS (gas cap), (d) PU, (e) PVC (gas hose), and (f) PVC (blood hose) treated with NO (80 ppm) for 30 minutes, one, two, four, and 17 hours. The experiments were performed according to chapters 3.2.1 and 3.2.3.

Gas treatment at 80 ppm resulted in visually weaker signal heights than treatment procedures at higher concentrations up to durations of 17 hours. Both PMP and PVC (blood hose) showed no visible signals even after 17 hours of treatment (see Figure 4.12 (a), (f)). For MABS samples, PU, and PVC (gas hose), additional signals only became visible after 17 hours, with only the signal at 3443/3480/3425 cm^{-1} increasing at shorter treatment periods (see Figure 4.12 (b)-(e)). The signals at 1554 and 968 cm^{-1} did not appear for PU. The material showed no signs of chain scission or cross-linking reactions either at this concentration, even with treatment durations of up to ten days (see Figures 8.3 and 8.4). Overall, these results meant that the effects of the gas treatment remained relevant even at concentrations close to the final application concentration.

4.2.1.3 Treatment with NO_2 (1000, 500, and 50 ppm)

The experiments presented so far were conducted using various concentrations of NO (see Chapters 4.2.1.1 and 4.2.1.2). The interpretations of the results of these experiments stated that the interactions between the treatment gas mixture and the polymers were due to reactions with NO_2 and HNO_3, but not NO itself. Experiments using NO_2 instead of NO at concentrations of 1000, 500, 100, and 50 ppm were conducted to confirm this interpretation.

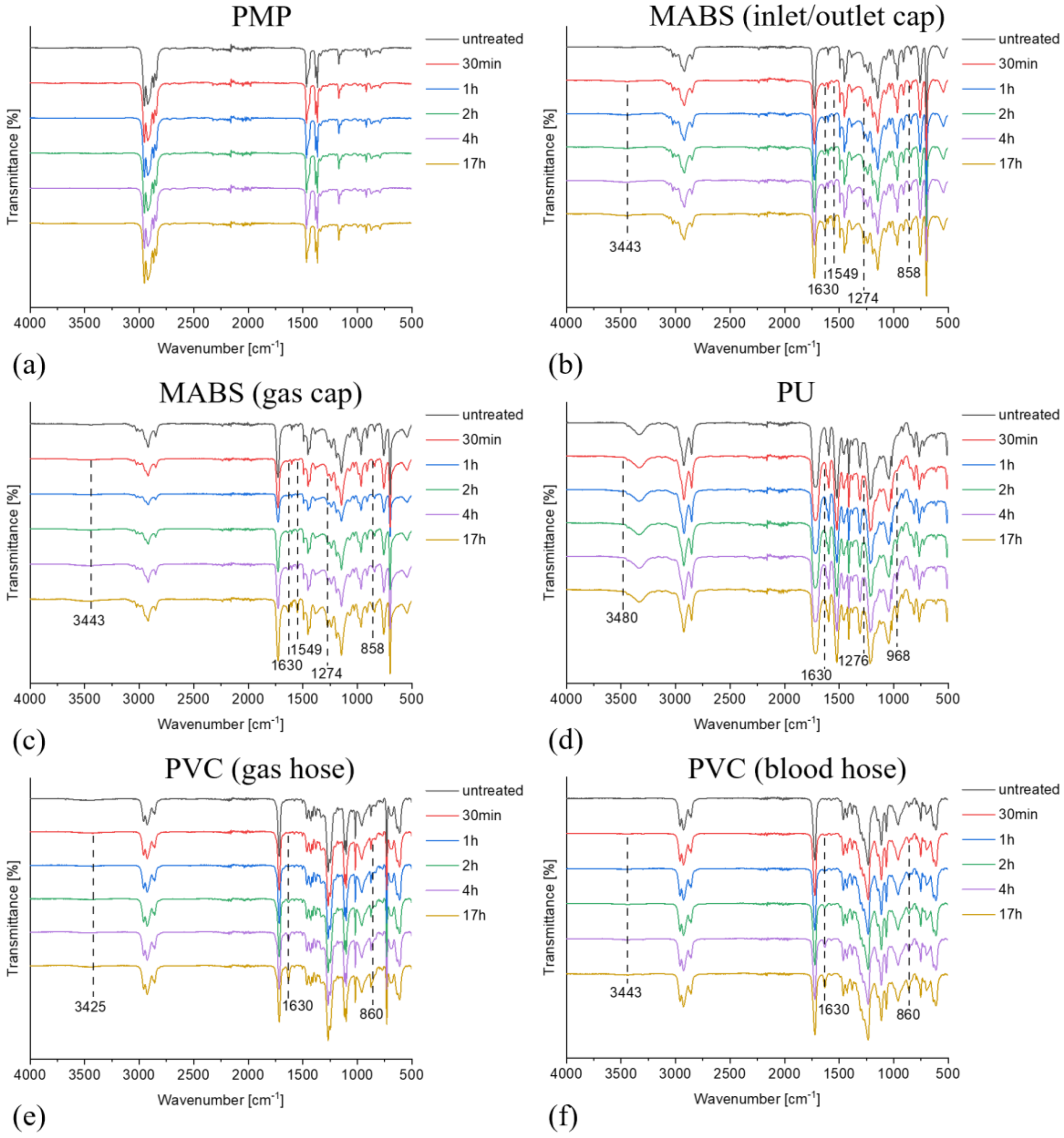

Figure 4.13: Overview of the spectra of (a) PMP, (b) MABS (inlet/outlet cap), (c) MABS (gas cap), (d) PU, (e) PVC (gas hose), and (f) PVC (blood hose) treated with NO_2 (1000 ppm) for 30 minutes, one, two, four, and 17 hours. The experiments were performed according to chapters 3.2.1 and 3.2.3.

The FTIR-ATR spectra resulting from the treatment with NO_2 (1000 ppm) showed essentially identical results to the treatment with the same concentration of NO. PMP showed no additional signal due to its lack of suitable structural features (see Figure 4.13 (a)). The rest of the materials meanwhile showed the same signal at 3425/3443/3480, 1630, 1549, 1274/1276, 968, and 858/860 cm^{-1} as with NO (see Figure 4.13 (b)-(f)). The signal at 1554 cm^{-1} was again not visible for PU at any NO_2 concentration again due to the heavy overlap with the PU signal at 1523 cm^{-1}. The material showed no signs of chain scission or cross-linking reactions either (see Figure 8.7). Going down in concentration resulted in the signals corresponding to the gas treatment appearing only after longer treatment times, similar to the results for NO (80 ppm) (see Figures 8.5, 8.6, and 4.12). The spectra obtained from these experiments confirmed the interpretations made in chapter 4.2.1.1. Not NO itself but NO_2 and HNO_3 resulting from reactions with oxygen and water (see Equations 57 and 58) were responsible for the reactions between the polymers and the treatment gas mixture.

4.2.2 Signal Height Analysis

So far, the signals caused by the treatment with NO have only been analyzed based on the position of the signals. To gain a better understanding of how the reactions discussed in chapter 4.1.1.1 progress, the signal heights of the peaks caused by the gas treatment were analyzed. This analysis was generally limited to signals above 1500 cm^{-1}, as the lack of separation from material signals in this region made peak height analysis impossible. PU was not analyzed for peak heights either, as the gas treatment signals overlapped too heavily with the signals of the material itself. For PMP, the signals chosen were located at 3377, 1712, 1642, and 1557 cm^{-1}. For both MABS samples, it was the signals at 3443, 1630, and 1549 cm^{-1}; for PVC, the signals at 3425 and 1630 cm^{-1}; for silicone, the signals at 3480 and 1630 cm^{-1}; and for the UV-activated adhesive, it was the signal at 3480 cm^{-1}. The spectra were normalized using the signal at 1466 cm^{-1} in the case of PMP, the signal at 1720 cm^{-1} in the case of MABS, the signal at 2927 cm^{-1} in the case of PVC, the signal at 1257 cm^{-1} in the case of silicone, and the signal at 1727 cm^{-1} in the case of the UV-activated adhesive.

4.2.2.1 Treatment with NO (10,000 ppm)

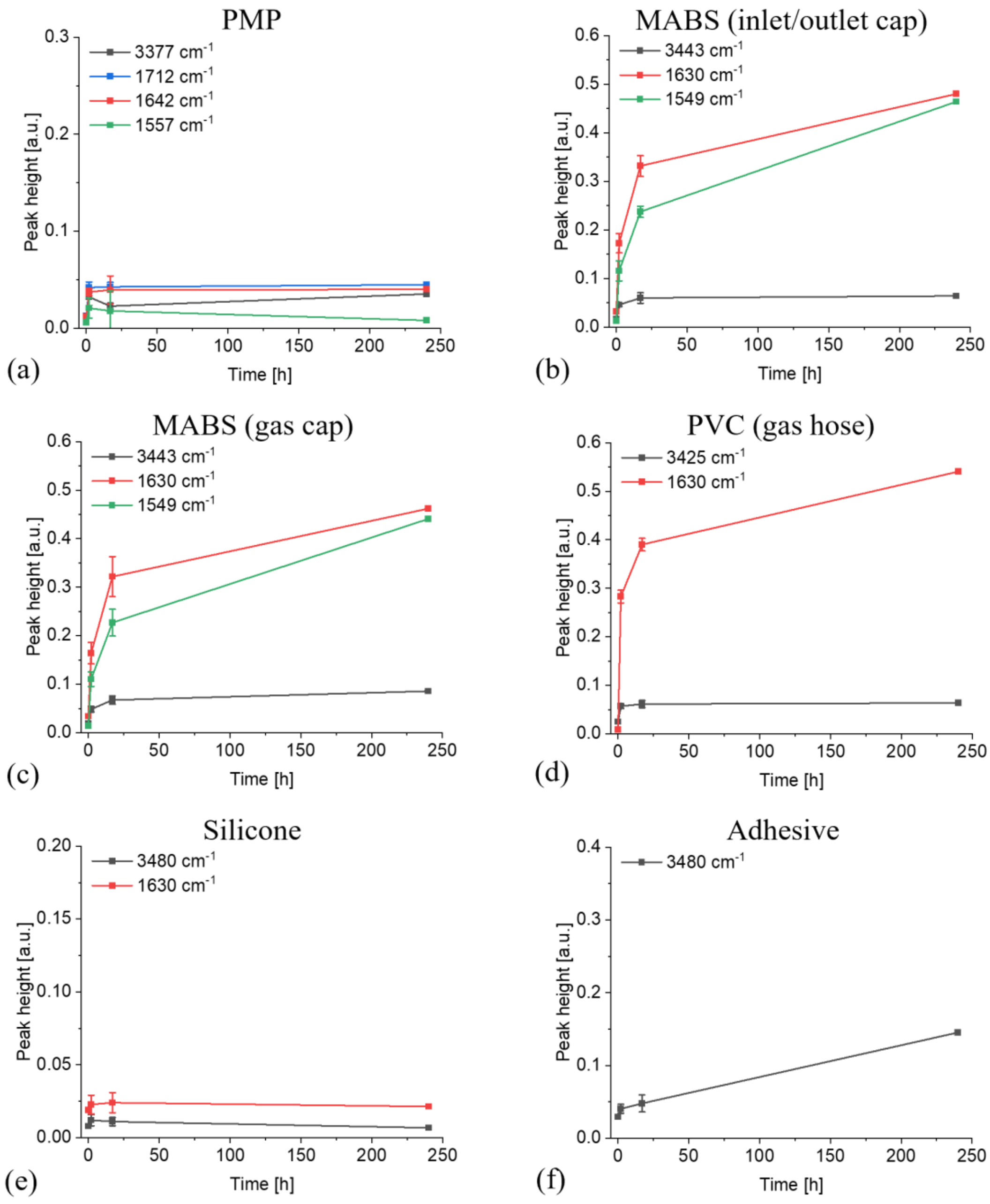

Figure 4.14: Signal heights of the signals caused by the treatment with NO (10,000 ppm) for (a) PMP, (b) MABS (inlet/outlet cap), (c) MABS (gas cap) (MABS), (d) PVC, (e) the silicone gasket, and (f) the UV-activated adhesive. The experiments were performed according to chapters 3.2.1 and 3.2.3.

PMP showed overall low signal intensities, with none of the signals increasing significantly over the treatment period after the initial rise in signal height after two hours of gas treatment (see Figure 4.14 (a)). These results fitted well with the previously made interpretations (see Chapter 4.2.1.1) that a lack of functional groups or C-C double bonds led to a low surface concentration of nitro- and nitrate ester groups, which could only form through reactions with residual monomers. Similar observations were made for silicone, where an equal lack of necessary structural features led to equally minuscule signal heights (see Figure 4.14 (e)).

With MABS, on the other hand, the signal heights caused were significant, being among the highest of any of the tested materials with a visible tendency towards saturation (see Figure 4.14 (b), (c)). After a quick initial rise of the signals at 1630 and 1549 cm^{-1} to values of 0.33 and 0.24, respectively, during the first 17 hours of gas treatment, the curves flattened significantly, leading to final values of 0.47 and 0.46 after ten days of treatment. The signal at 3443 cm^{-1} showed a similar development, with signal height rising to 0.06 within 17 hours and staying there after ten days of gas treatment. The samples taken from the inlet/outlet cap and the gas cap were largely identical regarding overall height and height development over time. These results aligned with the conclusions drawn in chapter 4.2.1.1, as MABS possessed a variety of functional groups and C-C double bonds, which made the formation of nitro and nitrate ester groups in large concentrations possible.

The results for PVC were very similar to those of MABS (see Figure 4.14 (d)), except for the absence of any signal at 1549 cm^{-1}. The signal heights at 3425 cm^{-1} and 1630 cm^{-1} were larger than with MABS, reaching values of 0.39 and 0.52 after 17 hours and ten days of gas treatment, respectively. A clear tendency towards saturation was visible for both signals for treatment periods beyond 17 hours. As discussed in chapter 4.2.1.1, the signal at 1630 cm^{-1} was likely caused by the treatment gas reacting with the plasticizer DOTP.

The UV-activated adhesive showed only one signal at 3480 cm^{-1} with a roughly linear increase in signal height over the entire gas treatment period (see Figure 4.14 (f)). The signal reached values of 0.04, 0.05, and 0.15 after two hours, 17 hours, and ten days, respectively. The signal showed no signs of saturation observed for both MABS and PVC (see Figure 4.14 (b)-(d)).

4.2.2.2 Treatment with NO (1000 ppm and 80 ppm)

The signal heights resulting from the gas treatment procedures at 1000 and 80 ppm of NO were analyzed analogous to the samples treated with 10,000 ppm (see Chapter 4.2.2.1). In addition to measurements covering the usual period of 17 hours, longer-term exposures of up to 15 days were also conducted to see whether these samples would display saturation phenomena similar to those treated with 10,000 ppm (see Figure 4.14). PMP was not analyzed at these concentrations due to the absence of any visible signals at either concentration.

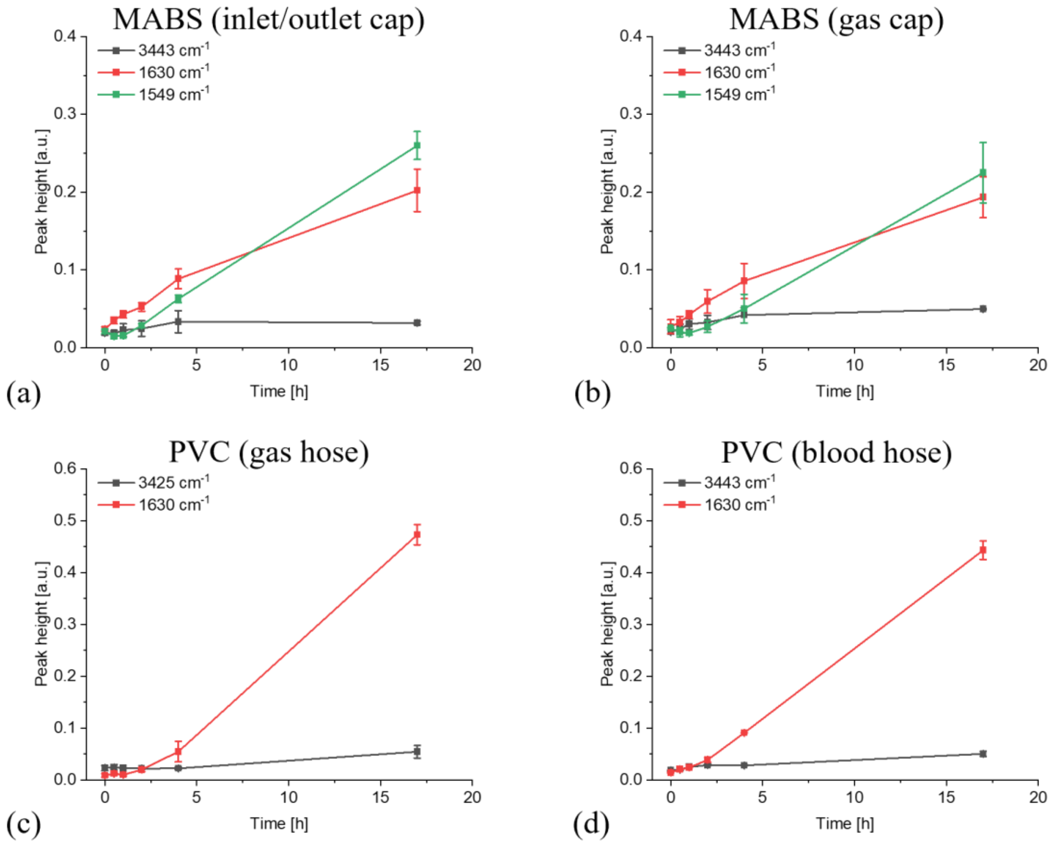

Figure 4.15: Signal heights of the signals caused by the treatment with NO (1000 ppm) for (a) MABS (inlet/outlet cap), (b) MABS (gas cap), (c) PVC (gas hose), and (d) PVC (blood hose). The experiments were performed according to chapters 3.2.1 and 3.2.3.

The initial increase in signal height during the treatment with NO (1000 ppm) was shallower compared to the treatment with NO (10,000 ppm). Two hours of treatment resulted in signal heights at 1630 cm^{-1} of 0.05, 0.06, 0.02, and 0.04 for the MABS and PVC samples, respectively (see Figure 4.15), compared to values of around 0.17 and 0.16 for MABS and 0.28 for PVC treated with 10,000 ppm (see Figure 4.14 (b)-(d)). The results were essentially the same for the signal at 1549 cm^{-1} with the treatment with NO

(1000 ppm), resulting in signal heights of 0.03 and 0.026 for MABS (inlet/outlet cap) and MABS (gas cap) after 2 hours. Treatment with NO (10,000 ppm) resulted in signal heights of 0.11 with both samples (see Figure 4.14 (b), (c)). The signal at 3443/3425 cm^{-1} also showed a slower initial increase with 1000 ppm than with 10,000 ppm (see Figures 4.15 (b-d) and 4.14 (b)-(d)). The signal heights of all samples increased largely linearly up to 17 hours for 1000 ppm, reaching values slightly below the treatment with NO (10,000 ppm) in the case of the MABS samples (see Figures 4.15 (a), (b) and 4.14 (b), (c)). For PVC, the signal height after 17 hours was similar, with values of 0.47 and 0.44 for NO (1000 ppm) (see Figure 4.15 (c), (d)) and 0.40 for NO (10,000 ppm) (see Figure 4.14 (d)). No tendency towards saturation could be observed for the samples treated with NO (1000 ppm) during the first 17 hours of treatment.

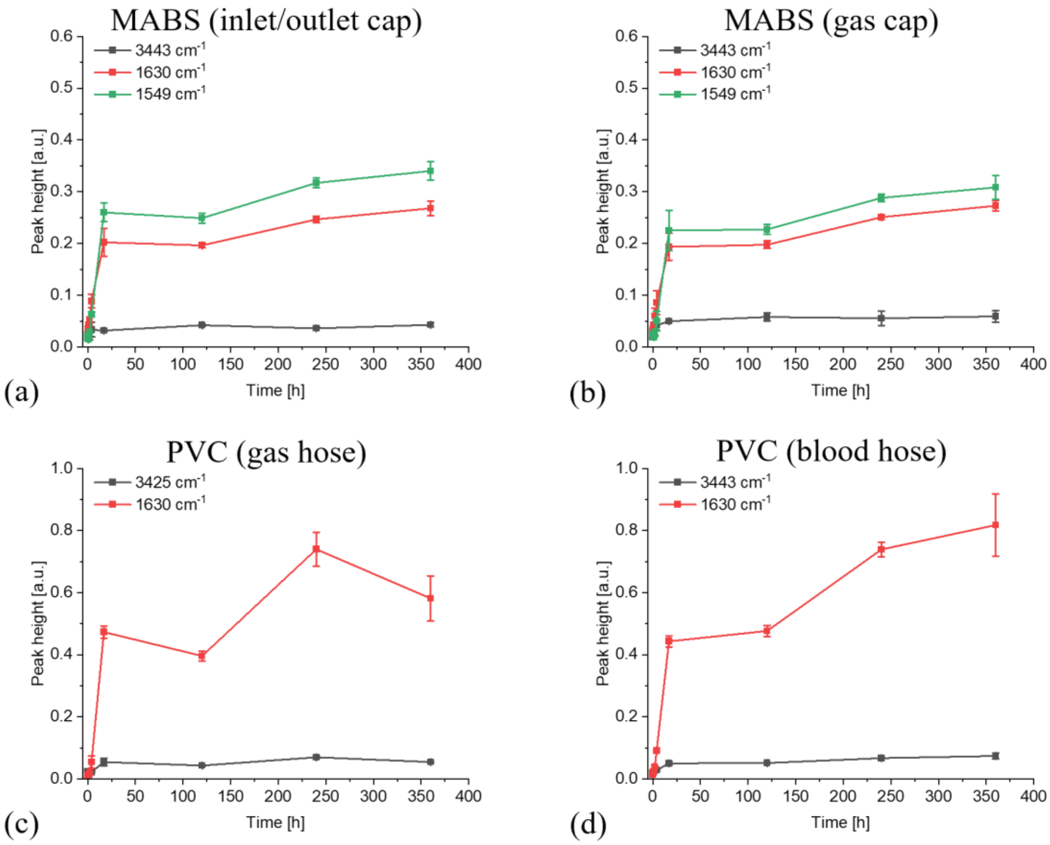

Figure 4.16: Signal heights of the signals caused by the treatment with NO (1000 ppm) for (a) MABS (inlet/outlet cap), (b) MABS (gas cap), (c) PVC (gas hose), and (d) PVC (blood hose) with extended treatment times of up to 15 days. The experiments were performed according to chapters 3.2.1 and 3.2.3.

Expanding the treatment time to 15 days showed a clear tendency toward saturation for all four samples. In all cases, the signal at 3443/3425 cm^{-1} showed little to no increase after 17 hours (see Figure 4.16). For MABS (inlet/outlet cap), the signal at 1630 cm^{-1}

increased from 0.20 to 0.27 (see Figure 4.16 (a)). MABS (gas cap) showed an increase from 0.17 to 0.27 (see Figure 4.16 (b)), PVC (gas hose) from 0.47 to 0.58 (see Figure 4.16 (c)), and PVC (blood hose) from 0.44 to 0.87 (see Figure 4.16 (d)). The signal at 1549 cm^{-1} increased from 0.26 to 0.34 for MABS (gas cap) and from 0.22 to 0.31 (see Figure 4.16 (a), (b)). The MABS samples' signal heights remained below the results for NO (10,000 ppm), while the signal heights for PVC were comparable or even slightly higher (see Figure 4.14).

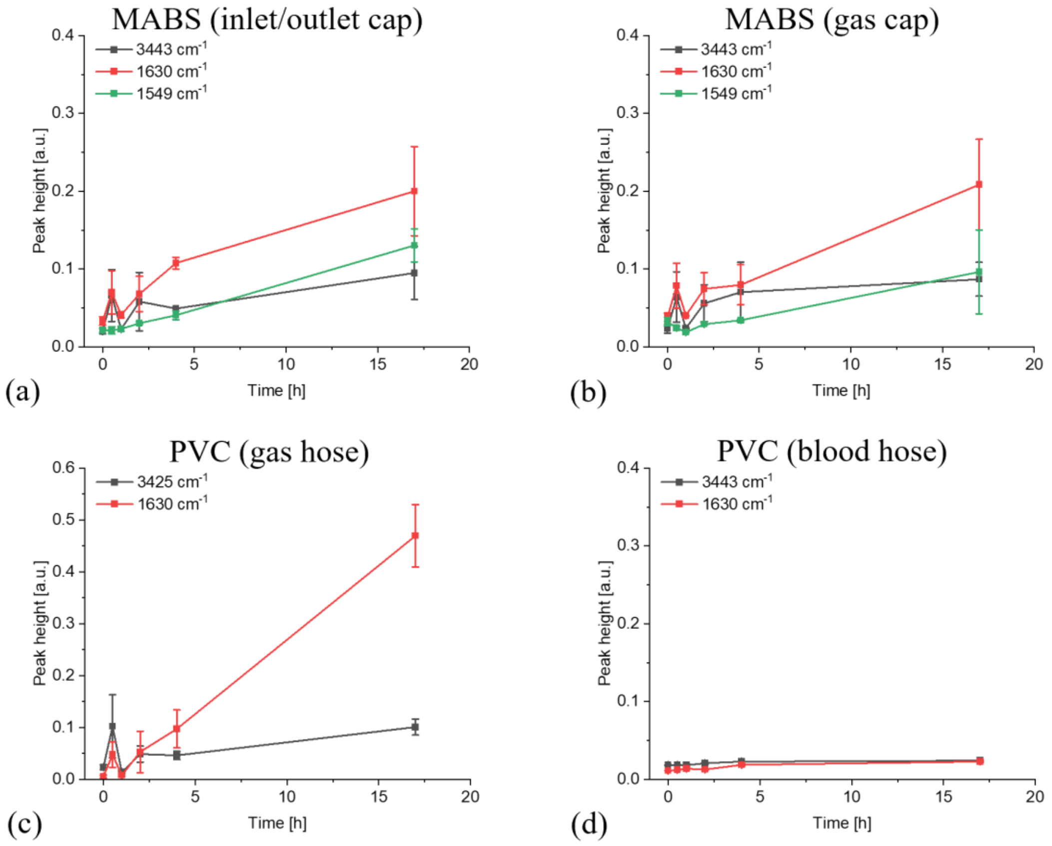

Figure 4.17: Signal heights of the signals caused by the treatment with NO (80 ppm) for (a) MABS (inlet/outlet cap), (b) MABS (gas cap), (c) PVC (gas hose), and (d) PVC (blood hose). The experiments were performed according to chapters 3.2.1 and 3.2.3.

Moving to 80 ppm resulted in broadly similar behavior of the signal at 1630 cm^{-1} to the treatment with NO (1000 ppm) (see Figures 4.16 and 4.17). In the case of the MABS samples and PVC (gas hose), the values reached around 0.2 and around 0.47, respectively (see Figure 4.17 (a)-(c)). The signal at 3443/3425 cm^{-1} also showed similar behavior with values slightly higher overall than NO (1000 ppm) (see Figures 4.16 and 4.17). The signal at 1549 cm^{-1}, on the other hand, had signal heights significantly lower than the signal at 1630 cm^{-1} while showing comparable or higher heights when treated with higher concentrations of NO (see Figures 4.17 (a), (b), and 4.16 (a), (b)). The outlier among the samples was the PVC (blood hose), with little to no increase in any of the signals (see Figure 4.17 (d)).

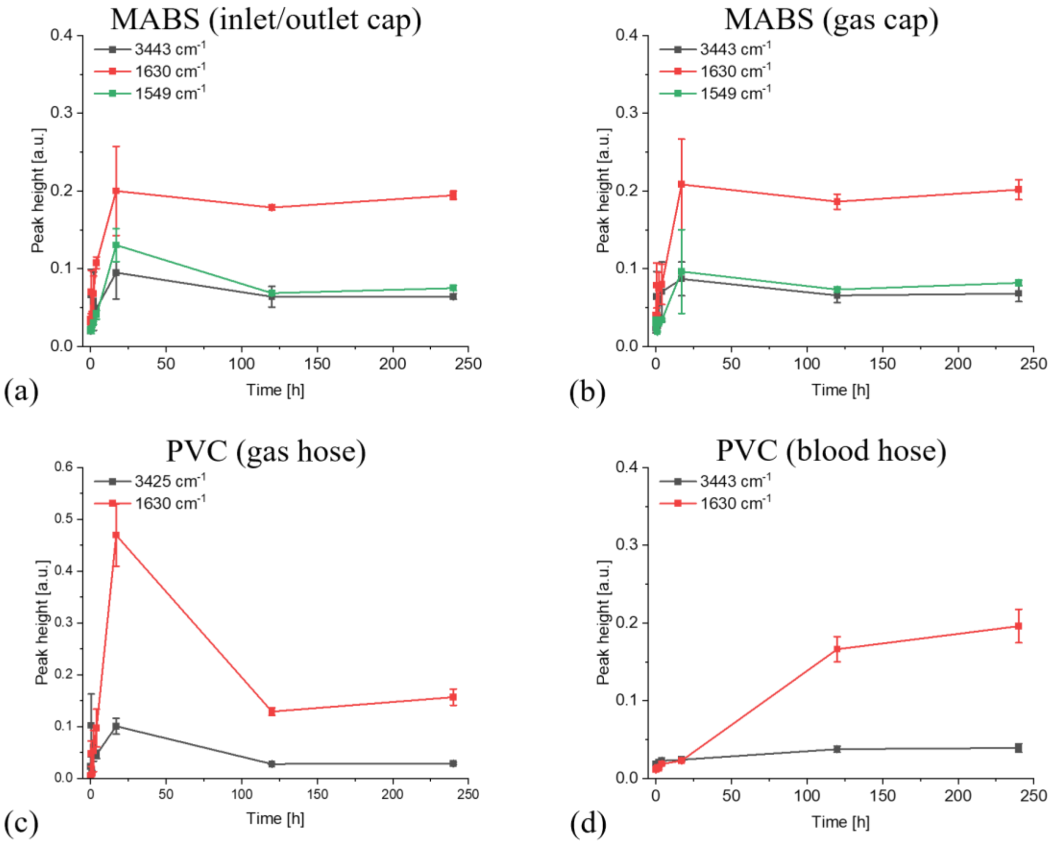

Figure 4.18: Signal heights of the signals caused by the treatment with NO (80 ppm) for (a) MABS (inlet/outlet cap), (b) MABS (gas cap), (c) PVC (gas hose), and (d) PVC (blood hose) with extended treatment times of up to ten days. The experiments were performed according to chapters 3.2.1 and 3.2.3.

Extending the treatment time to ten days resulted in stagnation of the signal heights in the case of the MABS signal. Compared to treatment at 1000 and 10,000 ppm, the signal heights leveled off at overall lower values (see Figures 4.16 and 4.17). For MABS, the signal at 1630 cm^{-1} reached values of around 0.2, while the signal at 1549 cm^{-1} reached values of just below 0.1, with the signal at 3443 cm^{-1} just below that (see Figure 4.18 (a), (b)). For the PVC (gas hose) samples, the results were less consistent, with the signal heights after 17 hours of treatment being significantly higher than the values after five and ten days (see Figure 4.18 (c)). The samples treated for up to 17 hours and those treated for five and ten days were treated and analyzed at different points in time, likely leading to the inconsistencies seen here. The signal heights reached for these samples were in line with the other polymers; the signal at 3425 cm^{-1} remained at a maximum of 0.03, and the signal at 1630 cm^{-1} reached 0.16 after ten days of treatment (see Figure 4.18 (c)). The PVC (blood hose samples) also showed similar results, with signal heights increasing to 0.04 and 0.20 for the signals at 3443 and 1630 cm^{-1}, respectively. Visible for all samples was a flattening of the curves beyond 17 hours of gas treatment (see Figure 4.18), analogous to the behavior shown with 10,000 and 1000 ppm.

The measurements using NO concentrations of 80 ppm showed that the reactions present at the higher NO concentrations (see Figure 4.14-4.16) persist even at a concentration 125/12.5 times lower, with signal heights of comparable dimension. These results, therefore, proved that the interaction between NO and the polymers remained relevant even at relatively low application concentrations below 100 ppm. The relative independence of the signal heights from the gas concentration used for the gas treatment was also interesting. A likely explanation for this similarity in signal heights between the different concentrations was that the reaction sites available under the reaction conditions were saturated by the end of the gas treatment, even at concentrations as low as 80 ppm. This interpretation is supported by the tendency towards saturation visible in the signal height graphs of all three NO concentrations (see Figures 4.14-4.18). The other interesting phenomenon that became visible through the analysis of the signal heights was the heights of the signals at 1630 and 1549 cm^{-1} relative to one another. At 10,000 and 1000 ppm, both signals reached very similar heights (see Figures 4.14 (b), (c), 4.15 (a), (b), and 4.16 (a), (b)). Lowering the concentration to 80 ppm resulted in a noticeable drop in height for the signal at 1549 cm^{-1}, while the signal at 1630 cm^{-1} stayed at similar heights compared to the measurements at higher concentrations (see Figure 4.18 (a), (b)). As discussed in chapter 4.2.1.1, nitro groups were formed exclusively through reactions with NO_2, while the nitrate ester groups could result from reactions with both NO_2 and HNO_3. The experiments at 10,000 and 1000 ppm were conducted with the bottle concentrations, while the experiments at 80 ppm were performed by mixing the bottled gas mixture of NO and nitrogen with the airflow produced by an air compressor. As already mentioned, NO_2 was formed through the reaction with oxygen reacted with the moisture in the air to form HNO_3. At 10,000 and 1000 ppm, this reaction only occurred at the beginning of the experiment, as the gas mixture displaced the air in the reaction chamber. However, at 80 ppm, the consistent supply of air containing moisture led to HNO_3 being produced throughout the gas treatment. This led to a lower concentration of NO_2 relative to HNO_3 compared to the experiments at higher concentrations. This led to the difference in signal height behavior at 1630 and 1549 cm^{-1} at 80 ppm of NO compared to 10,000 and 1000 ppm.

4.2.2.3 Treatment with NO_2 (1000, 500, and 50 ppm)

The samples treated with NO_2 at various concentrations were analyzed regarding peak height development to gauge the similarities between the use of NO and NO_2.

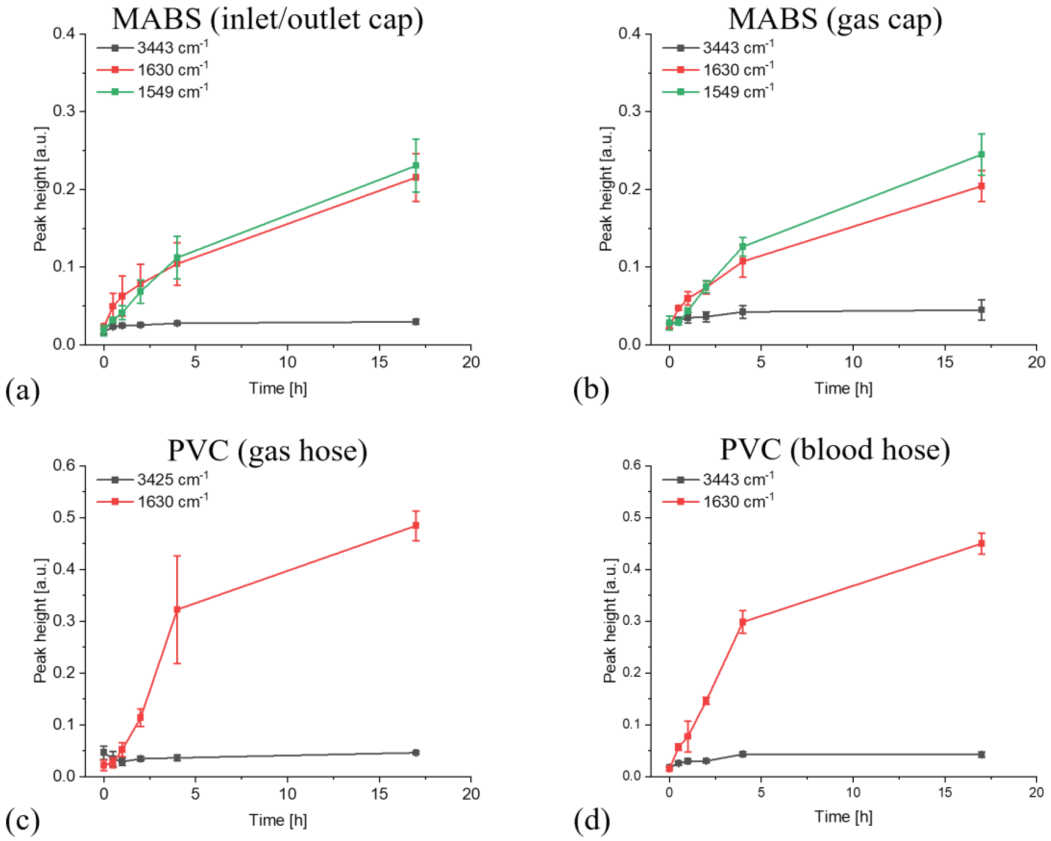

Figure 4.19: Signal heights of the signals caused by the treatment with NO_2 (1000 ppm) for (a) MABS (inlet/outlet cap), (b) MABS (gas cap), (c) PVC (gas hose), and (d) PVC (blood hose). The experiments were performed according to chapters 3.2.1 and 3.2.3.

Treatment with NO_2 (1000 ppm) resulted in peak heights very similar to the treatment with the same concentration of NO (see Figures 4.15 and 4.19). Both gases resulted in similar final peak heights of just above 0.2 for the signals at 1630 and 1549 cm^{-1} for the MABS samples (see Figure 4.19 (a), (b)), and a signal height between 0.4 and 0.5 for the signal at 1630 cm^{-1} for the PVC samples (see Figure 4.19 (c), (d)). The signal at 3443/3425 cm^{-1} stayed below a height of 0.1, increasing only slightly with increasing treatment durations. All signals showed a clear tendency towards saturation, with the increase in signal height visibly leveling off after four hours. Lowering the NO_2 concentration to 500 ppm resulted in broadly similar signal heights after 17 hours of gas treatment (see Figures 8.8, and 4.19). The MABS and the PVC (gas hose) samples showed the same tendency towards saturation at both concentrations. The primary difference at the lower concentration was the decrease in signal heights at 1549 cm^{-1} relative to the signal at 1630 cm^{-1}. At 500 ppm the signal at 1549 cm^{-1} showed lower signal heights over the entire duration of the gas treatment compared to the signal at 1630 cm^{-1} (see Figure 8.8 (a), (b)). At 1000 ppm, the heights of both signals were similar, with slightly greater heights shown by the signal at 1549 cm^{-1} (see Figure 4.19 (a), (b)). This difference in behavior between the experiments at 1000 ppm and 500 ppm was similar to the difference in behavior between high and low concentrations of NO (see Chapters 4.2.2.1 and 4.2.2.2). The experiments at 500 ppm were conducted by mixing the bottle gas mixture with air to reach the desired concentrations, while the experiments with 1000 ppm were performed using pure bottle gas. The airflow provided the moisture necessary to produce HNO_3 from NO_2, leading to a higher HNO_3 concentration relative to the NO_2 concentration. This, in turn, led to a decrease in the height of the signal at 1549 cm^{-1} compared to the signal at 1630 cm^{-1} at these concentrations (see Figure 8.8 (a), (b)). The similarity in signal heights between the different concentrations was again explained by the sample surfaces being saturated at both concentrations, similar to the experiments with NO (see Chapter 4.2.2.1). This interpretation was supported by the visible tendency towards saturation observed at all the examined concentrations (see Figures 4.19 and 8.8). The saturation starting earlier than with NO (see Figures 4.14-4.19 and 8.8) was likely because NO_2 was available from the start of the treatment rather than having to form through the reaction of NO with oxygen (see Equation 57). The treatment with NO_2 (50 ppm) finally resulted in very low signal heights compared to the other concentrations with no visible signs of saturation (see Figure 8.9). This gas concentration was likely too low to affect the polymer surfaces significantly with the treatment time limited to 17 hours.

4.2.3 Stability of the Signals Generated by Gas Treatment

The long-term stability of the functional groups formed because of the gas treatment was of particular interest when looking towards the application of these materials. For this reason, The FTIR-ATR measurements in this chapter were conducted several hours or days after the end of the gas treatment. The samples were left at room temperature in contact with air (see Chapters 4.2.3.1-4.2.3.3) or submerged in water or physiological saline solution (see Chapter 4.2.3.2) between measurements. The signals used to evaluate the signal stability were picked according to the same criteria as in chapter 4.2.2. The selection was limited to signals above 1500 cm^{-1}. Again, PU was not analyzed due to the strong overlap of the gas treatment signals with the signals caused by PU itself. The spectra were normalized using the signal at 1466 cm^{-1} in the case of PMP, the signal at 1720 cm^{-1} in the case of MABS, the signal at 2927 cm^{-1} in the case of PVC, the signal at 1257 cm^{-1} in the case of silicone, and the signal at 1727 cm^{-1} in the case of the UV-activated adhesive.

4.2.3.1 Signal Stability after Treatment with NO (10,000 ppm)

The first stability measurements were conducted with samples treated with NO (10.000 ppm) for ten days. The samples were measured directly after the gas treatment as well as 24 hours and eight days after the end of the gas treatment. The samples were left in contact with air at room temperature between the measurements.

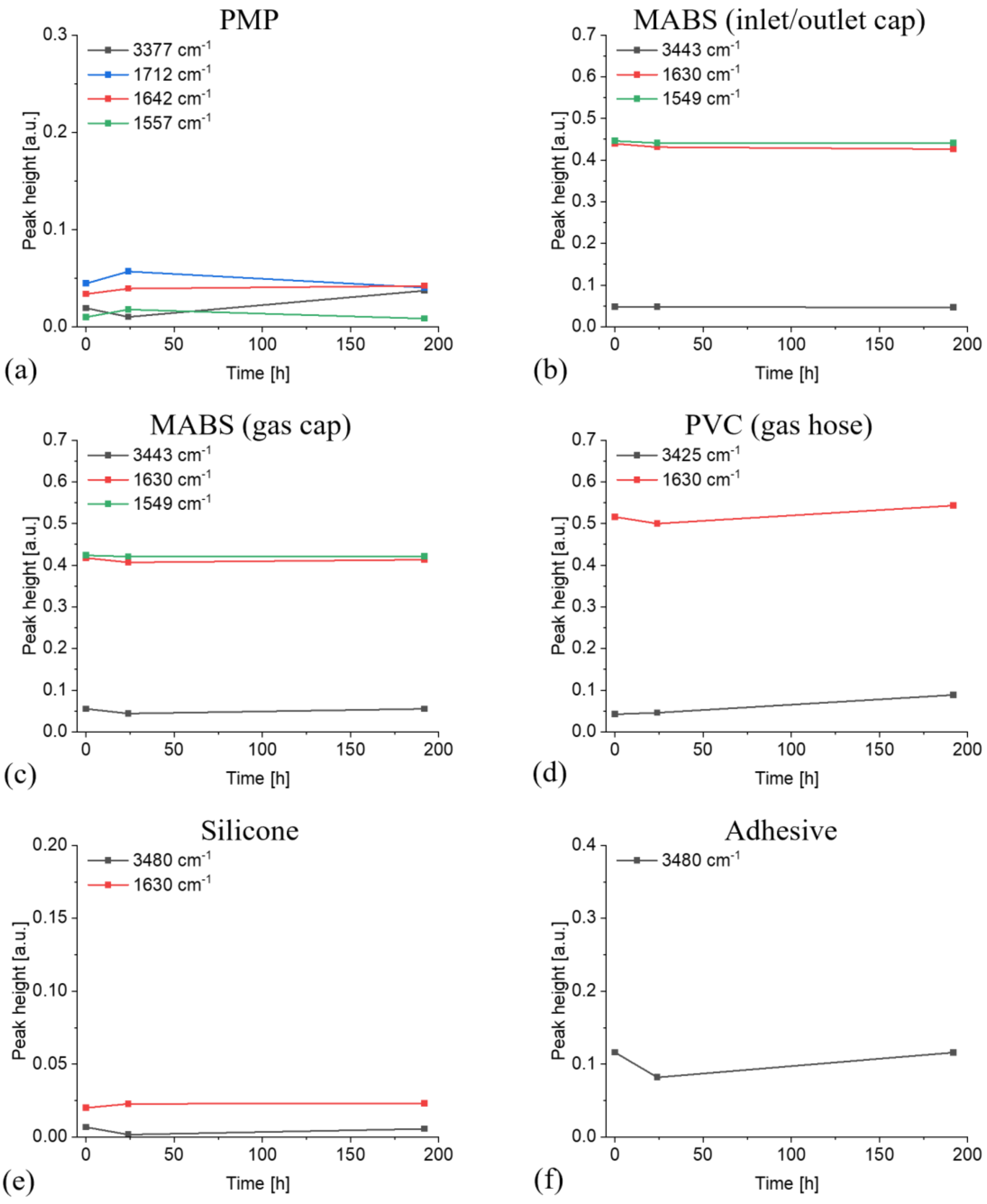

Figure 4.20: Development of signal heights after the end of a ten-day gas treatment with NO (10,000 ppm). Measurements were taken directly after the gas treatment, as well as 24 hours and eight days after the end of the gas treatment. The materials investigated were (a) PMP, (b) the inlet/outlet cap (MABS), (c) the gas cap (MABS), (d) PVC, (e) silicone, and (f) the UV-activated adhesive. The experiments were performed according to chapters 3.2.1, 3.2.2, and 3.2.3.

The signal heights caused by the nitro and nitrate ester groups and the adsorbed HNO_3 molecules proved largely stable over extended periods, in this case, a maximum of eight days (see Figure 4.20). The signals in the PMP spectra were the most unsteady overall, with signal heights rising and falling, likely due to the low overall signal intensities, which led to more significant uncertainties than the other materials (see Figure 4.20 (a)). The signals of the silicone gasket showed similar behavior, also likely due to the overall low signal intensity (see Figure 4.20 (e)). The signals for the MABS samples were very consistent, with little to no decrease in intensity for any of the three selected signals (see Figure 4.20 (b), (c)). PVC showed overall steady signal heights with a slight increase after eight days (see Figure 4.20 (d). The UV-activated adhesive also exhibited similar behavior with overall stable signal heights over eight days (see Figure 4.20 (f)). The instability of some of the signals seen with PMP, PVC, and the UV-activated adhesive, where the signal heights increased and decreased throughout the experiment and, in the case of PVC, even increased in overall heights compared to the values directly after the gas treatment should not be overinterpreted as these experiments were only conducted once due to the limited availability of NO at 10,000 ppm, leaving unknown uncertainties. The generally observed high stability of the signals did, however, give a positive first indication for the application of NO in ECMO circuits, as the release of the compounds formed on the polymer surfaces into the bloodstream of the patients should be unlikely. The stability measurements were expanded significantly using NO (1000 ppm) to confirm these first indications (see Chapter 4.2.3.2).

4.2.3.2 Signal Stability after the Treatment with NO (1000 ppm)

The long-term stability of the signals caused by treatment with NO (1000 ppm) was analyzed analogously to the treatment with NO (10,000 ppm) (see Chapter 4.2.3.1), leaving the samples in contact with air at room temperature after the end of the gas treatment. In addition to those experiments, the stability of the signals was also tested by submerging them in either Millipore water or physiological saline solution to mimic the conditions during the application of the ECMO circuit, where most of these materials are in direct contact with blood. Water was chosen as the simplest liquid system to introduce no additional influencing factors. Physiological sodium chloride solution was selected as the second liquid because of its significance in the application of ECMO circuits. It is commonly used as a priming liquid for these circuits before connecting them to the patient's bloodstream [319].

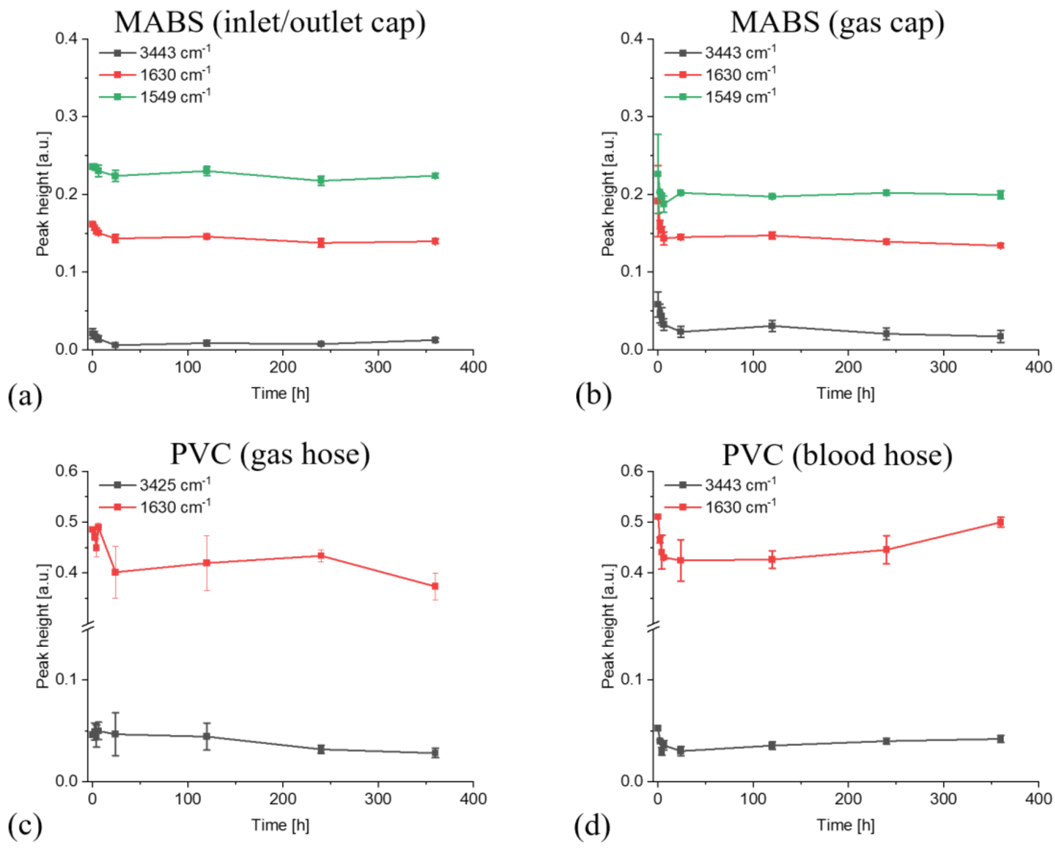

Figure 4.21: Development of signal heights after the gas treatment with NO (1000 ppm) for 17 hours. Measurements were taken directly after the gas treatment and two, four, and six hours and five, ten, and 15 days after the end of the gas treatment. The materials investigated were (a) MABS (inlet/outlet cap), (b) MABS (gas cap), (c) PVC (gas hose), and (d) PVC (blood hose). The experiments were performed according to chapters 3.2.1, 3.2.2, and 3.2.3.

Signal height stability under dry conditions was high. All signals showed a slight decrease during the first 24 hours of testing, with the signal heights staying mostly constant after that point (see Figure 4.21). The signal at 3443/3425 cm^{-1} lost around 40 % for MABS (inlet/outlet cap), 71 % for MABS (gas cap), 39 % for PVC (gas hose), and 20 % for PVC (blood hose) over the entire duration. The signal at 1630 cm^{-1} lost a total of 14 % for MABS (inlet/outlet cap), 30 % for MABS (gas cap), 23 % for PVC (gas hose), and 2 % for PVC (blood hose). The signal at 1549 cm^{-1} lost 5 % and 10 % for MABS (inlet/outlet cap) and MABS (gas cap), respectively. The signal at 3443/3425 cm^{-1} was the least stable overall compared to the signals at 1630 and 1549 cm^{-1}. The PVC samples showed overall greater signal stability than the MABS samples.

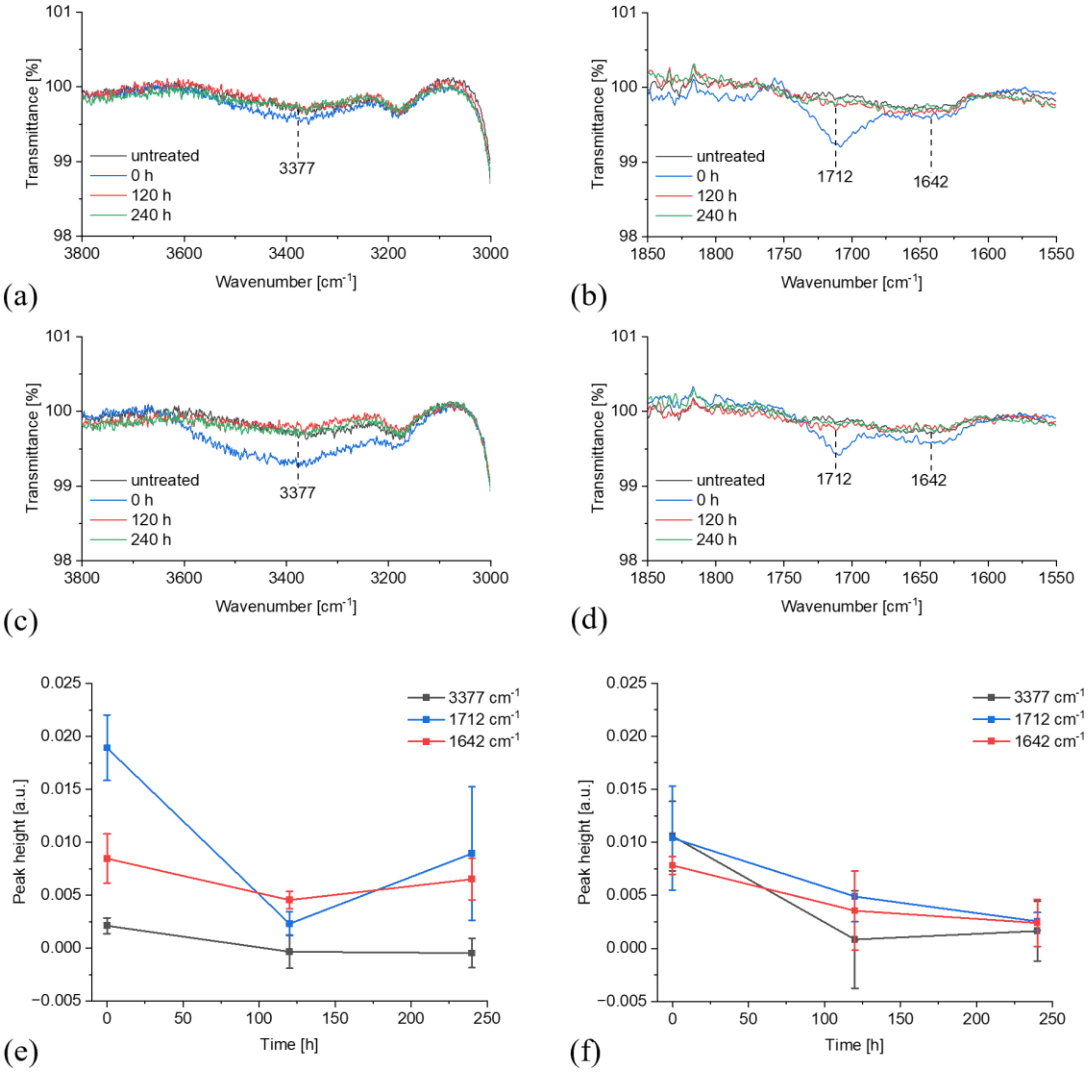

Figure 4.22: FTIR-ATR spectra of PMP treated with NO (1000 ppm) for 17 hours and then submersed in Millipore water ((a), (b)) and physiological sodium chloride solution ((c), (d)) for five (green) and ten (purple) days compared to an untreated sample (grey) and the sample directly of the NO treatment (red). (a), (c) Close-up of the broad signal at around 3377 cm^{-1}. (b), (d) Close-up of the spectra in the 1850 to 1550 cm^{-1} range. (e) Time evolution of the peak heights of the signal at 3377 (grey), 1712 (blue), and 1642 cm^{-1} (red) for PMP after the submersion in Millipore water and (f) physiological sodium chloride solution. The experiments were performed according to chapters 3.2.1, 3.2.2, and 3.2.3.

Submersing the PMP samples in either Millipore water or saline solution resulted in an almost complete decline of all relevant signals caused by the gas treatment (see Figure 4.22). The saline solution had an overall slightly more substantial impact on the signals than the Millipore water, looking at the signal at 1642 cm^{-1} in particular (see Figure 4.22 (e), (f)).

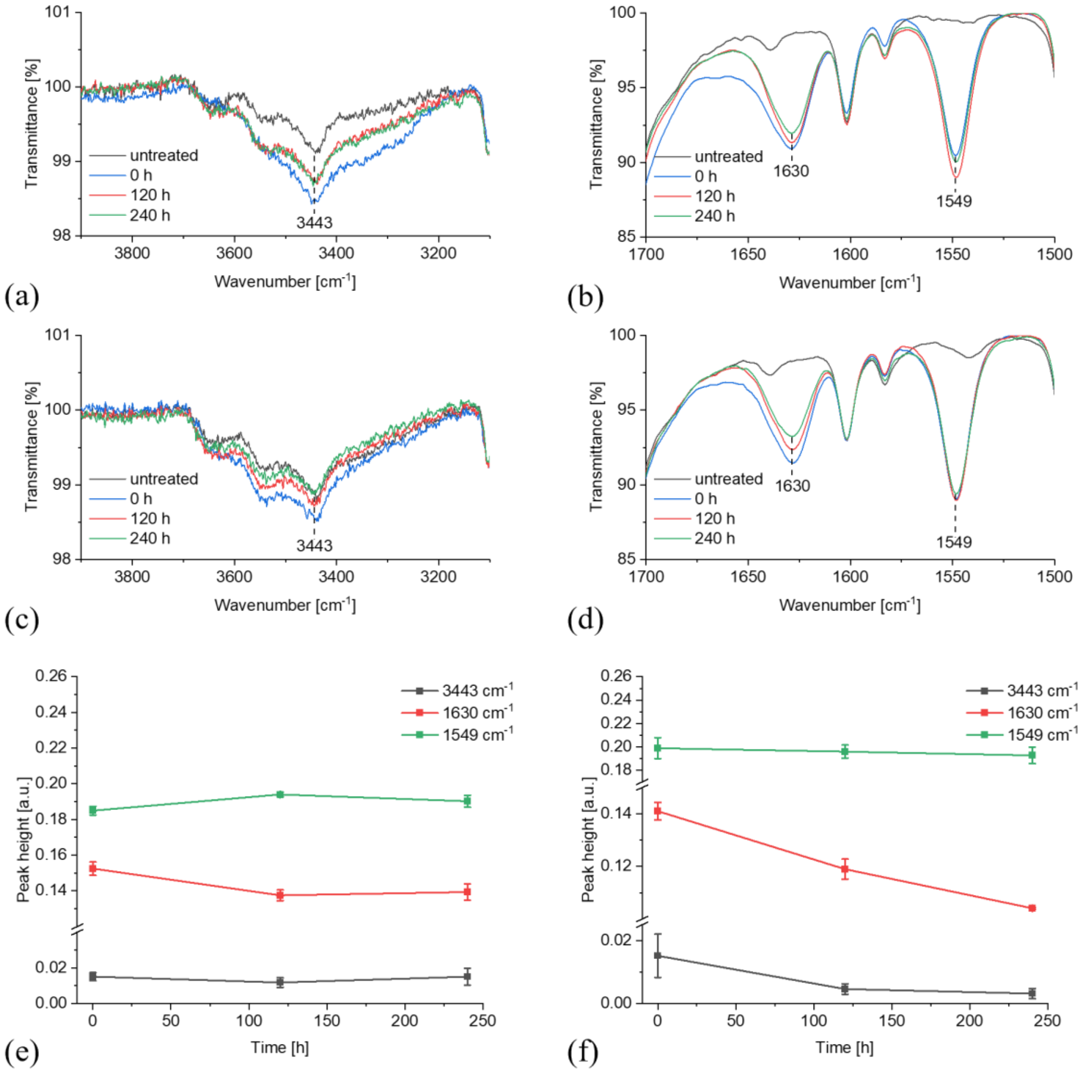

Figure 4.23: FTIR-ATR spectra of MABS (inlet/outlet cap) treated with NO (1000 ppm) for 17 hours and then submersed in Millipore water ((a), (b)) and physiological sodium chloride solution ((c), (d)) for 5 (green) and ten (purple) days compared to an untreated sample (grey) and the sample directly of the NO treatment (red). (a), (c) Close-up of the broad signal at around 3443 cm^{-1}. (b), (d) Close-up of the spectra in the 1700 to 1500 cm^{-1} range. (e) Time evolution of the peak heights of the signal at 3443 (grey), 1630 (red), and 1549 cm^{-1} (green) for MABS after the submersion in Millipore water and (f) physiological sodium chloride solution. The experiments were performed according to chapters 3.2.1, 3.2.2, and 3.2.3.

The MABS (inlet/outlet cap) results showed a pronounced difference between submersion in Millipore water and saline solution. The results for the submersion in Millipore water were largely identical to the results obtained for the stability tests under dry conditions (see Figures 4.21 (a) and 4.23 (e)). The signals at 3443 and 1630 cm^{-1} decreased slightly, losing 1 and 9 % of their original signal height, respectively. The signal at 1549 cm^{-1} meanwhile maintained its height entirely. Submersing the samples in saline solution, on the other hand, led to a decrease in signal height of 79 % and 26 % for

3443 and 1630 cm^{-1}, respectively. The signal at 1549 cm^{-1} decreased by 3 %, meaning submersion in saline solution led to an overall more substantial decrease in signal heights, particularly concerning the signal at 3443 cm^{-1}.

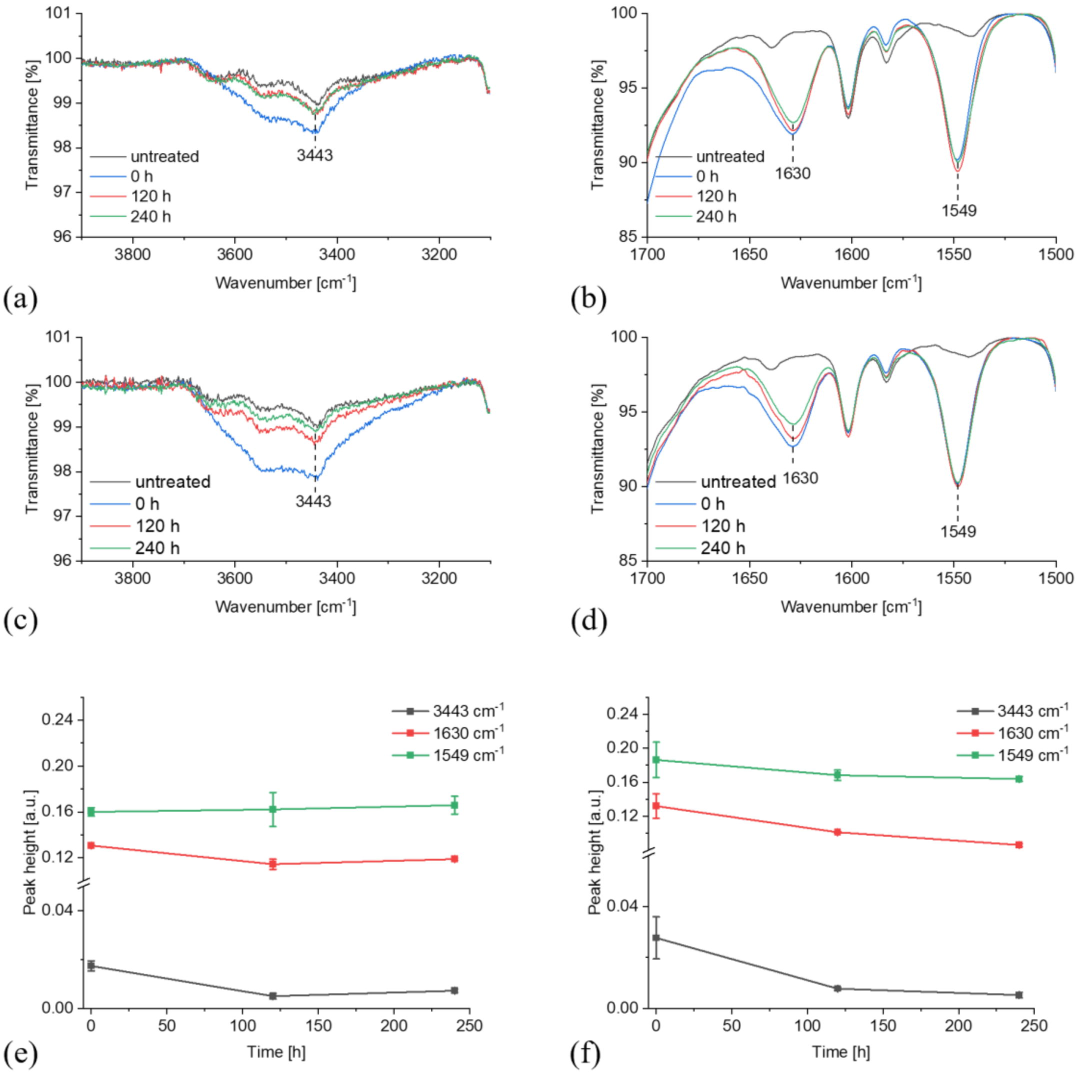

Figure 4.24: FTIR-ATR spectra of MABS (gas cap) treated with NO (1000 ppm) for 17 hours and then submersed in Millipore water ((a), (b)) and physiological sodium chloride solution ((c), (d)) for five (red) and ten (green) days compared to an untreated sample (grey) and the sample directly of the NO treatment (blue). (a), (c) Close-up of the broad signal at around 3443 cm^{-1}. (b), (d) Close-up of the spectra in the 1700 to 1500 cm^{-1} range. (e) Time evolution of the peak heights of the signal at 3443 (grey), 1630 (red), and 1549 cm^{-1} (green) for MABS after the submersion in Millipore water and (f) physiological sodium chloride solution. The experiments were performed according to chapters 3.2.1, 3.2.2, and 3.2.3.

The results for MABS (gas cap) were largely identical to those for MABS (inlet/outlet cap), with a more substantial decrease in signal height after submersion in saline solution than in Millipore water. The signal affected the most by the liquid submersion was again the signal at 3443 cm^{-1}, while the signals at 1630 and 1549 cm^{-1} remained largely steady (see Figure 4.24 (e), (f)).

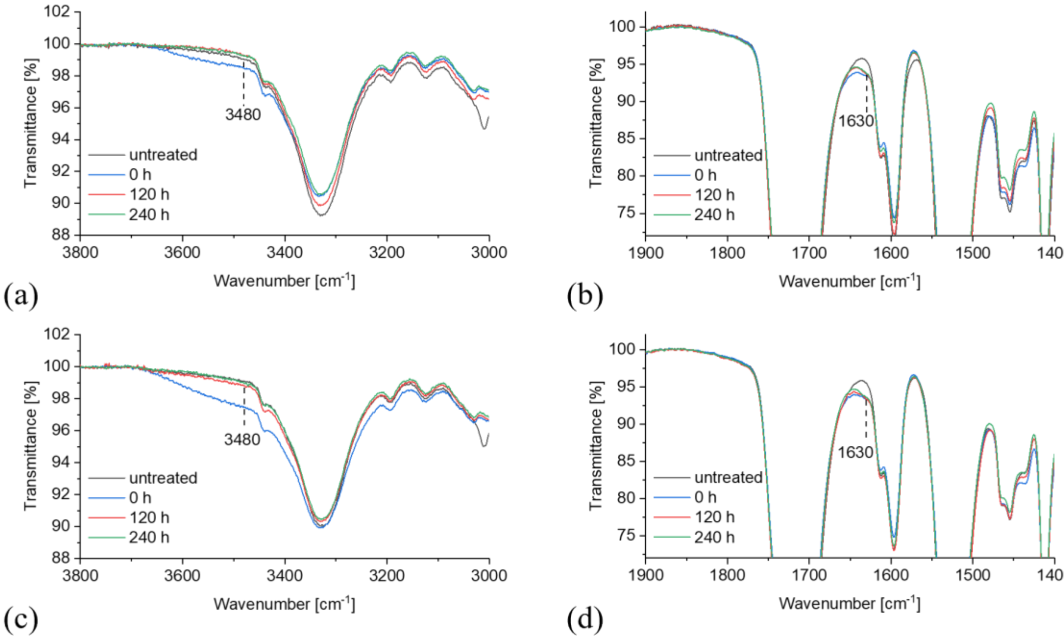

Figure 4.25: FTIR-ATR spectra of PU treated with NO (1000 ppm) for 17 hours and then submersed in Millipore water ((a), (b)) or physiological sodium chloride solution ((c), (d)) for five (red) and ten (green) days compared to an untreated sample (grey) and the sample directly after the NO treatment (blue). (a), (c) Close-up of the signal at around 3480 cm^{-1}. (b), (d) Close-up of the signal at around 1630 cm^{-1}. The experiments were performed according to chapters 3.2.1, 3.2.2, and 3.2.3.

As stated in chapter 4.2.3.1, a signal height analysis of PU was not possible due to the substantial overlap between the signals caused by the material, and the gas treatment overlapped too heavily. The signals at 3480 and 1630 cm^{-1} were, therefore, only visually observed. The signal at 3480 cm^{-1} disappeared almost entirely after only five days of submersion in both cases (see Figure 4.25 (a), (c)), while the signal at 1630 cm^{-1} remained constant throughout the experiment, with no observable decrease in signal height (see Figure 4.25 (b), (d)). No significant difference between the submersion in Millipore water and saline solution could be observed.

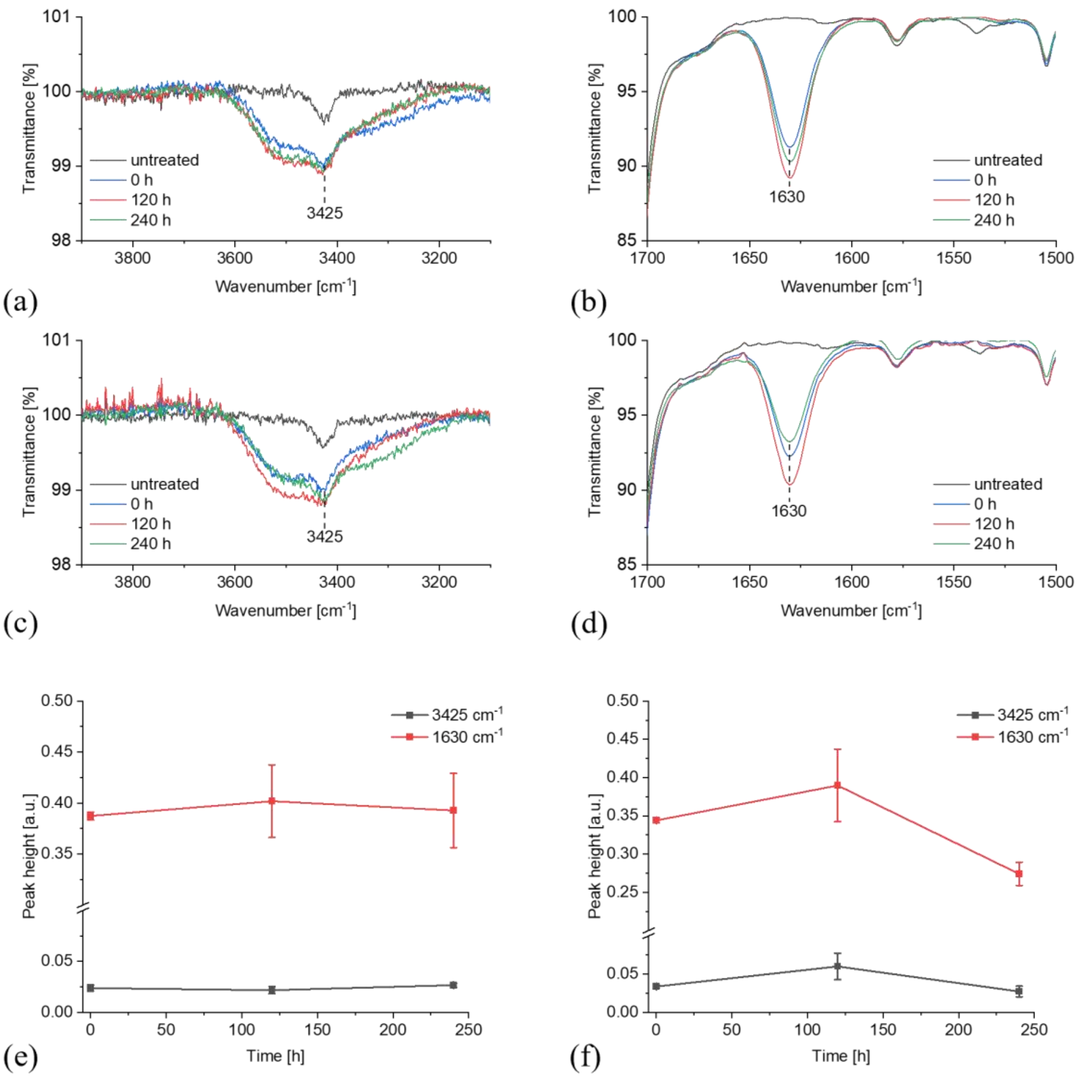

Figure 4.26: FTIR-ATR spectra of PVC (gas hose) treated with NO (1000 ppm) for 17 hours and then submersed in Millipore water ((a), (b)) and physiological sodium chloride solution ((c), (d)) for five (red) and ten (green) days compared to an untreated sample (grey) and the sample directly of the NO treatment (blue). (a), (c) Close-up of the broad signal at around 3425 cm^{-1}. (b), (d) Close-up of the spectra in the 1700 to 1500 cm^{-1} range. (e) Time evolution of the peak heights of the signal at 3425 (grey) and 1630 cm^{-1} (red) for PVC after the submersion in Millipore water and (f) physiological sodium chloride solution. The experiments were performed according to chapters 3.2.1, 3.2.2, and 3.2.3.

The PVC (gas hose) samples showed a clear difference in signal height development between submersion in saline solution and Millipore water. The water submersion did not impact the signal heights at either 3425 or 1630 cm^{-1}, with both signals remaining constant over the entire experiment duration (see Figure 4.26 (e)). Submersion in saline solution, on the other hand, resulted in a 20 % decrease in the signal height at 1630 cm^{-1}. The signal at 3425 cm^{-1} decreased by 19 % (see Figure 4.26 (f)).

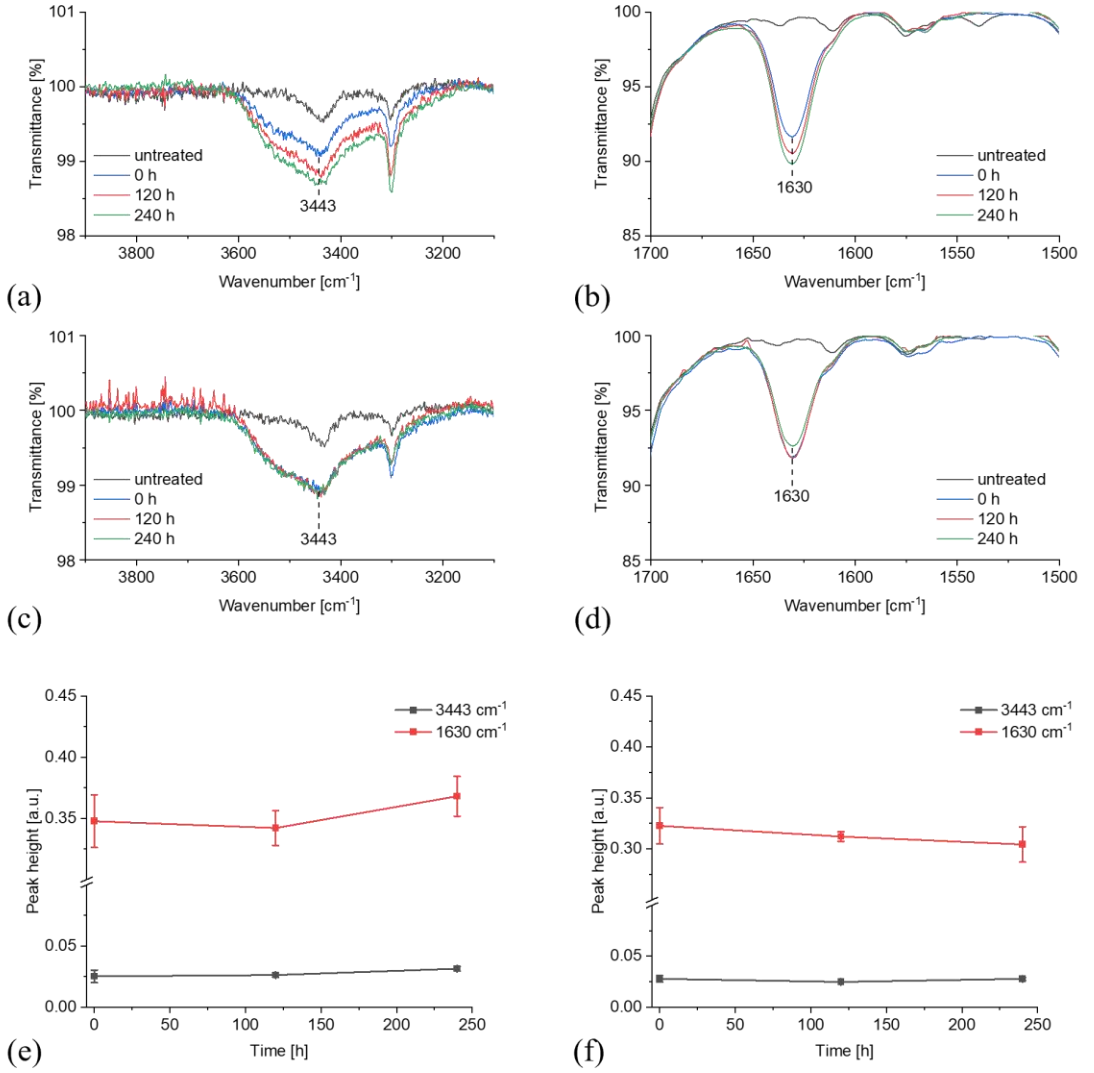

Figure 4.27: FTIR-ATR spectra of PVC (blood hose) treated with NO (1000 ppm) for 17 hours and then submersed in Millipore water ((a), (b)) and physiological sodium chloride solution ((c), (d)) for five (red) and ten (green) days compared to an untreated sample (grey) and the sample directly of the NO treatment (blue). (a), (c) Close-up of the broad signal at around 3443 cm^{-1}. (b), (d) Close-up of the spectra in the 1700 to 1500 cm^{-1} range. (e) Time evolution of the peak heights of the signal at 3443 (grey) and 1630 cm^{-1} (red) for PVC after the submersion in Millipore water and (f) physiological sodium chloride solution. The experiments were performed according to chapters 3.2.1, 3.2.2, and 3.2.3.

The measurements of PVC (blood hose) samples also displayed a higher stability of the relevant signals with water than with saline solution. The signals at 3443 and 1630 cm^{-1} remained stable with the samples submerged in Millipore water (see Figure 4.27 (e)). Submersion in saline solution resulted in a 6 % drop in signal height at 1630 cm^{-1}. The signal height at 3443 cm^{-1} remained stable throughout the experiment (see Figure 4.27 (f)).

The stability measurements with NO (1000 ppm) painted an overall similar picture to the measurements with NO (10,000 ppm) (see Figures 4.20 and 4.21). The signals generated by the gas treatment remain stable over extended periods, with the signals at 1630 and especially at 1549 cm^{-1} showing high degrees of stability (see Figure 4.21). This stability was largely maintained in contact with Millipore water and saline solution (see Figure 4.22-4.27 (e), (f)). The overall stability of these signals, even when in contact with the liquids, led to a positive outlook for the application of NO in ECMO circuits, as it indicated that the compounds formed on the surface of the polymers would not be transferred to the patient's blood in large quantities, as already mentioned in chapter 4.2.3.1. The experiments with liquid submersion also allowed for the differentiation between the signals caused by covalently bound functional groups in the shape of nitro and nitrate ester groups and HNO_3, which was adsorbed on the sample surface. The signals at 1630 and 1549 cm^{-1} corresponding to the covalently bound functional groups remained mostly stable, similar to the experiments under dry conditions. The signal at 3443 cm^{-1}, on the other hand, decreased more strongly when the samples were brought in contact with water (see Figures 4.22-4.27 (e), (f)). This difference in behavior supported the attribution of the signal at 3480/3443/3425 cm^{-1} to the adsorption of HNO_3, which was likely washed away during the submersion process or, in the case of the saline solution, potentially displaced by the adsorption of sodium chloride ions on the polymer surface [320, 321]. The stronger covalent bonds of the functional groups prevented this from happening, leading to more stable signal heights. The more substantial signal decrease observed for the submersion in the saline solution was likely due to the additional washing steps before the drying process (see Chapter 3.2.2). The slight reduction in signal height observed for the signal at 1630 cm^{-1} under both dry and wet conditions (see Figures 4.21-4.27) was likely due to acid-catalyzed hydrolysis, as Millipore water, saline solution, and humidity in the air were slightly acidic due to the absorption of CO_2 from the atmosphere [322, 323]. The overall more substantial decline of the signal heights with the saline solution compared to Millipore water (see Figures 4.22-4.27) was again likely due to the additional washing steps ahead of the drying process (see Chapter 3.2.2) already mentioned before. The sodium chloride in the solution should not have impacted the reaction rates at the concentration used in this context [324]. The signal with the overall highest stability was the signal at 1549 cm^{-1}, which showed little to no decrease over time, independent of treatment conditions (see Figures 4.21 (a), (b), 4.23, and 4.24).

4.2.3.3 Signal Stability after Treatment with NO_2 (1000 ppm)

The stability of the signal heights after the end of the gas treatment was also analyzed for the experiments using NO_2. In this case, the stability measurements were limited to experiments with NO_2 (1000 ppm). The signal stability was analyzed analogously to the treatment with NO (10,000 ppm) (see Chapter 4.2.3.1).

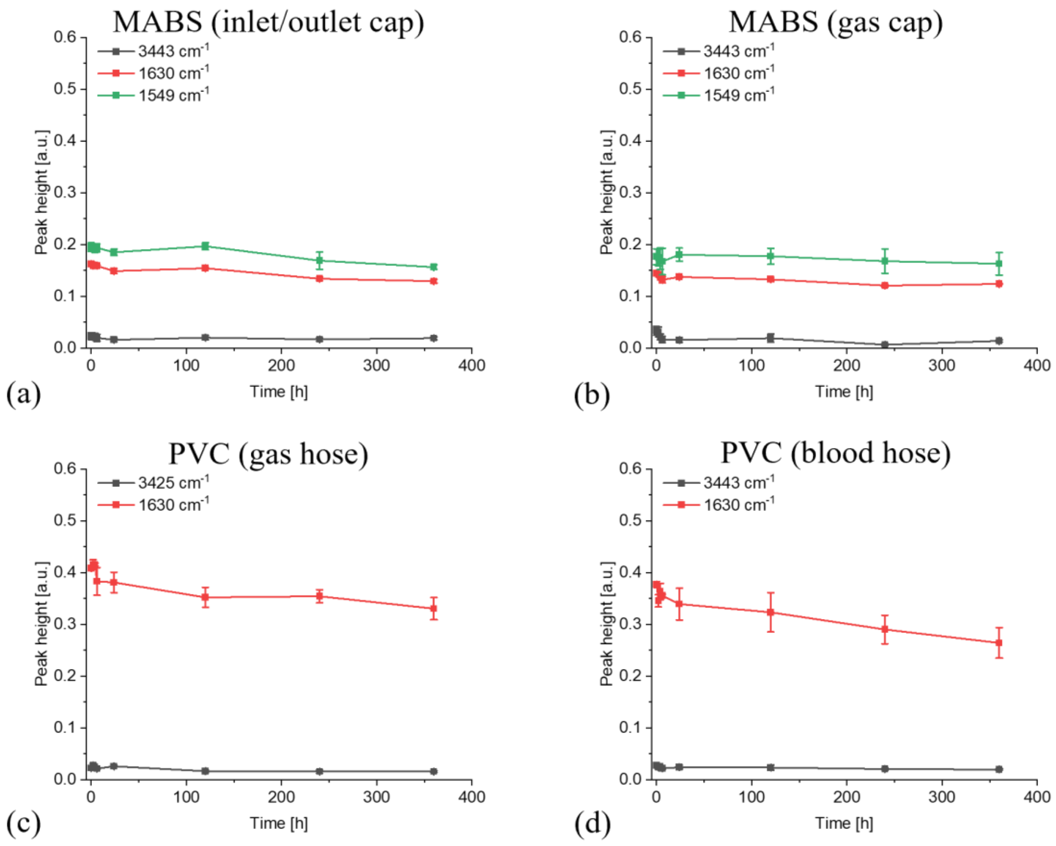

Figure 4.28: Development of signal heights after the gas treatment with NO_2 (1000 ppm) for 17 hours. Measurements were taken directly after the gas treatment and two, four, and six hours and five, ten, and 15 days after the end of the gas treatment. The materials investigated were (a) MABS (inlet/outlet cap), (b) MABS (gas cap), (c) PVC (gas hose), and (d) PVC (blood hose). The experiments were performed according to chapters 3.2.1, 3.2.2, and 3.2.3.

The results of the stability measurements with NO_2 were similar to the same experiments conducted with NO at the same concentration (see Figure 4.21). For the MABS samples, the signals at 1630 and 1549 cm^{-1} were stable throughout the experiment, with the signal at 1630 cm^{-1} losing 20 and 14 % of the initial signal height for MABS (inlet/outlet cap) and MABS (gas cap), respectively. The signal at 1549 cm^{-1} decreased by 20 % and 8 %, while the signal at 3443 cm^{-1} decreased by 18 % and 58 % (see Figure 4.28 (a), (b)). With the PVC samples, the signal at 1630 cm^{-1} decreased by 19 % and 30 %, respectively. The signal at 3443/3425 cm^{-1} decreased by 29 % and 18 % (see Figure 4.28 (c), (d)). The MABS samples showed the overall highest signal stability, with both PVC samples showing more substantial decreases over time. The stability of the signals at 1630 and 1549 cm^{-1} was overall lower compared to the same experiment using NO (1000 ppm). Meanwhile, the signal at 3443/3425 cm^{-1} was more stable than with NO (see Figure 4.21). The results, however, remained comparable despite these differences.

4.3 XPS Measurements

The XPS measurements were conducted to verify the results obtained with FTIR-ATR and to support the interpretations made so far. The method was also used to gain an understanding of whether the gas treatment only changed the surface chemistry of the polymers or also caused changes in the bulk material. For this purpose, a sputtering process that removed several nanometers from the surface of the polymer samples was employed (see Chapter 3.2.5). The selection of samples was again limited to the blood-contacting surfaces PMP, MABS (inlet/outlet cap), and PU. The PVC (gas hose) and PVC (blood hose) samples were unsuitable for these measurements due to their shape. A single NO concentration of 1000 ppm was used for these measurements. All spectra were aligned to the normal C-C peak position of the C-1s peak to compensate for a constant energetic shift of all spectra caused by charging effects. The spectra analysis focused on the N-1s peak located in the binding energy range from 398 to 400 eV (see Figures 4.29-4.31) to detect changes in the spectra caused by the formation of nitro and nitrate ester groups. The spectra were analyzed between 420 and 380 eV, focusing exclusively on the N-1s peaks present in the spectra. The spectra were fitted, and the visible peaks were deconvoluted using a Gauss peak function. The experiments were performed according to chapters 3.2.1 and 3.2.5. For the stability measurements, the peak area at 407.6 eV was determined for MABS and PU.

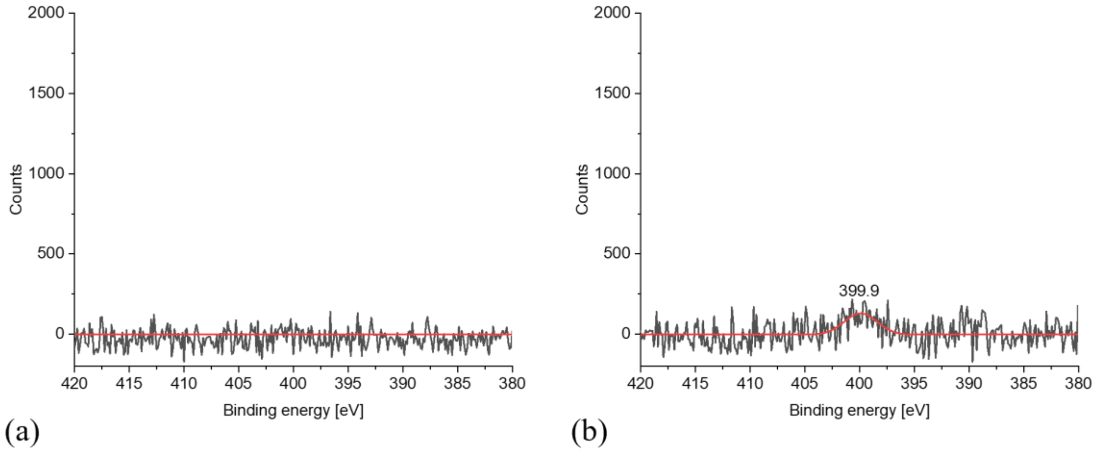

Figure 4.29: Results of the XPS measurements of PMP samples both (a) untreated and (b) treated with NO (1000 ppm) for 17 hours. None of the samples were sputtered. The experiments were performed according to chapters 3.2.1 and 3.2.5.

The XPS measurements with the PMP samples showed no changes caused by the gas treatment, with the weak nitrogen peak remaining at 399.9 eV (see Figure 4.29).

Sputtering of the samples proved to be impossible due to unstable and long-term charging effects of the samples. The measurements showed no significant impact of the gas treatment, with no peaks related to nitrogen-containing species such as nitro- and nitrate ester groups or HNO_3 molecules appearing. These results supported the findings of the FTIR-ATR measurements (see Figure 4.10 (a)). Both methods showed that the lack of suitable structural features of the polymer inhibited the formation of the mentioned functional groups (see Chapter 4.2.1.1).

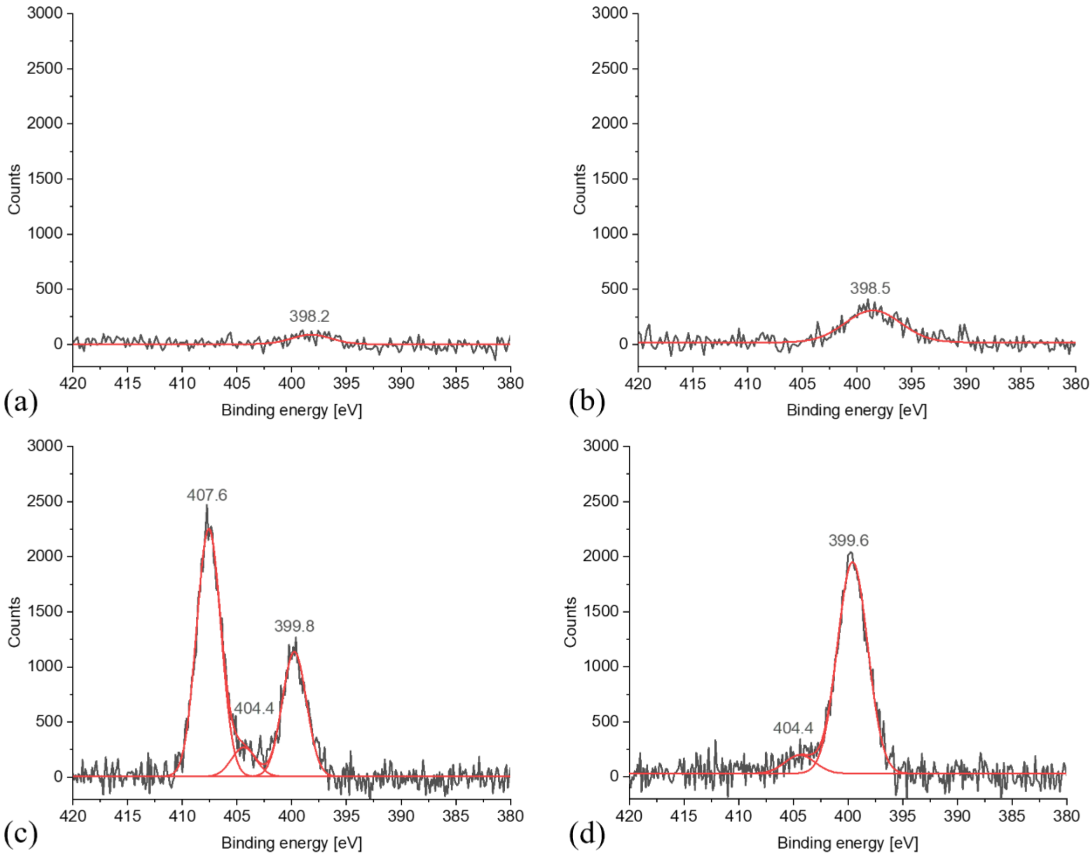

Figure 4.30: XPS spectra of (a) untreated, (b) untreated and sputtered, (c) treated, and (d) treated and sputtered MABS (inlet/outlet cap) samples. Gas treatment was conducted with NO (1000 ppm) for 17 hours. The experiments were performed according to chapters 3.2.1 and 3.2.5.

The MABS samples showed a clear impact of the gas treatment with a prominent additional peak at 407.6 eV and a small peak at 404.4 eV appearing in the spectrum of the treated sample in addition to the regular N-1s peak at 399.8 eV (see Figure 4.30 (c)). The peak at around 399 eV was likely caused by the nitrile groups present in the acrylonitrile monomers of MABS [325]. The peak at 407.6 eV was caused by the formation of nitrate ester groups and the adsorption of HNO_3 molecules [240, 326]. These results were confirmed by two additional samples used for stability measurements (see

Figure 8.10 (a), (b)). The peak at 407.6 eV disappeared after sputtering the treated sample, leaving the peak at 399.6 eV and a small shoulder at 404.4 eV (see Figure 4.30 (d)). The peak at 404.4 eV was within the fit error and, therefore, not attributable.

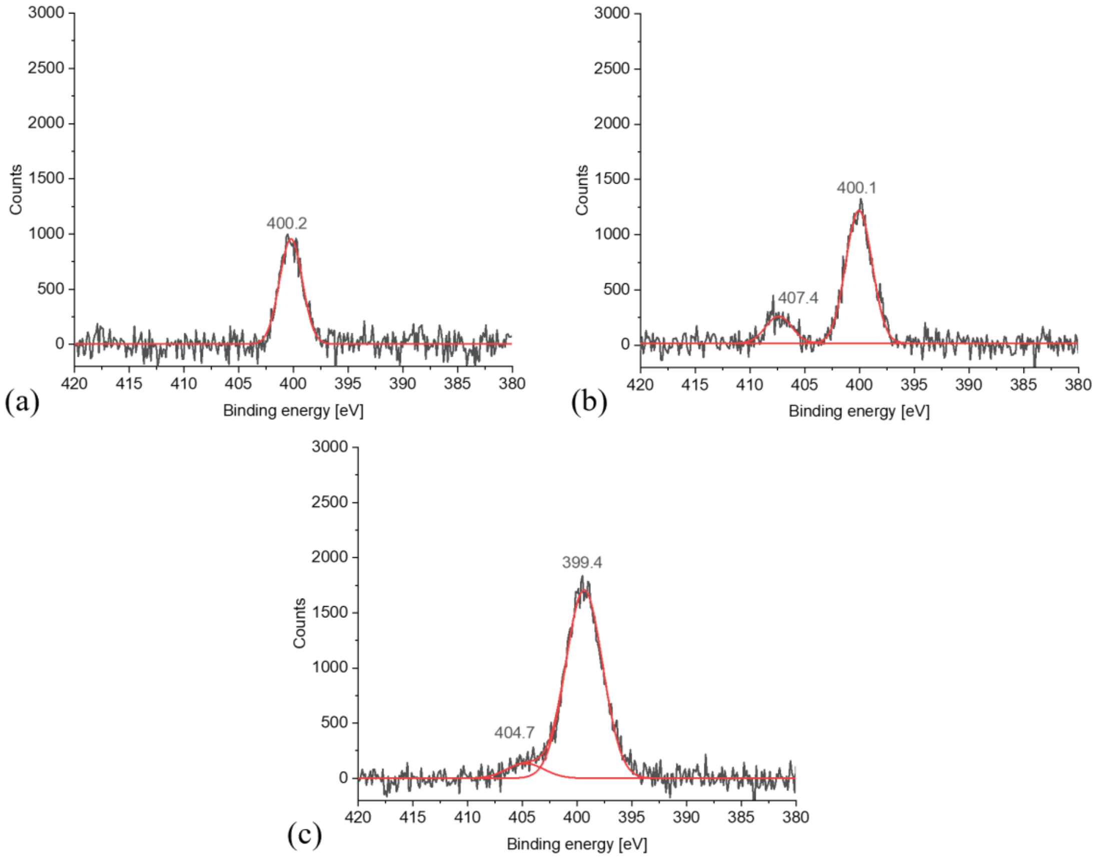

Figure 4.31: XPS spectra of (a) untreated, (b) treated, and (c) treated and sputtered PU samples. Gas treatment was conducted with NO (1000 ppm) for 17 hours. The experiments were performed according to chapters 3.2.1 and 3.2.5.

The spectra of PU again showed the regular N-1s peak around 400 eV caused by the urethane groups of the polymer (see Figure 4.31 (a)) [327]. After the gas treatment, a peak at 407.4 eV appeared, likely corresponding to both the formation of nitrate ester groups and HNO_3 adsorption on the surface (see Figure 4.31 (b)) [240, 326]. These results were confirmed by two additional samples used for stability measurements (see Figure 8.11 (a), (b)). The signal at 407.4 eV disappeared after the sputtering process, similar to MABS, with the peak at 399.4 eV remaining in place and a small shoulder appearing at 404.7 eV (see Figure 4.31 (c)). The peak at 404.7 eV was within the fit error and, therefore, not attributable. Measurements with the sputtered untreated sample were not possible due to excessive charging of the sample.

In addition to these experiments, stability measurements were conducted with MABS and PU to see whether the high degrees of stability observed during the FTIR-ATR measurements could also be observed with XPS (see Chapter 4.2.3).

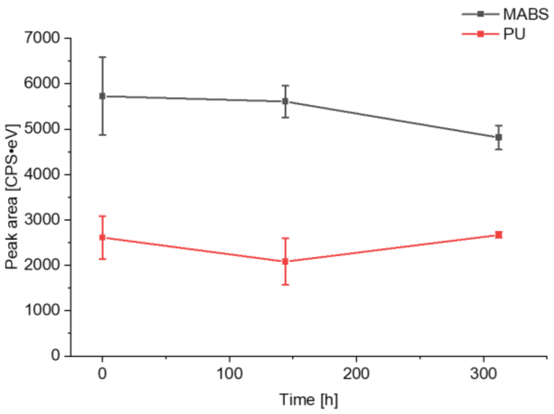

Figure 4.32: Development of the peak area at around 407.6 eV after the end of the gas treatment for both MABS (grey) and PU (red) samples. The experiments were performed according to chapters 3.2.1 and 3.2.5.

The peak area at 407.6 eV observed for MABS and PU showed high stability. With MABS, the area decreased from 5727 CPSeV to 4816 CPSeV after 13 days, a 16% drop. With PU, the peak area stayed completely stable (see Figure 4.32).

The results of the XPS measurement confirmed the results obtained from the FTIR-ATR measurements, with all three sample materials showing similar behaviors when treated with NO gas mixtures (see Figure 4.10 (a), (b), and (d)). PMP did not react at all due to missing any structural features necessary for interaction with the treatment gas, as already discussed in chapter 4.2.1.1. For both MABS and PU, XPS showed clear evidence of the formation of nitrate ester groups and the adsorption of HNO_3, with the peaks appearing at 407.6 and 407.4 eV, respectively, confirming the results of the FTIR-ATR measurements (see Chapter 4.2.1.1). A signal corresponding to nitro groups could not be observed for either polymer, likely due to limitations in the resolution of the spectra, as the corresponding peak would be expected around 406 to 407 eV [326, 328]. The stability measurements showed similar degrees of stability compared to the FTIR-ATR measurements, confirming the results in chapter 4.2.3 (see Figure 4.32). What the XPS measurements also clearly showed was that the changes caused by the gas treatment were entirely located at the surface of the polymers, as the peaks corresponding to these changes at 407.6 and 407.4 eV disappeared after the sputtering process had removed the topmost layer of material (see Figures 4.30 (d), and 4.31 (c)). This was of particular importance for PU, which had shown signs of chain scission and cross-linking reactions with the potential to influence the structural properties of the polymer. Based on these results, that should not be an issue, as the reactions only occurred on the surface of the polymer. The XPS measurements overall strongly indicated that the gas treatment of the oxygenator materials should not influence the structural properties of the polymers.

4.4 SEM Recordings of the Polymer Surfaces

SEM images were recorded to investigate whether the treatment of the polymer materials with NO would impact the surface morphology of the polymers. The primary concern was the hollow fiber membranes made of PMP. The gas permeability of these fibers is based on their microporous structure. Changes in morphology due to the gas treatment could potentially impact the gas permeability and, therefore, interfere with the functionality of the oxygenator. The secondary concern was that the gas treatment could change the surface morphology of the polymers. Materials such as PMP, MABS (inlet/outlet cap), PU, and PVC (blood hose) are in constant contact with the patient's blood throughout the device's application, meaning a change in surface morphology could have an impact on their blood compatibility [329]. The experiments were performed according to chapters 3.2.1 and 3.2.4.

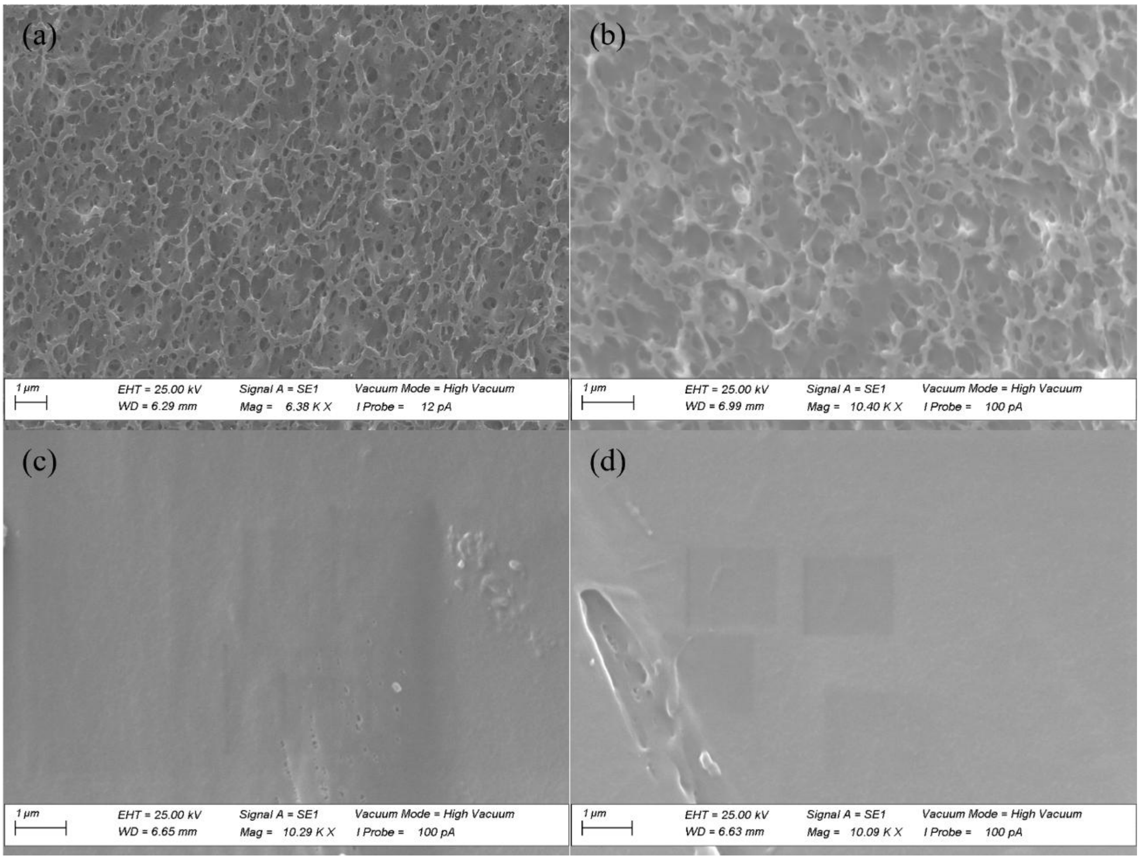

Figure 4.33: SEM images of (a) the inside of an untreated hollow fiber membrane, (b) the inside of a hollow fiber membrane treated with NO (1000 ppm) for 17h hours, (c) the outside of an untreated hollow fiber membrane, and (d) the outside of a hollow fiber membrane treated with NO (1000 ppm) for 17 hours at 10,000x magnification. The experiments were performed according to chapters 3.2.1 and 3.2.4.

For the PMP samples, images of the hollow fibers' inside and outside were recorded. Visible in the SEM images was the microporous structure inside the hollow fiber membranes (see Figure 4.33 (a), (b)). The images of the outside of the fiber show the smooth diffusion layer covering the outside surface of the fiber (see Figure 4.33 (c), (d)). The images of both the inside and the outside of the fiber clearly showed that the treatment with NO (1000 ppm) had no impact on the morphology of the polymer. The porous structure on the inside of the fiber remained unchanged, as did the diffusion layer on the outside. The visible gash in the diffusion layer was likely due to the handling of the hollow fiber (see Fig. 4.33 (d)).

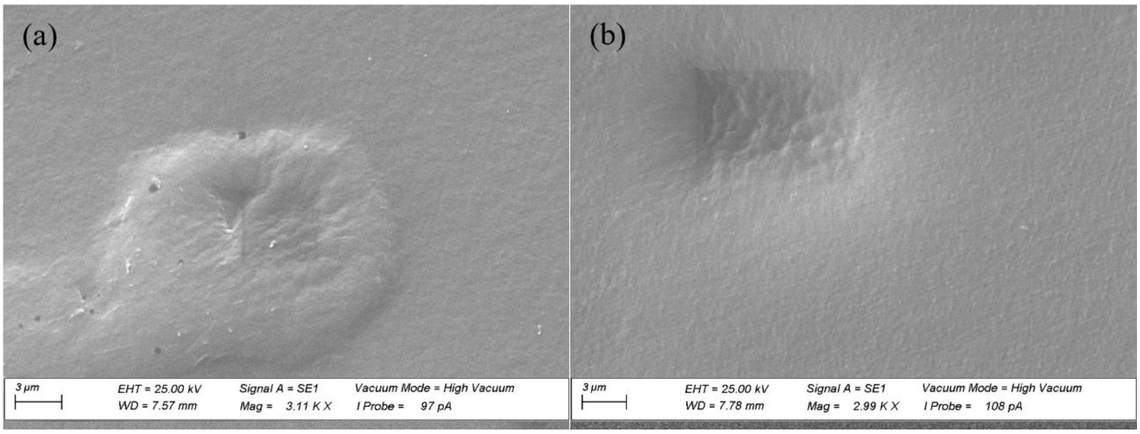

Figure 4.34: SEM images of (a) untreated MABS (inlet/outlet cap) and (b) MABS (inlet/outlet cap) treated with NO (1000 ppm) for 17 hours.

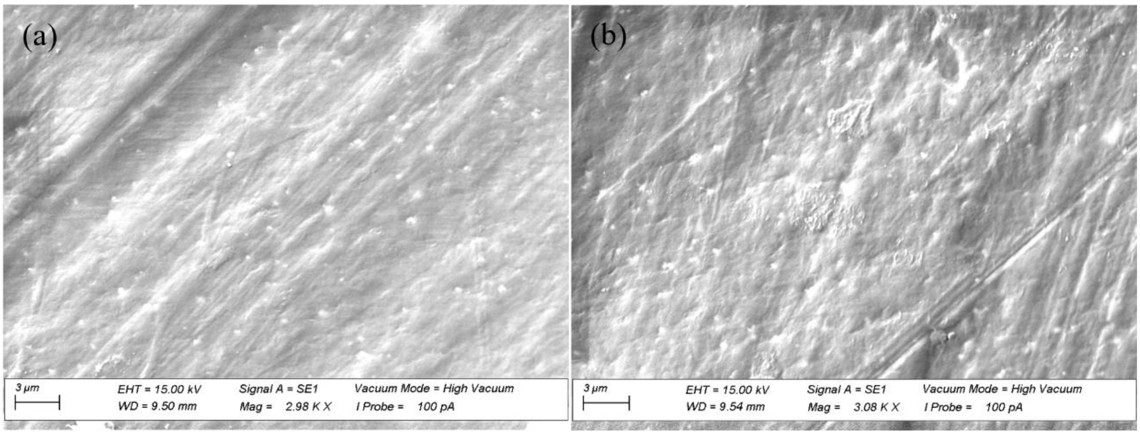

Figure 4.35: SEM images of (a) untreated MABS (gas cap) and (b) MABS (gas cap) treated with NO (1000 ppm) for 17 hours at 3000x magnification. The experiments were performed according to chapters 3.2.1 and 3.2.4.

MABS (inlet/outlet cap) was of secondary concern as it represented a major structural component of the oxygenator and is in constant contact with the patient's blood during the application of the oxygenator. It was, therefore, important that the material did not display changes to the material surfaces that would indicate either changes to the structural properties of the polymers or significant changes to the surface morphology of the materials. MABS (gas cap), on the other hand, was only of minor concern, as it represented a replaceable accessory to the body of the oxygenator, which is not in contact with the patient's blood during application. MABS (inlet/outlet cap) had an overall smooth surface (see Figure 4.34 (a)), while MABS (gas cap) showed clear signs of the machining done to the parts during production (see Figure 4.35 (a)). Neither material showed any significant change after the treatment with NO (see Figures 4.34 (b) and 4.35 (b).

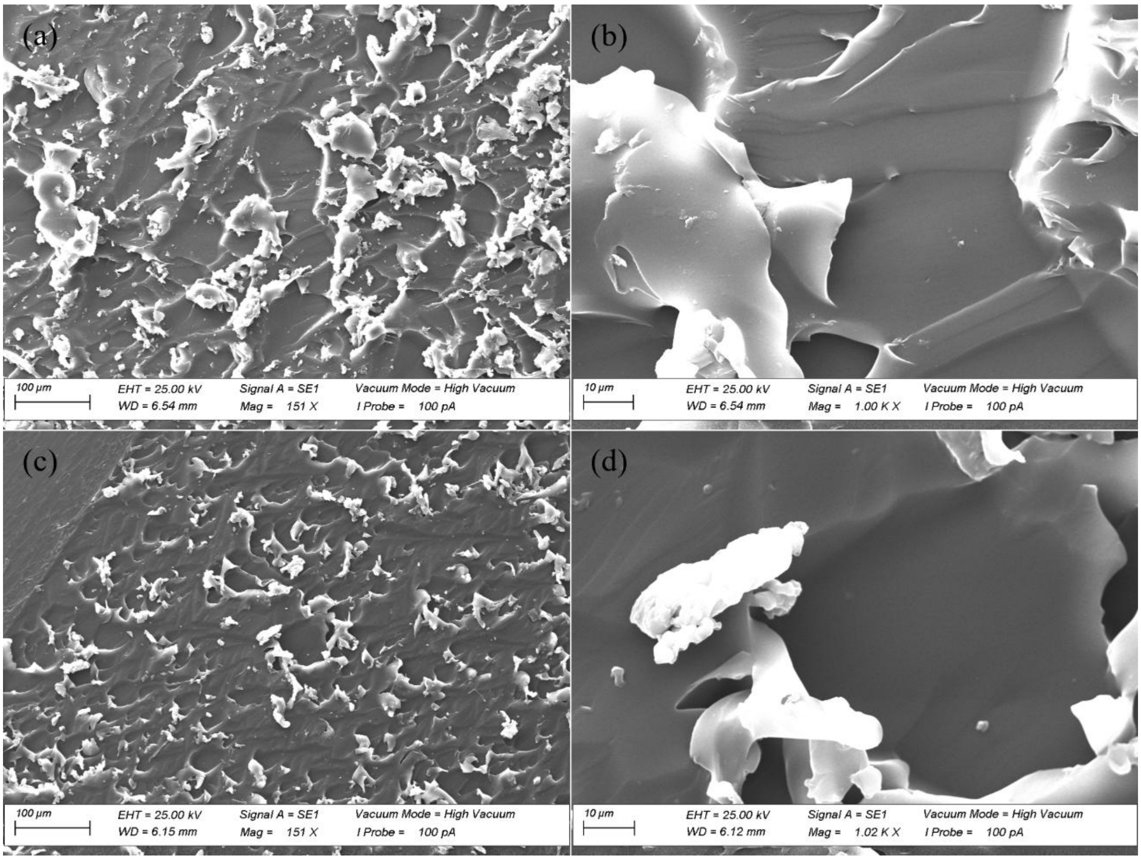

Figure 4.36: SEM images of (a) untreated PU at 151 times magnification, (b) untreated PU at 1000 times magnification, (c) PU treated with NO (1000 ppm) for 17 hours at 151x magnification, (d) PU treated with NO (1000 ppm) for 17 hours at 1000x magnification. The experiments were performed according to chapters 3.2.1 and 3.2.4.

Like MABS (inlet/outlet cap), PU represented a major structural component and a blood-contacting surface of the oxygenator. The investigated PU samples had a much rougher surface than the other materials (see Figure 4.36 (a)). This increased surface roughness resulted from the manufacturing process where PU was shaved down to the correct size. The surface facing the patient's blood is significantly smoother but inaccessible for sampling. Therefore, the rougher samples of cut off PU were chosen for practicality reasons. No change in surface morphology could be observed after the treatment with NO

(1000 ppm) (see Figure 4.36 (b)). This lack of change was also a strong indicator that chain scission and cross-linking reaction were not a significant part of the interaction between the treatment gas and the polymer. Significant degradation in the polymer structure would have led to visible changes in the surface morphology [318].

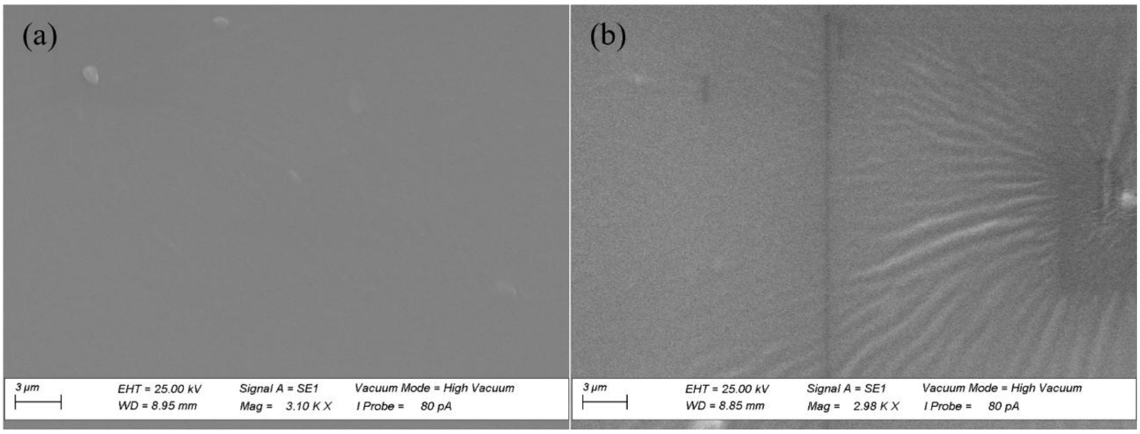

Figure 4.37: SEM images of (a) untreated PVC (gas hose) and (b) PVC (gas hose) treated with NO (1000 ppm) for 17 hours at 3000x magnification. The experiments were performed according to chapters 3.2.1 and 3.2.4.

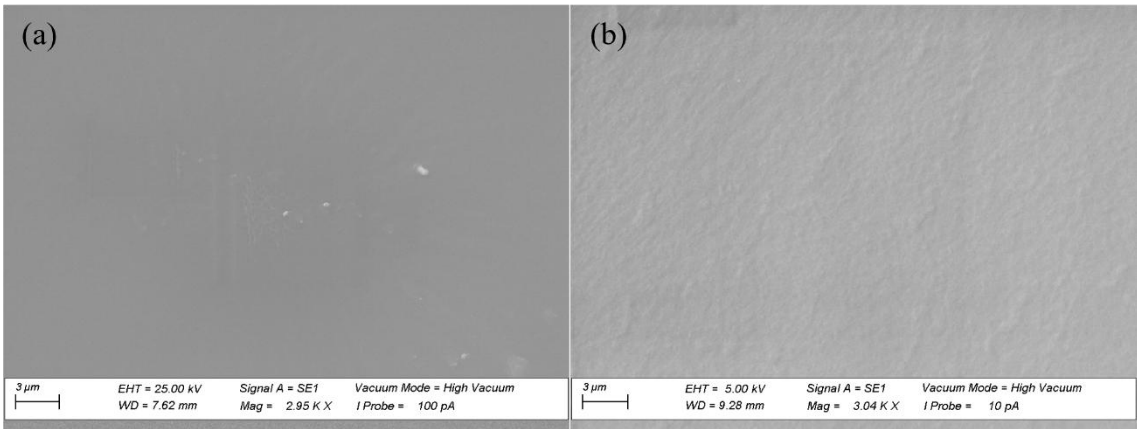

Figure 4.38: SEM images of (a) untreated PVC (blood hose) and (b) PVC (blood hose) treated with NO (1000 ppm) for 17 hours at 3000x magnification. The experiments were performed according to chapters 3.2.1 and 3.2.4.

The PVC samples were only of minor concern, as the gas hoses were only an accessory to the oxygenator, which would be quickly replaceable if needed. The blood hoses were also a minor concern, as they would not be in direct contact with the treatment gas mixture during the application of the oxygenator. The surface of the PVC (gas hose) sample was overall visually smooth (see Figure 4.37 (a)). The treated sample showed no change in surface morphology compared to the untreated sample. The wrinkles that formed on the surface were likely due to the electron beam being focused on one part of the sample for too long, visible on the right edge of the image (see Figure 4.37 (b)). The sample remained smooth on the undamaged left side of the image, indicating no significant changes happened due to the gas treatment. The PVC (blood hose) samples also showed a smooth surface in the untreated state (see Figure 4.38 (a)). Unlike the other materials (see Figures 4.33-4.37), the gas treatment with NO (1000 ppm) caused the surface of the material to become visibly slightly rougher (see Figure 4.38 (b)). The reason for this change in surface structure could have been the hydrolysis reaction of the plasticizer used in the PVC material, catalyzed by HNO_3 (see Chapter 4.2.1.1). Why the same effect was not visible for the PVC (gas hose) samples where the treatment gas also primarily reacted with the plasticizer remained unclear. As PVC (blood hose) is not in direct contact with the treatment gas mixture during the application of the oxygenator, this behavior should not have any consequences for the functionality of the oxygenator.

What the results of the SEM recordings showed overall was that the materials that are both in blood contact and in contact with the treatment gas mixture, namely PMP, MABS (inlet/outlet cap), and PU, were not affected by the NO treatment with regards to their surface morphology (see Figures 4.33, 4.34, and 4.36). This meant that the treatment with NO did not impact the materials' structural or blood-contacting properties. In the case of PMP, they showed that the gas treatment had no negative impact on the gas permeation properties of the material either. MABS (gas cap) and PVC (gas hose) samples showed no effect of the gas treatment either (see Figures 4.35 and 4.37). The only exception was the PVC (blood hose) samples, which showed a slight impact of the gas treatment on the surface roughness of the sample (see Figure 4.38). This effect, however, should have no relevance to the actual application conditions, as the blood hoses have no direct contact with the sweep gas of the oxygenator. These results showed that, overall, the addition of NO to the sweep gas of the oxygenator should have no negative impacts on its functionality or the blood-contacting properties of the polymer surfaces.

4.5 Contact Angle and Zeta Potential Measurements

Static and dynamic contact angle measurements and zeta potential measurements were performed to understand how the gas treatment with NO affected the surface properties. Surface hydrophilicity was of interest for the application of these materials, as an increase in surface hydrophilicity would improve the blood-contacting behavior of the oxygenator surfaces, leading to better blood compatibility [330–332].

4.5.1 Static Contact Angle Measurements

The static contact angle measurements were performed with MABS (inlet/outlet cap), MABS (gas cap), and PU, as these were the only materials where a flat sample geometry was achievable. The experiments were performed according to chapters 3.2.1 and 3.2.6.1.

4.5.1.1 Treatment with NO (10,000 ppm)

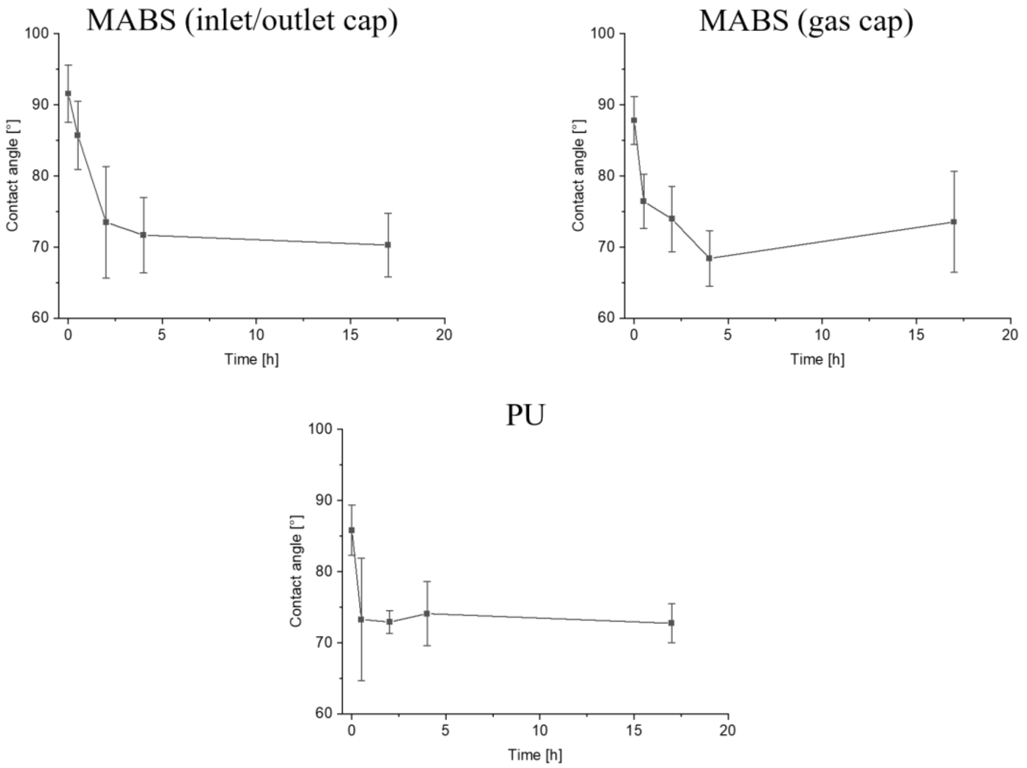
MABS (inlet/outlet cap)

MABS (gas cap)

PU

Figure 4.39: Static contact angle measurements of (a) MABS (inlet/outlet cap), (b) MABS (gas cap), and (c) PU treated with NO (10,000 ppm) for up to 17 hours. The experiments were performed according to chapters 3.2.1 and 3.2.6.1.

At an NO concentration of 10,000 ppm, all three samples showed a clear tendency towards lower contact angles with increasing treatment time. The contact angle for MABS (inlet/outlet cap) decreased from 91.6° to 70.3° (see Figure 4.39 (a)), while for MABS (gas cap), the angle decreased from 87.8° to 73.6° (see Figure 4.39 (b)). For PU, the contact angle decreased from 85.8° to 72.7° (see Figure 4.39 (c)). The contact angle curves of all three samples showed a steep initial decrease in contact angle, leveling off after four hours in the case of both MABS. The PU sample reached saturation after only 30 minutes of exposure. The conclusion from these results was that the formation of the nitro- and nitrate ester functional groups and the deposition of the HNO_3 on the polymer surface discussed in chapter 4.2.1.1 led to an increase in surface hydrophilicity.

Following these results, the contact angle measurements were expanded to test the stability of these effects. As already seen in chapter 4.2.3.1, the signal connected to the functional groups and HNO_3 showed a high degree of stability. The goal of repeating the contact angle measurements of the samples treated with 10,000 ppm of NO after one month was to see whether this stability visible in the FTIR-ATR spectra (see Figure 4.20) would translate into a permanent change in the surface properties of the polymers.

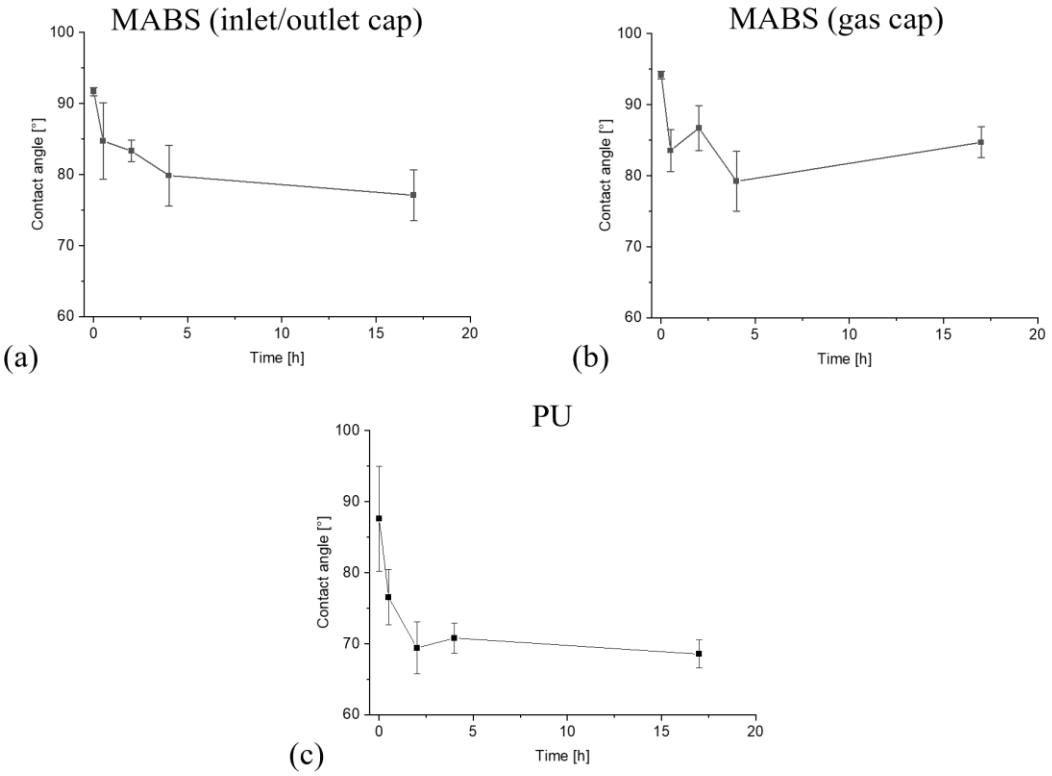

Figure 4.40: Static contact angle measurements of (a) MABS (inlet/outlet cap), (b) MABS (gas cap), and (c) PU treated with NO (10,000 ppm) for up to 17 hours after a waiting period of one month. The experiments were performed according to chapters 3.2.1 and 3.2.6.1.

The waiting period of one month resulted in a less pronounced drop in the contact angles in the case of both MABS samples (see Figure 4.40 (a), (b)). For the MABS (inlet/outlet cap), the contact angle dropped from 91.7° to 77.1° (see Figure 4.40 (a)). The total drop in contact angle, therefore, decreased from 21.3° directly after the gas treatment (see Figure 4.40 (a)) to 14.6° after the waiting period (see Figure 4.40 (a)). For MABS (gas cap), the contact angle dropped from 94.2° to 84.7°, with the difference in contact angle decreasing from 14.2° to 9.5° after the waiting period. For PU, the contact angle dropped from 87.6° to 68.6°, meaning the drop in contact angle increased slightly from 23.1° to 29° after the waiting period. These results aligned with the stability measurements conducted via FTIR-ATR (see Figure 4.20), with all samples retaining a significant drop in contact angle over increasing gas treatment time (see Figure 4.40).

The stability of the gas treatment effect was further analyzed by submersing the samples in Millipore water for 24 hours, drying them in a desiccator for another 24 hours, and analyzing them afterward.

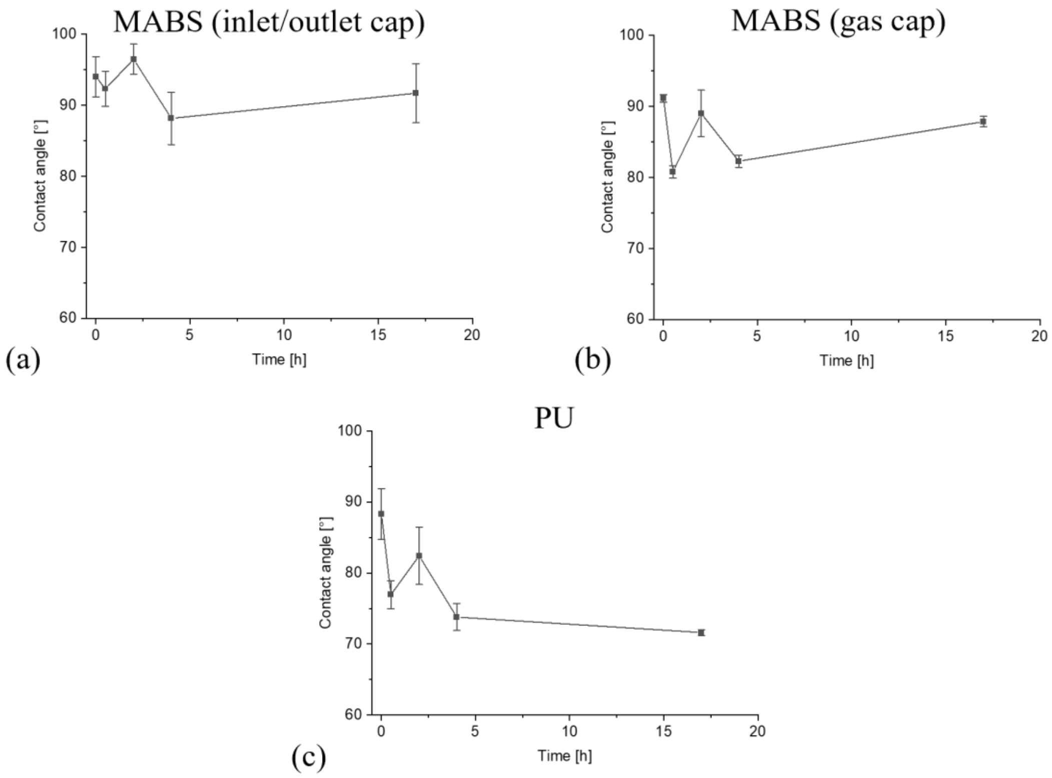

Figure 4.41: Static contact angle measurements of (a) MABS (inlet/outlet cap), (b) MABS (gas cap), and (c) PU treated with NO (10,000 ppm) for up to 17 hours after a waiting period of one month and submersion in Millipore water for 24 hours. The experiments were performed according to chapters 3.2.1 and 3.2.6.1.

The submersion in Millipore water resulted in the complete disappearance of the contact angle decrease for both MABS samples (see Figure 4.41 (a), (b)). PU retained part of the contact angle decrease with the angle dropping from 88.3° to 71.6° (see Figure 4.41 (c)). This meant the overall contact angle drop decreased from 23.1° and 29° for the previous measurements (see Figures 4.39 and 4.40) to 16.7° after the water submersion (see Figure 4.40). The results obtained after the water submersion indicated that some of the compounds formed on the surface of the polymer samples due to the gas treatment did not remain on the sample's surface after contact with water. The compound most likely affected by the submersion in water were the HNO_3 molecules adsorbed to the surface of the polymer, as that interaction is much weaker than the covalent bonds of the nitro and nitrate ester functional groups. This was also shown in chapter 4.2.3, with the signal corresponding to the HNO_3 molecules being less stable over extended periods than the nitro and nitrate ester signals. The strong impact of the water submersion on the contact angle curves, therefore, indicated that the HNO_3 molecules were likely the main contributors to the increase in surface hydrophilicity caused by the gas treatment with NO.

Under application conditions in contact with blood, the effect seen here with the materials in contact with air would likely be lessened significantly. The HNO_3 molecules mainly responsible for the increase in surface hydrophilicity would not adhere to the surface in significant numbers due to the constant liquid flow. The reactions of the treatment gas with the polymer would also likely be inhibited significantly due to the NO being consumed by the blood before it reaches polymers such as MABS and PU. So overall, while this effect on the surface hydrophilicity was observable under lab conditions, it would likely be much less pronounced under application conditions. A potential risk of the dissolution of the HNO_3 molecules into the surrounding liquid would be its influence on the pH value of the liquid. However, given the application concentration of NO of below 100 ppm, the already mentioned decreased effect of NO on the surfaces while in contact with blood, and the substantial buffering capacity of blood at 38.5 mEq/L/pH, this should not be an issue during the actual application [333]. The impact of the addition of NO to the sweep gas on the pH value of the liquid in the oxygenator was examined in more detail in chapter 5.2.2.

4.5.1.2 Treatment with NO (1000 ppm and 80 ppm)

Static contact angle measurements were also conducted at 1000 and 80 ppm of NO, analogous to the samples treated with NO (10,000 ppm) (see Chapter 4.5.1.1).

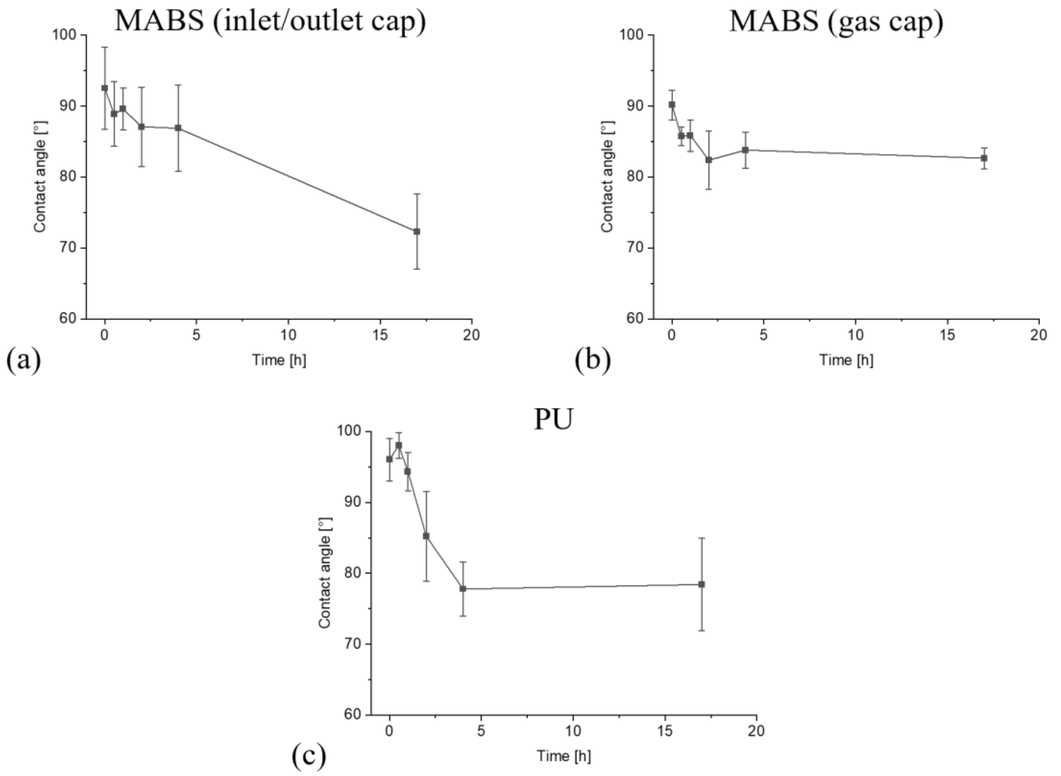

Figure 4.42: Static contact angle measurements of (a) MABS (inlet/outlet cap), (b) MABS (gas cap), and (c) PU treated with NO (1000 ppm) for up to 17 hours. The experiments were performed according to chapters 3.2.1 and 3.2.6.1.

Using 1000 ppm of NO resulted in a slower decline of the contact angle for MABS (inlet/outlet cap) compared to the treatment with NO (10,000 ppm) (see Figure 4.39 (a)). The contact angle decreased almost linearly by 20.2°, from 92.5° to 72.3° (see Figure 4.42 (a)). For MABS (gas cap), the decrease in contact angle was strongly reduced compared to the treatment with NO (10,000 ppm) (see Figure 4.39 (b)), with a total reduction of 7.4° from 90.1° to 82.7° (see Figure 4.42 (b)). PU showed essentially the same behavior as with NO (10,000 ppm), with a decrease of 17.7° from 96.1° down to 78.4° (see Figure 4.42 (c)). The total reduction of the contact angle for MABS (inlet/outlet cap) and PU was comparable to the drop caused by treatment with NO (10,000 ppm), although in both cases, the decrease took longer with 1000 ppm than with 10,000 ppm (see Figures 4.39 (a), (c) and 4.42 (a), (c)). The contact angle decrease for MABS (gas cap), on the other hand, was just overall weaker due to the drop in NO concentration (see Figures 4.39 (b) and 4.42 (b)).

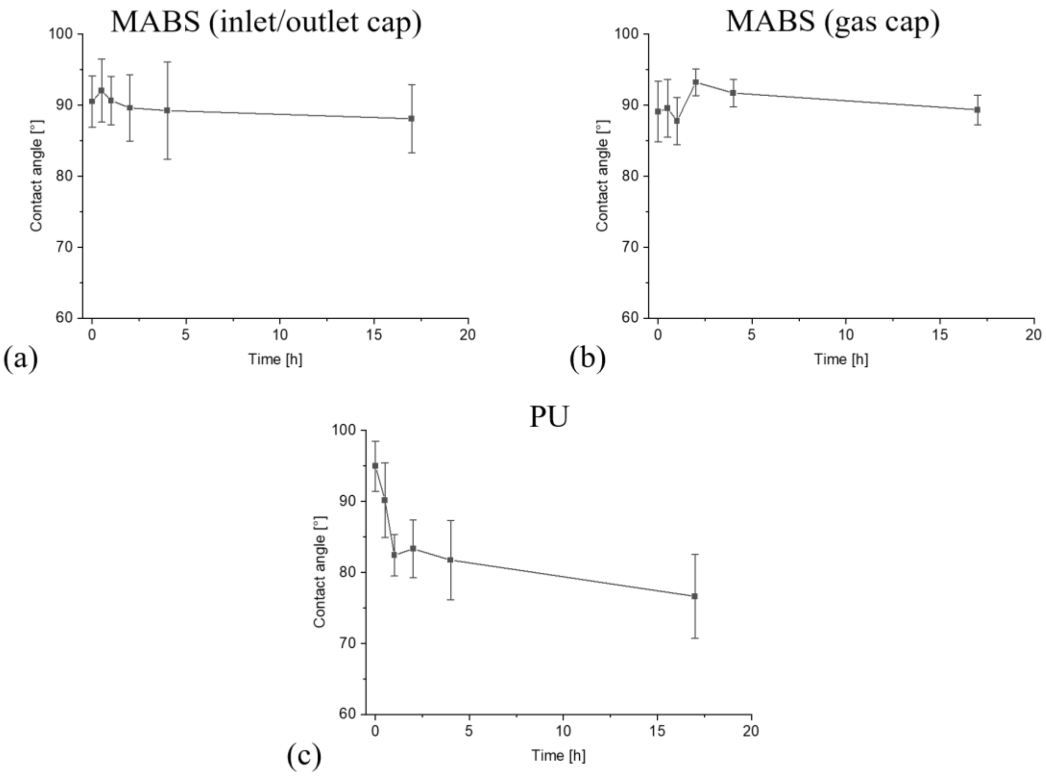

Figure 4.43: Static contact angle measurements of (a) MABS (inlet/outlet cap), (b) MABS (gas cap), and (c) PU treated with NO (80 ppm) for up to 17 hours. The experiments were performed according to chapters 3.2.1 and 3.2.6.1.

Reducing the concentration of NO further to 80 ppm resulted in both MABS samples displaying a constant contact angle independent of gas treatment duration (see Figure 4.43 (a), (b)). PU, however, still showed a noticeable decrease in contact angle despite the lower gas concentration. Overall, the contact angle decreased from 95.0° to 76.6°, a drop of 18.4°, comparable to the drop at higher gas concentrations. The decrease of the contact angle was slower than at 10.000 and 1000 ppm (see Figures 4.39 (c), 4.42 (c) and 4.43 (c)).

The results with NO (80 ppm) and NO (1000 ppm) showed that PU had a far higher affinity for the deposition of HNO_3 molecules compared to the MABS samples, assuming that HNO_3 molecules were the major contributors to the drop in contact angle (see Chapter 4.5.1.1). The results also showed that effects on the surface properties of the materials persisted even at concentrations as low as 80 ppm.

4.5.1.3 Treatment with NO_2 (1000, 500, and 50 ppm)

Contact angle measurements were also conducted using samples treated with various concentrations of NO_2, analogous to the FTIR-ATR measurements.

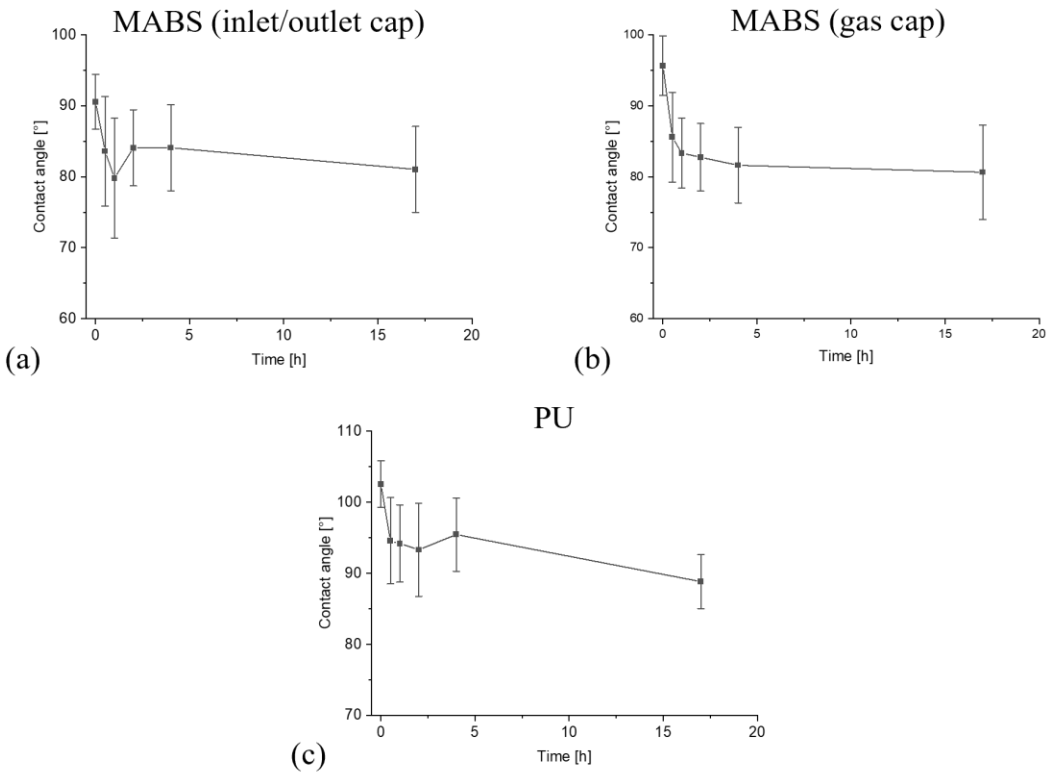

Figure 4.44: Static contact angle measurements of (a) MABS (inlet/outlet cap), (b) MABS (gas cap), and (c) PU treated with NO_2 (1000 ppm) for up to 17 hours. The experiments were performed according to chapters 3.2.1 and 3.2.6.1.

The treatment of the samples with NO_2 decreased contact angles for all tested materials, like the treatment with NO. For MABS (inlet/outlet cap), the contact angle decreased by 19.5° from 90.6° to 81.1° (see Figure 4.44 (a)). The contact angle for MABS (gas cap) decreased by 15.1° from 95.7° down to 80.6° (see Figure 4.43 (b), and for PU by 23.7° from 102.5° to 88.8° (see Figure 4.44 (c)). The impact of the gas treatment with NO_2 (1000 ppm) was weaker than the results of the same concentration of NO (see Figure 4.42). The drop in contact angle for MABS and PU was significantly smaller, and the decrease happened more slowly in the case of PU. For MABS (gas cap), the drop in contact angle was slightly larger than with NO (1000 ppm) (see Figures 4.42 (b) and 4.44 (b)). Decreasing the NO_2 concentration to 500 ppm resulted in similar results to 1000 ppm (see Figure 8.12). Reducing the concentration of NO_2 further to 50 ppm resulted in little or no drop in contact angle for MABS (gas cap) and PU (see Figure 8.13 (b), (c)). The contact angle for MABS (inlet/outlet cap) meanwhile still showed a decrease comparable to the results at 1000 ppm (see Figures 8.13 (a) and 4.44 (a)).

Treating the polymer samples with NO_2 had similar effects to the treatment with NO. The gas treatment caused the contact angle to lower with increasing treatment times (see Figures 4.44, 8.12, and 8.13). The impact of NO_2 was overall slightly weaker than comparatively concentrated NO. The material most affected by NO was PU, while with NO_2, it was MABS (inlet/outlet cap). The exact reason for the two gases' behavior differences is unknown. A likely explanation would be the significant uncertainties of the analytical method represented by the comparatively sizeable standard deviations present in the corresponding figures.

4.5.2 Dynamic Contact Angle and Zeta Potential Measurements

The selection of analytical methods was expanded beyond FTIR-ATR and static contact angle measurements for samples treated with NO (1000 ppm). This expansion included the dynamic contact angle and streaming potential measurements discussed in this chapter. Due to the limited measurement time and extensive preparations necessary for both analytical methods, samples were limited to the materials in direct blood contact during the application of the oxygenator, as well as a single NO concentration of 1000 ppm. The materials, therefore, included PMP, MABS (inlet/outlet cap), and PU. The experiments were performed according to chapters 3.2.1, 3.2.6.2, and 3.2.7.

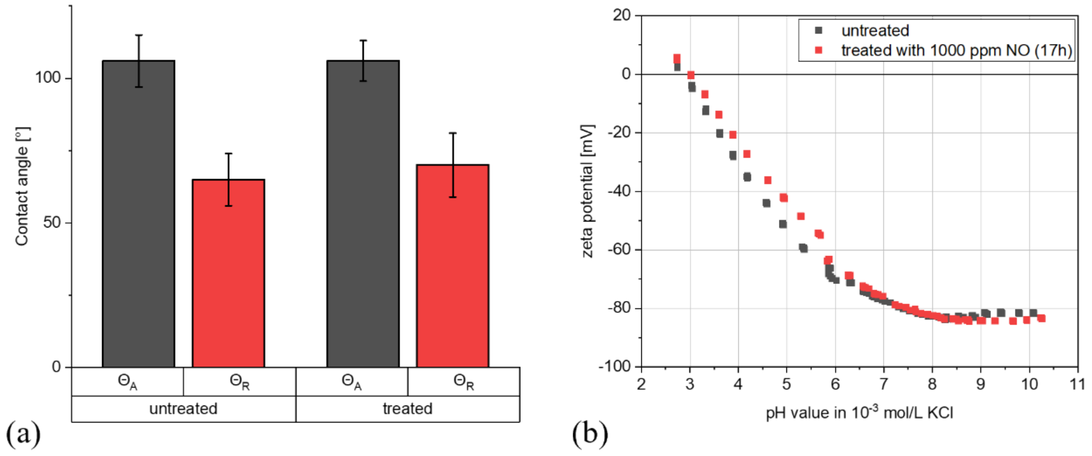

Figure 4.45: (a) Dynamic contact-angle measurements of PMP. Represented are the average results for both the untreated samples and samples treated with NO (1000 ppm) for 17 hours. The gray bars represent the advancing contact angle θ_A, and the red bars represent the receding contact angle θ_R. (b) Zeta potential measurements of PMP. Visible are the pH-dependent curves of an untreated sample (grey) and a sample treated with NO (1000 ppm) for 17 hours (red). The experiments were performed according to chapters 3.2.1, 3.2.6.2, and 3.2.7.

For PMP, neither the contact angle nor the zeta potential measurements showed significant changes due to the gas treatment (see Figure 4.45). The advancing angle θ_A showed a slight but insignificant change from 65° to 70°, with a standard deviation of 9° and 11°, respectively. Treated and untreated samples showed a contact angle hysteresis $(\theta_A - \theta_R)$ of 41° and 36° (see Figure 4.45 (a)).

The zeta potential measurements resulted in nearly identical values above pH 6, plateauing at approximately -85 mV (see Figure 4.45 (b)). A slight difference between the treated and untreated samples could be observed in the lower pH ranges, with the treated samples resulting in slightly higher values across the lower pH range. This effect was most likely caused by the samples' inhomogeneities, not the NO treatment. At the IEP, both samples converged again at a pH value of approximately three.

These results aligned with the FTIR-ATR measurements at the same gas concentration, which showed no changes in the spectra either (see Figure 4.10 (a)).

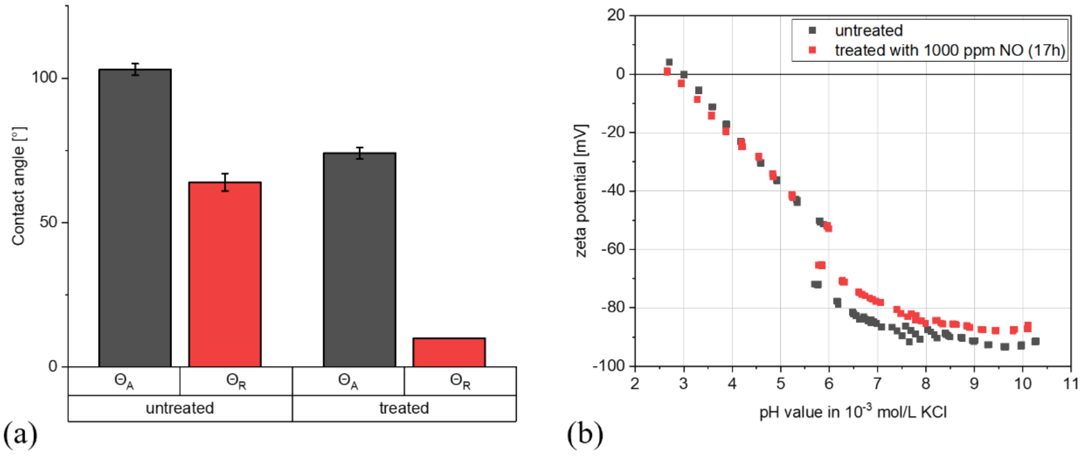

Figure 4.46: (a) Dynamic contact-angle measurements of MABS. Represented are the average results for both the untreated samples and samples treated with NO (1000 ppm) for 17 hours. The gray bars represent the advancing angle θ_{A}, and the red bars the receding angle θ_{R}. (b) Zeta-potential measurements of MABS. Visible are the pH-dependent curves of an untreated sample (grey) and a sample treated with NO (1000 ppm) for 17 hours (red). The experiments were performed according to chapters 3.2.1, 3.2.6.2, and 3.2.7.

For MABS (inlet/outlet cap), the contact angle measurements showed a significant decrease in both the advancing angle θ_A and the receding angle θ_R. θ_A decreased from 103° to 74° due to the gas treatment, while θ_R decreased from 64° to below 10°. This also meant that the contact angle hysteresis increased from 39° to more than 64° (see Figure 4.46 (a)).

The zeta potential measurements of MABS (inlet/outlet cap) showed no significant change between the untreated and treated samples. Below pH six, both curves were completely identical, reaching an IEP of roughly 3. Both samples reached a minimum value of around -90 mV, with the treated samples displaying slightly higher values than the untreated sample above pH 6 (see Figure 4.46 (b)). This difference in potential values was not significant and was caused by sample inhomogeneities, like with PMP. These sample inhomogeneities likely also caused the jump in values between the acidic and the basic measurements (see Figure 4.45 (b)).

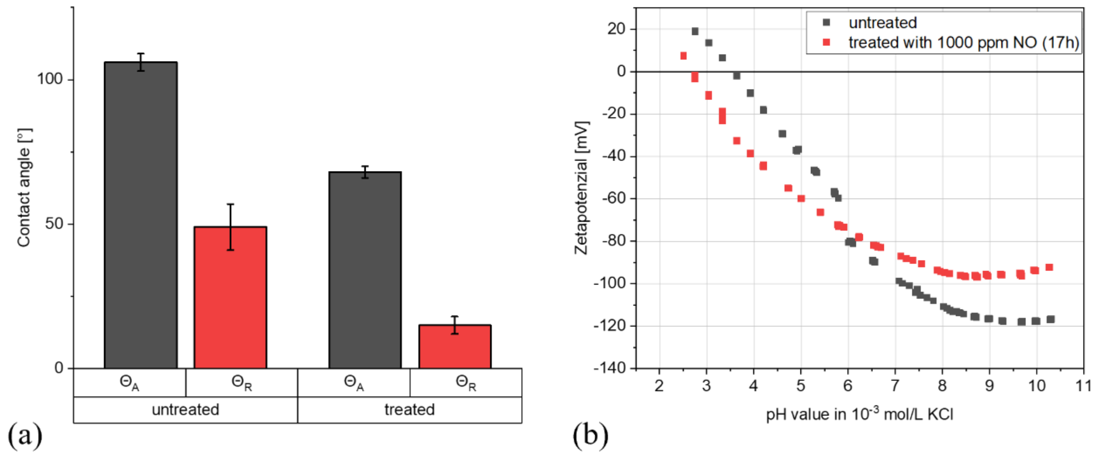

Figure 4.47: (a) Contact-angle measurements of PU. Represented are the average results for both the untreated samples and samples treated with NO (1000 ppm) for 17 hours. The gray bars represent the advancing angle θ_A, and the red bars the receding angle θ_R. (b) Zeta-potential measurements of PU. Visible are the pH-dependent curves of an untreated sample (grey) and a sample treated with NO (1000 ppm) for 17 hours (red). The experiments were performed according to chapters 3.2.1, 3.2.6.2, and 3.2.7.

The contact angle measurements for PU showed a significant decrease in both θ_A and θ_R caused by the gas treatment. θ_A decreased from 106° to 68° and θ_R from 49° to 15° (see Figure 4.47 (a)). Unlike MABS (inlet/outlet cap) (see Figure 4.47 (a)), there was no significant increase in contact angle hysteresis. Instead, contact angle hysteresis decreased slightly from 57° to 53° after the gas treatment (see Figure 4.47 (a)).

The zeta potential measurements of PU showed a significant difference between treated and untreated samples, unlike both PMP (see Figure 4.45 (b)) and MABS (inlet/outlet cap) (see Figure 4.46 (b)). The curve of the untreated PU samples decreased steeply with rising pH values, reaching a final potential of about -120 mV with little to no plateau formation at high pH values. The IEP was located at a pH of 3.6. The gas treatment resulted in a flattening of the curve, with the IEP shifting to a pH of 2.7. The curve also had a more pronounced plateau, with a minimum potential of around -100 mV (see Figure 4.47 (b)).

The dynamic contact angle measurements aligned with the results gathered from the FTIR-ATR measurements (see Figure 4.10 (a), (b), and (d)), with PMP showing no impact, while the gas treatments resulted in a significant decrease in both θ_A and θ_R for MABS (inlet/outlet cap) and PU (see Figures 4.45 (a), 4.46 (a), and 4.47 (a)). These results also fit with the static contact angle measurements conducted at 10,000 and 1000 ppm (see Figures 4.39 and 4.42), showing significant decreases in contact angle caused by the gas treatment. The conclusion from this decrease in contact angle was that the formation of nitro and nitrate ester groups and the adsorption of HNO_3 molecules onto the surface of the polymers led to an increase in surface hydrophilicity. The additional piece of information that the dynamic contact angle measurements provided compared to the static measurements was the contact angle hysteresis. Contact angle hysteresis could have been caused by various factors, with swelling, surface roughness, and chemical heterogeneity being of interest in this case [242, 246, 253, 334]. The results obtained from the dynamic contact angle measurements showed a significant increase in contact angle hysteresis for MABS (inlet/outlet cap) (see Figure 4.46 (a)) compared to PU, where it remained constant after the gas treatment, despite the overall drop in contact angle (see Figure 4.47 (a)). Of the factors mentioned above influencing the contact angle hysteresis, swelling, and surface roughness could be discounted as both factors should be constant between the samples. This left the chemical heterogeneity of the samples as the likely explanation for the increase in hysteresis seen for MABS (inlet/outlet cap). MABS was a copolymer consisting of four different monomers (methyl methacrylate, acrylonitrile, butadiene, and styrene) (see Figure 2.10). As discussed in chapters 2.3.4 and 4.2.1.1, the most likely points of attack for NO_2 and HNO_3 were the double bonds of the butadiene monomers, the phenyl group of the styrene monomers, and the ester groups of the methyl methacrylate. On the other hand, the acrylonitrile monomers lacked any suitable structural features to react with either NO_2 or HNO_3. This meant that reactions with the treatment gas only occurred on three out of four monomers. This led to increased chemical heterogeneity as the functional groups were not uniformly distributed across the polymer chain. The adsorption of HNO_3 also likely happened preferentially at monomers with polar functional groups such as methyl methacrylate, increasing chemical heterogeneity further. PU, on the other hand, had a more defined structure with alternating between TMP monomers and MDI-glycol prepolymers (see Figure 2.11). Potential reaction sites were free hydroxy groups of TMP and the aromatic rings of MDI. This meant that the functional groups formed due to the gas treatment were distributed more evenly across the polymer chain. The same logic applies to the HNO_3 molecules, which were likely adsorbed more evenly across the polymer surface. This, in turn, led to the chemical heterogeneity not increasing and to the contact angle hysteresis staying mostly constant after the gas treatment (see Figure 4.47 (a)).

The zeta-potential measurements of PMP showed no change caused by the gas treatment (see Figure 4.45 (b)), in agreement with both the FTIR-ATR and the contact angle measurements (see Figures 4.10 (a) and 4.45 (a)). MABS (inlet/outlet cap) showed no impact of the gas treatment on the zeta potential curves either (see Figure 4.46 (b)) despite the clearly visible effect of the gas treatment in both the FTIR-ATR and the contact angle measurements (see Figures 4.10 (b) and 4.46 (a)). PU was the only sample that showed a significant impact from the gas treatment, with the potential curve becoming flatter, indicating a more hydrophilic surface, and the IEP shifting from 3.6 to 2.7, indicating the formation of acidic compounds on the sample surface (see Figure 4.47 (b)) [265, 335]. The combination of these effects on the potential curves suggested that the adsorption of HNO_3 molecules to the surface of the polymer was the major influencing factor rather than the formation of nitro and nitrate ester groups. The difference between MABS (inlet/outlet cap) and PU regarding the zeta potential curves was likely explained by a difference in the surface concentration of HNO_3. The results of the liquid submersion experiments (see Figures 4.23 (a), (c), 4.25 (a), (c)) showed that the signal at 3480/3443 cm^{-1} was more pronounced for PU than for MABS (inlet/outlet cap). PU was also the sample material that showed the most substantial drop in contact angles throughout the static contact angle measurements (see Figures 4.39-4.43 (c)), an effect also mainly attributed to the adsorption of HNO_3 molecules (see Chapter 4.5.1.1). The impact of the gas treatment on the surface hydrophilicity of PU was the longest-lasting compared to the other materials (see Figures 4.40 and 4.41). This meant that the decrease in surface concentration of HNO_3 throughout the streaming potential measurements was less pronounced for PU than for MABS. Based on these results, the likely explanation for the different zeta potential results was that the HNO_3 concentration on the MABS surface was too low to influence the potential curve. In contrast, the surface concentration with PU was high enough to have a significant impact. These results aligned with the interpretation made in chapter 4.5.1.1 that the HNO_3 molecules deposited on the surface of the polymers were the main contributor to the reduction of the contact angles.

Overall, both the static and dynamic contact angle and the zeta potential measurements indicated an increase in surface hydrophilicity for both MABS and PU, likely improving the blood-contacting properties of these materials. Existing research suggested that this improvement took the shape of increased thromboresistance, which would be a positive indicator regarding the oxygenator lifespan [330–332]. However, further experiments would be necessary to confirm these findings for the polymers investigated in this thesis. This effect should also be attenuated significantly under application conditions due to the constant blood flow across these materials' surfaces by washing away the HNO_3

molecules and consuming at least part of the NO gas before it reaches the polymer surfaces, as already discussed in chapter 4.5.1.1.

5. Results and Discussion – Impact of NO Treatment on Hemolysis

The second smaller chapter of the “Results and Discussion” part of this thesis focused on the potential influence of NO on the oxygenator's hemolytic properties. This influence was analyzed using UV/Vis spectroscopy, vapor pressure osmometry, and pH measurements. The concentration of NO used in this chapter was reduced to 40 ppm to approximate the actual final application concentration more closely.

5.1 Impact of NO Treatment on the Optical Appearance of the Blood Samples

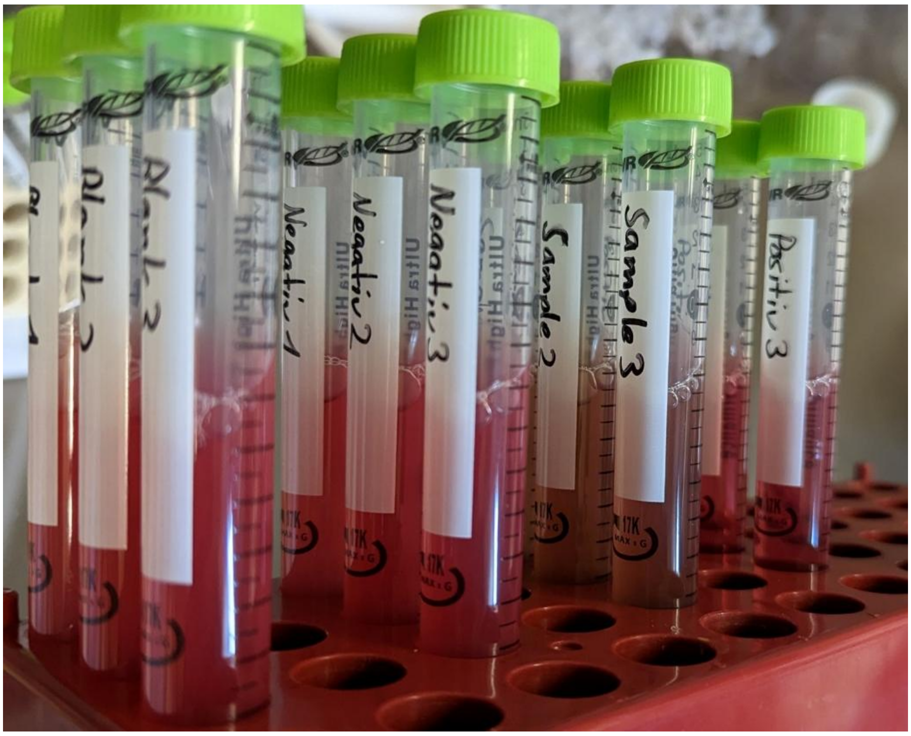

Figure 5.1: Photograph of the extraction and control samples after mixing with diluted blood and heating to 37 °C for three hours (see Chapter 3.3.2). The samples from left to right were the blank control samples, the negative control samples, the extraction samples, and the positive control samples. NO (40 ppm) was added to the perfusion gas.

The control and extraction samples resulted in several distinct optical appearances after completing both the extraction process and the mixing process with diluted blood. The blank and negative control samples were bright red and turbid. The positive control samples had a very similar red color while being completely clear. The extraction samples were identical in appearance to the blank and negative control samples when using just air as the perfusion gas. Adding NO to the perfusion gas resulted in the extraction samples with a distinct brownish color (see Figure 5.1). The reason for the color change was likely Met-Hb formation caused by nitrates and nitrites present in the extraction samples due to the perfusion with NO. The formation of Met-Hb did not affect the analysis of the extraction samples, as Drabkin’s method already utilized it as an intermediary. The formation of Met-Hb was one of the potential concerns for the application of NO to ECMO circuits. However, the results visible here (see Figure 5.1) should not be taken as an indication of methemoglobinemia, as the experiments were conducted with blood outside of a functioning organism, which could counteract the Met-Hb formation with Met-Hb reductase [130, 336].

5.2 Impact of the NO Treatment on the Oxygenator’s Hemolytic Properties

The impact of NO on the oxygenator's hemolytic properties was determined using UV/Vis spectroscopy as the primary analytical method, with VPO and pH measurements as supplementary methods. The experiments were performed according to chapters 3.3.1, 3.3.2, and 3.3.3.

5.2.1 UV/Vis Spectroscopy

5.2.1.1 Calibration

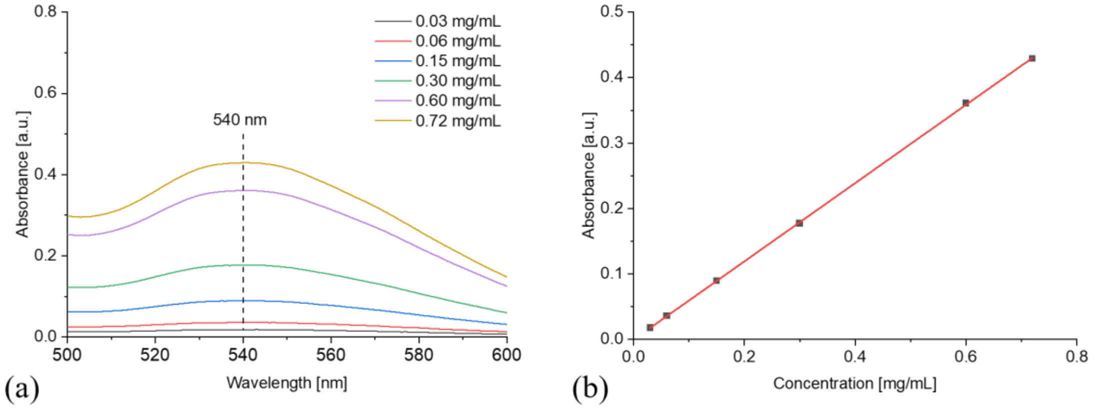

Figure 5.2: (a) UV/Vis spectra of the calibration measurements with Hb concentrations between 0.03 and 0.72 g/L. (b) Signal height at 540 nm plotted against the Hb concentration. The experiments were performed according to chapters 3.3.1.1, 3.3.1.2, and 3.3.3.1.

Calibration measurements were performed using lyophilized porcine Hb (see Chapter 3.3.1.2). The calibration samples showed a linear relationship between the Hb concentration and the absorbance at 540 nm (see Figure 5.2). The final calibration curve was defined by the following equation:

$$\mathrm{Absorbance(sample)} = 0.59818\frac{\mathrm{mL}}{\mathrm{mg}} \cdot \mathrm{c(Hb)} - 3.14441 \cdot 10^{-4} \qquad (70)$$

5.2.1.2 Determination of Total and Plasma Hb Concentrations

Each batch of pig's blood was analyzed for the total concentration of Hb in the blood and the concentration of free Hb in the blood plasma directly after receiving the blood sample to ensure its suitability for the following experiments. The aim was to mimic the parameters established by the previous investigation. There, the total Hb concentration range was set between 110 and 180 g/L, and the limit for free Hb at two g/L (see Chapter 3.3.1.3) [295].

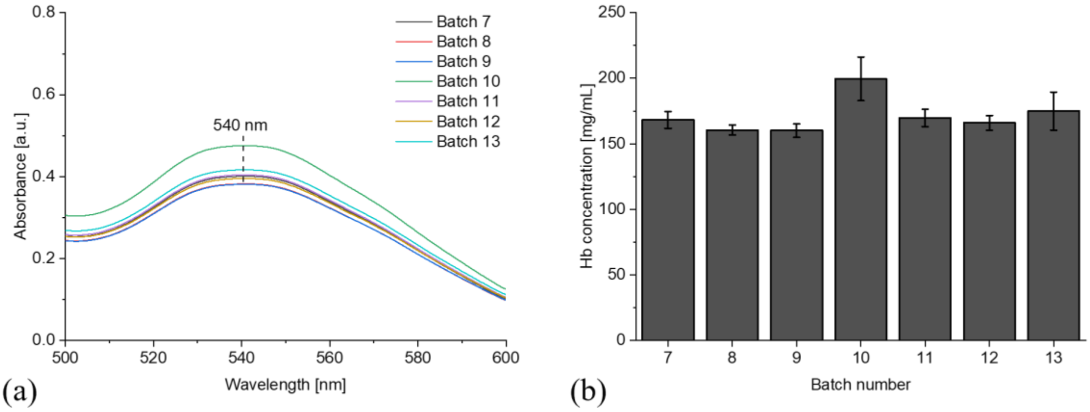

Figure 5.3: (a) UV/Vis signal at 540 nm of determining the total Hb concentration of the blood batches seven to thirteen. (b) Total Hb concentrations of the blood batches seven to 13. The experiments were performed according to chapters 3.3.1.1, 3.3.1.3, and 3.3.3.1.

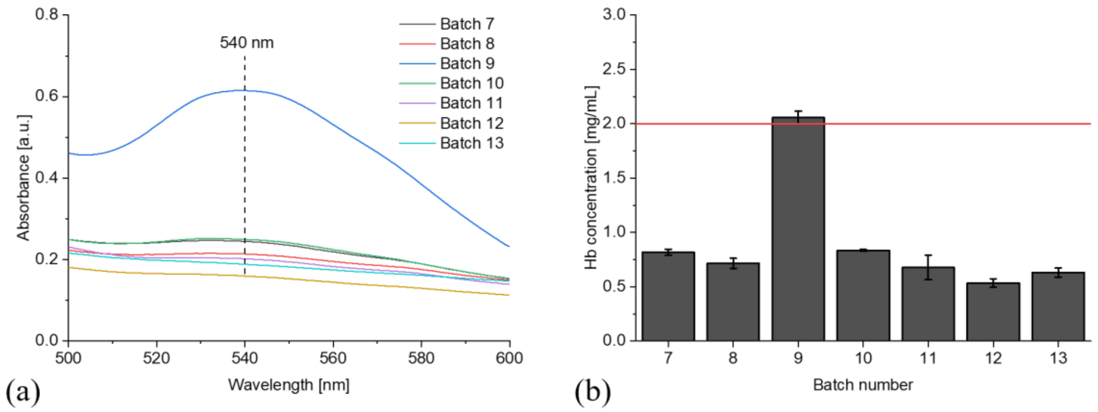

Figure 5.4: (a) UV/Vis signal at 540 nm of determining the plasma Hb concentration of the blood batches seven to thirteen. (b) Plasma Hb concentrations of the blood batches seven to 13, with the upper limit of 2 g/L indicated as a red line. The experiments were performed according to chapters 3.3.1.1, 3.3.1.2, and 3.3.3.1.

The blood batches ranged from around 160 to 175 g/L of total Hb concentration, except for batch ten, with 200 g/L (see Figure 5.3 (b)). This meant that all batches were broadly within an acceptable range of Hb concentration, which would indicate healthy source animals [337]. Differences in concentration between batches were equalized through the following dilution step (see Chapter 3.3.1.3). The analysis of the free Hb concentration showed acceptable values for all batches except batch nine, which had a free Hb concentration of 2.1 g/L (see Figure 5.4 (b)). Therefore, no experiments were performed using blood from batch nine. The remaining batches had free Hb contents well below one g/L and were suitable for the experiments.

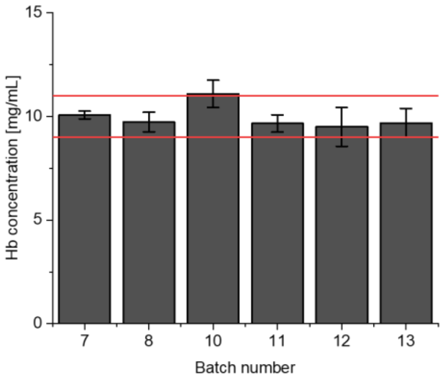

Figure 5.5: Blood Hb concentration after dilution with CMF-DPBS for batches seven, eight, ten, eleven, twelve, and 13. The lower limit of 9 g/l and the upper limit of 11 g/L are indicated in red. The experiments were performed according to chapters 3.3.1.1, 3.3.1.2, and 3.3.3.1.

After determining the total and plasma Hb concentrations, the blood was diluted with CMF-DPBS to achieve a Hb concentration between 9 and 11 g/L, ideally ten g/L (see Chapter 3.3.1.3). This concentration was achieved for batches seven, eight, ten, eleven, twelve, and 13. Diluted blood from batch ten was used despite the Hb concentration being marginally high at 11.1 g/L (see Figure 5.5).

5.2.1.3 Analysis of the Extraction Process

The extraction samples were analyzed in conjunction with the blank control, negative control, and positive control samples (see Chapter 3.3.2). The free Hb content of the samples was corrected by subtracting the value of the blank samples and expressed as a percentage of the total Hb concentration.

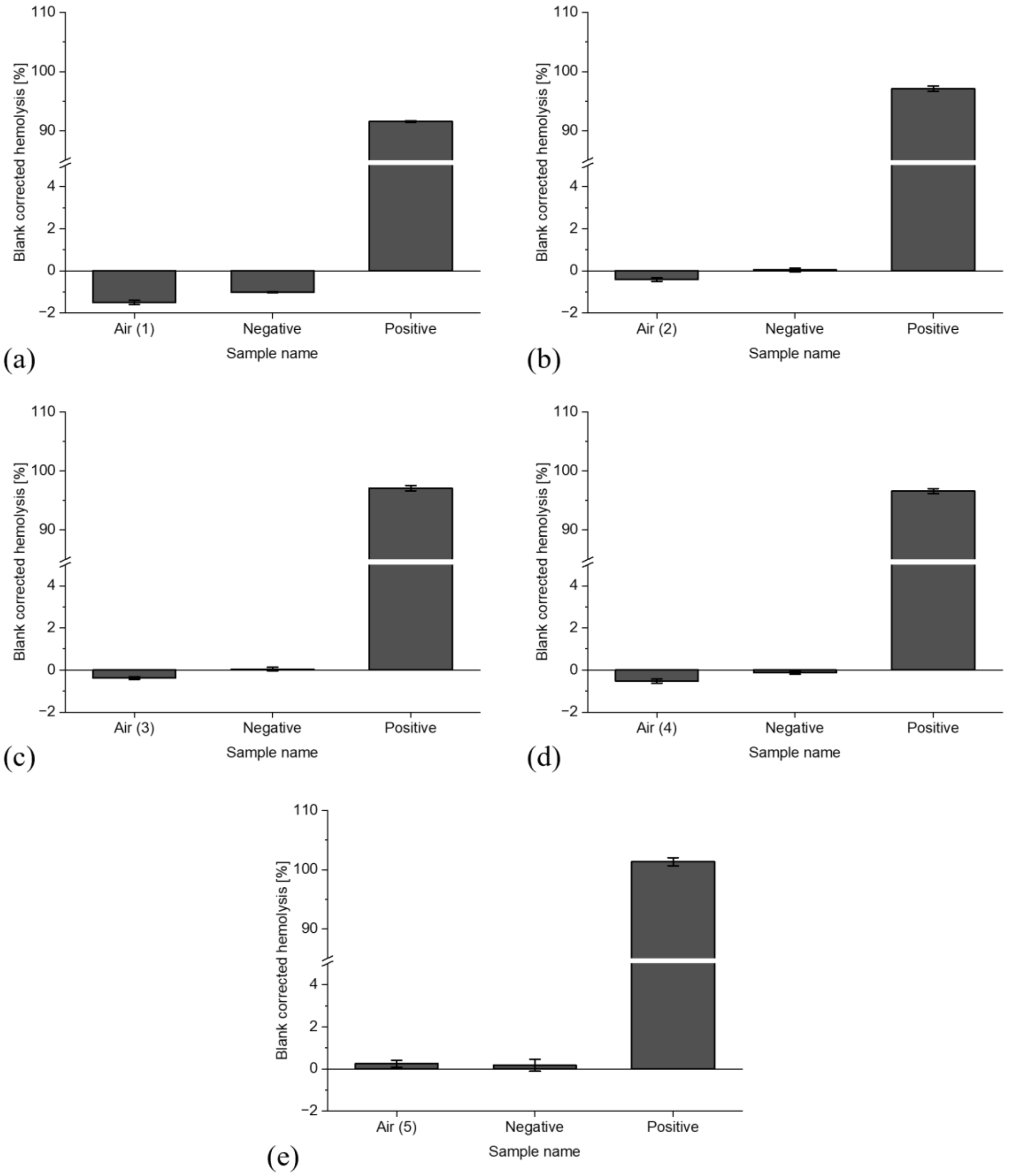

Figure 5.6: The percentage of blank corrected hemolysis of the extraction samples using just air as the perfusion gas, the negative control samples, and the positive control samples at the end of the experimental procedure. The experiments were performed according to chapters 3.3.1.1, 3.3.2, and 3.3.3.1.

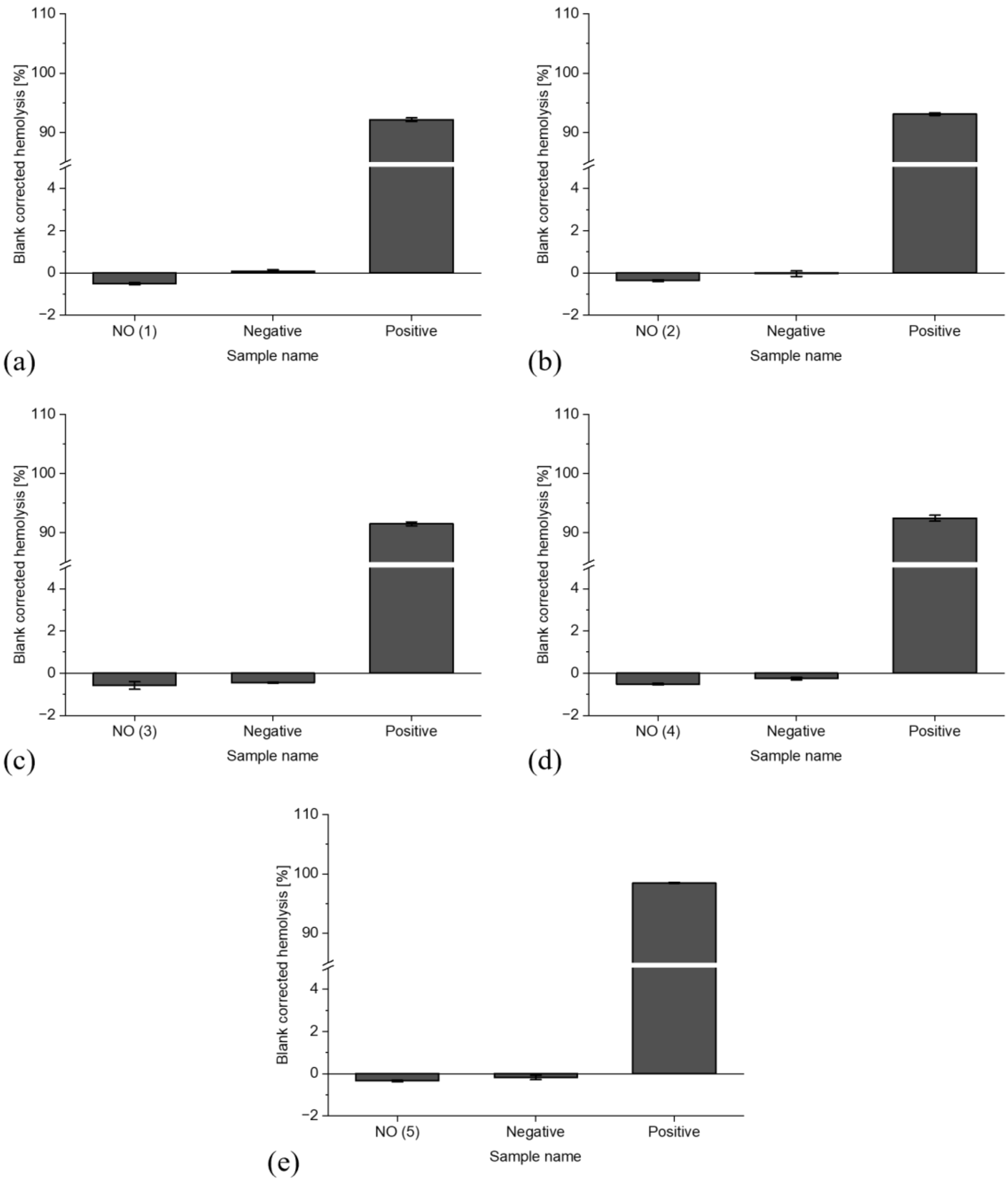

Figure 5.7: The percentage of blank corrected hemolysis of the extraction samples using air mixed with NO (40 ppm) as the perfusion gas, the negative control samples, and the positive control samples at the end of the experimental procedure. The experiments were performed according to chapters 3.3.1.1, 3.3.2, and 3.3.3.1.

The extraction experiments showed very similar low concentrations of free Hb in the extraction samples, the control blank, and the negative control samples. Using the free Hb concentrations of the positive samples as a reference showed that none of the other samples had any significant amount of free Hb (see Figures 8.16 and 8.17). The blank corrected hemolysis values showed that neither the perfusion with air nor the perfusion with NO resulted in any significant hemolytic effect with hemolysis values around 0 %

(see Figures 5.6 and 5.7). The results for the negative control samples reached values around 0 %, with the positive controls reaching between 90 and 100 % hemolysis (see Figure 5.6 and 5.7). Both results were as expected and proved that the testing methodology was sound.

Subtracting the negative control's blank-corrected hemolysis values from the extraction samples' blank-corrected hemolysis values led to the so-called hemolytic index. According to the previous investigation, the hemolytic index was subdivided into three parts. Samples with a hemolytic index between 0 and 2 % were non-hemolytic, samples between 2 and 5 % were slightly hemolytic, and samples above 5 % were hemolytic [295].

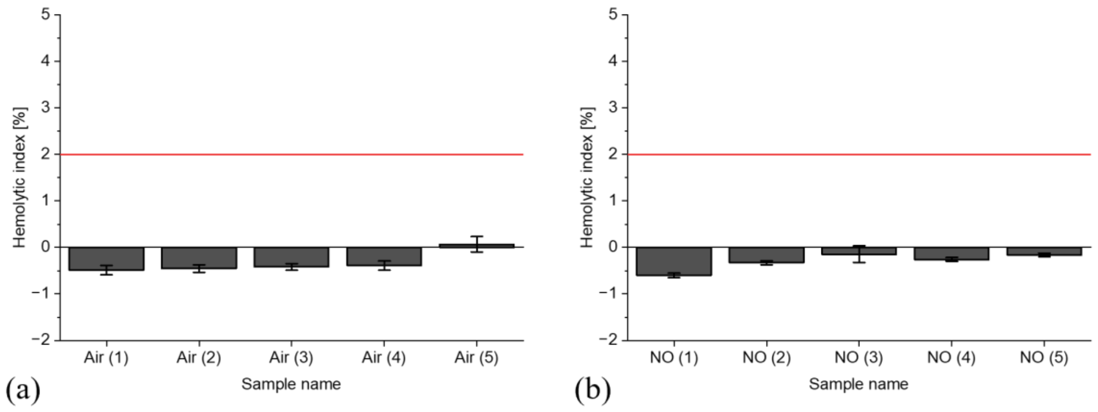

Figure 5.8: Hemolytic index of the extraction samples using (a) just air and (b) air mixed with NO (40 ppm) as the perfusion gas. The red line indicates the value of 2 %, above which the samples would have been considered slightly hemolytic. The experiments were performed according to chapters 3.3.1.1, 3.3.2, and 3.3.3.1.

The hemolytic indexes of the samples perfused with air and those perfused with NO (40 ppm) did not reach the upper limit of 2 %. In both cases, the values of the hemolytic index remained slightly below 0 % (see Figure 5.8). These results clearly showed that the addition of NO to the perfusion gas did not affect the hemolytic properties of the oxygenator. Therefore, the application of NO to the perfusion gas should be safe regarding hemolysis.

5.2.2 Vapor Pressure Osmometry and pH Measurements

VPO and pH measurements of the blank control and the extraction samples were conducted to determine the osmolality of the samples as well as their pH value. The samples analyzed here were taken before the extraction samples, and the control samples were mixed with the diluted blood.

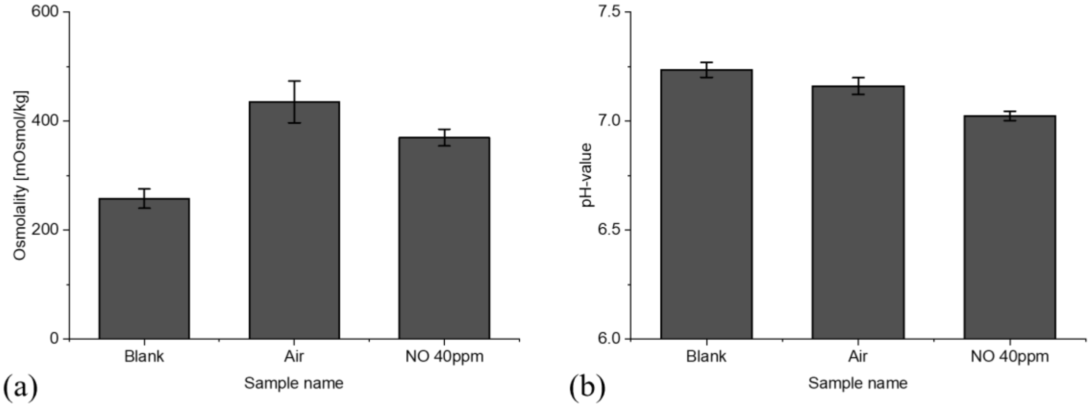

Figure 5.9: Results of the (a) vapor pressure osmometry measurements and (b) the pH measurements for the blank control samples, the extraction samples perfused with air, and the extraction samples perfused with NO (40 ppm). The experiments were performed according to chapters 3.3.1.1, 3.3.2, 3.3.3.2, and 3.3.3.3.

The extraction samples with air and with NO (40 ppm) possessed a significantly increased osmolality compared to the blank control samples. The blank control samples had an average osmolality of 258 mOsmol/kg. The extraction samples perfused with air reached an average value of 435 mOsmol/kg, while those perfused with NO (40 ppm) reached an average of 370 mOsmol/kg. This increase in osmolality for the extraction samples was likely due to the evaporation of the CMF-DPBS solution during the extraction duration due to the elevated temperature of 50 °C and the long hoses connecting the oxygenator to the peristaltic pump likely allowed for the evaporation of the fluid. This was also confirmed visibly; the liquid content in the oxygenator was significantly lower towards the end of the extraction process. These results showed that the addition of NO (40 ppm) did not increase the concentration of osmotically active compounds in the extraction liquid either, with the samples reaching slightly lower but similar values than the samples perfused with just air (see Figure 5.9 (a)).

The pH measurements showed a slight decrease in the pH values of the extraction samples compared to the blank control samples. The blank control samples had a pH of 7.24 on average. The extraction samples perfused with just air led to a slight decrease to a pH of

7.16. Adding NO (40 ppm) to the perfusion gas resulted in a further reduction to a value of 7.02 (see Figure 5.9 (b)). In both cases, at least part of the decrease was due to the dissolution of CO_2 from the air into the extraction liquid. For the extraction samples with added NO (40 ppm), the reaction between NO_2 and water also contributed to the lowering of the pH through the formation of HNO_3 in the extraction liquid, explaining the more significant decrease compared to the extraction samples perfused with just air (see Equations 57 and 58) [303, 304]. The pH decrease observed here could be a concern for the practical application of NO as part of the gas mixture added to an ECMO device, as the pH of the blood is essential to ensuring its functionality. However, the buffer capacity of the CMF-DPBS was very low compared to actual blood, with a buffer concentration of only 9.57 mM. The CMF-DPBS had a starting pH value of 7.23, meaning a buffer capacity of 5.2 mEq/L/pH. Blood, on the other hand, has a buffer capacity of 38.5 mEq/L/pH [333]. Therefore, it is unlikely that the addition of NO to the perfusion gas of the oxygenator would significantly impact the pH of the patient's blood at the desired application concentration below 100 ppm. Concentrations significantly above that, like the 1000 and 10.000 ppm of NO used in some of the experiments in this thesis, would, however, likely impact the blood pH, with the associated negative consequences for the patient [338].

6. Conclusion and Outlook

This thesis aimed to investigate whether the addition of NO to the sweep gas of an ECMO circuit was a viable pathway toward suppressing the thrombus formation inside these circuits. The focus of the investigation was on the impact of NO on the materials used in the oxygenator part of the ECMO circuit, with the majority of the measurements focusing on the hollow fiber membranes made from PMP, the inlet/outlet caps, and gas caps, both made from MABS, the PU materials forming the major structural component of the oxygenator, and the gas and blood hoses connected to the oxygenator both made from PVC with different plasticizers. The investigation of the materials incorporated FTIR-ATR and XPS measurements to determine the chemical interactions of the materials with NO. Static and dynamic contact angle and streaming potential measurements were performed to quantify the impact of NO on the surface properties. SEM images of the polymer surfaces were recorded to investigate the possible effects of the NO treatment on the surface morphology of the materials. Finally, the impact of NO on the hemolytic properties of the oxygenator was investigated using UV/vis spectroscopy, vapor pressure osmometry, and pH measurements.

The FITR-ATR measurements proved that the contact between the polymer materials used in the oxygenator with NO led to the formation of both nitro and nitrate ester groups as well as the deposition of the HNO_3 on the surface of the polymers (see Chapter 4.2.1.1). The silicone gasket and the UV-activated adhesive were only briefly investigated as neither showed any significant signs of interaction with NO at concentrations below 10,000 ppm. Materials such as MABS and PU showed signals for all three compounds even at NO concentrations as low as 80 ppm (see Chapter 4.2.1.2). The PVC samples did not show any signals related to the formation of nitro groups but behaved similarly to the MABS samples regarding the other two compounds. The big exception was PMP, which showed only a minor impact of NO at 10,000 ppm and no visible changes to the spectra at any of the lower concentrations (see Chapter 4.2.1). Additionally, PU and the UV-activated adhesive showed signs of chain scission and cross-linking reactions when treated with 10,000 ppm of NO. The softening of the adhesive, which was likely caused by these reactions, led to its removal from the oxygenator design. For PU, no signs of either reaction could be detected at lower concentrations of NO and NO_2, likely making them irrelevant at application concentrations.

The formation of these functional groups was attributed not to NO directly but to NO_2 and HNO_3 formed through reactions of NO with oxygen and the subsequent reaction of NO_2 with water, forming HNO_3 (see Equations 57 and 58). The nitro groups were formed through addition reactions between NO_2 and C-C double bonds. Nitrate ester groups were formed through reactions of HNO_3 with hydroxy and carbonyl groups. They were also formed through a reaction between nitrite ester groups and NO_2 following the already mentioned addition reaction (see Chapter 4.2.1.1). This interpretation of the FTIR-ATR results was further supported by measurement conducted with NO_2 replacing NO as the treatment gas, leading to essentially identical results (see Chapter 4.2.1.3). Gas treatment over more extended periods exposed a tendency towards saturation at all the trialed NO concentrations (see Chapter 4.2.1.2).

Stability measurements both under dry conditions and in contact with Millipore water and physiological saline solution showed in their FTIR-ATR spectra that the covalently bound nitro and nitrate ester groups remained stable on the sample surfaces even after extended periods. The HNO_3 molecules adsorbed to the surface showed a less stable bond to the sample surface (see Chapter 4.2.3). The high stability of the signals associated with the newly formed functional groups was the first positive indicator for using NO as a sweep gas additive, as it meant that these compounds were unlikely to dissolve into the patient’s blood during the actual application of the ECMO circuit.

XPS measurements of PMP, MABS, and PU were conducted to support the findings of the FTIR-ATR measurements and to determine how deep the reaction with the treatment gas reached into the polymer materials. The measurements confirmed the conclusions of the FTIR-ATR measurements, with both MABS and PU showing signals corresponding to nitro groups and HNO_3 molecules, with PMP again showing no impact from the gas treatment. These measurements proved that the interaction between the polymers and the treatment gas was only a surface phenomenon, as the sputtering process that removed a few nanometers from the sample surface resulted in the disappearance of the signals corresponding to the gas treatment (see Chapter 4.3). These results meant that the addition of NO would not impact the structural integrity of the oxygenator. Additionally, stability measurement conducted with MABS and PU samples using XPS measurements confirmed the results obtained with FTIR-ATR (see Chapters 4.2.3 and 4.3)

The SEM images recorded showed that the treatment with NO caused no macroscopic changes in surface morphology. This showed that the gas treatment had no negative impact on either the gas permeation abilities of PMP or the blood-contacting properties of materials such as MABS or PU. For PU in particular, this result proved that the gas treatment resulted in no significant degradation due to chain scission reactions. The only exception was the PVC (blood hose) samples, which showed slightly rougher surfaces (see Chapter 4.4). This should not be a concern for the actual application of NO as the blood hose is not in direct contact with the oxygenator sweep gas in that case.

Both static and dynamic contact angle measurements showed a strong impact of the NO treatment on the polymers' surface hydrophilicity, corresponding strongly to the results of the FTIR-ATR measurements. MABS and PU samples showed an apparent decrease in contact angle following the gas treatment, with PU exhibiting these effects even at concentrations as low as 80 ppm (see Chapter 4.5). In contrast to the chemical changes observed through FTIR-ATR, these changes in surface hydrophilicity proved less long-lasting. This led to the conclusion that the main compound responsible for the decrease in contact angle had been the adsorbed HNO_3 molecules to the polymer surface, as they had also proved to be less long-lasting than the nitro and nitrate ester functional groups (see Chapters 4.5.1 and 4.5.3). Of note was the increase in contact angle hysteresis observed during the dynamic contact angle measurements conducted with MABS, likely caused by increased chemical heterogeneity (see Chapter 4.5.2). The effect was only present for MABS, likely due to a more uneven distribution of adsorption and reaction sites than PU. The big exception was again PMP, which showed no change in contact angle independent of gas treatment (see Chapter 4.5). This behavior was expected, given the lack of any reaction with NO observed during the FTIR-ATR experiments (see Chapter 4.2.1.2).

The zeta potential measurements showed no impact of the gas treatment for PMP or MABS. In contrast, the measurements with PU resulted in a shift of the IEP to a lower pH value and flattening of the potential curve, indicating a more hydrophilic and acidic surface (see Chapter 4.5.2). These results again showed that the leading cause of surface property changes was likely the adsorbed HNO_3 molecules. The difference between PU and MABS was likely a matter of HNO_3 surface concentration, which was too low on the MABS surface to impact the zeta potential curve. This result was also in agreement with the contact angle measurements, where PU was overall the material showing the most substantial decrease in contact angle following the gas treatment (see Chapter 4.5.1). These results, therefore, supported the interpretation that the adsorption of HNO_3

molecules was the main cause of the changes in contact angle observed. The measurements with PMP showed no changes identically to both the FTIR-ATR and contact angle measurements (see Chapters 4.2.1.2 and 4.5.1). Both zeta potential and contact angle measurements indicated an increase in surface hydrophilicity for MABS and PU, which should positively impact their blood compatibility, specifically their thromboresistance (see Chapter 4.5.2). Under application conditions, these effects on both the zeta potential and the contact angles should be attenuated significantly due to constant blood flow across the material surfaces (see Chapter 4.5.1.1)

In addition to the analysis of the NO treatment on the polymer materials of the oxygenator, experiments were conducted to analyze the impact of NO on the hemolytic properties of the oxygenator. These experiments showed that the addition of NO to the sweep gas of the oxygenator did not affect the hemolytic properties of the oxygenator (see Chapter 5.2.1). The vapor pressure osmometry results showed no significant differences when adding NO to the sweep gas compared to just using air either. The only difference was a slightly lower pH observed for the samples treated with NO (see Chapter 5.2.2). This effect should, however, not be an issue under actual application conditions, as the buffer capacity of blood is much higher than that of the CMF-DPBS solution used for these experiments.

Overall, the results gathered throughout this thesis painted a widely neutral to slightly positive picture of NO as a sweep gas additive. The functional groups formed due to the NO treatment were highly stable, indicating a minimal risk to the patient connected to the ECMO circuit. The structural integrity of the oxygenator was not impacted, as the chemical reactions were only a surface phenomenon. The morphology of these surfaces remained unchanged, retaining the polymer materials' blood contacting and gas perfusion properties. The surface hydrophilicity of the polymer materials increased, likely leading to an improvement in the polymers’ thromboresistance properties, although this effect is likely not as strong under actual application conditions. Experiments showed that NO had no adverse effects on the hemolytic properties of the oxygenator either. So, in summary, no significant adverse effects of NO on the properties of the materials making up the oxygenator were detected, with existing literature indicating a potential slight improvement of the thromboresistance properties of the polymer surfaces.

The results presented in this thesis still leave room for further research. A possible next step would be a quantitative determination of the surface concentration of the nitro and nitrate ester functional groups and of the adsorbed HNO_3 molecules. Measurements with analytical methods such as zeta-potential or XPS were so far only conducted with a single concentration of NO and a limited set of polymer materials (see Chapters 4.3 and 4.4) and could, therefore, be expanded to a level of detail similar to the FTIR-ATR measurements. Investigations into the mechanical properties of the polymers and the impact of NO treatment on them would also be an interesting path forward. The results gathered so far stemmed from investigations conducted under conditions relatively far from the actual application of the ECMO circuit. Therefore, it would be beneficial to perform both animal and human trials with ECMO circuits with NO added to the sweep gas to test the results gathered so far for their applicability under real-world conditions. These trials would also be necessary because, while the experiments discussed in this thesis showed that NO had no adverse effects on the functionality of the oxygenator materials, its impact on the thrombotic properties of the ECMO circuit still remains to be analyzed.

7. References

[1] Hill, J.D.; O'Brien, T.G.; Murray, J.J.; Dontigny, L.; Bramson, M.L.; Osborn, J.J.; Gerbode, F. Prolonged Extracorporeal Oxygenation for Acute Post-Traumatic Respiratory Failure (Shock-Lung Syndrome). *N. Engl. J. Med.*, **1972**, *286,* 629–634. DOI: 10.1056/NEJM197203232861204.

[2] Makdisi, G.; Wang, I.-W. Extra Corporeal Membrane Oxygenation (ECMO) review of a lifesaving technology. *J. Thorac. Dis.*, **2015**, *7,* E166-E176. DOI: 10.3978/j.issn.2072-1439.2015.07.17.

[3] Hemmila, M.R.; Rowe, S.A.; Boules, T.N.; Miskulin, J.; McGillicuddy, J.W.; Schuerer, D.J.; Haft, J.W.; Swaniker, F.; Arbabi, S.; Hirschl, R.B.; Bartlett, R.H. Extracorporeal life support for severe acute respiratory distress syndrome in adults. *Ann. Surg.*, **2004**, *240,* 595-605; discussion 605-7. DOI: 10.1097/01.sla.0000141159.90676.2d.

[4] Sauer, C.M.; Yuh, D.D.; Bonde, P. Extracorporeal membrane oxygenation use has increased by 433% in adults in the United States from 2006 to 2011. *ASAIO J.*, **2015**, *61,* 31–36. DOI: 10.1097/MAT.0000000000000160.

[5] Uwumiro, F.; Otabor, N.; Okpujie, V.; Osiogo, E.O.; Osemwota, O.F.; Abesin, O.; Utibe, M.A.; Ekeh, N.; Onyekwe, A.E.; Fasoranti-Sowemimo, O.F. Rates, Outcomes, and Resource Burden of Extracorporeal Membrane Oxygenation Use in Hospitalizations in the United States During the Pandemic. *Cureus*, **2024**, *16,* 1–10. DOI: 10.7759/cureus.54081.

[6] Tsai, P.-H.; Lai, W.-Y.; Lin, Y.-Y.; Luo, Y.-H.; Lin, Y.-T.; Chen, H.-K.; Chen, Y.-M.; Lai, Y.-C.; Kuo, L.-C.; Chen, S.-D.; Chang, K.-J.; Liu, C.-H.; Chang, S.-C.; Wang, F.-D.; Yang, Y.-P. Clinical manifestation and disease progression in COVID-19 infection. *J. Chin. Med. Assoc.*, **2021**, *84,* 3–8. DOI: 10.1097/JCMA.0000000000000463.

[7] Allen, S.; Holena, D.; McCunn, M.; Kohl, B.; Sarani, B. A Review of the Fundamental Principles and Evidence Base in the Use of Extracorporeal Membrane Oxygenation (ECMO) in Critically Ill Adult Patients. *J. Intensive Care Med.*, **2011**, *26,* 13–26. DOI: 10.1177/0885066610384061.

[8] Karagiannidis, C.; Strassmann, S.; Larsson, A.; Brodie, D. The Hemovent Oxygenator: A New Low-Resistance, High-Performance Oxygenator. *ASAIO J.*, **2021**, *67,* e59–e61. DOI: 10.1097/MAT.0000000000001190.

[9] Olson, S.R.; Murphree, C.R.; Zonies, D.; Meyer, A.D.; Mccarty, O.J.T.; Deloughery, T.G.; Shatzel, J.J. Thrombosis and Bleeding in Extracorporeal Membrane Oxygenation (ECMO) Without Anticoagulation: A Systematic Review. *ASAIO J.*, **2021**, *67,* 290–296. DOI: 10.1097/MAT.0000000000001230.

[10] Andrabi, S.M.; Sharma, N.S.; Karan, A.; Shahriar, S.M.S.; Cordon, B.; Ma, B.; Xie, J. Nitric Oxide: Physiological Functions, Delivery, and Biomedical Applications. *Adv. Sci. (Weinh.)*, **2023**, *10,* 1–38. DOI: 10.1002/advs.202303259.

[11] Kuo, P.C.; Schroeder, R.A. The emerging multifaceted roles of nitric oxide. *Ann. Surg.*, **1995**, *221,* 220–235. DOI: 10.1097/00000658-199503000-00003.

[12] Cheung, P.Y.; Salas, E.; Schulz, R.; Radomski, M.W. Nitric oxide and platelet function: implications for neonatology. *Semin. Perinatol.*, **1997**, *21,* 409–417. DOI: 10.1016/s0146-0005(97)80006-7.

[13] Radomski, M.W.; Palmer, R.M.; Moncada, S. An L-arginine/nitric oxide pathway present in human platelets regulates aggregation. *Proc. Natl. Acad. Sci. USA*, **1990**, *87,* 5193–5197. DOI: 10.1073/pnas.87.13.5193.

[14] Annich, G.M.; Meinhardt, J.P.; Mowery, K.A.; Ashton, B.A.; Merz, S.I.; Hirschl, R.B.; Meyerhoff, M.E.; Bartlett, R.H. Reduced platelet activation and thrombosis in extracorporeal circuits coated with nitric oxide release polymers. *Crit. Care Med.*, **2000**, *28,* 915–920. DOI: 10.1097/00003246-200004000-00001.

[15] Lim, M.W. The history of extracorporeal oxygenators. *Anaesthesia*, **2006**, *61,* 984–995. DOI: 10.1111/j.1365-2044.2006.04781.x.

[16] Hewitt, R.L.; Creech, O., JR. History of the pump oxygenator. *Arch. Surg. (Chicago, Ill.: 1960)*, **1966**, *93*, 680–696. DOI: 10.1001/archsurg.1966.01330040144030.

[17] Hooker, D.R. A Study of the Isolated Kidney.—The Influence of Pulse Pressure Upon Renal Function. *Am. J. Physiol.*, **1910**, *27,* 24–44. DOI: 10.1152/ajplegacy.1910.27.1.24.

[18] Hooker, D.R. The Perfusion of the Mammalian Medulla: The Effect of Calcium and of Potassium on the Respiratory and Cardiac Centers. *Am. J. Physiol.*, **1915**, *38,* 200–208. DOI: 10.1152/ajplegacy.1915.38.2.200.

[19] Richards, A.N.; Drinker, C.K. An Apparatus for the Perfusion of Isolated Organs. *J. Pharmacol. Exp. Ther.*, **1915**, *7,* 467–483.

[20] McLean, J. The Thromboplastic Action of Cephalin. *Am. J. Physiol.*, **1916**, *41,* 250–257. DOI: 10.1152/ajplegacy.1916.41.2.250.

[21] Gibbon Jr., J.H. Artificial Maintenance of Circulation During Experimental Occlusion of Pulmonary Artery. *Arch. Surg.*, **1937**, *34,* 1105–1131. DOI: 10.1001/archsurg.1937.01190120131008.

[22] Gibbon Jr, J.H. An oxygenator with a large surface-volume ratio. *J. Lab. Clin. Med.*, **1939**, *24,* 1192.

[23] Gibbon Jr, J.H. Application of a mechanical heart and lung apparatus to cardiac surgery. *Minn. Med.*, **1954**, *37,* 171–185.

[24] Björk, V.O. *Brain perfusions in dogs with artificially oxygenated blood;* Berlingska Boktryck, **1948**.

[25] Clark, L.C.; Gollan, F.; Gupta, V.B. The Oxygenation of Blood by Gas Dispersion. *Science*, **1950**, *111,* 85–87. DOI: 10.1126/science.111.2874.85.b.

[26] Hurt, R. The technique and scope of open-heart surgery. *Postgrad. Med. J.*, **1967**, *43,* 668–674. DOI: 10.1136/pgmj.43.504.668.

[27] Kolff, W.J.; Berk, H.T.; Welle, M. ter; van der LEY, A.J.; van Dijk, E.C.; van Noordwijk, J. The artificial kidney: a dialyser with a great area. *Acta med. Scand.*, **1944**, *117,* 121–134. DOI: 10.1681/ASN.V8121959.

[28] Clowes Jr., G.; Hopkins, A.L.; Kolobow, T. OXYGEN DIFFUSION THROUGH PLASTIC FILMS. *ASAIO J.*, **1955**, *1,* 23–24.

[29] Clowes Jr., G.; Neville, W.E. Further Development of a Blood Oxygenator Dependent upon the Diffusion of Gases through Plastic Membranes. *ASAIO J.*, **1957**, *3,* 52–58.

[30] Burns, N. Production of a silicone rubber film for the membrane lung. *Biomed. Eng.*, **1969**, *4,* 356–359.

[31] Iwahashi, H.; Yuri, K.; Nosé, Y. Development of the oxygenator: past, present, and future. *J. Artif. Organs.*, **2004**, *7,* 111–120. DOI: 10.1007/s10047-004-0268-6.

[32] Marx, T.I.; Snyder, W.E.; St. John, A.D.; Moeller, C.E. Diffusion of oxygen into a film of whole blood. *J. Appl. Physiol.*, **1960**, *15,* 1123–1129. DOI: 10.1152/jappl.1960.15.6.1123.

[33] Bodell, B.R.; Head, J.M.; Head, L.R.; Formolo, A.J.; Head, J.R. A Capillary Membrane Oxygenator. *J. Thorac. Cardiovasc. Surg.*, **1963**, *46,* 639–650. DOI: 10.1016/S0022-5223(19)33636-0.

[34] Wilson, R.; Shepley, D.J.; Llewellyn-Thomas, E. A membrane oxygenator with low priming volume for extracorporeal circulation. *Can. J. Surg*, **1965**, *8,* 309–311. DOI: 10.1016/0022-3468(66)90048-0.

[35] McCaughan, J.S.; Weeder, R.; Schuder, J.C.; Blakemore, W.S. Evaluation of New Nonwettable Macroporous Membranes with High Permeability Coefficients for Possible Use in a Membrane Oxygenator. *J. Thorac. Cardiovasc. Surg.*, **1960**, *40,* 574–581. DOI: 10.1016/S0022-5223(19)32580-2.

[36] Gaylor, J. Membrane oxygenators: current developments in design and application. *J. Biomed. Eng.*, **1988**, *10,* 541–547. DOI: 10.1016/0141-5425(88)90113-6.

[37] Mora, C.T.; Guyton, R.A.; Finlayson, D.C.; Rigatti, R.L., Eds. *Cardiopulmonary Bypass: Principles and Techniques of Extracorporeal Circulation;* Springer New York: New York, NY, **1995**. ISBN: 978-1-4612-2484-6.

[38] Peek, G.J.; Killer, H.M.; Reeves, R.; Sosnowski, A.W.; Firmin, R.K. Early Experience with a Polymethyl Pentene Oxygenator for Adult Extracorporeal Life Support. *ASAIO J.*, **2002**, *48,* 480–482. DOI: 10.1097/00002480-200209000-00007.

[39] Toomasian, J.M.; Schreiner, R.J.; Meyer, D.E.; Schmidt, M.E.; Hagan, S.E.; Griffith, G.W.; Bartlett, R.H.; Cook, K.E. A Polymethylpentene Fiber Gas Exchanger for Long-Term Extracorporeal Life Support. *ASAIO J.*, **2005**, *51,* 390–397. DOI: 10.1097/01.mat.0000169111.66328.a8.

[40] Banfi, C.; Pozzi, M.; Siegenthaler, N.; Brunner, M.-E.; Tassaux, D.; Obadia, J.-F.; Bendjelid, K.; Giraud, R. Veno-venous extracorporeal membrane oxygenation: cannulation techniques. *J. Thorac. Dis.*, **2016**, *8,* 3762–3773. DOI: 10.21037/jtd.2016.12.88.

[41] Rao, P.; Khalpey, Z.; Smith, R.; Burkhoff, D.; Kociol, R.D. Venoarterial Extracorporeal Membrane Oxygenation for Cardiogenic Shock and Cardiac Arrest. *Circ. Heart Fail.*, **2018**, *11,* 1–17. DOI: 10.1161/CIRCHEARTFAILURE.118.004905.

[42] Jayaraman, A.L.; Cormican, D.; Shah, P.; Ramakrishna, H. Cannulation strategies in adult veno-arterial and veno-venous extracorporeal membrane oxygenation: Techniques, limitations, and special considerations. *Ann. Card. Anaesth.*, **2017**, *20,* S11-S18. DOI: 10.4103/0971-9784.197791.

[43] Ius, F.; Sommer, W.; Tudorache, I.; Avsar, M.; Siemeni, T.; Salman, J.; Puntigam, J.; Optenhoefel, J.; Greer, M.; Welte, T.; Wiesner, O.; Haverich, A.; Hoeper, M.; Kuehn, C.; Warnecke, G. Veno-veno-arterial extracorporeal membrane oxygenation for respiratory failure with severe haemodynamic impairment: technique and early outcomes. *Interact. Cardiovasc. Thorac. Surg.*, **2015**, *20,* 761–767. DOI: 10.1093/icvts/ivv035.

[44] Gattinoni, L.; Carlesso, E.; Langer, T. Clinical review: Extracorporeal membrane oxygenation. *Crit. Care*, **2011**, *15,* 243–248. DOI: 10.1186/cc10490.

[45] Cui, Y.; Zhang, Y.; Dou, J.; Shi, J.; Zhao, Z.; Zhang, Z.; Chen, Y.; Cheng, C.; Zhu, D.; Quan, X.; Zhu, X.; Huang, W. Venovenous vs. Venoarterial Extracorporeal Membrane Oxygenation in Infection-Associated Severe Pediatric Acute Respiratory Distress Syndrome: A Prospective Multicenter Cohort Study. *Front. Pediatr.*, **2022**, *10,* 1–9. DOI: 10.3389/fped.2022.832776.

[46] Kon, Z.K.; Bittle, G.J.; Pasrija, C.; Pham, S.M.; Mazzeffi, M.A.; Herr, D.L.; Sanchez, S.G.; Griffith, B.P. Venovenous Versus Venoarterial Extracorporeal Membrane Oxygenation for Adult Patients With Acute Respiratory Distress Syndrome Requiring Precannulation Hemodynamic Support: A Review of the ELSO Registry. *Ann. Thorac. Surg.*, **2017**, *104,* 645–649. DOI: 10.1016/j.athoracsur.2016.11.006.

[47] Horton, A.M.; Butt, W. Pump-induced haemolysis: is the constrained vortex pump better or worse than the roller pump? *Perfusion*, **1992**, *7,* 103–108. DOI: 10.1177/026765919200700204.

[48] Fiusco, F.; Broman, L.M.; Prahl Wittberg, L. Blood Pumps for Extracorporeal Membrane Oxygenation: Platelet Activation During Different Operating Conditions. *ASAIO J.*, **2022**, *68,* 79–86. DOI: 10.1097/MAT.0000000000001493.

[49] Bennett, M.; Horton, S.; Thuys, C.; Augustin, S.; Rosenberg, M.; Brizard, C. Pump-induced haemolysis: a comparison of short-term ventricular assist devices. *Perfusion*, **2004**, *19,* 107–111. DOI: 10.1191/0267659104pf729oa.

[50] Hastings, S.M.; Ku, D.N.; Wagoner, S.; Maher, K.O.; Deshpande, S. Sources of Circuit Thrombosis in Pediatric Extracorporeal Membrane Oxygenation. *ASAIO J.*, **2017**, *63,* 86–92. DOI: 10.1097/MAT.0000000000000444.

[51] Karagiannidis, C.; Joost, T.; Strassmann, S.; Weber-Carstens, S.; Combes, A.; Windisch, W.; Brodie, D. Safety and Efficacy of a Novel Pneumatically Driven Extracorporeal Membrane Oxygenation Device. *Ann. Thorac. Surg.*, **2020**, *109,* 1684–1691. DOI: 10.1016/j.athoracsur.2020.01.039.

[52] Fukuda, M. Evolutions of extracorporeal membrane oxygenator (ECMO): perspectives for advanced hollow fiber membrane. *J. Artif. Organs.*, **2023,** 1–6. DOI: 10.1007/s10047-023-01389-w.

[53] Kalbhenn, J.; Zieger, B. Bleeding During Veno-Venous ECMO: Prevention and Treatment. *Front. Med. (Lausanne)*, **2022**, *9,* 1–9. DOI: 10.3389/fmed.2022.879579.

[54] Australia and New Zealand Extracorporeal Membrane Oxygenation (ANZ ECMO) Influenza Investigators; Davies, A.; Jones, D.; Bailey, M.; Beca, J.; Bellomo, R.; Blackwell, N.; Forrest, P.; Gattas, D.; Granger, E.; Herkes, R.; Jackson, A.; McGuinness, S.; Nair, P.; Pellegrino, V.; Pettilä, V.; Plunkett, B.; Pye, R.; Torzillo, P.; Webb, S.; Wilson, M.; Ziegenfuss, M. Extracorporeal Membrane Oxygenation for 2009 Influenza A(H1N1) Acute Respiratory Distress Syndrome. *JAMA*, **2009**, *302,* 1888–1895. DOI: 10.1001/jama.2009.1535.

[55] Cornell, T.; Wyrick, P.; Fleming, G.; Pasko, D.; Han, Y.; Custer, J.; Haft, J.; Annich, G. A case series describing the use of argatroban in patients on extracorporeal circulation. *ASAIO J.*, **2007**, *53,* 460–463. DOI: 10.1097/MAT.0b013e31805c0d6c.

[56] Biran, R.; Pond, D. Heparin coatings for improving blood compatibility of medical devices. *Adv. Drug Deliv. Rev.*, **2017**, *112,* 12–23. DOI: 10.1016/j.addr.2016.12.002.

[57] Mateen, F.J.; Muralidharan, R.; Shinohara, R.T.; Parisi, J.E.; Schears, G.J.; Wijdicks, E.F.M. Neurological injury in adults treated with extracorporeal membrane oxygenation. *Arch. Neurol.*, **2011**, *68,* 1543–1549. DOI: 10.1001/archneurol.2011.209.

[58] Lidegran, M.K.; Mosskin, M.; Ringertz, H.G.; Frenckner, B.P.; Lindén, V.B. Cranial CT for diagnosis of intracranial complications in adult and pediatric patients during ECMO: Clinical benefits in diagnosis and treatment. *Acad. Radiol.*, **2007**, *14,* 62–71. DOI: 10.1016/j.acra.2006.10.004.

[59] Jain, A.; Mehta, Y. Sepsis Associated with Extracorporeal Membrane Oxygenation. *J. Cardiac Crit. Care TSS*, **2022**, *06,* 146–150. DOI: 10.1055/s-0042-1757392.

[60] Wo, Y.; Brisbois, E.J.; Bartlett, R.H.; Meyerhoff, M.E. Recent advances in thromboresistant and antimicrobial polymers for biomedical applications: just say yes to nitric oxide (NO). *Biomater. Sci.*, **2016**, *4,* 1161–1183. DOI: 10.1039/C6BM00271D.

[61] Zeibi Shirejini, S.; Carberry, J.; McQuilten, Z.K.; Burrell, A.J.C.; Gregory, S.D.; Hagemeyer, C.E. Current and future strategies to monitor and manage coagulation in ECMO patients. *Thrombosis J.*, **2023**, *21,* 1–20. DOI: 10.1186/s12959-023-00452-z.

[62] Gajkowski, E.F.; Herrera, G.; Hatton, L.; Velia Antonini, M.; Vercaemst, L.; Cooley, E. ELSO Guidelines for Adult and Pediatric Extracorporeal Membrane Oxygenation Circuits. *ASAIO J.*, **2022**, *68,* 133–152. DOI: 10.1097/MAT.0000000000001630.

[63] Considine, D.M., Ed. *Chemical and process technology encyclopedia;* McGraw-Hill: New York, NY, **1974**. ISBN: 978-0-07-012423-3.

[64] Knowles, R. Nitric oxide synthases. *Biochem. Soc. Trans.*, **1996**, *24,* 875–878. DOI: 10.1042/bst0240875.

[65] Jaeglé, L.; Steinberger, L.; Martin, R.V.; Chance, K. Global partitioning of NOx sources using satellite observations: relative roles of fossil fuel combustion, biomass burning and soil emissions. *Faraday discussions*, **2005**, *130,* 407-423; discussion 491-517, 519-524. DOI: 10.1039/b502128f.

[66] El Morabet, R. Effects of Outdoor Air Pollution on Human Health. In: *Encyclopedia of Environmental Health*; Elsevier, **2019**; pp. 278–286. ISBN: 9780444639523.

[67] Keith A. Smith. The impact of agriculture and other land uses on emissions of methane and nitrous and nitric oxides. *Environm. Sci.*, **2005**, *2*, 101–108. DOI: 10.1080/15693430500370423.

[68] Coskun, D.; Britto, D.T.; Shi, W.; Kronzucker, H.J. Nitrogen transformations in modern agriculture and the role of biological nitrification inhibition. *Nat. plants*, **2017**, *3,* 1–10. DOI: 10.1038/nplants.2017.74.

[69] Xunhua, Z.; Mingxing, W.; Yuesi, W.; Renxing, S.; Jing, L.; Heyer, J.; Koegge, M.; Papen, H.; Jisheng, J.; Laotu, L. Mitigation options for methane, nitrous oxide and nitric oxide emissions from agricultural ecosystems. *Adv. Atmos. Sci.*, **2000**, *17,* 83–92. DOI: 10.1007/s00376-000-0045-2.

[70] Kritsanaviparkporn, E.; Baena-Moreno, F.M.; Reina, T.R. Catalytic Converters for Vehicle Exhaust: Fundamental Aspects and Technology Overview for Newcomers to the Field. *Chemistry,* **2021**, *3,* 630–646. DOI: 10.3390/chemistry3020044.

[71] Bowman, C.T. Control of combustion-generated nitrogen oxide emissions: Technology driven by regulation. *Symp. (Int.) Combust.*, **1992**, *24,* 859–878. DOI: 10.1016/S0082-0784(06)80104-9.

[72] Hong, Z.; Wang, Z.; Li, X. Catalytic oxidation of nitric oxide (NO) over different catalysts: an overview. *Catal. Sci. Technol.*, **2017**, *7,* 3440–3452. DOI: 10.1039/C7CY00760D.

[73] Gibaldi, M. What is nitric oxide and why are so many people studying it? *J. Clin. Pharmacol.*, **1993**, *33,* 488–496. DOI: 10.1002/j.1552-4604.1993.tb04694.x.

[74] Arnold, W.P.; Mittal, C.K.; Katsuki, S.; Murad, F. Nitric oxide activates guanylate cyclase and increases guanosine 3':5'-cyclic monophosphate levels in various tissue preparations. *Proc. Natl. Acad. Sci. U.S.A.*, **1977**, *74,* 3203–3207.

DOI: 10.1073/pnas.74.8.3203.

[75] Furchgott, R.F.; Zawadzki, J.V. The obligatory role of endothelial cells in the relaxation of arterial smooth muscle by acetylcholine. *Nature*, **1980**, *288*, 373–376. DOI: 10.1038/288373a0.

[76] Cherry, P.D.; Furchgott, R.F.; Zawadzki, J.V.; Jothianandan, D. Role of Endothelial Cells in Relaxation of Isolated Arteries by Bradykinin. *Proc. Natl. Acad. Sci. USA*, **1982**, *79*, 2106–2110. DOI: 10.1073/pnas.79.6.2106.

[77] Furchgott, R.F. Role of endothelium in responses of vascular smooth muscle. *Circ. Res.*, **1983**, *53*, 557–573. DOI: 10.1161/01.res.53.5.557.

[78] Furchgott, R.F.; Carvalho, M.H.; Khan, M.T.; Matsunaga, K. Evidence for endothelium-dependent vasodilation of resistance vessels by acetylcholine. *Blood vessels*, **1987**, *24*, 145–149. DOI: 10.1159/000158689.

[79] Ignarro, L.J.; Buga, G.M.; Wood, K.S.; Byrns, R.E.; Chaudhuri, G. Endothelium-derived relaxing factor produced and released from artery and vein is nitric oxide. *Proc. Natl. Acad. Sci. U.S.A.*, **1987**, *84*, 9265–9269. DOI: 10.1073/pnas.84.24.9265.

[80] Knowles, R.G.; Moncada, S. Nitric oxide synthases in mammals. *Biochem. J.*, **1994**, *298 (Pt 2)*, 249–258. DOI: 10.1042/bj2980249.

[81] Bredt, D.S.; Snyder, S.H. Isolation of nitric oxide synthetase, a calmodulin-requiring enzyme. *Proc. Natl. Acad. Sci. USA*, **1990**, *87*, 682–685. DOI: 10.1073/pnas.87.2.682.

[82] Pollock, J.S.; Förstermann, U.; Mitchell, J.A.; Warner, T.D.; Schmidt, H.H.; Nakane, M.; Murad, F. Purification and characterization of particulate endothelium-derived relaxing factor synthase from cultured and native bovine aortic endothelial cells. *Proc. Natl. Acad. Sci. USA*, **1991**, *88*, 10480–10484. DOI: 10.1073/pnas.88.23.10480.

[83] Lyons, C.R.; Orloff, G.J.; Cunningham, J.M. Molecular cloning and functional expression of an inducible nitric oxide synthase from a murine macrophage cell line. *J. Biol. Chem.*, **1992**, *267*, 6370–6374. DOI: 10.1016/S0021-9258(18)42704-4.

[84] Alderton, W.K.; Cooper, C.E.; Knowles, R.G. Nitric oxide synthases: structure, function and inhibition. *Biochem. J.*, **2001**, *357*, 593–615. DOI: 10.1042/0264-6021:3570593.

[85] Förstermann, U.; Sessa, W.C. Nitric oxide synthases: regulation and function. *Eur. Heart J.*, **2012**, *33*, 829-37, 837a-837d. DOI: 10.1093/eurheartj/ehr304.

[86] Atakisi, E.; Merhan, O. Nitric Oxide Synthase and Nitric Oxide Involvement in Different Toxicities. In: *Nitric Oxide Synthase - Simple Enzyme-Complex Roles*. Saravi, S.S.S., Ed.; IntechOpen: London, UK, **2017**. ISBN: 978-953-51-3163-2.

[87] Crane, B.R.; Arvai, A.S.; Ghosh, D.K.; Wu, C.; Getzoff, E.D.; Stuehr, D.J.; Tainer, J.A. Structure of nitric oxide synthase oxygenase dimer with pterin and substrate. *Science,* **1998**, *279,* 2121–2126. DOI: 10.1126/science.279.5359.2121.

[88] Stuehr, D.; Pou, S.; Rosen, G.M. Oxygen reduction by nitric-oxide synthases. *J. Biol. Chem.*, **2001**, *276,* 14533–14536. DOI: 10.1074/jbc.R100011200.

[89] Faraci, F.M.; Brian Jr., J.E. Nitric oxide and the cerebral circulation. *Stroke,* **1994**, *25,* 692–703. DOI: 10.1161/01.str.25.3.692.

[90] Kontos, H.A. Nitric oxide and nitrosothiols in cerebrovascular and neuronal regulation. *Stroke,* **1993**, *24,* I155-I158.

[91] Iadecola, C. Does nitric oxide mediate the increases in cerebral blood flow elicited by hypercapnia? *Proc. Natl. Acad. Sci. USA,* **1992**, *89,* 3913–3916. DOI: 10.1073/pnas.89.9.3913.

[92] Sanders, K.M. Enteric Inhibitory Neurotransmission, Starting Down Under. *Adv. Exp. Med. Biol.,* **2016**, *891,* 21–29. DOI: 10.1007/978-3-319-27592-5_3.

[93] Freire, M.A.M.; Guimarães, J.S.; Leal, W.G.; Pereira, A. Pain modulation by nitric oxide in the spinal cord. *Front. Neurosci.,* **2009**, *3,* 175–181. DOI: 10.3389/neuro.01.024.2009.

[94] Miyamoto, E. Molecular mechanism of neuronal plasticity: induction and maintenance of long-term potentiation in the hippocampus. *J. Pharmacol. Sci.,* **2006**, *100,* 433–442. DOI: 10.1254/jphs.cpj06007x.

[95] Picón-Pagès, P.; Garcia-Buendia, J.; Muñoz, F.J. Functions and dysfunctions of nitric oxide in brain. *Biochim. Biophys. Acta,* **2019**, *1865*, 1949–1967. DOI: 10.1016/j.bbadis.2018.11.007.

[96] Gaston, B.; Drazen, J.M.; Jansen, A.; Da Sugarbaker; Loscalzo, J.; Stamler, J.S. Relaxation of human airways in vitro by S-nitrosothiols. *Am. Rev. Respir. Dis.,* **1992**, *145,* A383.

[97] Jansen, A.; Drazen, J.; Osborne, J.A.; Brown, R.; Loscalzo, J.; Stamler, J.S. The relaxant properties in guinea pig airways of S-nitrosothiols. *J. Pharmacol. Exp. Ther.,* **1992**, *261,* 154–160.

[98] Pearl, R.G. Inhaled nitric oxide. *West. J. Med.,* **1995**, *162,* 52–53.

[99] Pepke-Zaba, J.; Higenbottam, T.W.; Dinh-Xuan, A.T.; Stone, D.; Wallwork, J. Inhaled nitric oxide as a cause of selective pulmonary vasodilatation in pulmonary hypertension. *Lancet,* **1991**, *338,* 1173–1174. DOI: 10.1016/0140-6736(91)92033-x.

[100] Flavahan, N.A. Atherosclerosis or lipoprotein-induced endothelial dysfunction. Potential mechanisms underlying reduction in EDRF/nitric oxide activity. *Circulation*, **1992**, *85,* 1927–1938. DOI: 10.1161/01.cir.85.5.1927.

[101] Dinerman, J.L.; Lowenstein, C.J.; Snyder, S.H. Molecular mechanisms of nitric oxide regulation. Potential relevance to cardiovascular disease. *Circ. Res.*, **1993**, *73,* 217–222. DOI: 10.1161/01.res.73.2.217.

[102] Barnes, P.J. Nitric oxide and airways. *Eur. Respir. J.*, **1993**, *6,* 163–165. DOI: 10.1183/09031936.93.06020163.

[103] Thomas, G.R.; Thiemermann, C.; Walder, C.; Vane, J.R. The effects of endothelium-dependent vasodilators on cardiac output and their distribution in the anaesthetized rat: a comparison with sodium nitroprusside. *Br. J. Pharmacol.*, **1988**, *95,* 986–992. DOI: 10.1111/j.1476-5381.1988.tb11729.x.

[104] Walder, C.E.; Thiemermann, C.; Vane, J.R. Endothelium-derived relaxing factor participates in the increased blood flow in response to pentagastrin in the rat stomach mucosa. *Proc. Biol. Sci.*, **1990**, *241,* 195–200. DOI: 10.1098/rspb.1990.0085.

[105] Lundberg, J.O. Nitric Oxide Metabolites and Cardiovascular Disease. *J. Am. Coll. Cardiol.*, **2006**, *47,* 580–581. DOI: 10.1016/j.jacc.2005.11.016.

[106] Figueroa, X.F.; Lillo, M.A.; Gaete, P.S.; Riquelme, M.A.; Sáez, J.C. Diffusion of nitric oxide across cell membranes of the vascular wall requires specific connexin-based channels. *Neuropharmacol.*, **2013**, *75,* 471–478. DOI: 10.1016/j.neuropharm.2013.02.022.

[107] Münzel, T.; Feil, R.; Mülsch, A.; Lohmann, S.M.; Hofmann, F.; Walter, U. Physiology and pathophysiology of vascular signaling controlled by guanosine 3',5'-cyclic monophosphate-dependent protein kinase [corrected] *Circulation*, **2003**, *108,* 2172–2183. DOI: 10.1161/01.CIR.0000094403.78467.C3.

[108] Denninger, J.W.; Marletta, M.A. Guanylate cyclase and the .NO/cGMP signaling pathway. *Biochim. Biophys. Acta,* **1999**, *1411,* 334–350. DOI: 10.1016/s0005-2728(99)00024-9.

[109] Liaudet, L.; Soriano, F.G.; Szabó, C. Biology of nitric oxide signaling. *Crit. Care Med.*, **2000**, *28,* N37-N52. DOI: 10.1097/00003246-200004001-00005.

[110] Thomas, D.D.; Ridnour, L.A.; Isenberg, J.S.; Flores-Santana, W.; Switzer, C.H.; Donzelli, S.; Hussain, P.; Vecoli, C.; Paolocci, N.; Ambs, S.; Colton, C.A.; Harris, C.C.; Roberts, D.D.; Wink, D.A. The chemical biology of nitric oxide: implications in cellular signaling. *Free Radic. Biol. Med.*, **2008**, *45,* 18–31. DOI: 10.1016/j.freeradbiomed.2008.03.020.

[111] Martínez-Ruiz, A.; Araújo, I.M.; Izquierdo-Álvarez, A.; Hernansanz-Agustín, P.; Lamas, S.; Serrador, J.M. Specificity in S-nitrosylation: a short-range mechanism for NO signaling? *Antioxid. Redox Signal.*, **2013**, *19,* 1220–1235. DOI: 10.1089/ars.2012.5066.

[112] Fernando, V.; Zheng, X.; Walia, Y.; Sharma, V.; Letson, J.; Furuta, S. S-Nitrosylation: An Emerging Paradigm of Redox Signaling. *Antioxidants (Basel)*, **2019**, *8,* 1–32. DOI: 10.3390/antiox8090404.

[113] Murad, F. Regulation of cytosolic guanylyl cyclase by nitric oxide: the NO-cyclic GMP signal transduction system. *Adv. Pharmacol.*, **1994**, *26,* 19–33. DOI: 10.1016/s1054-3589(08)60049-6.

[114] Sarti, P.; Forte, E.; Mastronicola, D.; Giuffrè, A.; Arese, M. Cytochrome c oxidase and nitric oxide in action: molecular mechanisms and pathophysiological implications. *Biochim. Biophys. Acta*, **2012**, *1817,* 610–619. DOI: 10.1016/j.bbabio.2011.09.002.

[115] Sawicki, G.; Salas, E.; Murat, J.; Miszta-Lane, H.; Radomski, M.W. Release of gelatinase A during platelet activation mediates aggregation. *Nature*, **1997**, *386,* 616–619. DOI: 10.1038/386616a0.

[116] Malinski, T.; Radomski, M.W.; Taha, Z.; Moncada, S. Direct electrochemical measurement of nitric oxide released from human platelets. *Biochem. Biophys. Res. Commun.*, **1993**, *194,* 960–965. DOI: 10.1006/bbrc.1993.1914.

[117] Rubanyi, G.M.; Romero, J.C.; Vanhoutte, P.M. Flow-induced release of endothelium-derived relaxing factor. *Am. J. Physiol.*, **1986**, *250,* H1145-H1149. DOI: 10.1152/ajpheart.1986.250.6.H1145.

[118] Gkaliagkousi, E.; Ferro, A. Nitric oxide signalling in the regulation of cardiovascular and platelet function. *Front. Biosci. (Landmark Ed).*, **2011**, *16,* 1873–1897. DOI: 10.2741/3828.

[119] Riba, R.; Sharifi, M.; Farndale, R.W.; Naseem, K.M. Regulation of platelet guanylyl cyclase by collagen: evidence that Glycoprotein VI mediates platelet nitric oxide synthesis in response to collagen. *Thromb. Haemost.*, **2005**, *94,* 395–403.

DOI: 10.1160/TH05-01-0027.

[120] Matsuoka, I.; Nakahata, N.; Nakanishi, H. Inhibitory effect of 8-bromo cyclic GMP on an extracellular Ca2+-dependent arachidonic acid liberation in collagen-stimulated rabbit platelets. *Biochem. Pharmacol.*, **1989**, *38,* 1841–1847. DOI: 10.1016/0006-2952(89)90420-6.

[121] Trepakova, E.S.; Cohen, R.A.; Bolotina, V.M. Nitric oxide inhibits capacitative cation influx in human platelets by promoting sarcoplasmic/endoplasmic reticulum Ca2+-ATPase-dependent refilling of Ca2+ stores. *Circ. Res.*, **1999**, *84,* 201–209. DOI: 10.1161/01.res.84.2.201.

[122] Schlossmann, J.; Ammendola, A.; Ashman, K.; Zong, X.; Huber, A.; Neubauer, G.; Wang, G.X.; Allescher, H.D.; Korth, M.; Wilm, M.; Hofmann, F.; Ruth, P. Regulation of intracellular calcium by a signalling complex of IRAG, IP3 receptor and cGMP kinase Ibeta. *Nature*, **2000**, *404,* 197–201. DOI: 10.1038/35004606.

[123] Maurice, D.H.; Haslam, R.J. Molecular basis of the synergistic inhibition of platelet function by nitrovasodilators and activators of adenylate cyclase: inhibition of cyclic AMP breakdown by cyclic GMP. *Mol. Pharmacol.*, **1990**, *37,* 671–681.

[124] Pigazzi, A.; Heydrick, S.; Folli, F.; Benoit, S.; Michelson, A.; Loscalzo, J. Nitric oxide inhibits thrombin receptor-activating peptide-induced phosphoinositide 3-kinase activity in human platelets. *J. Biol. Chem.*, **1999**, *274,* 14368–14375. DOI: 10.1074/jbc.274.20.14368.

[125] Zhang, J.; Shattil, S.J.; Cunningham, M.C.; Rittenhouse, S.E. Phosphoinositide 3-kinase gamma and p85/phosphoinositide 3-kinase in platelets. Relative activation by thrombin receptor or beta-phorbol myristate acetate and roles in promoting the ligand-binding function of alphaIIbbeta3 integrin. *J. Biol. Chem.*, **1996**, *271,* 6265–6272. DOI: 10.1074/jbc.271.11.6265.

[126] Wang, G.R.; Zhu, Y.; Halushka, P.V.; Lincoln, T.M.; Mendelsohn, M.E. Mechanism of platelet inhibition by nitric oxide: in vivo phosphorylation of thromboxane receptor by cyclic GMP-dependent protein kinase. *Proc. Natl. Acad. Sci. USA*, **1998**, *95,* 4888–4893. DOI: 10.1073/pnas.95.9.4888.

[127] Mancardi, D.; Ridnour, L.A.; Thomas, D.D.; Katori, T.; Tocchetti, C.G.; Espey, M.G.; Miranda, K.M.; Paolocci, N.; Wink, D.A. The chemical dynamics of NO and reactive nitrogen oxides: a practical guide. *Curr. Mol. Med.*, **2004**, *4,* 723–740. DOI: 10.2174/1566524043359854.

[128] Gibson, Q.H.; Roughton, F.J. The kinetics and equilibria of the reactions of nitric oxide with sheep haemoglobin. *J. Physiol.*, **1957**, *136,* 507–524. DOI: 10.1113/jphysiol.1957.sp005777.

[129] Stepuro, T.L.; Zinchuk, V.V. Nitric oxide effect on the hemoglobin-oxygen affinity. *J. Physiol. Pharmacol.*, **2006**, *57,* 29–38.

[130] Taylor, M.B.; Christian, K.G.; Patel, N.; Churchwell, K.B. Methemoglobinemia: Toxicity of inhaled nitric oxide therapy. *Pediatr. Crit. Care Med.*, **2001**, *2,* 99–101. DOI: 10.1097/00130478-200101000-00019.

[131] Young, J.D.; Dyar, O.; Xiong, L.; Howell, S. Methaemoglobin production in normal adults inhaling low concentrations of nitric oxide. *Intensive Care Med.*, **1994**, *20,* 581–584. DOI: 10.1007/BF01705726.

[132] Heal, C.A.; Spencer, S.A. Methaemoglobinaemia with high-dose nitric oxide administration. *Acta Paediatr.*, **1995**, *84,* 1318–1319. DOI: 10.1111/j.1651-2227.1995.tb13558.x.

[133] Stamler, J.S. Redox signaling: nitrosylation and related target interactions of nitric oxide. *Cell*, **1994**, *78,* 931–936. DOI: 10.1016/0092-8674(94)90269-0.

[134] Wade, R.S.; Castro, C.E. Redox reactivity of iron(III) porphyrins and heme proteins with nitric oxide. Nitrosyl transfer to carbon, oxygen, nitrogen, and sulfur. *Chem. Res. Toxicol.*, **1990**, *3,* 289–291. DOI: 10.1021/tx00016a002.

[135] Brouwer, M.; Chamulitrat, W.; Ferruzzi, G.; Sauls, D.L.; Weinberg, J.B. Nitric oxide interactions with cobalamins: biochemical and functional consequences. *Blood*, **1996**, *88,* 1857–1864. DOI: 10.1182/blood.V88.5.1857.1857.

[136] Mirvish, S.S.; Sams, J.P. A nitrosating agent from the reaction of atmospheric nitrogen dioxide (NO2) with methyl linoleate: comparison with a product from the skins of NO2-exposed mice. *IARC Sci. Publ.*, **1984,** 283–289.

[137] Halliwell, B.; Gutteridge, J.M. Oxygen toxicity, oxygen radicals, transition metals and disease. *Biochem. J.*, **1984**, *219,* 1–14. DOI: 10.1042/bj2190001.

[138] Jarvis, D.J.; Adamkiewicz, G.; Heroux, M.-E.; Rapp, R.; Kelly, F.J., Eds. *WHO Guidelines for Indoor Air Quality: Selected Pollutants;* World Health Organization, **2010**. ISBN: 9789289002134.

[139] PubChem. Nitrogen Dioxide. https://pubchem.ncbi.nlm.nih.gov/compound/3032552 (Accessed February 16, 2024).

[140] Arashidani, K.; Yoshikawa, M.; Kawamoto, T.; Matsuno, K.; Kayama, F.; Kodama, Y. Indoor pollution from heating. *Ind. Health*, **1996**, *34*, 205–215. DOI: 10.2486/indhealth.34.205.

[141] Hesterberg, T.W.; Bunn, W.B.; McClellan, R.O.; Hamade, A.K.; Long, C.M.; Valberg, P.A. Critical review of the human data on short-term nitrogen dioxide (NO2) exposures: evidence for NO2 no-effect levels. *Crit. Rev. Toxicol.*, **2009**, *39*, 743–781. DOI: 10.3109/10408440903294945.

[142] Shammas, N.K.; Wang, L.K.; Wang, M.-H.S. Sources, Chemistry and Control of Acid Rain in the Environment. In: *Handbook of environment and waste management*: *Volume 3: Acid rain and greenhouse gas*. Hung, Y.-T., Wang, L.K., Shammas, N.K., Eds.; WORLD SCIENTIFIC: Singapore, Hackensack, NJ, **2020**; Vol. *03*; pp. 1–26. ISBN: 978-981-12-0712-9.

[143] US EPA. Effects of Acid Rain | US EPA. https://www.epa.gov/acidrain/effects-acid-rain (Accessed February 16, 2024).

[144] US EPA. Acid Rain Program Results | US EPA. https://www.epa.gov/acidrain/acid-rain-program-results (Accessed February 16, 2024).

[145] Chen, T.-M.; Gokhale, J.; Shofer, S.; Kuschner, W.G. Outdoor air pollution: nitrogen dioxide, sulfur dioxide, and carbon monoxide health effects. *Am. J. Med. Sci.*, **2007**, *333*, 249–256. DOI: 10.1097/MAJ.0b013e31803b900f.

[146] Air Quality, Energy and Health (AQE); Chemical Safety and Health Unit (CHE) *Air quality guidelines for Europe, 2nd edition;* World Health Organization Regional Office for Europe: Copenhagen, **2000**. ISBN: 978-92-890-1358-1.

[147] Ehrlich, R.; Henry, M.C. Chronic toxicity of nitrogen dioxide. I. Effect on resistance to bacterial pneumonia. *Arch. Environ. Health*, **1968**, *17*, 860–865. DOI: 10.1080/00039896.1968.10665342.

[148] Chauhan, A.J.; Inskip, H.M.; Linaker, C.H.; Smith, S.; Schreiber, J.; Johnston, S.L.; Holgate, S.T. Personal exposure to nitrogen dioxide (NO2) and the severity of virus-induced asthma in children. *Lancet*, **2003**, *361*, 1939–1944. DOI: 10.1016/s0140-6736(03)13582-9.

[149] Hwang, J.-S.; Chan, C.-C. Effects of air pollution on daily clinic visits for lower respiratory tract illness. *Am J. Epidemiol.*, **2002**, *155*, 1–10. DOI: 10.1093/aje/155.1.1.

[150] Maheswaran, R.; Haining, R.P.; Brindley, P.; Law, J.; Pearson, T.; Fryers, P.R.; Wise, S.; Campbell, M.J. Outdoor air pollution and stroke in Sheffield, United Kingdom: a small-area level geographical study. *Stroke*, **2005**, *36,* 239–243. DOI: 10.1161/01.STR.0000151363.71221.12.

[151] Barnett, A.G.; Williams, G.M.; Schwartz, J.; Best, T.L.; Neller, A.H.; Petroeschevsky, A.L.; Simpson, R.W. The effects of air pollution on hospitalizations for cardiovascular disease in elderly people in Australian and New Zealand cities. *Environ. Health Perspect.*, **2006**, *114,* 1018–1023. DOI: 10.1289/ehp.8674.

[152] Ogihara, T. Oxidative Degradation of Polyethylene in Nitrogen Dioxide. *Bull. Chem. Soc. Jpn.*, **1963**, *36,* 58–63. DOI: 10.1246/bcsj.36.58.

[153] Ogihara, T.; Tsuchiya, S.; Kuratani, K. Initial Stage of the Oxidation Reaction of Polyethylene by Nitrogen Dioxide. *Bull. Chem. Soc. Jpn.*, **1965**, *38,* 978–984. DOI: 10.1246/bcsj.38.978.

[154] Jellinek, H.H.G.; Toyoshima, Y. Reaction of nitrogen dioxide with polystyrene films. *J. Polym. Sci. A-1 Polym. Chem.*, **1967**, *5,* 3214–3218. DOI: 10.1002/pol.1967.150051221.

[155] Jellinek, H.H.G.; Flajsman, F. Reaction of nitrogen dioxide with polystyrene films. *J. Polym. Sci. A-1 Polym. Chem.*, **1969**, *7,* 1153–1168. DOI: 10.1002/pol.1969.150070412.

[156] Jellinek, H.H.G.; Flajsman, F.; Kryman, F.J. Reaction of SO2 and NO2 with polymers. *J. Appl. Polym. Sci.*, **1969**, *13,* 107–116. DOI: 10.1002/app.1969.070130112.

[157] Jellinek, H.H.G.; Flajsman, F. Chain scission of butyl rubber by nitrogen dioxide in absence and presence of air. *J. Polym. Sci. A-1 Polym. Chem.*, **1970**, *8,* 711–726. DOI: 10.1002/pol.1970.150080314.

[158] Jellinek, H.H.G.; Martin, F.; Wegener, H. Tensile strength of polyurethane exposed to nitrogen dioxide. *J. Appl. Polym. Sci.*, **1974**, *18,* 1773–1778. DOI: 10.1002/app.1974.070180615.

[159] Jellinek, H.H.G.; Wang, T.J.Y. Reaction of nitrogen dioxide with linear polyurethane. *J. Polym. Sci. Polym. Chem. Ed.*, **1973**, *11,* 3227–3242. DOI: 10.1002/pol.1973.170111216.

[160] Jellinek, H.H.G. Reactions of Linear Polymers with Nitrogen Dioxide and Sulfur Dioxide. *Text. Res. J.*, **1973**, *43,* 557–560. DOI: 10.1177/004051757304301001.

[161] Gray, P.; Williams, A. The Thermochemistry And Reactivity Of Alkoxyl Radicals. *Chem. Rev.*, **1959**, *59*, 239–328. DOI: 10.1021/cr50026a002.

[162] Davydov, E.; Gaponova, I.; Pariiskii, G.; Pokholok, T.; Zaikov, G. Reactivity of Polymers on Exposure to Nitrogen Dioxide. *Chem. Chem. Technol.*, **2010**, *4*, 281–290. DOI: 10.23939/chcht04.04.281.

[163] Giamalva, D.H.; Kenion, G.B.; Church, D.F.; Pryor, W.A. Rates and mechanisms of reactions of nitrogen dioxide with alkenes in solution. *J. Am. Chem. Soc.*, **1987**, *109*, 7059–7063. DOI: 10.1021/ja00257a025.

[164] Oluwoye, I.; Altarawneh, M.; Gore, J.; Bockhorn, H.; Dlugogorski, B.Z. Oxidation of Polyethylene under Corrosive NO x Atmosphere. *J. Phys. Chem. C*, **2016**, *120*, 3766–3775. DOI: 10.1021/acs.jpcc.5b10466.

[165] Powell, J.L.; Ridd, J.H.; Sandall, J.P.B. The mechanism of addition of nitrogen dioxide to alkenes. Evidence from 15N nuclear polarisation. *J. Chem. Soc., Chem. Commun.*, **1990,** 402–403. DOI: 10.1039/c39900000402.

[166] Lopez, L.C.; Wilkes, G.L.; Stricklen, P.M.; White, S.A. Synthesis, Structure, and Properties of Poly(4-Methyl-1 -Pentene). *J. Macromol. Sci. Polymer Rev.*, **1992**, *32*, 301–406. DOI: 10.1080/15321799208021429.

[167] Giannini, U.; Zucchini, U.; Albizzati, E. Polymerization of olefins with benzyl derivatives of titanium and of zirconium. *J. Polym. Sci. B Polym. Lett.*, **1970**, *8*, 405–410. DOI: 10.1002/pol.1970.110080604.

[168] Burfield, D.R.; McKenzie, I.D.; Tait, P. Ziegler-Natta catalysis: 1. A general kinetic scheme. *Polymer*, **1972**, *13*, 302–306. DOI: 10.1016/0032-3861(72)90095-X.

[169] Kissin, Y.V. Mechanism of Isospecific Olefin Polymerization. In: *Isospecific Polymerization of Olefins*. Kissin, Y.V., Ed.; Springer New York: New York, NY, **1985**; pp. 372–427. ISBN: 978-1-4612-9556-3.

[170] Ferraris, G.; Corno, C.; Priola, A.; Cesca, S. On the Cationic Polymerization of 4-Methyl-1-pentene and the Structure of the Product Polymer. *Macromolecules*, **1977**, *10*, 188–197. DOI: 10.1021/ma60055a038.

[171] Griffith, J.H.; Rånby, B.G. Dilatometric measurements on poly(4-methyl-1-pentene) glass and melt transition temperatures, crystallization rates, and unusual density behavior. *J. Polym. Sci.*, **1960**, *44*, 369–381.
DOI: 10.1002/pol.1960.1204414408.

[172] Isaacson, R.B.; Kirshenbaum, I.; Feist, W.C. Properties of semicrystalline polyolefins: Poly-4-methyl-1-pentene. *J. Appl. Polym. Sci.*, **1964**, *8,* 2789–2799. DOI: 10.1002/app.1964.070080624.

[173] Karasz, F.E.; Bair, H.E.; O'Reilly, J.M. Thermodynamic properties of poly-4-methyl-pentene-1. *Polymer,* **1967**, *8,* 547–560.
DOI: 10.1016/0032-3861(67)90066-3.

[174] Reginato, L. Thermal degradation of poly-4-methylpentene-1. Part 1. The products of degradation. *Makromol. Chem.*, **1970**, *132,* 113–123.
DOI: 10.1002/macp.1970.021320109.

[175] Soebianto, Y.S.; Yoshii, F.; Makuuchi, K.; Ishigaki, I. Radiation grafting of hydrophilic monomers onto poly(4-methylpentene-1), I. Grafting of acrylic acid. *Angew. Makromol. Chem.*, **1987**, *149,* 87–99. DOI: 10.1002/apmc.1987.051490106.

[176] Puleo, A.; Paul, D.; Wong, P. Gas sorption and transport in semicrystalline poly(4-methyl-1-pentene). *Polymer,* **1989**, *30,* 1357–1366.
DOI: 10.1016/0032-3861(89)90060-8.

[177] Entec Polymers. Methyl Methacrylate / ABS (MABS). https://www.entecpolymers.com/products/resin-types/methyl-methacrylate-abs-mabs (Accessed February 22, 2024).

[178] Terlux HD 2802 - Terlux® bei uns günstig einkaufen. http://www.ineos-styrolution.com/Product/-_Terlux-HD-2802_SKU401500230852_lang_de_DE.html (Accessed February 22, 2024).

[179] Chemieuro | Verkauf, Trading und Vertrieb von Polymeren. Methylmethacrylat-Acrylnitrit-Butadien-Styrol. MABS (Accessed February 22, 2024).

[180] TW Plastics. MABS – Methylmethacrylat-Acrylnitril-Butadien-Styrol - TW Plastics (Accessed February 22, 2024).

[181] INEOS Stryrolution Group GmbH *Terlux HD 2802 Methyl Metharcrylate Acrylonitrile Butadiene Styrene (MABS): Technical Datasheet*, **January 20, 2016.** http://www.ineos-styrolution.com/Product/-_Terlux-HD-2802_SKU401500230852_lang_de_DE.html (Accessed February 22, 2024).

[182] Sáenz-Pérez, M.; Lizundia, E.; Laza, J.M.; García-Barrasa, J.; Vilas, J.L.; León, L.M. Methylene diphenyl diisocyanate (MDI) and toluene diisocyanate (TDI) based polyurethanes: thermal, shape-memory and mechanical behavior. *RSC Adv.*, **2016**, *6,* 69094–69102. DOI: 10.1039/C6RA13492K.

[183] Owuna, F.J.; Dabai, M.U.; Sokoto, M.A.; Dangoggo, S.M.; Bagudo, B.U.; Birnin-Yauri, U.A.; Hassan, L.G.; Sada, I.; Abubakar, A.L.; Jibrin, M.S. Chemical modification of vegetable oils for the production of biolubricants using trimethylolpropane: A review. *Egypt. J. Pet.*, **2020**, *29*, 75–82. DOI: 10.1016/j.ejpe.2019.11.004.

[184] Petrović, Z.S.; Ferguson, J. Polyurethane elastomers. *Prog. Polym. Sci.*, **1991**, *16*, 695–836. DOI: 10.1016/0079-6700(91)90011-9.

[185] Akindoyo, J.O.; Beg, M.D.H.; Ghazali, S.; Islam, M.R.; Jeyaratnam, N.; Yuvaraj, A.R. Polyurethane types, synthesis and applications – a review. *RSC Adv.*, **2016**, *6*, 114453–114482. DOI: 10.1039/C6RA14525F.

[186] Peebles, L.H. Sequence Length Distribution in Segmented Block Copolymers. *Macromolecules*, **1974**, *7*, 872–882. DOI: 10.1021/ma60042a034.

[187] Abd El-Raheem, H.M.; Abdel-Monem, Y.K.; El-Sherbiny, I.M.; Lotfy, K.; Basuni, M.M.; Youssef, H.A. Synthesis of Polyurethane Elastomers by One-shot Technique and Study of Different Polyol Types and Hard Segment Content After Exposure to γ-Irradiation. *Appl. Math. Inf. Sci.*, **2018**, *12*, 705–715. DOI: 10.18576/amis/120405.

[188] Smith, T.L. Strength of elastomers—a perspective. *Polym. Eng. Sci.*, **1977**, *17*, 129–143. DOI: 10.1002/pen.760170302.

[189] Smith, T.L. Tensile strength of polyurethane and other elastomeric block copolymers. *J. Polym. Sci. Polym. Phys. Ed.*, **1974**, *12*, 1825–1848. DOI: 10.1002/pol.1974.180120907.

[190] Petrović, Z.S.; Budinski-Simendić, J. Study of the Effect of Soft-Segment Length and Concentration on Properties of Polyetherurethanes. I. The Effect on Physical and Morphological Properties. *Rubber Chem. Technol.*, **1985**, *58*, 685–700. DOI: 10.5254/1.3536086.

[191] Sika Deutschland GmbH *Biresin® DR404 Casting resin for dialyzers: Technical Data Sheet Version 01/2010*, **2010**.

[192] Sika Deutschland GmbH *Biresin® DH41 Komp. B: SICHERHEITSDATENBLATT gemäß Verordnung (EG) Nr. 1907/2006*, **March 01, 2023**.

[193] Sika Deutschland GmbH *Biresin® DR404 Komp. A: SICHERHEITSDATENBLATT gemäß Verordnung (EG) Nr. 1907/2006*, **May 24, 2023**.

[194] Statista. Global thermoplastic production by type 2050 | Statista. https://www.statista.com/statistics/1192886/thermoplastics-production-volume-by-type-globally/ (Accessed February 26, 2024).

[195] Regnault, V. Ueber die Zusammensetzung des Chlorkohlenwasserstoffs (Oel des ölbildenden Gases). *Ann. Pharm.*, **1835**, *14,* 22–38. DOI: 10.1002/jlac.18350140105.

[196] Braun, D. Poly(vinyl chloride) on the way from the 19th century to the 21st century. *J. Polym. Sci. A Polym. Chem.,* **2004**, *42,* 578–586. DOI: 10.1002/pola.10906.

[197] Patrick, S.; Rapra Technology Limited *Practical guide to polyvinyl chloride;* Rapra Technology: Shrewsbury, Shropshire, **2005**. ISBN: 1847350526.

[198] Endo, K. Synthesis and structure of poly(vinyl chloride). *Prog. Polym. Sci.*, **2002**, *27,* 2021–2054. DOI: 10.1016/S0079-6700(02)00066-7.

[199] Wilson, A.S. *Plasticisers - selection, applications and implications;* Rapra Technology Ltd: Shawbury, Shrewsbury, **1996**. ISBN: 1859570631.

[200] Extrusion: ECC Schlauch und Konnektoren | Raumedic. https://www.raumedic.com/de/kompetenzen/produktion/extrusion/ecc-schlauch (Accessed April 24, 2023).

[201] Bui, T.T.; Giovanoulis, G.; Cousins, A.P.; Magnér, J.; Cousins, I.T.; Wit, C.A. de. Human exposure, hazard and risk of alternative plasticizers to phthalate esters. *Sci. Total. Environ.*, **2016**, *541,* 451–467. DOI: 10.1016/j.scitotenv.2015.09.036.

[202] Jamarani, R.; Erythropel, H.C.; Nicell, J.A.; Leask, R.L.; Marić, M. How Green is Your Plasticizer? *Polymers*, **2018**, *10,* 1–17. DOI: 10.3390/polym10080834.

[203] Grymel, A.; Latos, P.; Matuszek, K.; Erfurt, K.; Barteczko, N.; Pankalla, E.; Chrobok, A. Sustainable Method for the Synthesis of Alternative Bis(2-Ethylhexyl) Terephthalate Plasticizer in the Presence of Protic Ionic Liquids. *Catalysts*, **2020**, *10,* 1–11. DOI: 10.3390/catal10040457.

[204] Murphy, J. Modifying Processing Characteristics: Plasticizers. In: *Additives for Plastics Handbook (Second Edition)*; Elsevier: Amsterdam, **2001**; pp. 169–175. ISBN: 9781856173704.

[205] Consumer Product Safety Commission *Prohibition of Children's Toys and Child Care Articles Containing Specified Phthalates*, **December 30, 2014**.

[206] European Parliament; European Council *Directive 2005/84/EC of the European Parliament and of the Council of 14 December 2005 amending for the 22nd time*

Council Directive 76/769/EEC on the approximation of the laws, regulations and administrative provisions of the Member States relating to restrictions on the marketing and use of certain dangerous substances and preparations (phthalates in toys and childcare articles), **December 27, 2005**.

[207] Grass, M. Dialkyl terephthalates and their use. US7964658B2, January 12, 2007.

[208] Bee, S.-T.; Mok, W.-R.; Lee, T.S.; Tee, T.-T.; Issabayeva, G.; Rahmat, A.R. Evaluation performance of multiple plasticizer systems on the physicomechanical, crystallinity and thermogravimetry of polyvinyl chloride. *J. Polym. Eng. J.*, **2014**, *34*, 521–529. DOI: 10.1515/polyeng-2013-0324.

[209] Iwase, H. Biological Effects of the Plasticizer Tris (2-Ethylhexyl) Trimellitate. *Clinic. Pharmacol. Biopharm.*, **2014**, *S2*, 1–7. DOI: 10.4172/2167-065X.S2-004.

[210] Malarvannan, G.; Onghena, M.; Verstraete, S.; van Puffelen, E.; an Jacobs; Vanhorebeek, I.; Verbruggen, S.C.A.T.; Joosten, K.F.M.; van den Berghe, G.; Jorens, P.G.; Covaci, A. Phthalate and alternative plasticizers in indwelling medical devices in pediatric intensive care units. *J. Hazard. Mater.*, **2019**, *363*, 64–72. DOI: 10.1016/j.jhazmat.2018.09.087.

[211] Pingping, J.; Xian, J.; Xuejun, Y.; Meihua, W. Study On the Synthesis of Tri(2-ethylhexyl)trimellitate. *Acta Chim. Sin.*, **2002**, *60*, 1102–1105.

[212] Zhang, L.; Zhang, J.; Ding, X.; Zhu, J.; Liu, Y.; Fan, Y.; Wu, Y.; Wei, Y. Synthesis and Application of a New Environmental Friendly Plasticizer. *Am. J. Biomed. Sci. Eng.*, **2015**, *1*, 9–19.

[213] Larkin, P. *Infrared and Raman spectroscopy: Principles and spectral interpretation;* Elsevier: Amsterdam, **2018**. ISBN: 9780128042090.

[214] Barrow, G.M. *Introduction to molecular spectroscopy,* 12th ed.; McGraw-Hill: Auckland [u.a.], **1981**. ISBN: 0070859043.

[215] Pauling, L.; Wilson, E.B. *Introduction to quantum mechanics: With applications to chemistry;* Dover Publications: New York, NY, **1963**. ISBN: 978-0486648712.

[216] Diem, M. *Introduction to modern vibrational spectroscopy;* Wiley: New York, NY, **1993**. ISBN: 978-0471595847.

[217] Herzberg, G. *Infrared and Raman Spectra of Polyatomic Molecules;* Van Nostrand: New York, NY, **1945**.

[218] Schrader, B. *Infrared and Raman spectroscopy: Methods and applications;* VCH: Weinheim, **1995**. ISBN: 978-3-527-61542-1.

[219] Colthup, N.B.; Daly, L.H.; Wiberly, S.E. *Introduction to infrared and Raman spectroscopy,* 3rd ed.; Academic Press: San Diego, CA, **1998**. ISBN: 9780121825546.

[220] Socrates, G. *Infrared and Raman characteristic group frequencies: Tables and charts,* 3rd ed.; Wiley: Chichester, **2010**. ISBN: 9780470093078.

[221] Griffiths, P.R.; Haseth, J.A. de *Fourier transform infrared spectrometry,* 2nd ed.; Wiley-Interscience: Hoboken, NJ, **2007**. ISBN: 978-0-471-19404-0.

[222] Hind, A.R.; Bhargava, S.K.; McKinnon, A. At the solid/liquid interface: FTIR/ATR--the tool of choice. *Adv. Colloid Interface Sci.*, **2001**, *93,* 91–114. DOI: 10.1016/s0001-8686(00)00079-8.

[223] Coleman, P.B. *Practical sampling techniques for infrared analysis,* 1st ed.; CRC Press: Boca Raton, FL, **1993**. ISBN: 9780367449766.

[224] Ardenne, M. von. Das Elektronen-Rastermikroskop. *Z. Phys.*, **1938**, *109,* 553–572. DOI: 10.1007/BF01341584.

[225] Goldstein, J.I.; Yakowitz, H. *Practical Scanning Electron Microscopy;* Springer US: Boston, MA, **1975**. ISBN: 978-1-4613-4424-7.

[226] Kirkland, E.J. *Advanced Computing in Electron Microscopy;* Springer US: Boston, MA, **2010**. ISBN: 978-1-4419-6532-5.

[227] Abbe, E. Beiträge zur Theorie des Mikroskops und der mikroskopischen Wahrnehmung. *Arch. Mikr. Anat.*, **1873**, *9,* 413–468. DOI: 10.1007/BF02956173.

[228] Karin Nienhaus; G. Ulrich Nienhaus. Where Do We Stand with Super-Resolution Optical Microscopy? *J. Mol. Biol.*, **2016**, *428,* 308–322. DOI: 10.1016/j.jmb.2015.12.020.

[229] Subramian, K.S.; Janavi, G.J.; Marimuthu, S.; Kannan, M.; Raja, K.; Haripriya S.; Jeya Sundara Sharmila, D.; Sathya Moorthy, P. *Textbook on Fundamentals and Applications of Nanotechnology;* Daya Publishing House: New Delhi, **2018**. ISBN: 978-9390384600.

[230] Calbick, C.J. Historical Background of Electron Optics. *J. Appl. Phys.*, **1944**, *15,* 685–690. DOI: 10.1063/1.1707371.

[231] Ruska, E. The development of the electron microscope and of electron microscopy. *Rev. Mod. Phys.*, **1987**, *59,* 627–638. DOI: 10.1103/RevModPhys.59.627.

[232] McMullan, D. Scanning electron microscopy 1928–1965. *Scanning*, **1995**, *17,* 175–185. DOI: 10.1002/sca.4950170309.

[233] Lloyd, G.E. Atomic number and crystallographic contrast images with the SEM: a review of backscattered electron techniques. *Mineral. Mag.*, **1987**, *51,* 3–19. DOI: 10.1180/minmag.1987.051.359.02.

[234] Radzimski, Z.J. Scanning electron microscope solid state detectors. *Scanning Microsc.*, **1987**, *1,* 975–982.

[235] Robinson, V.N.E. The construction and uses of an efficient backscattered electron detector for scanning electron microscopy. *J. Phys. E: Sci. Instr.*, **1974**, *7,* 650–652. DOI: 10.1088/0022-3735/7/8/019.

[236] Siegbahn, K.; Kungl. Vetenskaps-societeten i Uppsala *ESCA; Atomic, Molecular and Solid State Structure Studied by Means of Electron Spectroscopy;* Almqvist & Wiksells: Uppsala, **1967**.

[237] Chan, C.M.; Weng, L.-T. Surface Characterization of Polymer Blends by XPS and ToF-SIMS. *Materials (Basel),* **2016**, *9,* 655–673. DOI: 10.3390/ma9080655.

[238] Stevie, F.A.; Donley, C.L. Introduction to x-ray photoelectron spectroscopy. *J. Vac. Sci. Technol. A*, **2020**, *38,* 1–20. DOI: 10.1116/6.0000412.

[239] Chastain, J., Ed. *Handbook of X-ray photoelectron spectroscopy: A reference book of standard spectra for identification and interpretation of XPS data;* Physical Electronics: Eden Prairie, MN, **1995**. ISBN: 978-0964812413.

[240] Rouxhet, P.G.; Doren, A.; Dewez, J.L.; Heuschling, O. Chemical composition and physico-chemical properties of polymer surfaces. *Prog. Org. Coat.*, **1993**, *22,* 327–344. DOI: 10.1016/0033-0655(93)80034-8.

[241] Young, T. III. An essay on the cohesion of fluids. *Phil. Trans. R. Soc.*, **1805**, *95,* 65–87. DOI: 10.1098/rstl.1805.0005.

[242] Hebbar, R.S.; Isloor, A.M.; Ismail, A.F. Chapter 12 - Contact Angle Measurements. In: *Membrane Characterization*. Hilal, N., Ismail, A.F., Matsuura, T., Oatley-Radcliffe, D., Eds.; Elsevier: Amsterdam, **2017**; pp. 219–255. ISBN: 978-0-444-63776-5.

[243] Grundke, K. Characterization of Polymer Surfaces by Wetting and Electrokinetic Measurements - Contact Angle, Interfacial Tension, Zeta Potential. In: *Polymer Surfaces and Interfaces: Characterization, Modification and Applications*. Stamm, M., Ed.; Springer: Berlin, Heidelberg, **2008**; pp. 103–138. ISBN: 978-3-540-73865-7.

[244] Gibbs, J.W. *The scientific papers of J. Willard Gibbs;* Ox. Bow. Pr.: Woodbridge, CT, **1970**. ISBN: 0486607216.

[245] Pethica, B.A. The contact angle equilibrium. *J. Colloid Interface Sci.*, **1977**, *62,* 567–569. DOI: 10.1016/0021-9797(77)90110-2.

[246] Marmur, A. Solid-Surface Characterization by Wetting. *Annu. Rev. Mater. Res.*, **2009**, *39,* 473–489. DOI: 10.1146/annurev.matsci.38.060407.132425.

[247] Gauss, C.F. Principia generalia theoriae figurae fluidorum in statu aequilibrii. In: *Werke*: *Fünfter Band*. Gauss, C.F., Ed.; Springer: Berlin, Heidelberg, s.l., **1877**; pp. 287–292. ISBN: 978-3-642-49319-5.

[248] Cassie, A.B.D. Contact angles. *Discuss. Faraday Soc.*, **1948**, *3,* 11–16. DOI: 10.1039/DF9480300011.

[249] Bartell, F.E.; Shepard, J.W. Surface Roughness as Related to Hysteresis of Contact Angles. II. The Systems Paraffin–3 Molar Calcium Chloride Solution–Air and Paraffin–Glycerol–Air. *J. Phys. Chem.*, **1953**, *57,* 455–458. DOI: 10.1021/j150505a015.

[250] Johnson, R.E.; Dettre, R.H. Contact Angle Hysteresis. III. Study of an Idealized Heterogeneous Surface. *J. Phys. Chem.*, **1964**, *68,* 1744–1750. DOI: 10.1021/j100789a012.

[251] Kwok, D.Y.; Neumann, A.W. Contact angle interpretation in terms of solid surface tension. *Colloids Surf. A Physicochem. eng. Asp.*, **2000**, *161,* 31–48. DOI: 10.1016/S0927-7757(99)00323-4.

[252] Kwok, D.Y.; Neumann, A.W. Contact angle interpretation: re-evaluation of existing contact angle data. *Colloids Surf. A Physicochem. eng. Asp.*, **2000**, *161,* 49–62. DOI: 10.1016/S0927-7757(99)00324-6.

[253] Lam, C.; Ko, R.; Yu, L.; Ng, A.; Li, D.; Hair, M.L.; Neumann, A.W. Dynamic Cycling Contact Angle Measurements: Study of Advancing and Receding Contact Angles. *J. Colloid Interface Sci.*, **2001**, *243,* 208–218. DOI: 10.1006/jcis.2001.7840.

[254] Brozova, T.; Raudensky, M. Determination of surface wettability of polymeric hollow fibres. *J. Elastomers Plast.*, **2018**, *50,* 737–746. DOI: 10.1177/0095244318765041.

[255] Bigelow, W.; Pickett, D.L.; Zisman, W. Oleophobic monolayers: I. Films adsorbed from solution in non-polar liquids. *J. Colloid Sci.*, **1946**, *1,* 513–538. DOI: 10.1016/0095-8522(46)90059-1.

[256] Drechsler, A.; Frenzel, R.; Caspari, A.; Michel, S.; Holzschuh, M.; Synytska, A.; Curosu, I.; Liebscher, M.; Mechtcherine, V. Surface modification of poly(vinyl

alcohol) fibers to control the fiber-matrix interaction in composites. *Colloid Polym. Sci.*, **2019**, *297,* 1079–1093. DOI: 10.1007/s00396-019-04528-z.

[257] Jacobasch, H.-J. Characterization of solid surfaces by electrokinetic measurements. *Prog. Org. Coat.*, **1989**, *17,* 115–133. DOI: 10.1016/0033-0655(89)80018-4.

[258] Zimmermann, R.; Rein, N.; Werner, C. Water ion adsorption dominates charging at nonpolar polymer surfaces in multivalent electrolytes. *Phys. Chem. Chem. Phys.*, **2009**, *11*, 4360–4364. DOI: 10.1039/b900755e.

[259] Oatley-Radcliffe, D.L.; Aljohani, N.; Williams, P.M.; Hilal, N. Chapter 18 - Electrokinetic Phenomena for Membrane Charge. In: *Membrane Characterization*. Hilal, N., Ismail, A.F., Matsuura, T., Oatley-Radcliffe, D., Eds.; Elsevier: Amsterdam, **2017**; pp. 405–422. ISBN: 978-0-444-63776-5.

[260] Delgado, A.; González-Caballero, F.; Hunter, R.J.; Koopal, L.; Lyklema, J. Measurement and Interpretation of Electrokinetic Phenomena (IUPAC Technical Report). *Pure Appl. Chem.*, **2005**, *77,* 1753–1805. DOI: 10.1351/pac200577101753.

[261] Stern, O. Zur Theorie der Elektrolytischen Doppelschicht. *Z. Electrochem. Angew. P.*, **1924**, *30,* 508–516.

[262] Lyklema, J.; Rovillard, S.; Coninck, J. de. Electrokinetics: The Properties of the Stagnant Layer Unraveled. *Langmuir*, **1998**, *14,* 5659–5663. DOI: 10.1021/la980399t.

[263] Chang, M.Y.; Robertson, A.A. Zeta potential measurements of fibres. D-C. Streaming current method. *Can. J. Chem. Eng.*, **1967**, *45,* 66–71. DOI: 10.1002/cjce.5450450202.

[264] van Wagenen, R.A.; Andrade, J.D. Flat plate streaming potential investigations: Hydrodynamics and electrokinetic equivalency. *J. Colloid Interface Sci.*, **1980**, *76,* 305–314. DOI: 10.1016/0021-9797(80)90374-4.

[265] Temmel, S.; Kern, W.; Luxbacher, T. Zeta Potential of Photochemically Modified Polymer Surfaces. In: *Characterization of polymer surfaces and thin films*. Grundke, K., Stamm, M., Adler, H.-J., Eds.; Springer: Berlin, Heidelberg, **2006**; Vol. *132*; pp. 54–61. ISBN: 978-3-540-31241-3.

[266] van den Hoven, T.; Bijsterbosch, B.H. Streaming currents, streaming potentials and conductances of concentrated dispersions of negatively-charged, monodisperse polystyrene particles. Effect. *Colloids Surf.*, **1987**, *22,* 171–185. DOI: 10.1016/0166-6622(87)80219-6.

[267] Luna-Vázquez-Gómez, R.; Arellano-García, M.E.; García-Ramos, J.C.; Radilla-Chávez, P.; Salas-Vargas, D.S.; Casillas-Figueroa, F.; Ruiz-Ruiz, B.; Bogdanchikova, N.; Pestryakov, A. Hemolysis of Human Erythrocytes by Argovit™ AgNPs from Healthy and Diabetic Donors: An In Vitro Study. *Materials*, **2021**, *14,* 1–12. DOI: 10.3390/ma14112792.

[268] Phillips, J.; Henderson, A.C. Hemolytic Anemia: Evaluation and Differential Diagnosis. *Am. Fam. Physician*, **2018**, *98,* 354–361.

[269] Blackshear, P.L., JR.; Dorman, F.D.; Steinbach, J.H. Some Mechanical Effects that Influence Hemolysis. *Trans. Am. Soc. Artif. Intern Organs.*, **1965**, *11,* 112–117. DOI: 10.1097/00002480-196504000-00022.

[270] Monroe, J.M.; Lijana, R.C.; Williams, M.C. Hemolytic Properties of Special Materials Exposed to a Shear Flow, and Plasma Changes with Shear. *Biomater. Med. Devices Artif. Organs*, **1980**, *8,* 103–144. DOI: 10.3109/10731198009118976.

[271] Sowemimo-Coker, S.O. Red blood cell hemolysis during processing. *Transfus. Med. Rev.*, **2002**, *16,* 46–60. DOI: 10.1053/tmrv.2002.29404.

[272] Grant, M.S. The effect of blood drawing techniques and equipment on the hemolysis of ED laboratory blood samples. *J. Emerg. Nurs.*, **2003**, *29,* 116–121. DOI: 10.1067/men.2003.66.

[273] Lippi, G.; Blanckaert, N.; Bonini, P.; Green, S.; Kitchen, S.; Palicka, V.; Vassault, A.J.; Plebani, M. Haemolysis: an overview of the leading cause of unsuitable specimens in clinical laboratories. *Clin. Chem. Lab. Med.*, **2008**, *46,* 764–772. DOI: 10.1515/CCLM.2008.170.

[274] Drabkin, D.L.; Austin, J.H. Spectrophotometric Studies: I. Spectrophotometric Constants for Common Hemoglobin Derivatives in Human, Dog, and Rabbit Blood. *J. Biol. Chem.*, **1932**, *98,* 719–733. DOI: 10.1016/S0021-9258(18)76122-X.

[275] Han, V.; Serrano, K.; Devine, D.V. A comparative study of common techniques used to measure haemolysis in stored red cell concentrates. *Vox Sang.*, **2010**, *98,* 116–123. DOI: 10.1111/j.1423-0410.2009.01249.x.

[276] Acker, J.P.; M Croteau, I.; Yi, Q.-L. An analysis of the bias in red blood cell hemolysis measurement using several analytical approaches. *Clin. Chim. Acta*, **2012**, *413,* 1746–1752. DOI: 10.1016/j.cca.2012.06.028.

[277] Owen, T. *Fundamentals of Modern UV-visible Spectroscopy: A Primer;* Hewlett-Packard: Böblingen, **1996**.

[278] Knowles, A.; Burgess, C. *Practical Absorption Spectrometry;* Springer Netherlands: Dordrecht, **1984**. ISBN: 978-94-010-8949-4.

[279] Beer, A. Bestimmung der Absorption des rothen Lichts in farbigen Flüssigkeiten. *Ann. Phys.*, **1852**, *162,* 78–88. DOI: 10.1002/andp.18521620505.

[280] Mayerhöfer, T.G.; Pipa, A.V.; Popp, J. Beer's Law-Why Integrated Absorbance Depends Linearly on Concentration. *Chem. Phys. Chem.*, **2019**, *20,* 2748–2753. DOI: 10.1002/cphc.201900787.

[281] Chanda, M. *Introduction to Polymer Science and Chemistry: A Problem-Solving Approach, Second Edition*, 2nd ed.; CRC Press: Hoboken, **2013**. ISBN: 9781466553842.

[282] Armstrong, J.L., Ed. *Modern Methods for Determining Number-Average Molecular Weights;* Interscience: New York, NY, **1969**.

[283] Madden, M.J.; Ellis, S.N.; Riabtseva, A.; Wilson, A.D.; Cunningham, M.F.; Jessop, P.G. Comparison of vapour pressure osmometry, freezing point osmometry and direct membrane osmometry for determining the osmotic pressure of concentrated solutions. *Desalination*, **2022**, *539,* 1–22. DOI: 10.1016/j.desal.2022.115946.

[284] Pena-Verdeal, H.; García-Resúa, C.; Miñones, M.; Giraldez, M.J.; Yebra-Pimentel, E. Accuracy of a Freezing Point Depression Technique Osmometer. *Optom. Vis. Sci.*, **2015**, *92,* e273-e283. DOI: 10.1097/OPX.0000000000000669.

[285] Tan, C.H.; Ng, H.Y. Modified models to predict flux behavior in forward osmosis in consideration of external and internal concentration polarizations. *J. Membr. Sci.*, **2008**, *324,* 209–219. DOI: 10.1016/j.memsci.2008.07.020.

[286] Wachter, A.H.; Simon, W. Molecular weight determination of polystyrene standards by vapor pressure osmometry. *Anal. Chem.*, **1969**, *41,* 90–94. DOI: 10.1021/ac60270a001.

[287] Raoult, F.-M. Loi générale des tensions de vapeur des dissolvants. *CR Hebd. Seances Acad. Sci*, **1887**, *104,* 1430–1433.

[288] Lewis, G.N. The Osmotic Pressure of Concentrated Solutions, and the Laws of the Perfect Solution. *J. Am. Chem. Soc.*, **1908**, *30,* 668–683. DOI: 10.1021/ja01947a002.

[289] Adams, E.T.; Wan, P.J.; Crawford, E.F. [5] Membrane and vapor pressure osmometry. In: *Methods in Enzymology: Enzyme Structure Part F*; Academic Press: Cambridge, MA, **1978**; Vol. *48*; pp. 69–154. ISBN: 978-0121819484.

[290] Brady, A.P.; Huff, H.; McBain, J.W. Measurement of vapor pressures by means of matched thermistors. *J. Phys. Colloid Chem.*, **1951**, *55,* 304–311. DOI: 10.1021/j150485a017.

[291] Dr. Ing. Herbert Knauer GmbH *K-7000 Vapor Pressure Osmometer Dampfdruckosmometer: User Manual/Handbuch*, **2007**.

[292] Lo, F.Y.F.; Escott, B.M.; Fendler, E.J.; Adams, E.T.; Larsen, R.D.; Smith, P.W. Temperature-dependent self-association of dodecylammonium propionate in benzene and cyclohexane. *J. Phys. Chem.*, **1975**, *79,* 2609–2621. DOI: 10.1021/j100591a009.

[293] Yumpu.com. 1197-M SERIES - Dymax Corporation. https://www.yumpu.com/fr/document/read/49268252/1197-m-series-dymax-corporation (Accessed February 8, 2024).

[294] Schnitzer, C.; Ripperger, S. Influence of Surface Roughness on Streaming Potential Method. *Chem. Eng. Technol.*, **2008**, *31,* 1696–1700. DOI: 10.1002/ceat.200800180.

[295] Briotet, D.; Dos Santos, F. *Final GLP Report: ISO 10993 and ASTM Hemolysis*, **2018**.

[296] Siller-Matula, J.M.; Plasenzotti, R.; Spiel, A.; Quehenberger, P.; Jilma, B. Interspecies differences in coagulation profile. *Thromb. Haemost.*, **2008**, *100,* 397–404. DOI: 10.1160/TH08-02-0103.

[297] Köglmaier, M.; Joost, T.; Kronseder, M.; Kunz, W. Characterization of the interaction of nitric oxide/nitrogen dioxide with the polymer surfaces in ECMO devices. *J. Polym. Res.*, **2024**, *31,* 1–17. DOI: 10.1007/s10965-024-04109-x.

[298] Köglmaier, M.; Caspari, A.; Michel, S.; Auernhammer, G.K.; Kunz, W. Impact of nitric oxide on the surface properties of selected polymers. *J. Polym. Res.*, **2024,** Submitted.

[299] Smith, A.L.; McHard, J.A. Spectroscopic Techniques for Identification of Organosilicon Compounds. *Anal. Chem.*, **1959**, *31,* 1174–1179. DOI: 10.1021/ac60151a029.

[300] Johnson, L.M.; Gao, L.; Shields IV, C.W.; Smith, M.; Efimenko, K.; Cushing, K.; Genzer, J.; López, G.P. Elastomeric microparticles for acoustic mediated bioseparations. *J. Nanobiotechnology*, **2013**, *11,* 1–8. DOI: 10.1186/1477-3155-11-22.

[301] Arkles, B.; Larson, G.L. *Silicon compounds: Silanes and silicones,* 3rd ed.; Gelest: Morrisville, PA, **2013**. ISBN: 978-0-578-12235-9.

[302] Marcus, R.A.; Fresco, J.M. Infrared Absorption Spectra of Nitric Acid and Its Solutions. *J. Chem. Phys.*, **1957**, *27,* 564–568. DOI: 10.1063/1.1743769.

[303] England, C.; Corcoran, W.H. Kinetics and Mechanisms of the Gas-Phase Reaction of Water Vapor and Nitrogen Dioxide. *Ind. Eng. Chem. Fund.*, **1974**, *13,* 373–384. DOI: 10.1021/i160052a014.

[304] Svensson, R.; Ljungström, E.; Lindqvist, O. Kinetics of the reaction between nitrogen dioxide and water vapour. *Atmos. Environ. (1967)*, **1987**, *21,* 1529–1539. DOI: 10.1016/0004-6981(87)90315-5.

[305] Tsukahara, H.; Ishida, T.; Mayumi, M. Gas-Phase Oxidation of Nitric Oxide: Chemical Kinetics and Rate Constant. *Nitric Oxide*, **1999**, *3,* 191–198. DOI: 10.1006/niox.1999.0232.

[306] Skalska, K.; Miller, J.; Ledakowicz, S. Kinetics of nitric oxide oxidation. *Chem. Pap.*, **2010**, *64,* 269–272. DOI: 10.2478/s11696-009-0105-8.

[307] Ridd, J.H. Mechanism of aromatic nitration. *Acc. Chem. Res.*, **1971**, *4,* 248–253. DOI: 10.1021/ar50043a003.

[308] Queiroz, J.F. de; Carneiro, J.W.d.M.; Sabino, A.A.; Sparrapan, R.; Eberlin, M.N.; Esteves, P.M. Electrophilic aromatic nitration: understanding its mechanism and substituent effects. *J. Org. Chem.*, **2006**, *71,* 6192–6203. DOI: 10.1021/jo0609475.

[309] Boschan, R.; Merrow, R.T.; van Dolah, R.W. The Chemistry of Nitrate Esters. *Chem. Rev.*, **1955**, *55,* 485–510. DOI: 10.1021/cr50003a001.

[310] Urbański, T. *Chemistry and technology of explosives;* Pergamon Pr: Oxford, **1983**. ISBN: 978-0080102382.

[311] Shi, H.; Wang, Y.; Hua, R. Acid-catalyzed carboxylic acid esterification and ester hydrolysis mechanism: acylium ion as a sharing active intermediate via a spontaneous trimolecular reaction based on density functional theory calculation and supported by electrospray ionization-mass spectrometry. *Phys. Chem. Chem. Phys.*, **2015**, *17,* 30279–30291. DOI: 10.1039/C5CP02914G.

[312] Pariiskii, G.B.; Gaponova, I.S.; Davydov, E.Y. Reactions of nitrogen oxides with polymers. *Russ. Chem. Rev.*, **2000**, *69,* 985–999. DOI: 10.1070/RC2000v069n11ABEH000611.

[313] Wilhelm, C.; Gardette, J.-L. Infrared analysis of the photochemical behaviour of segmented polyurethanes: aliphatic poly(ether-urethane)s. *Polymer*, **1998**, *39,* 5973–5980. DOI: 10.1016/S0032-3861(97)10065-9.

[314] Rosu, D.; Rosu, L.; Cascaval, C.N. IR-change and yellowing of polyurethane as a result of UV irradiation. *Polym. Degrad. Stab.*, **2009**, *94,* 591–596. DOI: 10.1016/j.polymdegradstab.2009.01.013.

[315] Tcharkhtchi, A.; Farzaneh, S.; Abdallah-Elhirtsi, S.; Esmaeillou, B.; Nony, F.; Baron, A. Thermal Aging Effect on Mechanical Properties of Polyurethane. *Int. J. Polym. Anal. Ch.*, **2014**, *19,* 571–584. DOI: 10.1080/1023666X.2014.932644.

[316] Kontou, E.; Spathis, G.; Niaounakis, M.; Kefalas, V. Physical and chemical cross-linking effects in polyurethane elastomers. *Colloid Polym. Sci.*, **1990**, *268,* 636–644. DOI: 10.1007/BF01410405.

[317] Tsai, Y.-M.; Yu, T.-L.; Tseng, Y.-H. Physical properties of crosslinked polyurethane. *Polym. Int.*, **1998**, *47,* 445–450. DOI: 10.1002/(SICI)1097-0126(199812)47:4<445::AID-PI82>3.0.CO;2-B.

[318] Christenson, E.M.; Anderson, J.M.; Hiltner, A. Biodegradation mechanisms of polyurethane elastomers. *Corros. Eng. Sci. Techn.*, **2007**, *42,* 312–323. DOI: 10.1179/174327807X238909.

[319] Riley, B.; Sapatnekar, S.; Cornell, D.T.; Anderson, J.; Walsh-sukys, M. Impact of prolonged saline solution prime exposure on integrity of extracorporeal membrane oxygenation circuits. *J. Perinatol.*, **1997**, *17,* 444–449.

[320] Siretanu, I.; Chapel, J.-P.; Bastos-González, D.; Drummond, C. Ions-induced nanostructuration: effect of specific ionic adsorption on hydrophobic polymer surfaces. *J. Phys. Chem. B*, **2013**, *117,* 6814–6822. DOI: 10.1021/jp400531x.

[321] Jacobasch, H.-J.; Simon, F.; Weidenhammer, P. Adsorption of ions onto polymer surfaces and its influence on zeta potential and adhesion phenomena. *Colloid Polym. Sci.*, **1998**, *276,* 434–442. DOI: 10.1007/s003960050263.

[322] Camera, E.; Modena, G.; Zotti, B. On the Behaviour of Nitrate Esters in Acid Solution. II. Hydrolysis and oxidation of nitroglycol and nitroglycerin. *Propellants Explo. Pyrotec.*, **1982**, *7,* 66–69. DOI: 10.1002/prep.19820070303.

[323] Martínez, I.; Casas, P.A. Simple model for CO2 absorption in a bubbling water column. *Braz. J. Chem. Eng.*, **2012**, *29,* 107–111. DOI: 10.1590/S0104-66322012000100012.

[324] Khalil, F.Y.; Hanna, M.T. Kinetic salt effects in the acid hydrolysis of potassium ethyl malonate in water and in 50% dioxane – Water mixture. *Monatsh. Chem.*, **1980**, *111,* 841–849. DOI: 10.1007/BF00899249.

[325] Accolla, M.; Pellegrino, G.; Baratta, G.A.; Condorelli, G.G.; Fedoseev, G.; Scirè, C.; Palumbo, M.E.; Strazzulla, G. Combined IR and XPS characterization of organic refractory residues obtained by ion irradiation of simple icy mixtures. *Astron. Astrophys.*, **2018**, *620,* 1–9. DOI: 10.1051/0004-6361/201834057.

[326] Beard, B.C. Cellulose nitrate as a binding energy reference in N(1s) XPS studies of nitrogen-containing organic molecules. *Appl. Surf. Sci.*, **1990**, *45,* 221–227. DOI: 10.1016/0169-4332(90)90005-K.

[327] Sakagami, Y.; Horiguchi, K.; Narita, Y.; Sirithep, W.; Morita, K.; Nagase, Y. Syntheses of a novel diol monomer and polyurethane elastomers containing phospholipid moieties. *Polym. J.*, **2013**, *45,* 1159–1166. DOI: 10.1038/pj.2013.48.

[328] Erkal, A.; Erdoğan, M.S.; Aşık, İ.; Ekşi, H.; Jeon, S.; Solak, A.O.; Üstündağ, Z. Electrografting and Surface Properties of Some Substituted Nitrophenols on Glassy Carbon Electrode and Simultaneous Pb 2+ - Cd 2+ Analysis via Assist of Graphene Oxide Terminated Surface. *J. Electrochem. Soc.*, **2014**, *161,* H696-H704. DOI: 10.1149/2.1081410jes.

[329] Tsunoda, N.; Kokubo, K.; Sakai, K.; Fukuda, M.; Miyazaki, M.; Hiyoshi, T. Surface roughness of cellulose hollow fiber dialysis membranes and platelet adhesion. *ASAIO J.*, **1999**, *45,* 418–423. DOI: 10.1097/00002480-199909000-00010.

[330] Ikada, Y.; Iwata, H.; Horii, F.; Matsunaga, T.; Taniguchi, M.; Suzuki, M.; Taki, W.; Yamagata, S.; Yonekawa, Y.; Handa, H. Blood compatibility of hydrophilic polymers. *J. Biomed. Mater. Res.*, **1981**, *15,* 697–718. DOI: 10.1002/jbm.820150507.

[331] Pelosi, C.; Constantinescu, I.; Son, H.H.; Tinè, M.R.; Kizhakkedathu, J.N.; Wurm, F.R. Blood Compatibility of Hydrophilic Polyphosphoesters. *ACS Appl. Bio. Mater.*, **2022**, *5,* 1151–1158. DOI: 10.1021/acsabm.1c01210.

[332] Kuo, Z.-K.; Fang, M.-Y.; Wu, T.-Y.; Yang, T.; Tseng, H.-W.; Chen, C.-C.; Cheng, C.-M. Hydrophilic films: How hydrophilicity affects blood compatibility and cellular compatibility. *Adv. Polym. Technol.*, **2018**, *37,* 1635–1642. DOI: 10.1002/adv.21820.

[333] Ellison, G.; Straumfjord, J.V.; Hummel, J.P. Buffer Capacities of Human Blood and Plasma. *Clin. Chem.*, **1958**, *4*, 452–461. DOI: 10.1093/clinchem/4.6.452.

[334] Kwok, D.Y.; Gietzelt, T.; Grundke, K.; Jacobasch, H.-J.; Neumann, A.W. Contact Angle Measurements and Contact Angle Interpretation. 1. Contact Angle Measurements by Axisymmetric Drop Shape Analysis and a Goniometer Sessile Drop Technique. *Langmuir*, **1997**, *13*, 2880–2894. DOI: 10.1021/la9608021.

[335] Böhme, F.; Klinger, C.; Bellmann, C. Surface properties of polyamidines. *Colloid. Surface. A*, **2001**, *189*, 21–27. DOI: 10.1016/S0927-7757(01)00593-3.

[336] Fewtrell, L. Drinking-water nitrate, methemoglobinemia, and global burden of disease: a discussion. *Environ. Health Perspect.*, **2004**, *112*, 1371–1374. DOI: 10.1289/ehp.7216.

[337] Hollema, B.L.; Zwiers, S.; Hermesch, S. Genetic parameters for haemoglobin levels in sows and piglets as well as sow reproductive performance and piglet survival. *Animal.*, **2020**, *14*, 688–696. DOI: 10.1017/S1751731119002532.

[338] Rosival, V. Dangers of very low blood pH. *Indian J. Crit. Care Med.*, **2011**, *15*, 194. DOI: 10.4103/0972-5229.84887.

8. Appendix

8.1 NO Treatment of the Oxygenator Materials

8.1.1 FTIR-ATR Spectra

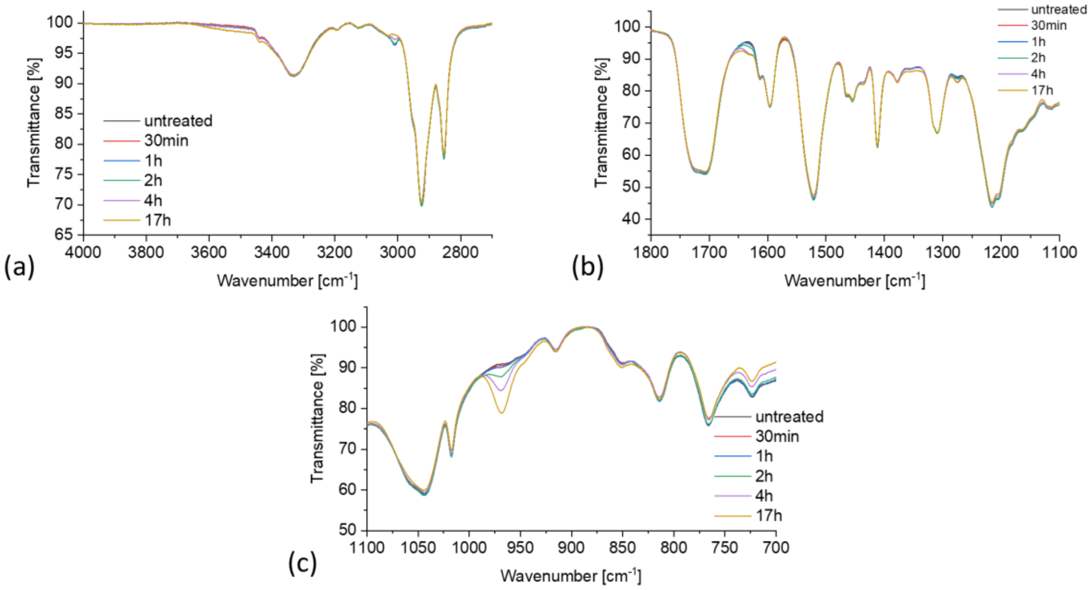

Figure 8.1: Close-up FTIR-ATR spectra of PU treated with NO (1000 ppm) for 30 minutes, one, two, four, and 17 hours in the wavenumber ranges of (a) 4000 to 2700 cm^{-1}, (b) 1800 to 1100 cm^{-1}, and (c) 1100 to 700 cm^{-1}. The experiments were performed according to chapters 3.2.1 and 3.2.3.

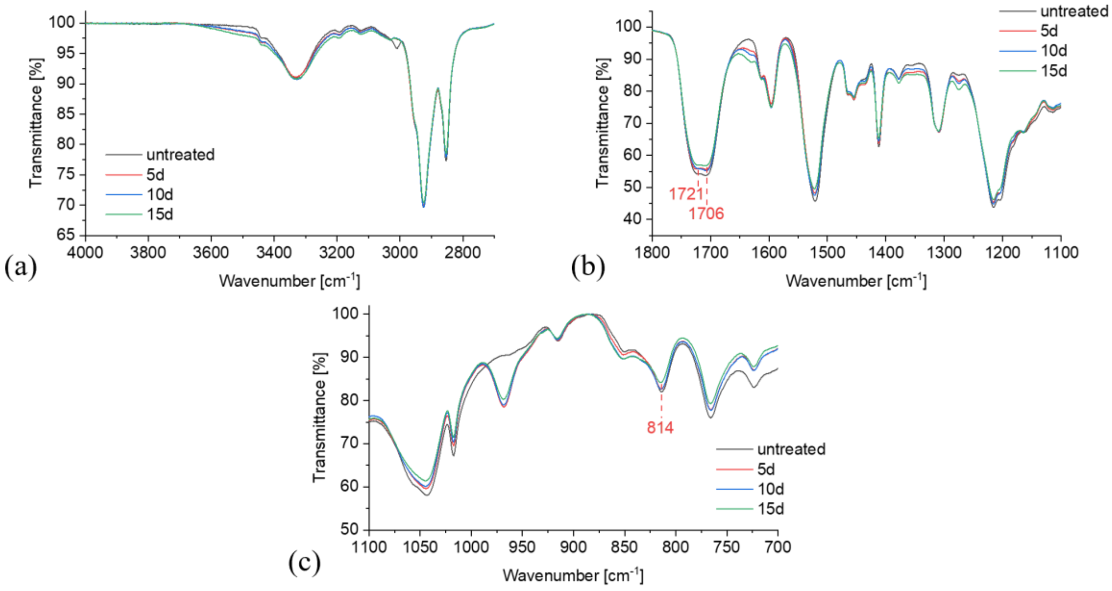

Figure 8.2: Close-up FTIR-ATR spectra of PU treated with NO (1000 ppm) for five, ten, and 15 days in the wavenumber ranges of (a) 4000 to 2700 cm^{-1}, (b) 1800 to 1100 cm^{-1}, and (c) 1100 to 700 cm^{-1}. The experiments were performed according to chapters 3.2.1 and 3.2.3.

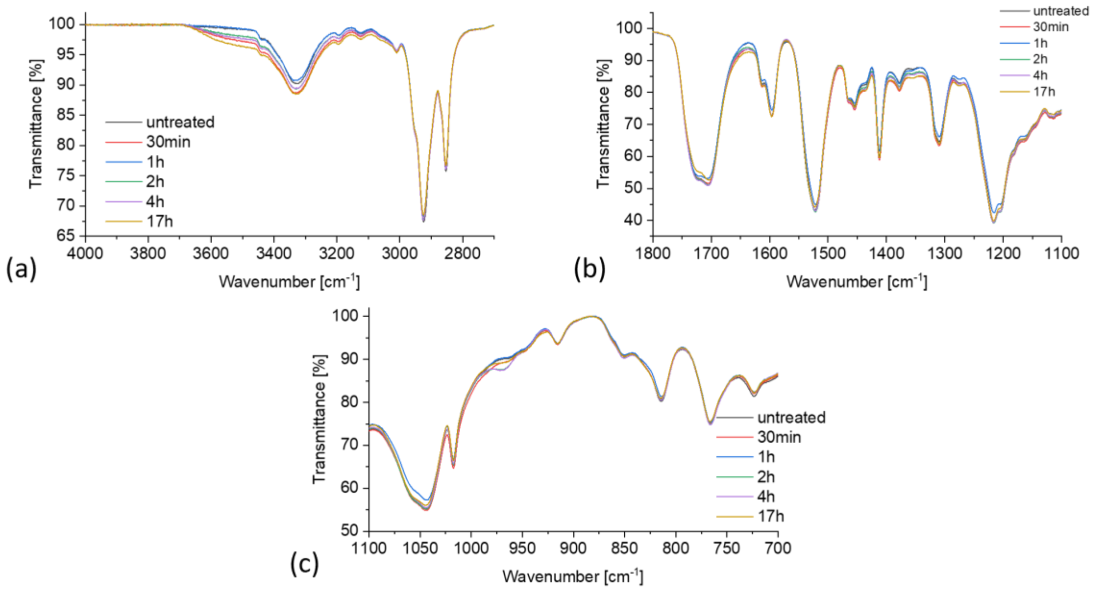

Figure 8.3: Close-up FTIR-ATR spectra of PU treated with NO (80 ppm) for 30 minutes, one, two, four, and 17 hours in the wavenumber ranges of (a) 4000 to 2700 cm^{-1}, (b) 1800 to 1100 cm^{-1}, and (c) 1100 to 700 cm^{-1}. The experiments were performed according to chapters 3.2.1 and 3.2.3.

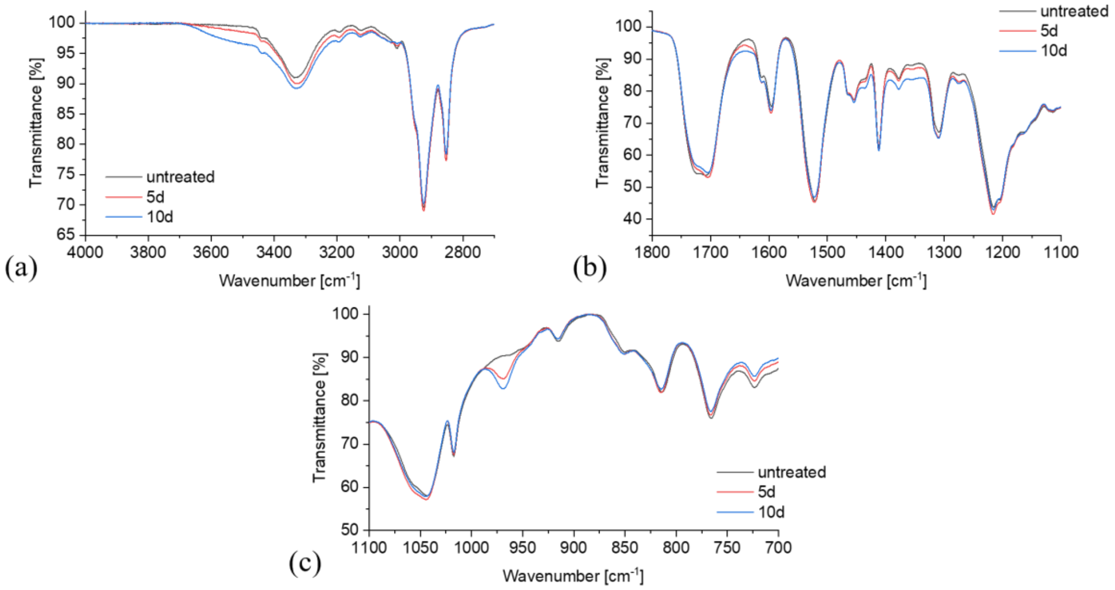

Figure 8.4: Close-up FTIR-ATR spectra of PU treated with NO (80 ppm) for five and ten days in the wavenumber ranges of (a) 4000 to 2700 cm^{-1}, (b) 1800 to 1100 cm^{-1}, and (c) 1100 to 700 cm^{-1}. The experiments were performed according to chapters 3.2.1 and 3.2.3.

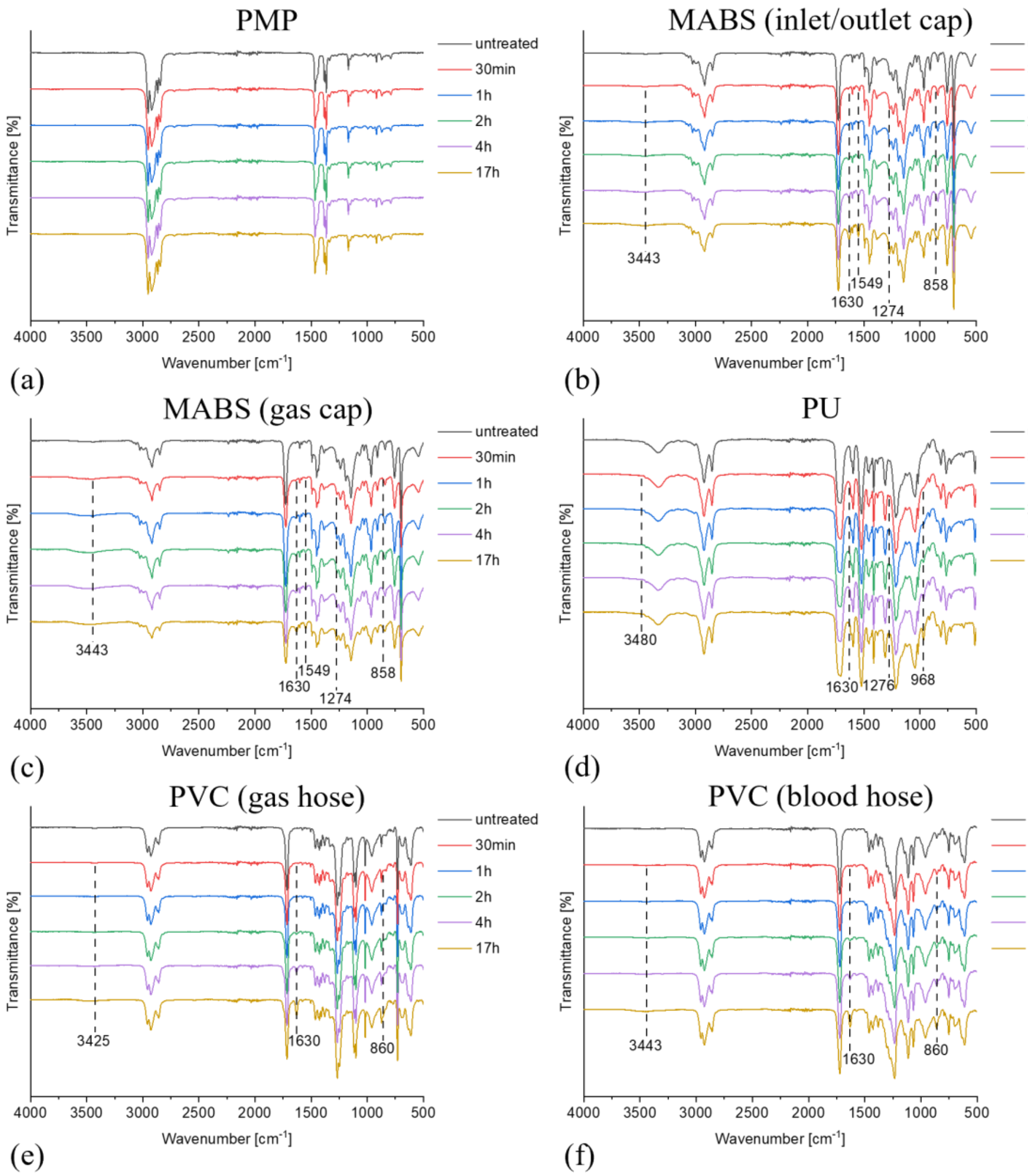

Figure 8.5: Overview of the spectra of (a) PMP, (b) MABS (inlet/outlet cap), (c) MABS (gas cap), (d) PU, (e) PVC (gas hose), and (f) PVC (blood hose) treated with NO_2 (500 ppm) for 30 minutes, one, two, four, and 17 hours. The experiments were performed according to chapters 3.2.1 and 3.2.3.

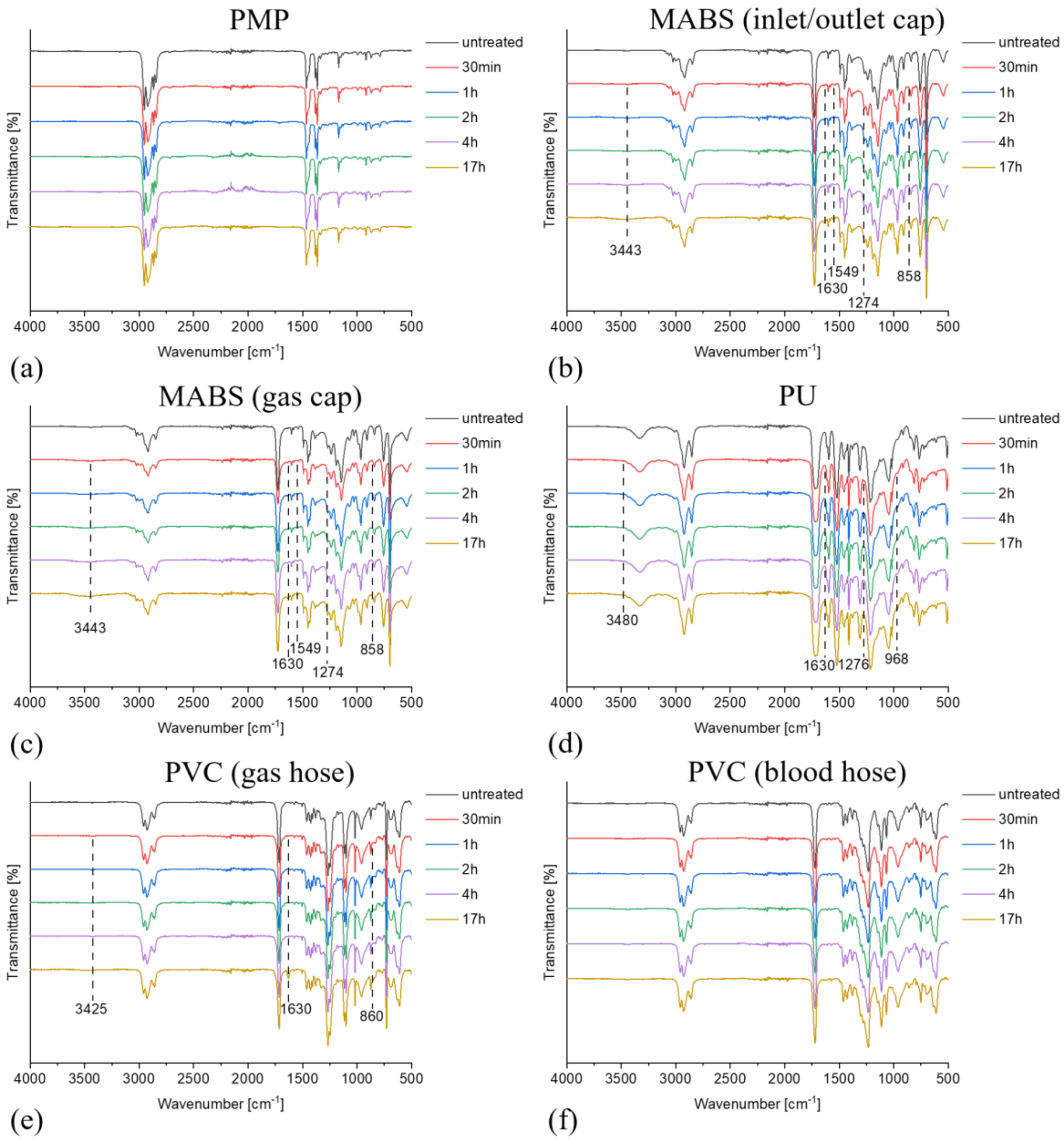

Figure 8.6: Overview of the spectra of (a) PMP, (b) MABS (inlet/outlet cap), (c) MABS (gas cap), (d) PU, (e) PVC (gas hose), and (f) PVC (blood hose) treated with NO_2 (50 ppm) for 30 minutes, one, two, four, and 17 hours. The experiments were performed according to chapters 3.2.1 and 3.2.3.

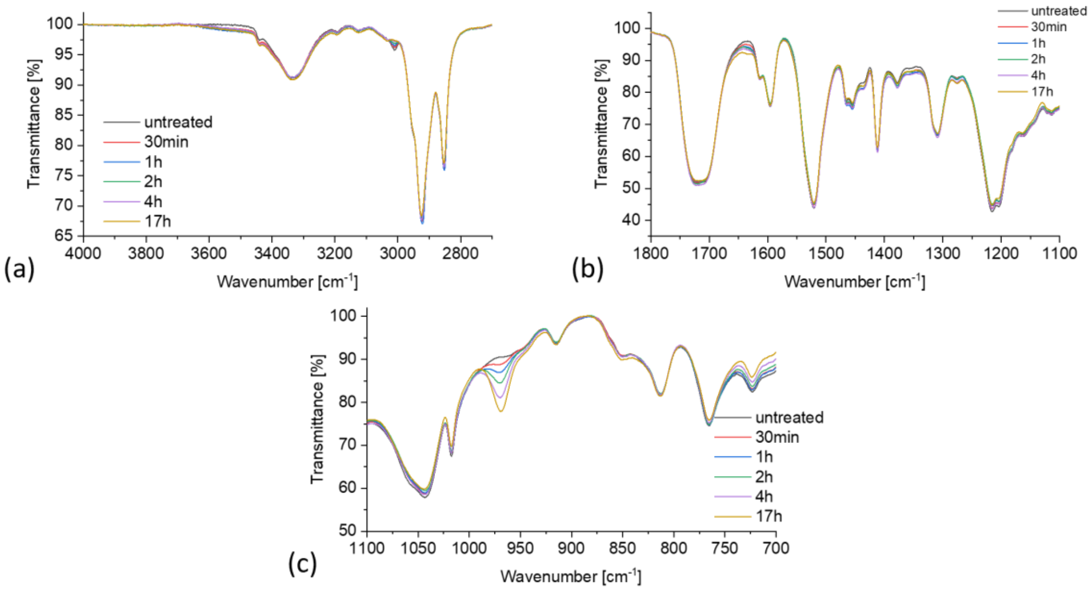

Figure 8.7: Close-up FTIR-ATR spectra of PU treated with NO_2 (1000 ppm) for 30 minutes, one, two, four, and 17 hours in the wavenumber ranges of (a) 4000 to 2700 cm^{-1}, (b) 1800 to 1100 cm^{-1}, and (c) 1100 to 700 cm^{-1}. The experiments were performed according to chapters 3.2.1 and 3.2.3.

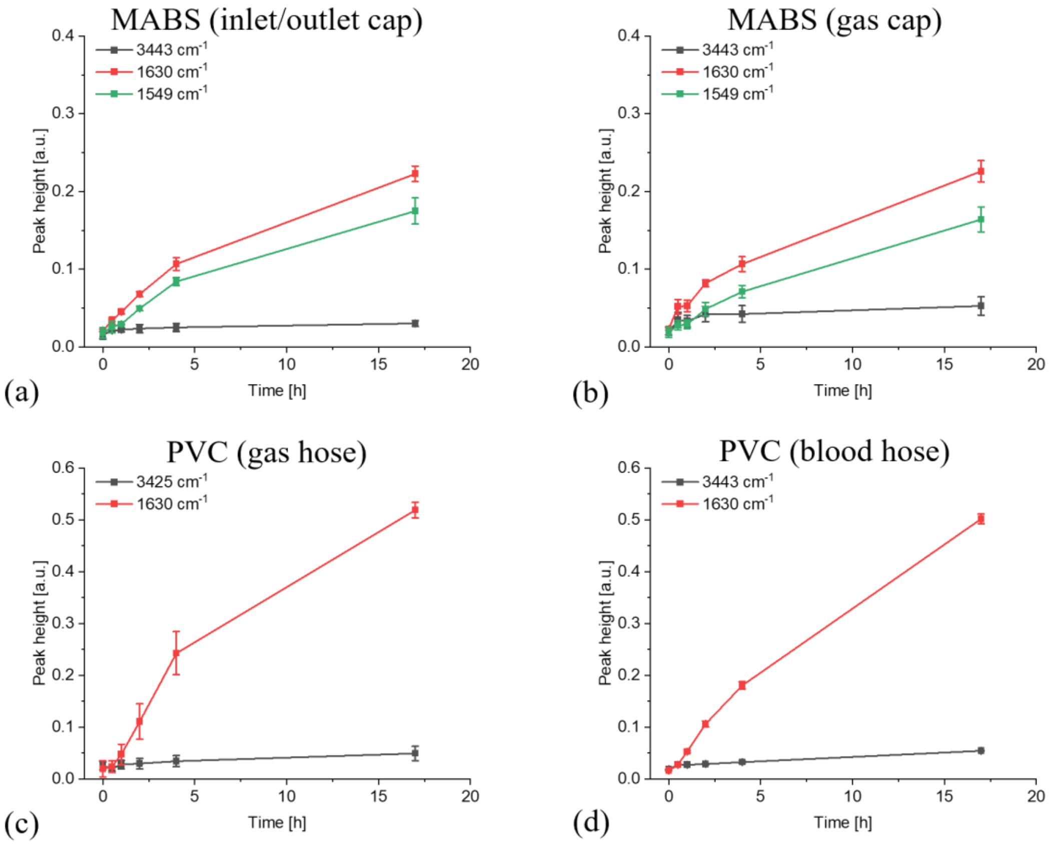

Figure 8.8: Signal heights of the signals caused by the treatment with NO_2 (500 ppm) for (a) MABS (inlet/outlet cap), (b) MABS (gas cap), (c) PVC (gas hose), and (d) PVC (blood hose). The experiments were performed according to chapters 3.2.1 and 3.2.3.

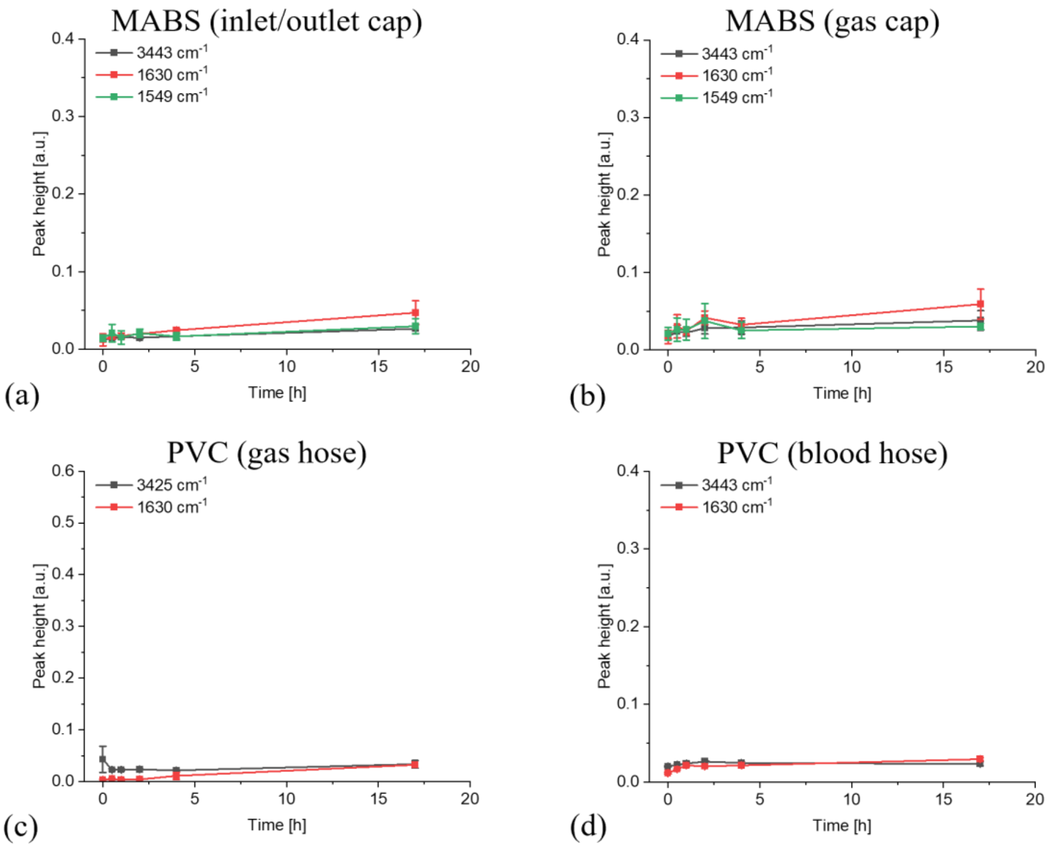

Figure 8.9: Signal heights of the signals caused by the treatment with NO_2 (50 ppm) for (a) MABS (inlet/outlet cap), (b) MABS (gas cap), (c) PVC (gas hose), and (d) PVC (blood hose). The experiments were performed according to chapters 3.2.1 and 3.2.3.

8.1.2 XPS Measurements

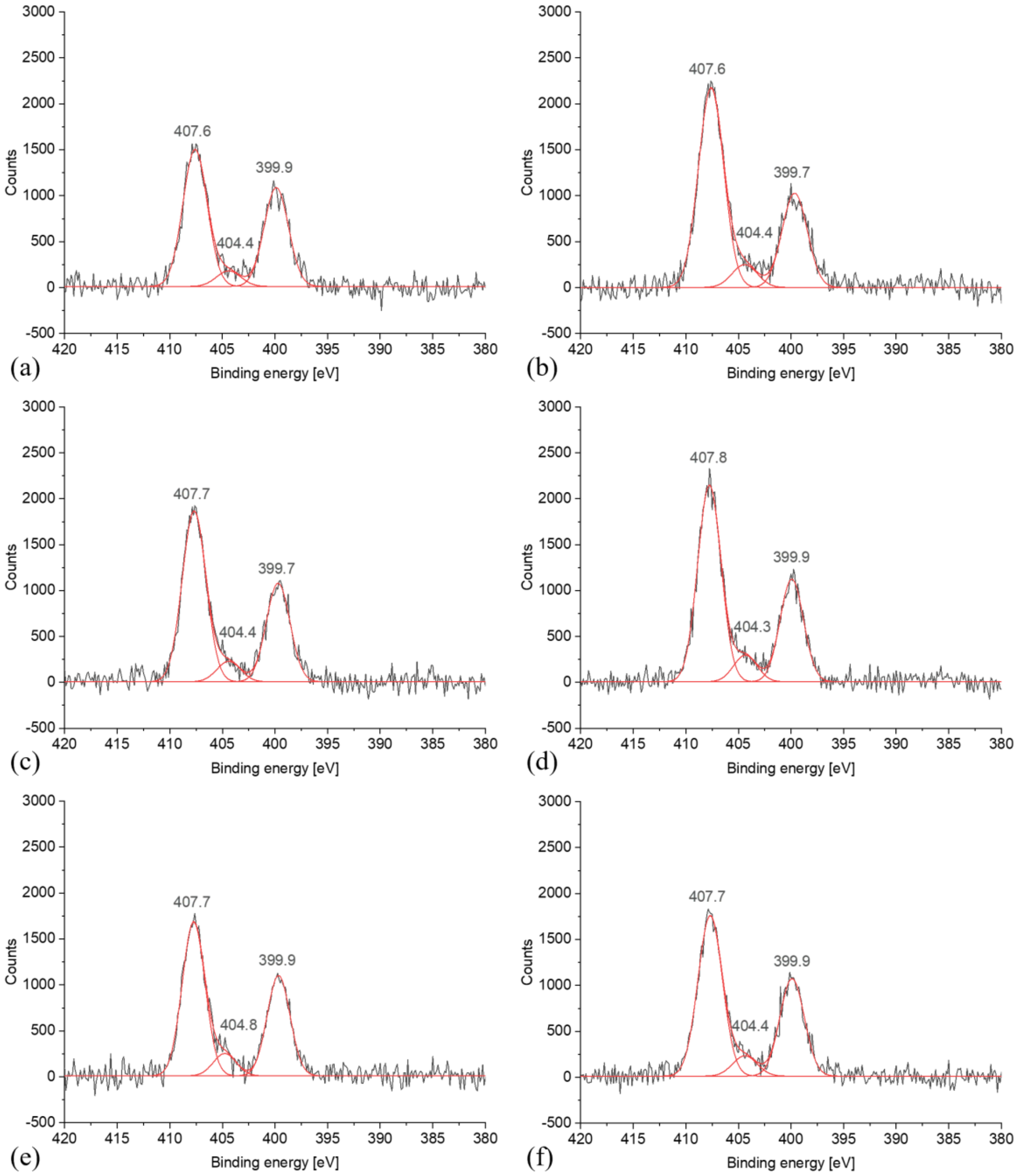

Figure 8.10: Results of the XPS measurements of MABS samples treated with NO (1000 ppm) for 17 hours (a), (b) directly after the gas treatment, (c), (d) six days, and (e), (f) 13 days after the end of the gas treatment. The experiments were performed according to chapters 3.2.1 and 3.2.5.

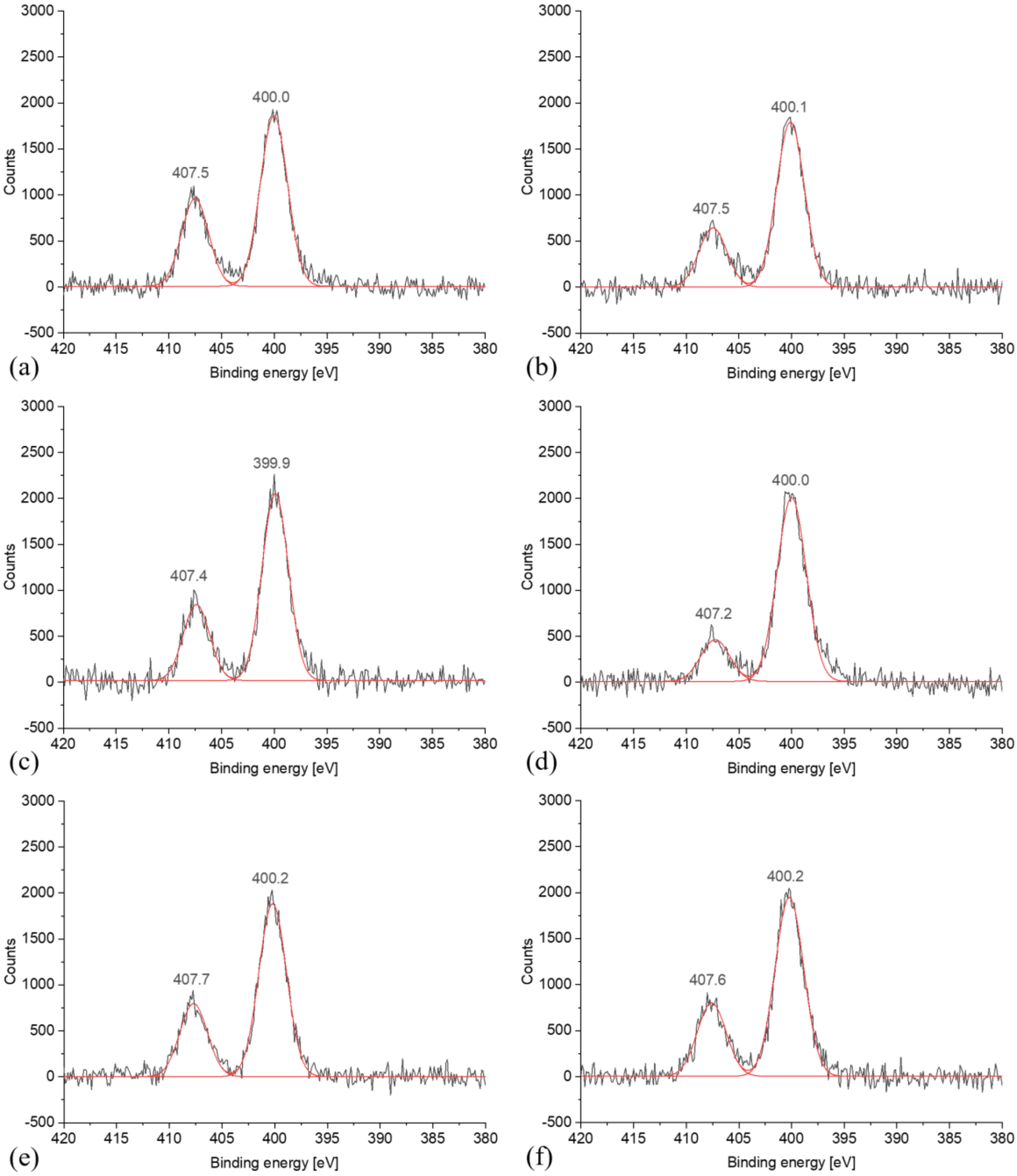

Figure 8.11: Results of the XPS measurements of PU samples treated with NO (1000 ppm) for 17 hours (a), (b) directly after the gas treatment, (c), (d) six days, and (e), (f) 13 days after the end of the gas treatment. The experiments were performed according to chapters 3.2.1 and 3.2.5.

8.1.3 Contact Angle Measurements

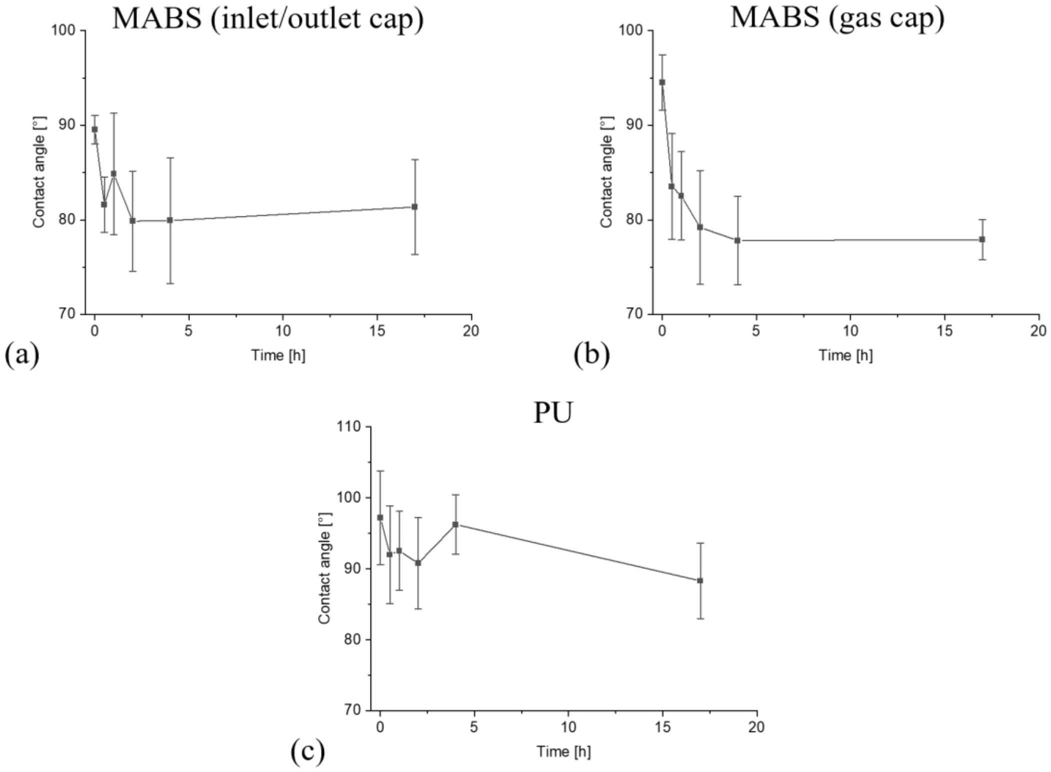

Figure 8.12: Static contact angle measurements of (a) MABS (inlet/outlet cap), (b) MABS (gas cap), and (c) PU treated with NO_2 (500 ppm) for up to 17 hours. The experiments were performed according to chapters 3.2.1 and 3.2.6.1.

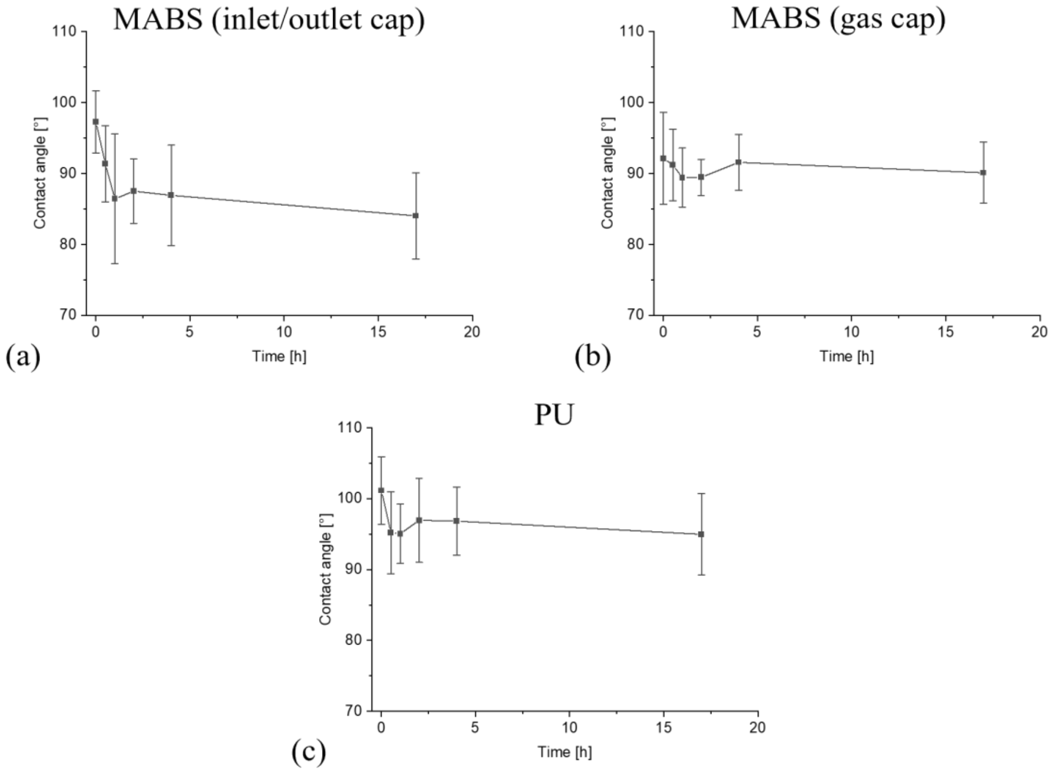

Figure 8.13: Static contact angle measurements of (a) MABS (inlet/outlet cap), (b) MABS (gas cap), and (c) PU treated with NO_2 (50 ppm) for up to 17 hours. The experiments were performed according to chapters 3.2.1 and 3.2.6.1.

8.2 Impact of NO Treatment on Hemolysis

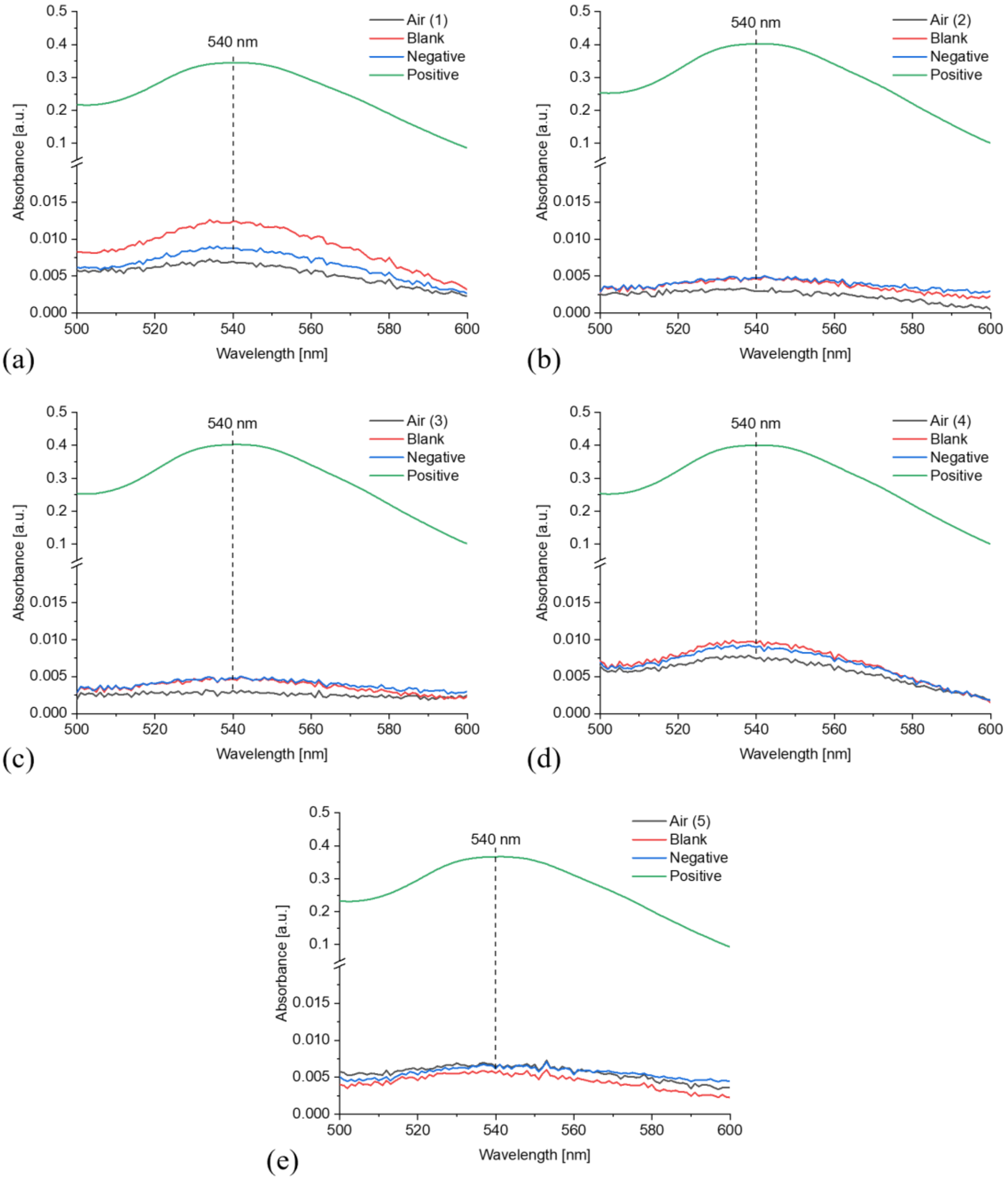

(a) (b) (c) (d) (e)

Figure 8.14: UV/Vis spectra of the signal at 540 nm for the extraction samples of oxygenators perfused with air (grey), the blank control samples (red), the negative control samples (blue), and the positive control samples (green). The experiments were performed according to chapters 3.3.1.1, 3.3.2, and 3.3.3.1.

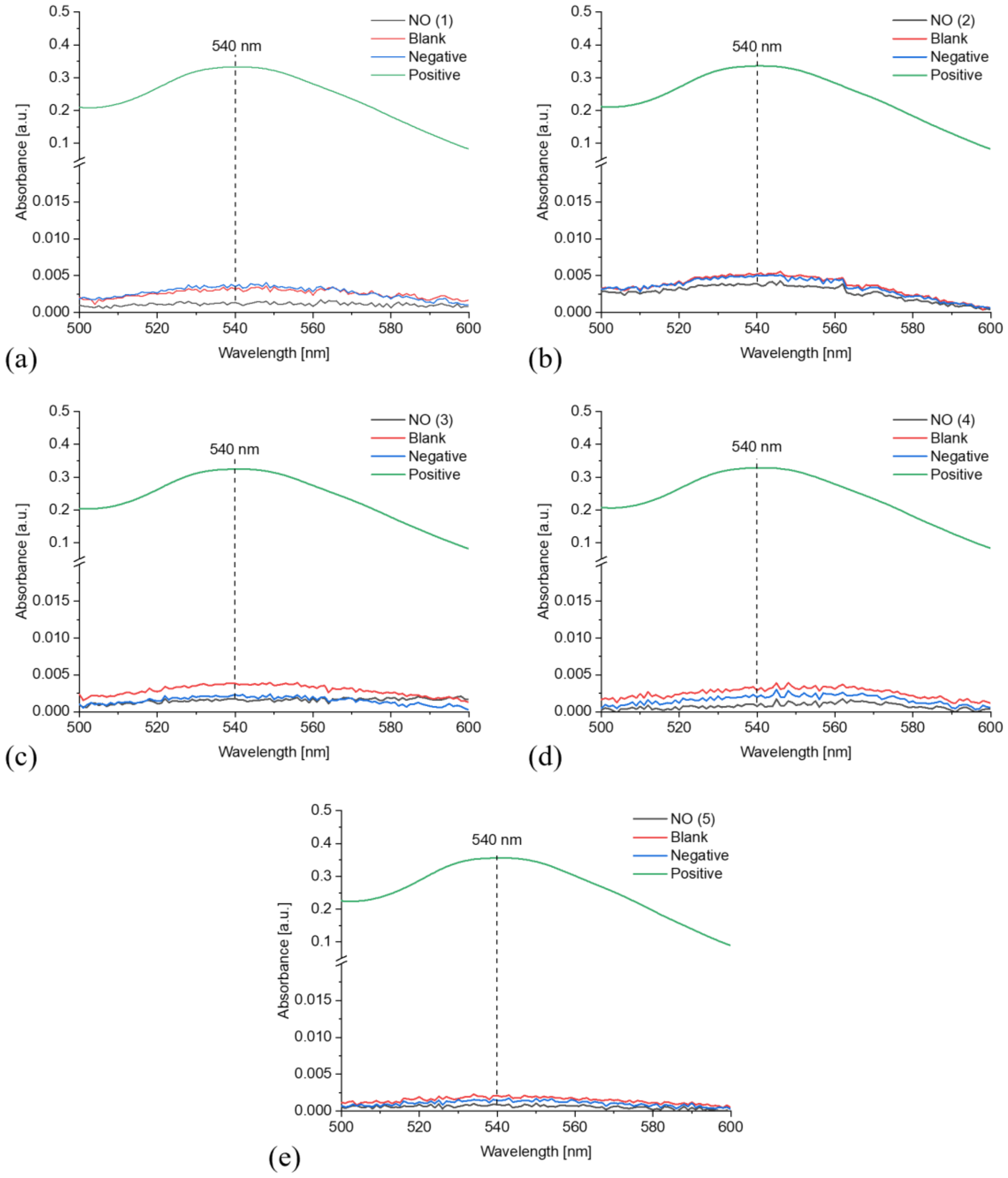

Figure 8.15: UV/Vis spectra of the signal at 540 nm for the extraction samples of oxygenators perfused with NO (40 ppm) (grey), the blank control samples (red), the negative control samples (blue), and the positive control samples (green). The experiments were performed according to chapters 3.3.1.1, 3.3.2, and 3.3.3.1.

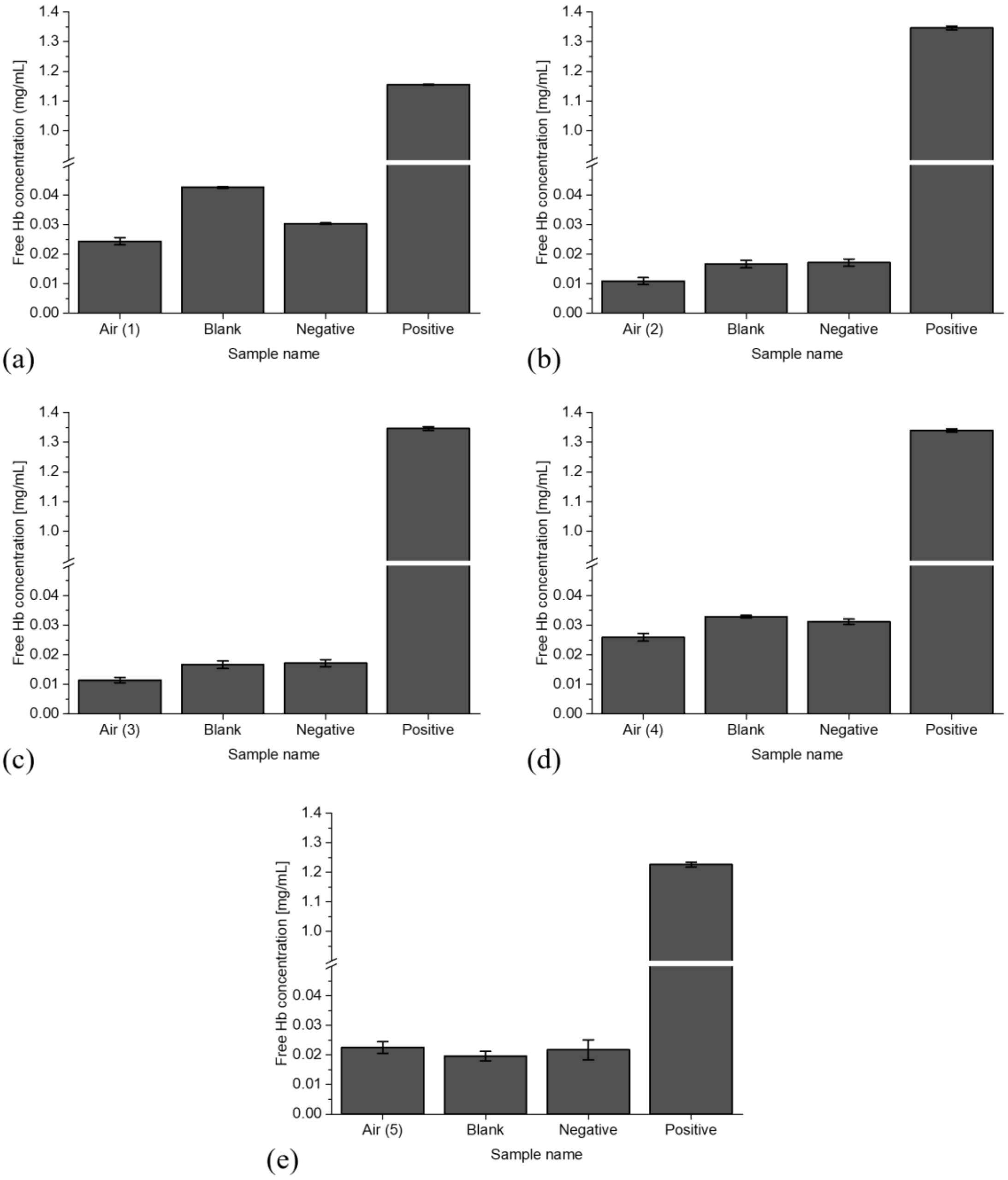

Figure 8.16: Free Hb concentrations of the extraction samples using only air as the perfusion gas, the blank control, negative control, and positive control samples at the end of the experimental procedure. The experiments were performed according to chapters 3.3.1.1, 3.3.2, and 3.3.3.1.

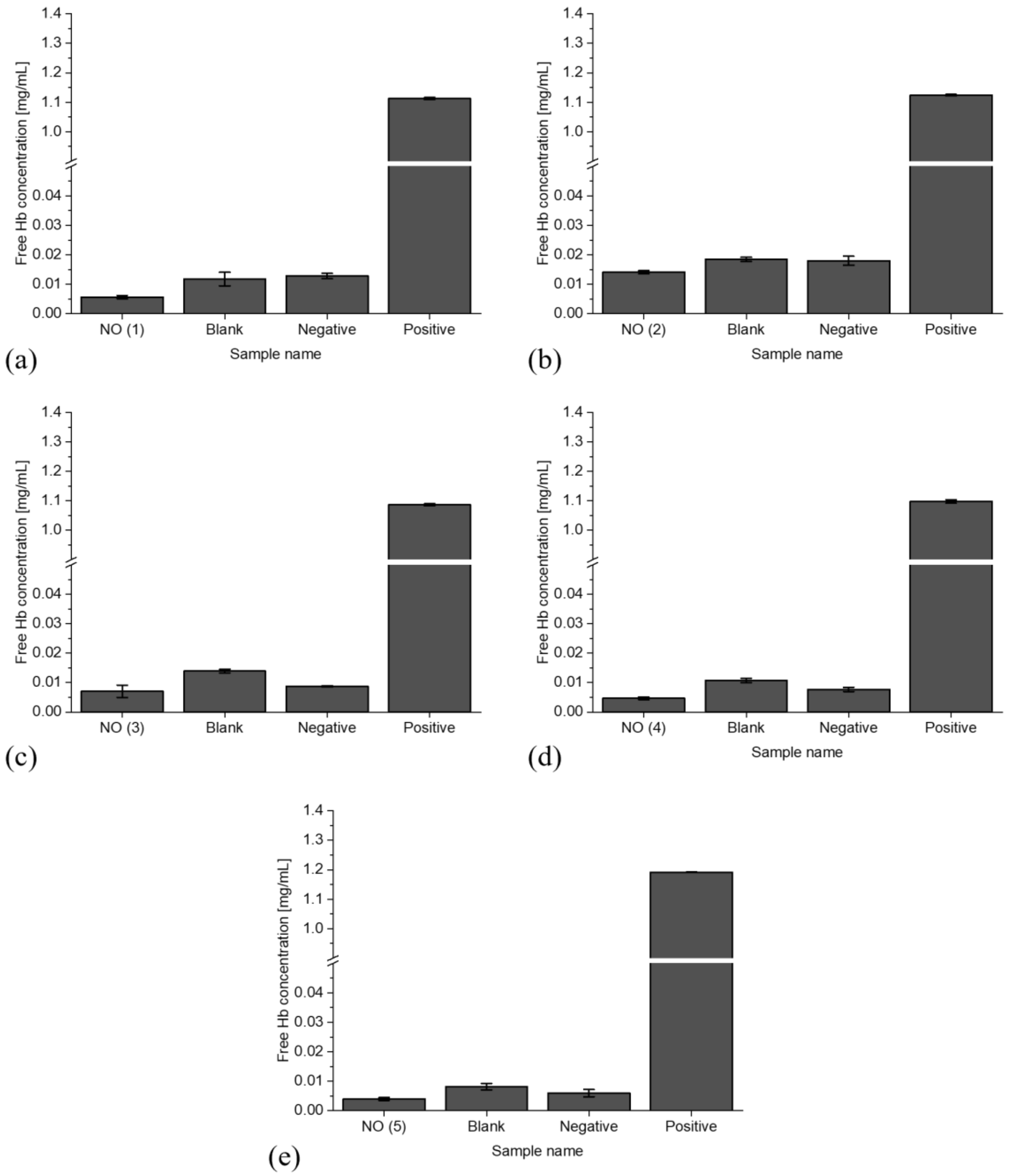

Figure 8.17: Free Hb concentrations of the extraction samples using air mixed with NO (40 ppm) as the perfusion gas, the blank control, negative control, and positive control samples at the end of the experimental procedure. The experiments were performed according to chapters 3.3.1.1, 3.3.2, and 3.3.3.1.

List of Figures

Declaration

Eidesstattliche Erklärung

Ich erkläre hiermit an Eides statt, dass ich die vorliegende Arbeit ohne Hilfe Dritter und ohne Benutzung anderer als der angegebenen Hilfsmittel angefertigt habe. Die aus anderen Quellen direkt oder indirekt übernommenen Daten und Konzepte sind unter Angabe des Literaturzitats gekennzeichnet.

Weitere Personen waren an der inhaltlich-materiellen Herstellung der vorliegenden Arbeit nicht beteiligt. Insbesondere habe ich hierfür nicht die entgeltliche Hilfe eines Promotionsberaters oder anderer Personen in Anspruch genommen. Niemand hat von mir weder unmittelbar noch mittelbar geldwerte Leistungen für Arbeiten erhalten, die im Zusammenhang mit dem Inhalt der vorgelegten Dissertation stehen.

Die Arbeit wurde bisher weder im In- noch im Ausland in gleicher oder ähnlicher Form einer anderen Prüfungsbehörde vorgelegt.

Regensburg, den 03.09.2024

……………………………………………..
Moritz Köglmaier

Statutory Declaration

I herewith declare in lieu of oath that I have composed this thesis without any inadmissible help of a third party and without the use of aids other than those listed. The data and concepts that have been taken directly from other sources have been acknowledged and referenced.

Other persons have not helped to produce this work as regards its content or making. In particular, I have not used the services of any professional agencies in return for payment of those other persons. Nobody has received payment in kind – neither directly nor indirectly – from me for any work that is connected with the content of this doctoral dissertation.

The thesis has not been submitted, wholly or substantially, neither in this country nor abroad for another degree or diploma at any university or institute.

Regensburg, 3rd September 2024

………………………………………………..
Moritz Köglmaier